Analysis of Combustion LES using an Eulerian Monte Carlo PDF Method

Vom Fachbereich Maschinenbau
an der Technischen Universität Darmstadt
zur
Erlangung des Grades eines Doktor-Ingenieurs (Dr.-Ing.)
eingereichte

D i s s e r t a t i o n

vorgelegt von

Dipl.-Ing. Jens Kühne

aus Ehringshausen

Berichterstatter:	Prof. Dr.-Ing. J. Janicka
Mitberichterstatter:	Prof. Dr.-Ing. J. Y. Chen
Tag der Einreichung:	07. Februar 2011
Tag der mündlichen Prüfung:	22. März 2011

Darmstadt 2011

D17

Preface

The present work is the result of my time as a doctoral candidate at the Institute for Energy and Powerplant Technology (EKT) at the Technische Universität Darmstadt.

I would like to thank the head of the institute, Prof. Dr.-Ing. Johannes Janicka, for his support and his large interest in my work. Additionally to the supervision of my work he enabled me to open up my professional as well as my personal horizon by giving me the opportunity to participate in international conferences and to realize my research stay at the University of California at Berkeley.

I also wish to thank Prof. Dr. J. Y. Chen (University of California at Berkeley) for his willingness to report on my work. Furthermore, he has been a supportive reference person during the last five years of my doctorate and especially during the pleasant time I spent in his research group.

In the past five years at the EKT, I have met a multitude of nice colleagues, some of which have become close friends. In this context I would like to thank them for their help and support in professional matters as well as for the fun times we had during my doctorate. These were in the beginning Dr.-Ing. Frederik Hahn and Dr.-Ing. Clemens Olbricht, who helped me getting started and strongly supported me during our shared time at the institute. I am also very grateful to my office mates Michael Baumann, Thomas Breitenberger and Dr.-Ing. Jan Brübach for the motivating atmosphere that was a basis for both interesting discussions and fruitful distractions. I am obliged to Anja Ketelheun, not only for being a respected colleague and friend, but also for providing all employed chemistry tables of this work. Special thanks go to Christian Klewer, who has been a close friend for all my life and has also been one of my closest colleagues during the last five years. In addition, I wish to thank Simone Eisenhuth for all her help related to this work and for being a particular friend.

Finally, I want to express my gratitude to my parents and my family for supporting me wherever and whenever they could. All my friends beyond the EKT are mentioned for being just who they are.

Darmstadt, February 2011 Jens Kühne

Hiermit erkläre ich, dass ich die vorliegende Dissertation selbstständig verfasst und keine anderen als die von mir angegebenen Hilfsmittel verwendet habe. Ich erkläre außerdem, dass ich bisher noch keinen Promotionsversuch unternommen habe.

Jens Kühne

Darmstadt, den 07. Februar 2011

Als Kind ist einem doch die Welt ziemlich klar-
und wenn man stirbt, weiß man gar nichts.

Hans-Joachim Kulenkampff

Contents

Nomenclature

Latin Symbols, Upper Case		Unit
$\mathcal{C}$	Convective/diffusive fractional step	
$\mathcal{F}$	Fine-grained Density Function	–
$\mathcal{M}$	Mixing related fractional step	
$\mathcal{P}$	Probability Density Function	–
$\mathcal{P}_\beta$	Presumed β-PDF	–
$\mathcal{P}_\delta$	Presumed δ-PDF	–
$\mathcal{R}$	Reaction related fractional step	
$\mathcal{Y}$, $\mathcal{Y}_i$	Progress variable	–
$\mathcal{Y}^*$, $\mathcal{Y}_i^*$	Normalized progress variable	–
$\mathcal{Y}_{eq}$, $\mathcal{Y}_{i,eq}$	Equilibrium value for the chosen progress variable	–
A	Surface	m^2
$B(r)$	Flux-limiter Function	–
C_G	Germano constant	–
C_S	Smagorinsky constant	–
C_Ω	Constant for the mixing frequency model	–
D, D_α	Binary diffusion coefficient (of species α)	m^2/s
D_t	Turbulent diffusion coefficient	m^2/s
D_{eff}	Effective diffusion coefficient	m^2/s
D_{jet}	Jet diameter	m
E	Error square	$\mathrm{m}^4/\mathrm{s}^4$
$E(\kappa)$	Spectrum of the turbulent kinetic energy	$\mathrm{m}^2/\mathrm{s}^2$
E_a	Activation energy	J
F_f	Flux over surface f	$*$
$J_i^{Y_\alpha}$	Mass flux vector of species α	$\mathrm{kg}/\mathrm{m}^2\mathrm{s}$
L_c	Characteristic length scale	m
L_{ij}	Leonard stress tensor	$\mathrm{m}^2/\mathrm{s}^2$
M, M_α	Molar mass (of species α)	kg/mol
M_{ij}	Scaled composite rate-of-strain tensor	$\mathrm{m}^2/\mathrm{s}^2$
N	Particle density	–
N_r	Number of elementary reactions	–
N_s	Number of species	–
R	Specific gas constant	$\mathrm{m}^2/\mathrm{s}^2\mathrm{K}$
R_{ij}	Correlation factor	–
S_{ij}	Rate-of-strain tensor	1/s
S_{ij}^{d}	Deviatoric rate-of-strain tensor	1/s
T	Temperature	K

T_{ij}	Cauchy stress tensor	$\mathrm{kg/ms^2}$
U	Bulk velocity	m/s
U_c	Characteristic velocity	m/s
V	Volume	$\mathrm{m^3}$
Y_α	Mass fraction of species α	–
Y_{PV}	Normalized progress variable	–
Y_{PV}	Progress variable	–
Z_i	Element mass fraction	–

Latin Symbols, Lower Case		**Unit**
ω_{PV}	Chemical source term for the progress variable	–
a	Strain rate	1/s
c	Combustion progress	–
c_A	Concentration of species A	$\mathrm{mol/m^3}$
c_p	Specific heat capacity at constant pressure	$\mathrm{J/kg\,K}$
h	Enthalpy	J/kg
h	Filter function	$\mathrm{1/m^3}$
k	Turbulent kinetic energy	$\mathrm{m^2/s^2}$
k_f	Velocity coefficient of the forward reaction	$\mathrm{m^3/mol\,s}$
k_i	Body force vector per unit mass	$\mathrm{m/s^2}$
l_0	Integral length scale	m
m	Mass	kg
m^f_{UDS}	Mass flux on surface f by an UDS discretization	$\mathrm{kg/m^2s}$
m_i	Mass of element i	kg
n	Number of processors	–
n^n_{conv}	Amount of particles representing convective transport	–
n^n_{diff}	Amount of particles representing diffusive transport	–
n_i	Outwards directed unit normal vector	–
n_p	Number of interacting particle pairs	–
p	Pressure	$\mathrm{kg/ms^2}$
q_i	Heat flux vector	$\mathrm{kg/s^3}$
r	Gradient ratio	–
r	Radial coordinate in an axisymmetric coordinate system	m
$r(x, y)$	Empiric correlation coefficient for x and y	–
r_f, r_b	Forward (backward) reaction rate	$\mathrm{mol/m^3s}$
r_k	Spatial increment	m
r_ϵ	Global reaction rate of elementary reaction ϵ	$\mathrm{mol/m^3s}$
s	Flame coordinate	m
$s(Y_{\alpha,eq})$	Flame coordinate at equilibrium value of species α	m
s_L	Laminar flame speed	m/s
t	Time	s
t_0	Integral time scale	s
u_i	Cartesian velocity component	m/s
w_α	Weighting factor	$*$
x, y, z	Cartesian coordinates	m
x_i	Cartesian coordinate	m

Greek Symbols, Upper Case		Unit
Δ	Average filter width	m
$\Gamma\, dW$	Diffusive term	m
Ω_{mix}	Mixing frequency	1/s
Ψ	Momentum correction	$\text{kg/m}^2\text{s}$

Greek Symbols, Lower Case		Unit
α_a	Preexponential factor	$*$
β_a	Reaction constant	–
χ	Scalar dissipation rate	1/s
δ_{ij}	Kronecker symbol	–
ϵ	Counter for elementary reactions	–
η_k	Kolmogorov length scale	m
κ	Wave number	1/m
λ	Thermal conductivity	kg m/Ks^3
λ_B	Batchelor length scale	m
μ	Dynamic viscosity	kg/ms
ν	Kinematic viscosity	m^2/s
$\nu''_{\alpha,\epsilon}$	Stoichiometric coefficient on product's side for species α in reaction ϵ	–
$\nu'_{\alpha,\epsilon}$	Stoichiometric coefficient on reactant's side for species α in reaction ϵ	–
ν_t	Turbulent kinematic viscosity	m^2/s
ν_{eff}	Effective kinematic viscosity	m^2/s
ω^*_{i-1}	Modulated weighting factor for control volume $(i-1)$	–
ω_j	Weighting factor for control volume j	–
ω_α	Chemical source term of species α	$\text{kg/m}^3\text{s}$
$\omega_{\mathcal{Y}}$, $\omega_{\mathcal{Y},i}$	Chemical source term for the progress variable	$\text{kg/m}^3\text{s}$
ϕ	Arbitrary scalar	$*$
ψ	Arbitrary scalar	$*$
ρ	Density	kg/m^3
ρ_{chem}	Density from tabulated chemistry	kg/m^3
τ	Temporal increment	s
τ_k	Kolmogorov time scale	s
τ_{chem}	Chemical time scale	s
τ_{turb}	Turbulent time scale	s
τ_{ij}	Residual stress tensor	m^2/s^2
τ^{sgs}_{ij}	Subgrid stress tensor	m^2/s^2
ε	Dissipation rate of the turbulent kinetic energy	m^2/s^3
ε	Statistical error	$*$
φ	Circumferential coordinate in an axisymmetric coordinate system	rad
ξ	Mixture fraction	–
ξ_{st}	Stoichiometric mixture fraction	–

Subscripts	
amb	Ambient conditions
bb	Bluff body related quantity

fuel	Fuel related quantity
jet	Jet related quantity
ox	Oxidizer related quantity

Superscripts

sgs	Sub-grid scale
test	Test-filtered quantity

Operators and Symbols

$< \phi'^2 >$	Variance
$< \phi'^2 >^{1/2}$	Standard deviation
$< \phi >$	Time-averaged quantity
$\bar{\phi}$	Averaged or filtered quantity
$\hat{\phi}$	Test-filtered quantity
ϕ'	Fluctuating part of an averaged or filtered quantity
ϕ''	Fluctuating part of a Favre-filtered quantity
int	Integer operation
$\widetilde{\phi''^2}$	Sub-filter variance in Favre-filtered context
$\widetilde{\phi}$	Favre-filtered quantity

Abbreviations

B4C2	Non-reacting Bluff Body Configuration
CDS	Central Differencing Scheme
CFD	Computational Fluid Dynamics
CFL	Courant-Friedrichs-Lewy
CHARM	Cubic/Parabolic High-accuracy Resolution Method
CNG	Compressed Natural Gas
cv	Control volume
DNS	Direct Numerical Simulation
EMST	Euclidean Minimum Spanning Tree
FDF	Filtered Density Function
FGM	Flamelet Generated Manifolds
FV	Finite Volume
GRI	Gas Research Institute
HM1e	Reacting Hydrogen Methane Bluff Body Configuration, low speed
HM3e	Reacting Hydrogen Methane Bluff Body Configuration, high speed
IEA	International Energy Agency
IEM	Interaction by Exchange with the Mean
ILDM	Intrinsic Low-dimensional Manifolds
LES	Large Eddy Simulation
LIF	Laser Induced Fluorescence
LSME	Linear Mean Square Estimation
MCPDF	Monte Carlo Probability Density Function
MPI	Message Passing Interface
PDF	Probability Density Function

PIV	Particle Image Velocimetry
ppc	Particle per Cell
PWS	Positive Weighting Scheme
RANS	Reynolds Averaged Navier-Stokes
SF	Steady Flamelet
TNF	Turbulent Non-premixed Flames
TPDF	Transported Probability Density Function
TVD	Total Variation Diminishing
UDS	Upwind Differencing Scheme
URANS	Unsteady Reynolds Averaged Navier-Stokes

Dimensionless Numbers

Da	Damköhler number
Kn	Knudsen number
Le	Lewis number
Ma	Mach number
Re	Reynolds number
$\mathrm{Re}_{\mathrm{crit}}$	Transitional Reynolds number
Re_t	Turbulent Reynolds number
Sc	Schmidt number
Sc_t	Turbulent Schmidt number

Chapter 1.

Introduction

1.1. Background

Fire and combustion has affected mankind from its early beginnings, whether unintentionally or on purpose. But it was only after the controlled creation, preservation and usage, more than half a million years ago, that fire started its on-going story of success as one of the oldest and most important technologies in the history of mankind. Fire and the related chemical process of combustion provided light and heat in the early days and represents the largest percentage of primary energy nowadays. More than 80% of the global demand of primary energy is still generated using combustion of fossil fuels [36] and especially for that reason in consideration of the most commonly agreed anthropogenic climate change, understanding of combustion is tremendously important. The increasing need of energy of developing and advanced developing countries due to their industrialization, but also due to their growth of population poses a further problem in delaying and stopping the global rise in temperature. Studies of the International Energy Agency (IEA) predict an increase of 50% in the global energy consumption in between the years 2005 and 2030 [35], which will still be mainly covered by the combustion of fossil fuels.

International as well as national summits and conferences have worked out strategies to decrease the percentage of fossil fuel consuming ways of primary energy generation in order to stop global warming. The most prominent solution procedure included in the presented plans is the distinct increase of so called renewable energy sources in order to reduce greenhouse gas emissions, especially CO_2, immensely. When talking about renewable energy, solar or hydro energy sources are considered to be the most important parts in a CO_2 neutral energy supply, but currently, a vast majority of renewable energy is generated by the combustion of renewable fuels, like bio-fuels. This explains the on-going popularity of combustion sciences and elucidates, that understanding the chemical phenomenon of combustion and the prediction of pollutant emissions is still a key feature for the solution procedure of the global warming issue.

Besides costly experimental investigations and empirical methods, numerical simulations of combustion processes take on greater significance in the development and optimization of combustion related systems in energy generation as well as in the transportation sector. Here, the technique of computational fluid dynamics (CFD) shows a variety of advantages compared to the classical approaches. These are amongst others the lower costs, shorter development phases and hence the resulting possibility to make parameter studies with a strikingly decreased effort in time and costs. In addition, the computationally obtained results usually provide more information than experimental ones.

In technical applications of combustion, like in stationary or airborne gas turbines and also in internal combustion engines, the flow mode is commonly chosen to be turbulent in order to increase mixing processes and thus the efficiency of the considered device. The combination of turbulence with chemical reactions results in a broad band of existent time and length scales that need to be considered in numerical simulations. A direct numerical simulation (DNS) of technically relevant configurations resolving all time and length scales by use of the Navier-Stokes equations is under current terms definitely not feasible related to the enormous efforts in CPU power and storage capacities. The commonly applied CFD method in industry is the so called RANS (Reynolds Averaged Navier-Stokes) approach, that is based on the temporal averaged transport equations and is thus less costly in terms of computational needs. However, due to a complete modeling of the turbulent energy spectrum in RANS methods, transient mixing and combustion processes cannot be represented adequately. For this reason RANS is only to a limited extent suitable for the simulation and accurate prediction of turbulent combustion advices, but represents at this moment the most reasonable compromise in respect of the cost-benefit ratio. The increase of computational power following Moore's law allows simulations of continuously rising complexity and the usage of alternative simulation techniques. A promising alternative to RANS is the Large Eddy Simulation (LES), which can be considered as a compromise between DNS and RANS as it solves for the large flow structures and models the influence of the small turbulent structures onto the flow. Additionally, LES provides temporal flow information that can be very interesting within construction or optimization of combustion related devices. The separation of the large energy containing from the small universal turbulent structures is obtained by a spatial low pass filtering of the subjacent Navier-Stokes equations. Especially for simulations of reactive flows, the additional temporal information of LES represents an obvious advantage in contrast to RANS, which under certain circumstances even enables LES to be predictive. However, LES has not yet become a commonly applied tool in development processes in industry of non-reactive and reactive flow simulations due to its comparatively large requirements of computational time. Nevertheless, a variety of LES related joint projects between industry and academics testify a high interest for the future application within the industrial environment. Likewise, developers of commercial CFD tools have started to integrate and implement LES into their solvers, but are still in their early stages. With the rising popularity of Large Eddy Simulation in reactive flow calculation and prediction, the need for reliable models increases as well. Especially the search and development of models, which allow sophisticated computations across all regimes of combustion is one of the major remaining tasks in the field of combustion research. Currently, a large range of different models limited to certain applications, like predetermined regimes, have been developed and used but the need for general combustion models in order to simulate complex processes such as those occurring in gas turbines is pressing. Therefore, the necessity to understand the behavior and the impact of state-of-the-art combustion models is of high interest to the entire scientific combustion community.

1.2. Objective of this Work

The present work aims at the analysis and improvement of numerical models and approaches applied in current LES of reactive and non-reactive flows. Therefore, a hybrid tool combining LES with a transported probability density function (PDF) approach is applied on non-premixed combustion problems, where a particle-based Eulerian Monte Carlo method solves for the PDF transport equation. With this combination of sophisticated numerical methods, it is possible to get further insights into the mixing phenomenon and the interaction between turbulence and chemistry. The Monte Carlo PDF transport provides the stochastic distribution of the sub-filter amount of the transported scalars, which can be alternatively used for model verification and validation instead of DNS data. Since DNS data for mixing and combustion devices similar to technically relevant applications is and will not be available in the near future, the additional information obtained by the PDF transport represents an adequate tool for analyses of applied LES models. The main goals of this work include the improvement, verification and validation of the implemented hybrid LES - transported PDF tool and the utilization of this tool in order to evaluate and assess the impact of currently implemented numerical models. This work will also provide data which can be used for the development of sub-models for the application in LES codes in order to achieve higher accuracy in the prediction of thermo-chemical properties and pollutant emissions in technically relevant turbulent flow and combustion problems.

1.3. State of Research

The computation of turbulent reactive flows employing the large eddy simulation technique has mainly been developed during the last two decades. In the beginnings of combustion LES most of the applied approaches and models have just been adapted from earlier RANS developments, while new approaches increasingly pay more attention to the unique behavior and unsteady characteristics of Large Eddy Simulations. A description of the current research state will be given below, but with respect to the wide range of the scientific field of combustion, the focus lies on LES of non-premixed combustion only.

The fundamental research, model development and validation in numerical simulations of combustion are principally based on the investigation of generic test configurations. Therefore, a widespread variety of test cases has been developed and investigated experimentally. On the basis of both phenomenological observations and quantitative results obtained by highly sophisticated diagnostic methods including laser spectroscopy, model development takes place. A substantial contribution in the compilation of test configurations is made by the ”International Workshop on Measurement and Computation of Turbulent Nonpremixed Flames” (TNF), which is a work group consisting of leading research teams in experiments and numerics in combustion. The main objective of the TNF is to generate a database of generic configurations somehow related to technical applications and to make up comparisons of different modeling approaches based on that database. The increasing consolation and the constant success over the past 15 years brought up the idea to additionally include partially premixed as well as premixed test configurations to the program of non-premixed flames [37].

The first scientific publications about Large Eddy Simulations are all related to early findings in computational climate sciences. The most important ones are published by Smagorinsky [96], Lilly [59] and Deardorff [20], introducing a new mathematical description for the computation of meteorologic flow phenomena. First calculations for validation of that new LES approach were already performed on isotropic turbulence and turbulent channel flows [54], [19]. Based on this validation test cases, the interest in LES for the application of engineering problems rose and with increasing computational power, the complexity of the considered flow configurations increased as well. Besides the application in computation and prediction of pure flow problems, models for reactive flow simulations were adapted from known RANS approaches [74] to fit the demands of LES. A very important model for non-premixed combustion simulation is the conserved scalar approach [4] and the strongly connected so called steady flamelet approach [70], [71]. Following these approaches non-premixed combustion can be described by a single conserved scalar, the mixture fraction, representing a combination of all reactive scalars. Furthermore, a flame front can be assumed to be thin compared to the occurring integral length scales and hence being composed and characterized by small one-dimensional flames and their thermo-chemical properties. However, this steady flamelet concept does not include finite rate chemistry effects and so further improvements were necessary. Therefore, the flamelet ansatz was being extended to an unsteady form [75], including time-dependency and effects of finite-rate chemistry. An alternative approach is the addition of further reactive scalars, representing the progress of the reaction as proposed by Pitsch et al. [76] and Pierce et al. [73], in combination with an adequate underlying chemistry, like ILDM (Intrinsic Low Dimensional Manifolds) [61] or FGM (Flamelet Generated Manifolds) [66]. Due to the continuously increasing computational power, even calculations including reduced chemistry mechanisms are performed in reasonable simulation times. In general, transported Monte Carlo PDF methods are applied for this purpose because of the high dimensionality of the transported scalars and in order to adequately represent the turbulence-chemistry interaction. Applications for this kind of simulations are calculations featuring highly transient phenomena like ignition, auto-ignition or extinction [44], where finite-rate chemistry effects are definitely not negligible.

The transported PDF (TPDF) methods have actually been developed for the more accurate representation of turbulence-chemistry interaction. The modeling of this interaction is necessary, since the common simulation techniques, such as RANS and LES, only provide mean values (either temporal or spatial) of the flow and scalar fields. In order to consider the effect of turbulence on the chemistry, further information about the fluctuations are needed and hence have to be modeled. In the context of pre-tabulated chemistry, this impact is represented by distributions of the scalars on the sub-grid level. Since no detailed information of this distributions is provided a statistical modeling is chosen. Therefore, presumed shapes of the probability density function on the sub-grid level of each control volume are defined. A common shape assumption for the mixture fraction follows the so called β-function, determining the sub-filter PDF shape by the calculated mean value and its variance. But when it comes to other scalars besides the mixture fraction, the sub-grid PDF cannot be sufficiently characterized by β-distributions [55]. An alternative and more sophisticated approach to represent turbulence-chemistry interaction is given by the already mentioned transported PDF methods [77], [78]. Here,

the shape of the PDF is not modeled directly, but is obtained by solving for a transport equation. Due to the high dimensionality of the solution and the related increased computational demands, the PDF transport is most often computed using statistical Monte Carlo methods. These methods are more efficient than the commonly applied finite volume approaches. In the past years, research in the field of transported PDF methods has mainly focused on the development and application of alternative Monte Carlo methods [42], [13]. The most important ones are the Lagrangian [81] and the Eulerian particle based approaches [13] as well as the Eulerian stochastic fields method [101]. As already mentioned above, the TPDF approach has also become very important in the simulation of transient effects in combustion like ignition, auto-ignition and extinction and has recently been used for the calculation of spray combustion [41]. Furthermore, the range of TPDF simulations have been extended from jet flames over bluff body flames to more complex geometries, which is only possible with reasonable effort due to the continuously increasing computational power during the last years.

A drawback of the Monte Carlo PDF methods is the occurring statistical error, which is caused by the finite number of stochastic particles or fields used within the Monte Carlo method. However, for an infinite amount of particles the statistical methods would converge to the analytical solution. This error generates additional fluctuations on the transported scalars and hence the density field, which again may lead to stability problems of the numerical procedure. For that reason, in most cases the direct coupling of LES and TPDF methods through the density field is a severe problem. Therefore, different implicit coupling strategies have been developed in the past, for example solving an extra filtered enthalpy transport equation with a finite volume method and provide the occurring source term from the Monte Carlo procedure [82].

1.4. Overview of this Work

The present work is about turbulent combustion and hence the following chapter will introduce the basic theories of fluid flow and chemical reactions. Therefore, the fundamental equations for the detailed mathematical description of flow problems in general are derived and presented. Additionally, the turbulence phenomenon is discussed in its theoretical as well as in its modeling aspects, which is followed by the principles of chemical reactions and the corresponding commonly applied models and approaches. After the isolated consideration of turbulence and chemistry, also the interaction between both physical phenomena is discussed and the concept of transported probability density functions is described. This chapter also provides the general idea of computational fluid dynamics and particularly discusses the Large Eddy Simulation, which represents the basis of this work.

Chapter three acts as a bridge between theory and the practical application by transferring the introduced equations into applicable models employing numerical mathematics and related approaches. This also includes the description of the used LES solver FLOWSI and the applied models for discretization in space and time and the employed global solution algorithm. Furthermore, the theory of Monte Carlo methods is presented, which provides a basis for an efficient application of the TPDF method in turbulent combustion problems.

On this foundation, the following chapters will show results achieved by the application of the LES solver FLOWSI. The fourth chapter will additionally provide a validation of the implemented models and discusses their performance by reference to two generic test cases. The subsequent chapter five represents the main part of this work in which numerous investigations and analyses are conducted in order to evaluate commonly used LES sub-models in terms of their general suitability and accuracy. Therefore, an experimentally well documented bluff body configuration with variations in the employed boundary conditions is considered. In this context, various studies concerning inflow boundary conditions, statistical errors in the Monte Carlo method, general capabilities of presumed sub-filter PDF and the application of a more complex chemistry model are performed.

In chapter six, the findings and hypotheses made on the basis of the bluff body configuration results are reconsidered on a different well documented combustion device, which is a piloted methane-air jet flame. The aim of this chapter is the confirmation of the theories made using an alternative geometry and chemistry basis to avoid unfunded hypotheses based on a single configuration.

The last chapter concludes the work and gives an overview of all hypotheses and findings made within the previous chapters.

Chapter 2.

Theoretical Background and Modeling

The following chapter gives an overview of a set of equations and modeling strategies, which provides the basis of today's reactive fluid flow simulations. In the first part, the fundamental fluid flow physics together with the corresponding transport equations and laws of conservation are presented. This is followed by a description of turbulence and the most common computational approaches to solve for turbulent flows. The third section deals with the theory of combustion related chemistry and describes methods for the application in computational fluid dynamics. Eventually, in the last section of this chapter the aspect and problem-oriented approaches of turbulence-chemistry interaction are introduced in order to combine both per se challenging phenomena turbulence and chemistry.

2.1. Fluid Dynamics

Fluid flows can be described by a set of coupled partial differential equations. The physical and mathematical descriptions in this work are based on the continuum hypothesis. This hypothesis is verified, when the Knudsen number, Kn, which relates the mean free path of molecules with a characteristic length scale of interest, is small ($\mathrm{Kn} \ll 1$). In technical applications, which are considered in this contribution, this assumption is valid. Using this approach, the fluid itself can be treated as a continuum instead of considering each and every single molecule. This results in a continuous representation in space and time of all fluid flow properties.

2.1.1. Conservation of Mass

Mass cannot be destroyed nor created. Hence, the conservation of mass is valid and can be described by the continuity equation:

$$\frac{\partial \rho}{\partial t} + \frac{\partial}{\partial x_i}(\rho u_i) = 0. \tag{2.1}$$

The local change of density ρ in time is equal to the convective transport of mass. Equation (2.1) is valid for both compressible and incompressible flows. For incompressible flows, it is assumed that the density does not change due to pressure changes. This assumption is usually applied when the fluid velocity is low compared to the speed of

sound and so the Mach number is small compared to unity (Ma $\leq$ 0.3). For constant density flows, the continuity equation collapses to the presumption of a divergence free fluid velocity field. Due to mixing and reaction occurring in all investigated configurations in this work, this simplification is not applicable here.

2.1.2. Conservation of Momentum

Analog to the mass, conservation of momentum ρu_i can be described by eq. (2.2). The basis of this conservation equation of momentum is given by Newton's second and third law of motion. The former indicates, that a change in the motion of a body (in an inertial system) is always the result of the sum of all external forces. The latter represents the interaction of bodies which is commonly known as "actio = reactio".

$$\frac{\partial}{\partial t}(\rho u_i) + \frac{\partial}{\partial x_j}(\rho u_i u_j) = \rho k_i + \frac{\partial}{\partial x_j}(T_{ij}) \tag{2.2}$$

In eq. (2.2) k_i represents the vector of all volumetric forces and T_{ij} is the stress tensor defined by properties of the described material. The closure of this tensor is discussed in detail in section 2.1.5.

2.1.3. Conservation of Energy

Energy is also a conserved quantity and hence is described by eq. (2.3). Here, the energy is represented by the enthalpy, which is the common ansatz for reacting fluid flows. Alternatively, a conservation equation of the internal energy can be used.

$$\frac{\partial}{\partial t}(\rho h) + \frac{\partial}{\partial x_i}(\rho h u_i) = T_{ij}\frac{\partial u_i}{\partial x_j} + \frac{Dp}{Dt} - \frac{\partial q_i}{\partial x_i} \tag{2.3}$$

In the presented form, volumetric enthalpy sources (e.g. radiation) are neglected. The first term on the right hand side stands for enthalpy generation due to deformation, whilst reversible work by pressure changes is represented by the second one. The heat flux vector q_i also depends on material properties and is therefore described in section 2.1.5.

2.1.4. Species Transport

If one defines the species mass fractions $Y_\alpha = m_\alpha/m$, with m_α being the mass of species α and m the total mass of the mixture, the transport equation for the species mass fraction can be written analogously to the mass conservation equation.

$$\frac{\partial}{\partial t}(\rho Y_\alpha) + \frac{\partial}{\partial x_i}(\rho u_i Y_\alpha) = -\frac{\partial}{\partial x_i}(J_i^{Y_\alpha}) + \omega_\alpha. \tag{2.4}$$

Here, $J_i^{Y_\alpha}$ denotes the mass flux vector of species α. This vector depends again on material properties and is discussed in detail in section 2.1.5. Another difference to the equations shown above is the source term ω_α, which stands for the change of species mass fraction Y_α due to chemical reactions. In order to describe a mixture with N_s components,

$N_s - 1$ mass fraction equations have to be solved. In addition it is required, that the sum of all species mass fractions must be equal to unity.

$$\sum_{\alpha=1}^{N_s} Y_\alpha = 1 \tag{2.5}$$

Equation (2.4) can also be seen as the most general transport equation for scalars.

2.1.5. Constitutive Laws

All equations mentioned above, except for the continuity equation, include terms, that depend on properties of the used fluid. These are in detail, the stress tensor T_{ij} in the momentum and enthalpy equation, the heat flux vector q_i in the enthalpy equation and the mass flux vector $J_i^{Y_\alpha}$.

Most of technically relevant fluids are so called Newtonian fluids. Those fluids' shear stress tensor can be assumed to be linearly dependent on the strain rate tensor $S_{ij} = \frac{1}{2}(\partial u_i/\partial x_j + \partial u_j/\partial x_i)$ with the dynamic viscosity μ as the belonging proportionality factor. Using this relation, the stress tensor can be written as

$$T_{ij} = -p\delta_{ij} - \mu\frac{2}{3}\frac{\partial u_k}{\partial x_k}\delta_{ij} + \mu\left(\frac{\partial u_i}{\partial x_j} + \frac{\partial u_j}{\partial x_i}\right). \tag{2.6}$$

By replacing T_{ij} in eq. (2.2) with relation (2.6) one obtains the Navier-Stokes equations:

$$\frac{\partial}{\partial t}(\rho u_i) + \frac{\partial}{\partial x_j}(\rho u_i u_j) = \frac{\partial}{\partial x_j}\left[\mu\left(\frac{\partial u_i}{\partial x_j} + \frac{\partial u_j}{\partial x_i}\right) - \mu\frac{2}{3}\frac{\partial u_k}{\partial x_k}\delta_{ij}\right] - \frac{\partial p}{\partial x_i} + \rho k_i. \tag{2.7}$$

The heat flux vector q_i in the enthalpy equation can be described in a similar way as the stress tensor. According to Fourier's law, this vector depends linearly on the temperature gradient $\partial T/\partial x_i$ and for multi-component fluids an additional term resulting from species diffusion is included.

$$q_i = -\lambda\frac{\partial T}{\partial x_i} + \sum_{\alpha=1}^{N_s} h_\alpha J_i^{Y_\alpha} \tag{2.8}$$

In this case the constant of proportionality is the thermal conductivity λ.

Another constitutive law is used in order to close the mass flux vector $J_i^{Y_\alpha}$. Here, Fick's law defines the relation between the mass flux vector and the gradient of the species mass fraction. It follows

$$J_i^{Y_\alpha} = -\rho D_\alpha \frac{\partial Y_\alpha}{\partial x_i}, \tag{2.9}$$

with D_α being the binary diffusion coefficient of species α.

2.1.6. Equations of State

Besides the discussed conservation laws two additional equations of state are necessary to determine all unknowns. The first equation of state is the so called ideal gas law. It relates the properties density ρ, pressure p and the temperature T.

$$\rho = \frac{p\bar{M}}{RT} \tag{2.10}$$

In this equation R is the universal gas constant and $\bar{M}$ is the mean molar mass of the mixture calculated by eq. (2.11).

$$\bar{M} = \left[\sum_{\alpha=1}^{N_s} Y_\alpha / M_\alpha \right]^{-1} \tag{2.11}$$

The second equation describes the enthalpy h as a function of the temperature. For a mixture of gases the enthalpy is defined by

$$h = \sum_{\alpha=1}^{N_s} Y_\alpha h_\alpha \qquad \text{with} \qquad h_\alpha = h_\alpha^{\text{ref}} + \int_{T^{\text{ref}}}^{T} c_{p,\alpha}(T')\, dT'. \tag{2.12}$$

With some transformations of the equations the enthalpy equation can be further simplified. Therefore, the derivative with respect to x_i of eq. (2.12) is calculated and it follows:

$$\frac{\partial h}{\partial x_i} = c_p \frac{\partial T}{\partial x_i} + \sum_{\alpha=1}^{N_\alpha} h_\alpha \frac{\partial Y_\alpha}{\partial x_i}. \tag{2.13}$$

Including the definition of the mass flux vector $J_i^{Y_\alpha}$ in eq. (2.8) and applying relation (2.13) one obtains the following definition for the heat flux vector q_i.

$$q_i = -\frac{\lambda}{c_p} \frac{\partial h}{\partial x_i} - \sum_{\alpha=1}^{N_\alpha} \left(\rho D_\alpha - \frac{\lambda}{c_p} \right) h_\alpha \frac{\partial Y_\alpha}{\partial x_i} \tag{2.14}$$

Using eq. (2.14) with the enthalpy equation (2.3) leads to

$$\frac{\partial}{\partial t}(\rho h) + \frac{\partial}{\partial x_i}(\rho h u_i) = \frac{\partial}{\partial x_i}\left(\frac{\lambda}{c_p} \frac{\partial h}{\partial x_i} \right) + \frac{\partial}{\partial x_i}\left(\sum_{\alpha=1}^{N_\alpha} \left(\rho D_\alpha - \frac{\lambda}{c_p} \right) h_\alpha \frac{\partial Y_\alpha}{\partial x_i} \right). \tag{2.15}$$

In order to derive this equation, the low Mach number assumption for combustion systems [10] is applied. Since in flames moderate velocities and high temperatures occur, the characteristic Mach number can be assumed to be small compared to unity (Ma ≤ 0.3). Due to the low Mach number formulation and the fact, that only open systems are simulated in this work, the pressure term in the energy equation vanishes. Furthermore, the energy dissipation related to deformation of the fluid can be neglected.

The Lewis number Le relates thermal conduction to species diffusion and is defined as

$$\text{Le} = \frac{\lambda}{\rho c_p D_\alpha}. \tag{2.16}$$

Assuming the Lewis number to be unity leads to the consistency of all diffusion coefficients ($D_\alpha = D$). This hypothesis is valid for most of the simple hydrocarbons, e.g. methane, which is used as fuel for the investigated flames in this work. With this simplification the energy equation can be written as

$$\frac{\partial}{\partial t}(\rho h) + \frac{\partial}{\partial x_i}(\rho h u_i) = \frac{\partial}{\partial x_i}\left(\rho D \frac{\partial h}{\partial x_i} \right). \tag{2.17}$$

The mathematical basis for the description of combustion systems is now given by equations (2.1), (2.4) with (2.5), (2.7) and (2.17).

2.2. Turbulence

The theory of fluid dynamics differs between two major flow modes, laminar and turbulent flows. Laminar ones are characterized by regular flow patterns. Here, streamlines are parallel to each other and the flow can be interpreted as slipping layers with an infinitesimal thickness. In laminar flows, mixing perpendicular to the major streamwise direction is dominated by molecular diffusion.

In contrast, turbulent flows are pseudo-random, three-dimensional, unsteady, swirled and dissipative. Therefore, mixing is dominated by convective transport due to three-dimensional structures. Most technical applications are characterized by turbulent flows, e.g. combustion chambers of aircraft engines. For combustion problems turbulent flows are used to increase the mixing between fuel and oxidizer, which makes combustion become more efficient and less pollutants are built.

The first known documented investigations on turbulence reach back to the 15^{th} century, when Leonardo da Vinci sketched turbulent structures of whirlpools. Thereafter, it lasted four more centuries to publish the first quantitative turbulence investigations. Here, Reynolds scientifically described the phenomenon turbulence in his first contribution [83] and later [84] introduced a dimensionless characteristic parameter for the determination of turbulent flows. This parameter is still known as the Reynolds number Re. The definition of the Reynolds number (2.18) includes a characteristic length scale L_c, a velocity U_c and the fluid's kinematic viscosity $\nu = \mu/\rho$. Both properties, L_c and U_c are related to the global geometrical scale of the problem configuration.

$$\mathrm{Re} = \frac{L_c U_c}{\nu} \tag{2.18}$$

The Reynolds number relates inertia forces ρU_c^2 to viscous forces $\mu U_c / L_c$ in a system. Inertia forces destabilize a flow whereas the viscous term stabilizes. To a certain system dependent critical Reynolds number $\mathrm{Re}_{\mathrm{crit}}$, the viscous term dominates and hence a laminar flow is established. While increasing the Reynolds number, the influence of the destabilizing inertia forces becomes more significant up to a point, where the flow mode becomes turbulent and $\mathrm{Re} \geq \mathrm{Re}_{\mathrm{crit}}$ is valid. Since the critical Reynolds number cannot be clearly defined, the region close to that value is called transition region.

The destabilization process by inertia forces leads to the creation of three-dimensional eddies, which are mainly generated by shear layers producing the turbulent kinetic energy E. Following the idea of the energy cascade, proposed by Richardson [86], the energy is produced in the large turbulent structures and is transferred to successively smaller eddies. Finally, the turbulent structures become the size of the Kolmogorov scale η_k [53] where the contained energy is dissipated into heat.

Figure 2.1 depicts a schematic turbulent energy spectrum $E(\kappa)$ as a function of the wave number $\kappa = (2\pi)/l)$. The turbulent energy is produced in large structures, where the length scales range between the characteristic length L_c and the integral length scale l_0. The energy is then transferred to smaller eddies through a region called the inertial subrange. The turbulent structures collapse to successively smaller eddies and hence the energy decreases. The scaling factor represented in this region is $\kappa^{-5/3}$ and can also be mathematically derived [79]. In the dissipation range the viscous effects become dominant

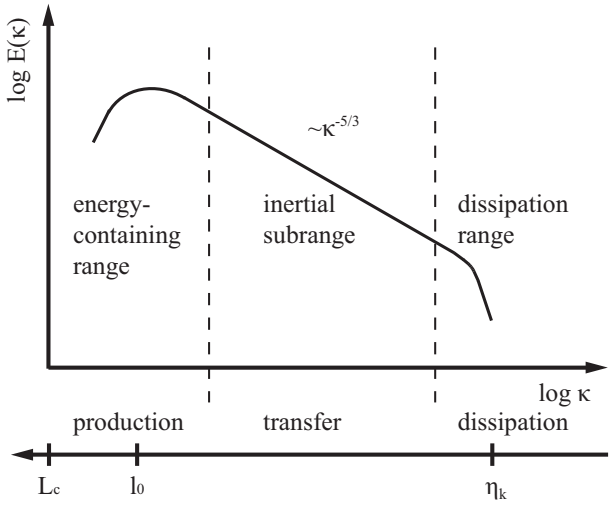

Figure 2.1.: Schematic of a turbulent kinetic energy spectrum $E(\kappa)$ as a function of the wave number $\kappa = (2\pi)/l$. The different ranges, processes and length scales of the turbulent spectrum are shown.

and so the energy is dissipated into thermal energy on the smallest occurring scales, the Kolmogorov length scale η_k.

The above mentioned length scales L_c, l_0 and η_k are characteristical for turbulent flow systems. The characteristic length scale L_c defines the largest structures, which correspond to global geometrical dimensions of the considered device, like nozzle diameters or channel widths. However, both remaining scales cannot be defined with analog estimations, but can be obtained by mathematical correlations to the characteristic length scale L_c. Therefore, a turbulent velocity field u_i is split into a mean field $\bar{u}_i$ and a superposed field of turbulent fluctuations u_i'.

$$u_i(x_j, t) = \bar{u}_i(x_j, t) + u_i'(x_j, t) \tag{2.19}$$

The turbulent fluctuation term u_i' includes all transient motions, that are not coherent structures of the flow. The distribution of turbulent fluctuations cannot be just random, but rather shows somehow correlated structures. The underlying correlation of the turbulent fluctuations can be represented by eq. (2.20).

$$R_{ij}(x_k, t, r_k, \tau) = \frac{\overline{u_i'(x_k, t) u_j'(x_k + r_k, t + \tau)}}{\sqrt{\overline{u_i'^2}(x_k, t)\overline{u_j'^2}(x_k + r_k, t + \tau)}} \tag{2.20}$$

This equation associates turbulent fluctuations of two considered spatially and temporally differing coordinates. In this context, r_k denotes the distance in space between the two considered points in the flow, whilst τ stands for an arbitrary time interval in order to show correlations in time. For randomly distributed fluctuations in time or space one obtains $R_{ij} = 0$. Perfectly correlated values give $R_{ij} = 1$, while $R_{ij} = -1$ is calculated for anticorrelated distributions. For $i = j$ eq. (2.20) turns into the autocorrelation in time or space and the integral of this function leads to the integral length scale l_0 and the related integral time scale t_0, respectively.

$$l_0 = \int_0^\infty R_{11}(x_k, t, r_k, 0)\, dr \qquad \text{and} \qquad t_0 = \int_0^\infty R_{11}(x_k, t, 0, \tau)\, d\tau \tag{2.21}$$

Furthermore, a Fourier transformation of the autocorrelation function R_{11} leads to the energy spectrum E_κ shown in figure 2.1. The smallest occurring turbulent scales, Kolmogorov length η_k and time τ_k, depend on the kinematic viscosity ν and the dissipation rate ε. These two properties define the transfer of turbulent kinetic energy to heat by viscous effects. The Kolmogorov length and time scales are estimated by

$$\eta_k = \left(\frac{\nu^3}{\varepsilon}\right)^{1/4} \qquad \text{and} \qquad \tau_k = \left(\frac{\nu}{\varepsilon}\right)^{1/2}, \tag{2.22}$$

where the dissipation rate can be approximated by $\varepsilon \approx u_i'^3/l_0$ [58], relating the Kolmogorov scale to the turbulent Reynolds number Re_t.

$$\frac{\eta_k}{l_0} \sim \mathrm{Re}_t^{3/4} \qquad \text{and} \qquad \frac{\tau_k}{t_0} \sim \mathrm{Re}_t^{1/2} \tag{2.23}$$

2.2.1. Modeling of Turbulent Flows

Based on the equations described in the previous chapter, turbulent flows are mathematically defined. However, the solution of these equations for real technical applications cannot be obtained easily. The reasons for that and strategies to avoid occurring issues are presented and described in detail in the following sections.

There are three major approaches of calculating turbulent flows, Direct Numerical Simulation, Large Eddy Simulation and Reynolds Averaged Navier-Stokes. These approaches differ from each other in terms of the total amount as well as the way of modeling and the resulting necessary computational effort. The following chapter gives a brief overview of the three different approaches DNS, LES and RANS. Even though the computational effort or the percentage of modeling of the mentioned methods would suggest a different sorting, in the context of this contribution it is reasonable to describe the approaches in the following order. Since this contribution is about LES, the explanation for it will be much more detailed than the other ones. Therefore, DNS and RANS will be described first and will be followed by an elaborated section about Large Eddy Simulations.

2.2.1.1. Direct Numerical Simulation

The Direct Numerical Simulation is the most costly approach regarding the computational needs but therefore the most reliable one. For DNS no modeling is applied at all and hence the described equations in section 2.1 are solved numerically for the entire range of turbulent scales shown in fig. 2.1. DNS is not applicable for technically relevant systems, but is rather used for research purposes as a numerical experiment [11]. With adequate numerical schemes and a feasible grid resolution, a DNS calculates the exact solution for the problem given. Especially this appropriate grid resolution is the major disadvantage of this method. In order to calculate all turbulent structures the numerical grid size of a DNS

must be at least as small as the smallest occurring scale, the Kolmogorov length scale η_k. From eq. (2.23) the relation between the Kolmogorov scales and the integral length scale is given to $\mathrm{Re}_t^{3/4}$. Extending this to three dimensions, the number of grid points increases with $\mathrm{Re}_t^{9/4}$. Furthermore, the temporal resolution is directly connected to the spatial resolution by the Courant-Friedrichs-Lewy criterion (CFL) [15], which leads to a relation of the computational cost proportional to Re_t^3. Hence, it is not practicable to simulate configurations with Reynolds numbers in the order of $\mathcal{O}(10^4)$ and higher even with today's high performance super computing facilities. In addition to this enormously increasing computing time, the storage space and the evaluation of calculated DNS data represent an almost unmanageable issue. Nevertheless, DNS give a valuable insight into turbulent flows that cannot be achieved by experimental investigations. Besides analyses of the turbulence phenomenon in general validation data for proving and calibrating existing models or for the development of new models can also be obtained by evaluating DNS data. Another advantage of DNS over experiments of turbulent flows is the completeness of all properties that are calculated and can be used for validation processes.

2.2.1.2. Reynolds Averaged Navier-Stokes

In terms of computational costs the approach of Reynolds Averaged Navier-Stokes simulations is the cheapest of the ones presented here. For this reason, its robustness and its speed, RANS is state-of-the-art in today's industrial CFD applications. In contrast to DNS, where no modeling is used, the entire range of scales in the turbulent kinetic energy spectrum is modeled. This leads to statistics of turbulent flows, which do not include temporal information of the turbulent fields. This is gained by averaging all transport equations in time by the operator defined in eq. (2.24).

$$\bar{\phi}(x_i) = \lim_{\Delta t \to \infty} \frac{1}{\Delta t} \int_{t-\Delta t/2}^{t+\Delta t/2} \phi(x_i, t')\, dt' \tag{2.24}$$

With this procedure, the variables ϕ are no longer functions in time and space but only functions in space. Furthermore, due to the averaging, the unclosed term $\overline{u_i u_j}$ in the momentum equation appears and needs to be modeled. The approaches applied for a closure of this term are based on a modeling of the so called Reynolds stress tensor

$$\overline{u_i' u_j'} = \overline{u_i u_j} - \overline{u}_i \overline{u}_j. \tag{2.25}$$

A variety of models for the Reynolds stress tensor exists [79], which differ in terms of the statistical order of accuracy and the number of the additionally solved equations. The following list gives a brief overview of the approaches used in RANS calculations:

First order closure These approaches are based on the modeling of a turbulent viscosity and can be further classified regarding the amount of additionally solved transport equations. All of them use mean quantities in order to close the Reynolds stress tensor and include the mean velocity gradients $\partial \overline{u}_i / \partial x_j$, a specific turbulent length L and a turbulent time scale τ.

- **Zero equation models** In these models the Reynolds stresses are described by algebraic relations and are most commonly based on the mixing-length model [80].

- **One equation models** An additional transport equation for the turbulent kinetic energy $k = 1/2(\overline{u_i' u_j'})$ is solved. The dissipation rate ε in the transport of k is modeled as a sink by algebraic relations.
- **Two equation models** Here, two additional equations are solved, e.g. one for the turbulent kinetic energy k and one for the dissipation rate ε. From these two quantities, the characteristic length scale can be calculated as $L = k^{3/2}/\varepsilon$ and the corresponding time scale as $\tau = k/\varepsilon$.

Second order closure These closures compute the entire Reynolds stress tensor $\overline{u_i' u_j'}$. Due to symmetry of this tensor, six additional transport equations for the individual components and one for the dissipation rate ε need to be applied. By modeling the transport equations for $\overline{u_i' u_j'}$ other unclosed terms appear, like triple correlation terms and the pressure rate-of-strain correlations, which again must be described by models.

Higher order closure The triple correlations $\overline{u_i' u_j' u_k'}$ can also be transported by model equations, which again include unclosed terms that need to be modeled. The modeling of these quadruple correlations is challenging, since the behavior of quadruple correlations is not well known yet.

In order to include transient effects into RANS, the so called unsteady RANS (URANS) has been developed. A major requirement for URANS computations is a distinct differentiation between the frequencies of the transient phenomenon of interest and the turbulence.

2.2.1.3. Large Eddy Simulation

LES is able to capture transient effects of turbulent flows with an adequate computational effort that lies in between DNS and RANS. The idea of Large Eddy Simulation is a scale separation within the turbulent spectrum. Therefore, the large energy containing scales are calculated, whereas the small dissipative scales are modeled with comparably simple approaches due to their isotropic behavior. The separation of scales is achieved by convolution with a filter function $h(x_j')$ shown in eq. (2.26).

$$\bar{\phi}(x_j, t) = \int_{-\infty}^{\infty} \phi(x_j - x_j') h(x_j')\, dx_j' \tag{2.26}$$

In order to remove the fine turbulent structures a low-pass filter function is used, leaving a spatially filtered field $\bar{\phi}(x_j, t)$. The separation can be represented by

$$\phi - \bar{\phi} = \phi' \qquad \text{or} \qquad \phi = \bar{\phi} + \phi', \tag{2.27}$$

where ϕ' denotes the small scale turbulent fluctuations. By filtering the governing equations for reactive flows with non-constant density, unclosed terms appear, which can be avoided by a distinct averaging procedure called the density-weighted Favre-filtering [22]. Favre-filtered quantities are characterized by the tilde $\tilde{}$ and are defined by eq. (2.28).

$$\tilde{\phi} = \frac{\overline{\rho\phi}}{\bar{\rho}} \qquad \text{with} \qquad \phi = \tilde{\phi} + \phi'' \tag{2.28}$$

Analog to eq. (2.27) the separation can be performed for Favre-filtered quantities $\tilde{\phi}$, where ϕ'' stands for the sub-filter part. The application of the low-pass filter operation eq. (2.26) and the Favre-filter from eq.(2.28) on the continuity equation and the transport equation for the momentum leads to eq. (2.29) and (2.30).

$$\frac{\partial \bar{\rho}}{\partial t} + \frac{\partial}{\partial x_i}(\bar{\rho}\tilde{u}_i) = 0. \tag{2.29}$$

$$\frac{\partial}{\partial t}(\bar{\rho}\tilde{u}_i) + \frac{\partial}{\partial x_j}(\bar{\rho}\widetilde{u_i u_j}) = \frac{\partial}{\partial x_j}\left[\bar{\rho}\tilde{\nu}\left(\frac{\partial \tilde{u}_i}{\partial x_j} + \frac{\partial \tilde{u}_j}{\partial x_i}\right) - \bar{\rho}\tilde{\nu}\frac{2}{3}\frac{\partial \tilde{u}_k}{\partial x_k}\delta_{ij}\right] - \frac{\partial \bar{p}}{\partial x_i} + \bar{\rho}k_i \tag{2.30}$$

In equation (2.30) the kinematic viscosity ν is assumed to be statistically independent of the velocity gradient and therefore the following simplification can be applied.

$$\widetilde{\nu\frac{\partial \tilde{u}_i}{\partial x_j}} = \tilde{\nu}\frac{\partial \tilde{u}_i}{\partial x_j} \tag{2.31}$$

Furthermore, in the context of this work a so called implicit filtering procedure is used, where the computational grid acts as the filter function. Here, the filter width corresponds to the grid size Δ of the computational mesh. The implicit filtering is also known as the Schumann filter [92]. Equation (2.30) includes the unclosed velocity correlation $\widetilde{u_i u_j}$ resulting from convection. In order to close this filtered correlation it is split into a resolved part $\tilde{u}_i\tilde{u}_j$ and a unresolved sub-filter part τ_{ij}, which is also called residual stress tensor [79]. The separation is shown in eq. (2.32).

$$\widetilde{u_i u_j} = \tilde{u}_i\tilde{u}_j + \tau_{ij} \qquad \text{or} \qquad \tau_{ij} = \widetilde{u_i u_j} - \tilde{u}_i\tilde{u}_j \tag{2.32}$$

By another splitting operation, the residual stress tensor can be written as the sum of a deviatoric term τ_{ij}^{sgs} and an isotropic part, eq.(2.33). Within the context of the Navier-Stokes equations, the isotropic term is added to the pressure term and builds the pressure parameter $\bar{P}$.

$$\tau_{ij} = \tau_{ij}^{\text{sgs}} + \frac{1}{3}\tau_{kk}\delta_{ij} \tag{2.33}$$

$$\bar{P} = \bar{p} + \frac{1}{3}\tau_{kk}\delta_{ij} \tag{2.34}$$

The sub-filter stress tensor τ_{ij}^{sgs} is the only remaining unclosed term in the filtered Navier-Stokes equation. For the closure of this term several models have been developed and two consecutive approaches are described in detail in the following sections.

Before describing the two models, an introduction of the basic idea is given. It is called the eddy viscosity hypothesis. This approach assumes, that the sub-grid stress tensor τ_{ij}^{sgs} is linearly correlated to the filtered deviatoric rate-of-strain tensor $\tilde{S}_{ij}^{\text{d}}$ with a proportionality factor called the turbulent viscosity ν_t [45]. In addition, the sum of the kinematic and the turbulent viscosity is defined as the effective viscosity ν_{eff}.

$$\nu_{\text{eff}} = \tilde{\nu} + \nu_t \tag{2.35}$$

Applying this model for the sub-grid stress τ_{ij}^{sgs} one obtains equation (2.36).

$$\tau_{ij}^{\text{sgs}} = \nu_t\left(\frac{\partial \tilde{u}_i}{\partial x_j} + \frac{\partial \tilde{u}_j}{\partial x_i}\right) - \frac{2}{3}\nu_t\frac{\partial \tilde{u}_k}{\partial x_k}\delta_{ij} \tag{2.36}$$

However, the trace of the tensor τ_{ij}^{sgs} is zero. In order to avoid this issue one can make the approach:

$$\tau_{ij}^{\text{sgs}} - \frac{1}{3}\tau_{kk}^{\text{sgs}}\delta_{ij} \approx \nu_t\left(\frac{\partial\tilde{u}_i}{\partial x_j} + \frac{\partial\tilde{u}_j}{\partial x_i}\right) - \frac{2}{3}\nu_t\frac{\partial\tilde{u}_k}{\partial x_k}\delta_{ij}. \tag{2.37}$$

By using this relation the trace of the stress tensor remains unknown.

In equation (2.38) the Navier-Stokes equation with the inserted eddy-viscosity approach is presented .

$$\frac{\partial}{\partial t}(\bar{\rho}\tilde{u}_i) + \frac{\partial}{\partial x_j}(\bar{\rho}\tilde{u}_i\tilde{u}_j) = \frac{\partial}{\partial x_j}\left[\bar{\rho}\nu_{\text{eff}}\left(\frac{\partial\tilde{u}_i}{\partial x_j} + \frac{\partial\tilde{u}_j}{\partial x_i}\right) - \frac{2}{3}\bar{\rho}\nu_{\text{eff}}\frac{\partial\tilde{u}_k}{\partial x_k}\delta_{ij}\right] - \frac{\partial\bar{P}}{\partial x_i} + \bar{\rho}k_i \tag{2.38}$$

Smagorinsky Model The Smagorinsky model [96] now derives the turbulent viscosity ν_t by using resolved large-scale quantities. In this model the turbulent viscosity is assumed to be related to the filtered deformation velocity tensor $\tilde{S}_{ij}$ and the LES filter width $\bar{\Delta}$. Furthermore, a proportionality factor C_S is introduced, which is most often referred to as the Smagorinsky constant. Equation (2.39) depicts the obtained correlation.

$$\nu_t = (C_S\bar{\Delta})^2\left|\frac{1}{2}\left(\frac{\partial\tilde{u}_i}{\partial x_j} + \frac{\partial\tilde{u}_j}{\partial x_i}\right)\right| \qquad \text{or} \qquad \nu_t = (C_S\bar{\Delta})^2|\tilde{S}| \tag{2.39a}$$

$$\text{with} \qquad \tilde{S} = \frac{1}{2}\left(\frac{\partial\tilde{u}_i}{\partial x_j} + \frac{\partial\tilde{u}_j}{\partial x_i}\right) \qquad \text{and} \qquad |\tilde{S}| = \sqrt{2\tilde{S}_{lk}\tilde{S}_{lk}} \tag{2.39b}$$

In this work the averaged filter width $\bar{\Delta}$ is derived by equation (2.40).

$$\bar{\Delta} = \sqrt{\frac{1}{3}(\Delta_x^2 + \Delta_y^2 + \Delta_z^2)} \tag{2.40}$$

From equation (2.39) one can obviously see the influence of the filter width on the subgrid scale stresses and the relation between LES and DNS. Through consecutive refinement of the computational grid, the amount of the unresolved subgrid scale stresses decrease and for the edge case that the mesh resolution reaches the Kolmogorov scales the LES coincides with DNS.

An apparent drawback of the Smagorinsky model is the determination of the constant C_S. Simulations with different values for C_S have shown, that the model constant depends on the flow configuration and the Reynolds number and should be chosen in the range $C_S = 0.065 - 0.1$ [8]. This issue leads to the development of a dynamic procedure for the determination of the Smagorinsky constant.

Germano Procedure Germano et al. [27] invented a method which dynamically changes the Smagorinsky constant C_S, which is defined as the square of the Germano constant C_G.

$$C_G = C_S^2 \tag{2.41}$$

A test filter is introduced, which has a larger filter width $\widehat{\bar{\Delta}}$ than the original $\bar{\Delta}$, described in equation (2.39). The keynote is, that the constant C_S should remain the same for both filter widths, in order to calculate the same overall amount of turbulence. The following

equations will describe the procedure to obtain the Germano constant C_G and accordingly the Smagorinsky constant C_S.

The test filter is now applied to the already filtered field with its sub-grid stress τ_{ij}^{sgs}.

$$\widetilde{u_i u_j} = \tilde{u}_i \tilde{u}_j - \tau_{ij}^{\text{sgs}} \qquad \rightarrow \qquad \widehat{\widetilde{u_i u_j}} = \widehat{\tilde{u}}_i \widehat{\tilde{u}}_j - \tau_{ij}^{\text{test}} \tag{2.42}$$

The test-filtered sub-grid stress is shown in equation (2.43).

$$\widehat{\tau_{ij}^{\text{sgs}}} = \widehat{\tilde{u}_i \tilde{u}_j} - \widehat{\widetilde{u_i u_j}} \tag{2.43}$$

Summation of equation (2.42) and (2.43) obtains the Germano identity (2.44), where L_{ij} represents the Leonard stress tensor.

$$\widehat{\tau_{ij}^{\text{sgs}}} - \tau_{ij}^{\text{test}} = L_{ij} \tag{2.44a}$$

$$L_{ij} = \widehat{\tilde{u}_i \tilde{u}_j} - \widehat{\tilde{u}}_i \widehat{\tilde{u}}_j \tag{2.44b}$$

The sub-grid stresses $\widehat{\tau_{ij}^{\text{sgs}}}$ and τ_{ij}^{test} are now modeled with the Smagorinsky model but using the Germano constant C_G instead of the Smagorinsky constant.

$$\tau_{ij}^{\text{sgs}} - \frac{1}{3}\tau_{kk}^{\text{sgs}}\delta_{ij} \approx \; 2C_G \bar{\Delta}^2 |\tilde{S}| \left[\tilde{S}_{ij} - \frac{1}{3}\tilde{S}_{kk}\delta_{ij} \right] = 2C_G m_{ij}^{\text{sgs}} \tag{2.45}$$

$$\tau_{ij}^{\text{test}} - \frac{1}{3}\tau_{kk}^{\text{test}}\delta_{ij} \approx \; 2C_G \widehat{\bar{\Delta}}^2 |\tilde{S}| \left[\widehat{\tilde{S}_{ij}} - \frac{1}{3}\widehat{\tilde{S}_{kk}}\delta_{ij} \right] = 2C_G m_{ij}^{\text{test}} \tag{2.46}$$

By using the definition $M_{ij} = \tilde{m}_{ij}^{sgs} - m_{ij}^{\text{test}}$, equation (2.44) can be written as

$$2C_G M_{ij} = L_{ij} - \frac{1}{3}L_{kk}\delta_{ij}. \tag{2.47}$$

Equation (2.47) shows a system of five equations to derive the constant C_G. Hence, Lilly [60] proposed to minimize the error-square E.

$$E = \left(L_{ij} - \frac{1}{3}L_{kk}\delta_{ij} - 2C_G M_{ij} \right)^2 \tag{2.48}$$

The conditions for a minimum of the error-square lead to a solution of C_G, which is given below in eq. (2.49).

$$C_G = \frac{L_{ij} M_{ij}}{2M_{ij}^2} \tag{2.49}$$

If the Germano constant is calculated by using this equation, it will be possible to get a negative solution for C_G. Negative values for the Germano constant would correspond to an energy transfer from the small scales to the larger scales. To avoid this unreasonable backscattering several approaches are known. In the present work cut-off clipping is used, which just avoids a negative constant by finding the maximum of the calculated value and zero.

$$C_G = \max\left\{ \frac{L_{ij} M_{ij}}{2M_{ij}^2}, 0 \right\} \tag{2.50}$$

2.3. Combustion

The first two sections gave an overview of computational basics and methods to describe fluid flows in general and turbulent flows in particular. The following section deals with the fundamentals of combustion related chemistry and presents some of the most common computational approaches.

The first part of this section gives an insight into chemical reactions and the principles of reaction kinetics. Motivated by this complexity, approaches for the simplification and applicability for the relevant combustion chemistry of this work are introduced and described in detail.

2.3.1. Reaction Kinetics

Chemical reactions are often specified by their global form. For example, the reaction of methane and oxygen, which is important for this work, is represented by its global form (2.51).

$$CH_4 + 2O_2 \rightarrow CO_2 + 2H_2O \tag{2.51}$$

Here, the reactants methane and oxygen are dissociated and build the products carbon dioxide and water. This description of chemical reactions does neither give detailed information about the temporal progress of the reaction nor the creation of intermediate species, but rather represents the stoichiometric relations between the reactants and the dominating products. The actual complete reaction mechanism of the oxidation of methane includes about 1000 elementary reactions and hundreds of intermediate species and radicals, respectively. The time dependent aspect of chemistry is described by chemical kinetics, which determine the temporal progress of chemical reactions. Hence, the most important quantity in chemical kinetics is the reaction rate, which represents the probability of two reactants to collide with an adequate amount of energy to react with each other.

In the following, a model equation for an elementary reaction (2.52) will be used:

$$A + B \rightleftharpoons C + D \tag{2.52}$$

A chemical reaction in general consists of a forward and a backward reaction demonstrated by the bidirectional arrow. For each direction there is a reaction rate r_f and r_b, which depends on the concentrations of the reactants, e.g. for the forward reaction c_A and c_B, viz

$$r_f = k_f c_A c_B. \tag{2.53}$$

k_f describes the velocity coefficient of the forward reaction, that is calculated depending on the temperature T using the Arrhenius law (2.54).

$$k_f = \alpha_a T^{\beta_a} \exp(-E_a/RT) \tag{2.54}$$

α_a and β_a are characteristic constants of the reaction, while E_a stands for the activation energy. Analogously, the backward reaction rate can be obtained and the relation between the forward and backward reaction rate r_f and r_b determines the main direction of the reaction.

As already mentioned, combustion processes include a multitude of elementary reactions with different orders, that can be described by equations like (2.52). Generally, chemical reactions can be differentiated by their order, regarding the number of reactants. For example, the dissociation of water is a first order reaction, while the oxidation of methane in eq. (2.51) is of second order.

In order to handle large mechanisms, a compact notation is necessary and makes sense. The description of a mechanism including N_r elementary reactions ϵ involving N_s species α is shown in eq. (2.55).

$$\sum_{\alpha=1}^{N_s} \nu'_{\alpha,\epsilon}\alpha \rightleftharpoons \sum_{\alpha=1}^{N_s} \nu''_{\alpha,\epsilon}\alpha \qquad \text{with} \qquad \epsilon = 1, ..., N_r \tag{2.55}$$

$\nu'_{\alpha,\epsilon}$ and $\nu''_{\alpha,\epsilon}$ represent the stoichiometric coefficients for species α in elementary reaction ϵ for the reactants' and the products' side, respectively. Analog to this notation, the global reaction rate for each reaction can be expressed as

$$r_\epsilon = k_{f,\epsilon} \prod_{\alpha=1}^{N_s} c_\alpha^{\nu'_{\alpha,\epsilon}} - k_{r,\epsilon} \prod_{\alpha=1}^{N_s} c_\alpha^{\nu''_{\alpha,\epsilon}} \qquad \text{with} \qquad \epsilon = 1, ..., N_r. \tag{2.56}$$

With this information, the source term ω_α for each species transport equation (eq. (2.4)) is obtained by (2.57).

$$\omega_\alpha = M_\alpha \sum_{\epsilon=1}^{N_r} (\nu''_{\alpha,\epsilon} - \nu'_{\alpha,\epsilon}) r_\epsilon \qquad \text{with} \qquad \alpha = 1, ..., N_s \tag{2.57}$$

As already described above, the usage of complete chemical reaction mechanisms within CFD simulations is not feasible and applicable. Therefore, efficiently reduced or so called skeletal mechanisms are developed, that include only the most important reactions in order to reasonably represent the global reaction. The most common detailed mechanism for the description of methane oxidation involving nitrogen, is the GRI-mechanism (Gas Research Institute). Version 3.0 includes 53 reactions with 325 different chemical species [97] and is able to represent even transient effects like ignition. Based on the GRI mechanisms, several reduced mechanisms have been published (e.g. [62]), in order to obtain applicable chemistry for the incorporation into simulations of turbulent combustion systems. These mechanisms reduce the number of elementary reactions and species to a necessary limit in order to get reasonable results, like major species profiles or peak temperatures [12]. Here it needs to be mentioned that after the reduction a chemical mechanism is not generally valid for all types of combustion anymore.

2.3.2. Flame Modes

In combustion science, flames are categorized by the way how fuel and oxidizer are mixed prior to the combustion reaction itself. There are three different categories: the premixed, the non-premixed and the partially-premixed combustion mode. The two former ones are characteristical and easily distinguishable, while the latter case lies in between the other ones and represents a wide range of flames, that cannot be specified as either premixed

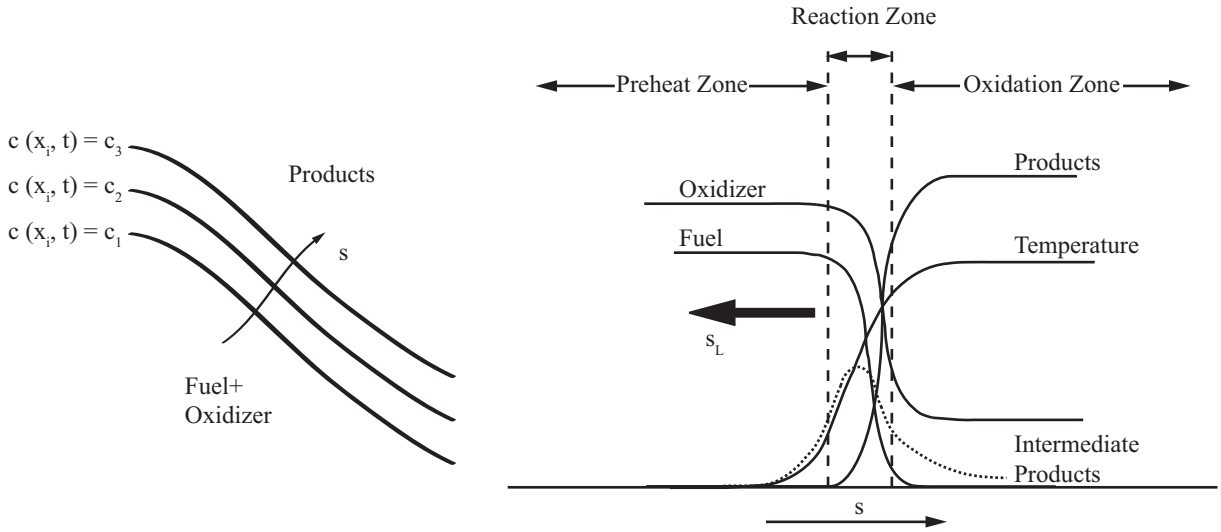

Figure 2.2.: Schematic of a premixed flame. Visualization of the flame front (left); Profiles of characteristic quantities over the flame coordinate s in a premixed flame front (right).

or non-premixed. The chosen numerical combustion model strongly depends on the mode of combustion and hence has to be known before the simulation, even though a precise classification is not always possible. The present contribution is all about non-premixed and partially-premixed flame configurations, but for the sake of completeness the premixed combustion mode is explained as well. The following section will give a brief overview of the three categories mentioned above.

2.3.2.1. Premixed Flames

In premixed flames, fuel and oxidizer are mixed on the molecular level prior to the combustion reaction. Their major technical relevance lies in stationary gas turbines for power generation, where the combustion process takes place in a well defined and constant manner. Due to the perfect premixing, the combustion is characterized by a high efficiency and low emissions. Contrarily, there is a safety issue called flashback, which is a synonym for a flame front motion, that proceeds through the unburnt gas mixture towards the fuel supply. This implies a very high risk and thus costly arrangements to avoid flashbacks need to be installed for premixed flame applications.

For a theoretical consideration the schematic of a premixed flame front is shown in figure 2.2. The sketch on the left represents the cross section of a flame front with three lines of constant combustion progress $c(x_i, t) = c_1, ..., c_3$ and the flame coordinate s. In premixed flames, the flame front separates the mixture of fuel and oxidizer from the created products. On the right side of figure 2.2, where characteristic profiles of relevant quantities are plotted over the flame coordinate s, one can see how oxidizer and fuel are consumed and products and intermediate products are built. A premixed flame front consists of three regions, the preheat zone, where the temperature of the mixture is slightly increased by heat conduction and the first radicals are formed. The adjacent reaction zone is defined by the highest temperature gradient and includes the region,

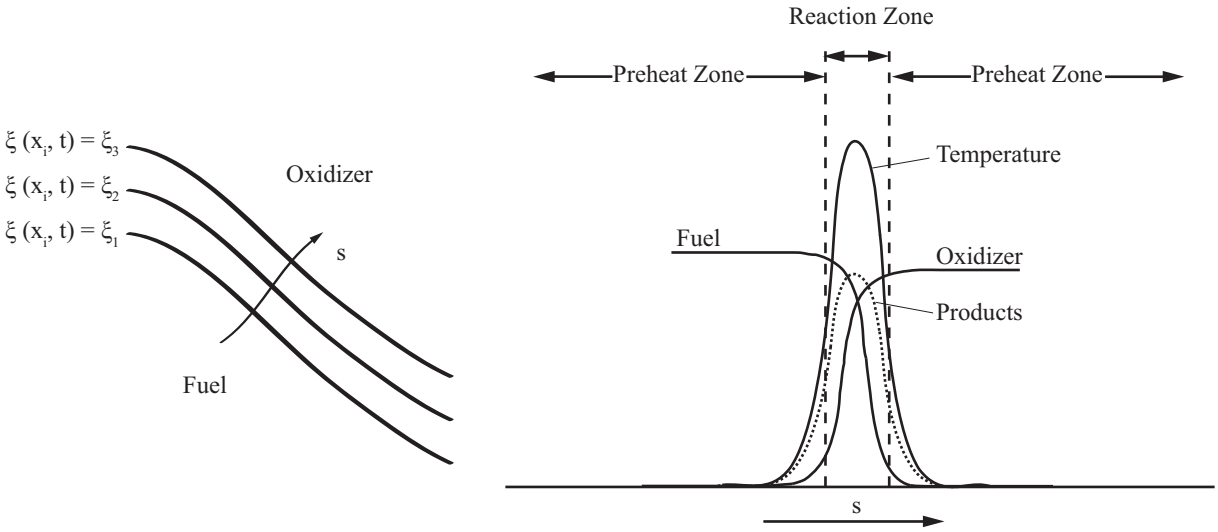

Figure 2.3.: Schematic of a non-premixed flame. Visualization of the flame front (left); Profiles of characteristic quantities over the flame coordinate s in a non-premixed flame front (right).

where the intermediate products reach their peak values. Within the so called oxidation zone, only very slow chemical reactions occur and the temperature reaches its peak value. A premixed flame front moves orthogonally to its dimensions into the unburnt gas mixture with a characteristic velocity, the laminar flame speed s_L, which strongly depends on the fuel-oxidizer mixture.

2.3.2.2. Non-premixed Flames

Non-premixed flames differ from premixed flames in terms of the mixing of fuel and oxidizer. As figure 2.3 shows, the flame front separates fuel and oxidizer and thus flashback events cannot occur. Technical applications of the non-premixed combustion mode are for example airborne gas turbines, where the safety during operation plays a major role. Commonly, the non-premixed combustion of carbohydrate fuel is connected to sooting flames, which is a disadvantage compared to premixed flames.

On the left side of fig. 2.3 a sketch of a non-premixed flame front is presented. Here, fuel and oxidizer are initially segregated and the reaction zone is located where diffusion and convection create a flammable mixture. This means, non-premixed flames are controlled by mixing processes and can therefore be described by the degree of mixing, called mixture fraction $\xi(x_i, t) = \xi_1, ..., \xi_3$. Looking at the profiles of the relevant quantities over the flame coordinate s in figure 2.3 (right), one can obviously see the differences to premixed combustion. Fuel and oxidizer enter the flame front from opposite directions and are consumed by chemical reactions, which results in the creation of products within the reaction. In contrast to premixed flames, the products' mass fractions and the temperature reach their peak values in there. Due to the flammability limits of the mixture, there is no distinct flame velocity, but rather a diffusion and convection driven motion of the flame front. A further detailed description of the mixture fraction approach mentioned above is given in section 2.3.3.

2.3.2.3. Partially-premixed Flames

The regime of partially-premixed combustion is not as clearly defined as the former two. Actually, every technical application of combustion includes premixed as well as non-premixed combustion regions. All modes in between can be described as a partially premixed flame. Interestingly, there are modes of the two ideal ones, that can be seen as partially premixed, e.g. premixed flames with a slight variation of the mixture fraction or lifted non-premixed flames with a premixing region before the flame front. Therefore, today's most common approach for numerical simulations of partially-premixed flame is a combination of premixed and non-premixed flame models.

2.3.3. Mixture Fraction Approach

In simulations of non-premixed flames, the chemical time scales τ_{chem} are assumed to be much smaller than the turbulent ones τ_{turb}, which can be described by the characteristic non-dimensional parameter Damköhler number Da, as $\text{Da} = \tau_{\text{turb}}/\tau_{\text{chem}} \rightarrow \infty$. For that reason, non-premixed combustion is described by the 'mixed is burnt' idea and can be defined by the degree of fuel and oxidizer mixing. This approach is based on the works of Shvab [95] and Zel'dovich [107], where the transport equations for all species (2.4) and the enthalpy (2.17) collapse into a single transport equation for the mixture fraction ξ. The following section will give a brief overview of this procedure.

Within the derivation of the mixture fraction approach some assumptions need to be applied in order to transform the equations. These are:

- Identical diffusion coefficients for all species α, D_α=D
- Thermal diffusivity consistent to species diffusivity, Le = 1
- Neglected radiation, $q_R = 0$
- No consideration of compressible heating
- Negligible importance of Dufour-, Soret- and similar diffusion effects
- No effect of dissipation on the enthalpy

The idea of the mixture fraction formalism is based on the fact that instead of using the species mass fractions Y_α to describe a chemical mechanism the element mass fractions Z_i can be used. The element mass fraction is defined analogously to the species mass fraction Y_α in section 2.1.4 as $Z_i = m_i/m$, where m_i represents the mass of the element i. Contrarily to eq. (2.4), the set of transport equations for Z_i is source free, since elements are neither destroyed nor created by transport or combustion reactions.

Applying all assumptions presented earlier, the form of the element mass fraction transport equation is now identical to the enthalpy conservation (2.17) and reads as

$$\frac{\partial}{\partial t}(\rho Z_i) + \frac{\partial}{\partial x_j}(\rho Z_i u_j) = \frac{\partial}{\partial x_j}\left(\rho D \frac{\partial Z_i}{\partial x_j}\right). \tag{2.58}$$

Even though the form of the equations is identical, the boundary conditions for the element mass fractions and the enthalpy certainly differ. For a two stream problem it is possible

to normalize the element mass fraction and the enthalpy in the way it is described in eq. (2.59) and so the quantities are set to be zero in the oxidizer and unity in the fuel stream.

$$Z_i^* = \frac{Z_i - Z_{i,\mathrm{ox}}}{Z_{i,\mathrm{fuel}} - Z_{i,\mathrm{ox}}} \qquad \text{and} \qquad h^* = \frac{h - h_{\mathrm{ox}}}{h_{\mathrm{fuel}} - h_{\mathrm{ox}}} \tag{2.59}$$

Here, the subscripts $_{\mathrm{ox}}$ and $_{\mathrm{fuel}}$ denote the conditions for the oxidizer stream and the fuel stream, respectively. Based on equation (2.59), the mixture fraction ξ can be defined by

$$\xi = Z_i^* = h^* \tag{2.60}$$

and the transport equation without any source term included reads as

$$\frac{\partial}{\partial t}(\rho\xi) + \frac{\partial}{\partial x_i}(\rho\xi u_i) = \frac{\partial}{\partial x_i}\left(\rho D \frac{\partial \xi}{\partial x_i}\right). \tag{2.61}$$

In this context the stoichiometric mixture fraction ξ_{st} is of particular importance, because it defines the mixture, where a complete consumption of fuel and oxidizer is fulfilled. ξ_{st} is defined as

$$\xi_{st} = \frac{1}{1 + \frac{\nu'_{O_2} M_{O_2} Y_{\mathrm{fuel},1}}{\nu'_{\mathrm{fuel}} M_{\mathrm{fuel}} Y_{O_2,0}}}, \tag{2.62}$$

with the molecular weights M_α and given the fact, that oxygen enters in stream 0 and the fuel in stream 1. In order to transfer the mixture fraction ξ into the commonly used equivalence ratio ϕ, equation (2.63) can be applied.

$$\phi = \frac{\xi}{1-\xi} \cdot \frac{1-\xi_{st}}{\xi_{st}} \tag{2.63}$$

For lean mixtures with $\xi < \xi_{st}$ the equivalence ratio lies in the region of $\phi < 1$ and for rich mixtures with an excess of fuel the equivalence ratio takes values larger than unity.

2.3.3.1. Filtered Mixture Fraction Transport Equation

Similar to the momentum transport equations (2.38) in the context of Large Eddy Simulations, the previously defined filtering procedure needs to be applied onto the mixture fraction transport equation. The resulting equation reads as

$$\frac{\partial}{\partial t}(\bar{\rho}\tilde{\xi}) + \frac{\partial}{\partial x_i}(\bar{\rho}\tilde{\xi}\tilde{u}_i) = \frac{\partial}{\partial x_i}\left(\bar{\rho}\tilde{D}\frac{\partial \tilde{\xi}}{\partial x_i} - \bar{\rho} J_i^{\mathrm{sgs}}\right). \tag{2.64}$$

For the sub-grid scalar flux J_i^{sgs} an approach analog to the eddy-viscosity model is used. Therefore, the filtered turbulent diffusivity D_t is introduced and the sub-grid scalar flux is defined by

$$J_i^{\mathrm{sgs}} = \widetilde{\xi u_i} - \tilde{\xi}\tilde{u}_i = -D_t \frac{\partial \tilde{\xi}}{\partial x_i} \tag{2.65}$$

Both of the diffusivity coefficients $\tilde{D}$ and D_t are related to their viscosity counterparts by the laminar and the turbulent Schmidt numbers Sc and Sc_t by

$$\tilde{D} = \frac{\tilde{\nu}}{\mathrm{Sc}} \qquad \text{and} \qquad D_t = \frac{\nu_t}{\mathrm{Sc}_t} \qquad \text{with} \qquad D_{\mathrm{eff}} = \tilde{D} + D_t \tag{2.66}$$

The application of all sub models leads to the eventual filtered mixture fraction transport equation

$$\frac{\partial}{\partial t}(\bar{\rho}\tilde{\xi}) + \frac{\partial}{\partial x_i}(\bar{\rho}\tilde{\xi}\tilde{u}_i) = \frac{\partial}{\partial x_i}\left(\bar{\rho}D_{\text{eff}}\frac{\partial\tilde{\xi}}{\partial x_i}\right). \tag{2.67}$$

In the context of this work, the turbulent Schmidt number is set to a constant value in the domain. Usually, values in the range of $\text{Sc}_t = 0.33, ..., 0.7$ are applied [8]. Furthermore, there are comparable dynamic approaches for the turbulent Schmidt number [76], where a non-uniform distribution of Sc_t is obtained.

2.3.4. Modeling of Non-premixed Combustion

As previously described in section 2.3.1, the application of detailed chemical reaction mechanisms like the GRI 3.0 [97] is not feasible in Large Eddy Simulations of turbulent flows. Due to the high numbers of transported species and the related elementary reactions, a reasonable inclusion of detailed reaction mechanisms has only been realized for transient simulations of one or two dimensional laminar reacting flows. The issue in the representation of chemical reactions is the variety of the involved time scales, that are typically in the order of $\tau_{\text{chem}} \approx 10^{-10}, ..., 1s$. However, the physical turbulent time scales are situated in the region of $\tau_{\text{turb}} \approx 10^{-2}, ..., 10^{-4}s$ [103]. With this knowledge, it is possible to reduce reaction mechanisms by orders of magnitudes in terms of the involved species and reactions. The keyword for the reduction of chemical mechanisms is the assumption of quasi-steady state for intermediate species' reactions. Further information about reduction strategies can be found in Smooke [98].

Instead of using reduced mechanisms the chemistry can be represented by only a few scalars, like the previously described mixture fraction. Models based on that approach are introduced in the following sections in the order of increasing complexity. The more complex the model becomes, the more additional quantities are necessary to characterize the thermo-kinetic state and hence more chemical dynamics and kinetics are included. The simplest model employs with only a single quantity, the mixture fraction, to define the thermo-kinetic state, while the most complex one corresponds to the detailed mechanism with all species included.

2.3.4.1. Burke-Schumann or 'Mixed-is-Burnt'

The Burke-Schumann or 'Mixed-is-Burnt' model, originally proposed by H. Rummel [28], is the simplest model available for the description of chemical reactions in the context of numerical simulations. It is based on the mixture fraction ξ and defines the thermo-kinetic state of the fluid as linear functions, viz $\phi_{BS} = f(\xi)$. This corresponds to a representation of the chemistry as a pure mixing problem between the unburnt or burnt state and the stoichiometric point, which can be seen in figure 2.4. The major assumption in this model is that the combustion takes place in a singular sheet related to the stoichiometric mixture fraction, where fuel and oxidizer are fully consumed, while the temperature and the product mass fractions reach their maximum. Since the model considers only a global reaction formulation, no intermediate products appear and hence cannot be simulated. Furthermore, this model obtains too high temperatures within the stoichiometric mixture,

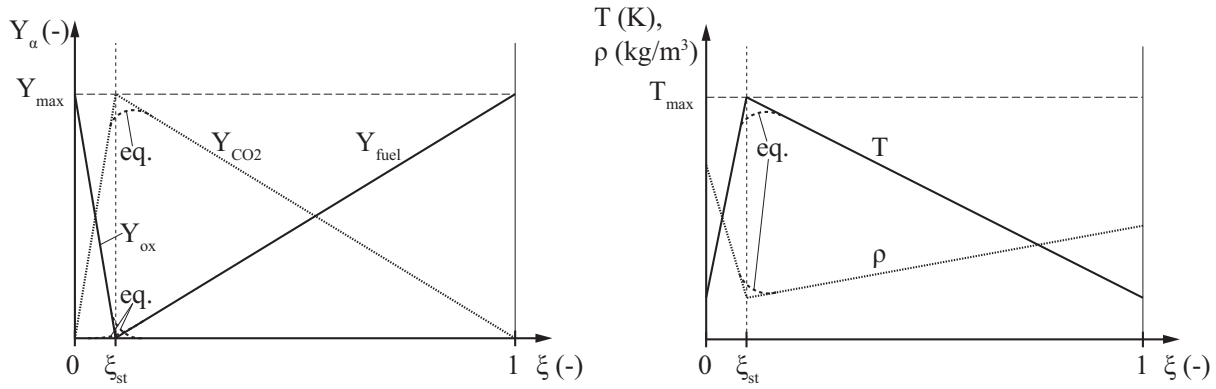

Figure 2.4.: Schematic distributions of mass fractions (left), temperature and density (right) calculated by a Burke-Schumann flame sheet model. Furthermore, the effects of equilibrium chemistry for the mass fractions, the temperature and the density are added.

for this reason the Burke-Schumann approach has no relevance for today's industrial simulation practice, but is rarely used for academic purposes only.

2.3.4.2. Equilibrium Chemistry

In contrast to the Burke-Schumann approach, where only a global chemical reaction is described, the equilibrium model represents a set of elementary reactions, that can be chosen arbitrarily. In this set, the forward and the backward direction of each reaction is assumed to be in chemical equilibrium. Figure 2.4 shows the differences between the mixed-is-burnt model and the equilibrium approach. Variations can only be determined in the region around stoichiometry, where the distributions are continuous instead of having a discrete kink. Furthermore, the equilibrium model also allows fuel and oxidizer to be coexistent at the same time. Due to the diversity of involved reactions, distributions for intermediate species of the combustion process are obtained. The disadvantage of this model lies in the assumption of steady-state for all reactions and hence, transient phenomena cannot be represented. Nevertheless, this ansatz gives satisfactory results for temperature and major species distributions by only using the mixture fraction to determine the thermo-kinetic state $\phi_{eq} = f(\xi)$.

2.3.4.3. Steady Flamelet Model

The flamelet approach [105] basically describes a turbulent non-premixed flame front as a sequence of so called laminar flamelets. The key hypothesis behind the steady flamelet approach is that the flame sheet is always thin compared to turbulent structures and hence the reaction zone remains locally planar and consumes reactants in a laminar fashion. The model was extended by Peters [72] with the steady flamelet equation, which is based on the species transport equation (2.4). The obtained equation (2.68) relates the species mass fractions Y_α with the mixture fraction ξ and reads as

$$-\rho\frac{\chi}{2}\frac{\partial^2 Y_\alpha}{\partial\xi^2} = \omega_\alpha \qquad \text{with} \qquad \chi = 2D\frac{\partial\xi}{\partial x_i}\frac{\partial\xi}{\partial x_i}. \tag{2.68}$$

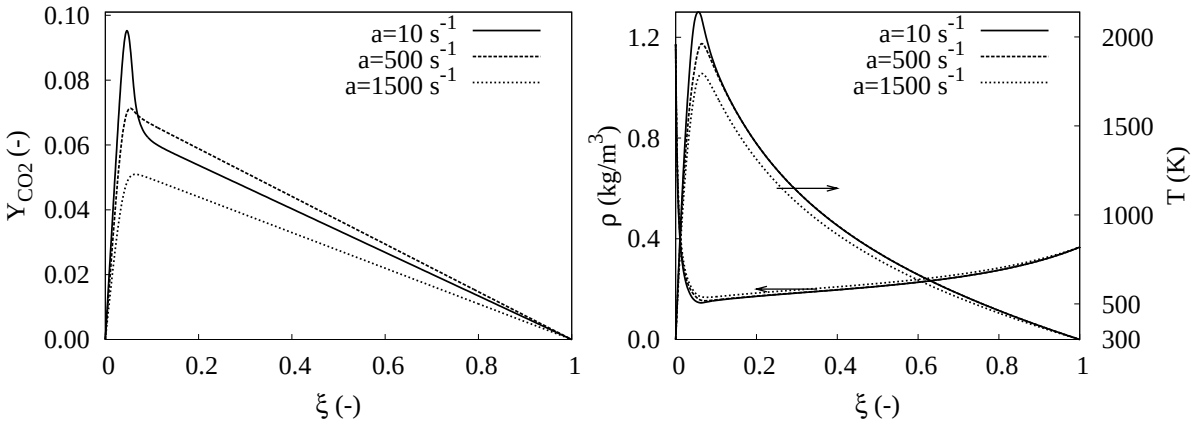

Figure 2.5.: Flamelet solutions for the CO_2 mass fraction, the density ρ and the temperature T for different strain rates, $a = 10, 500, 1500\,s^{-1}$. The fuel consists of methane and hydrogen with a mixing ratio of 1:1.

This form is achieved by transforming eq. (2.4) and neglecting the accumulating term by the assumption of small chemical time scales. The steady flamelet equation introduces the scalar dissipation rate χ which is used as a parameter to quantify the deviation from the equilibrium. Here, χ acts as a substitution for the strain rate a, which is a measure for the actual effective shear within the flame. With relation (2.68) and analog formulations for the density and the temperature, the determination of the thermo-chemical state in the steady flamelet model corresponds to two quantities, viz $\phi_{SF} = f(\xi, \chi)$. Figure 2.5 shows flamelet distributions for the mass fraction of CO_2, the density and temperature for a configuration with a methane/hydrogen fuel and air as oxidizer. The present contribution addresses a number of flames using this fuel/oxidizer composition. The profiles in mixture fraction space are shown for three different strain rates $a = 10, 500, 1500 s^{-1}$ in each case, where the lowest value corresponds to a hardly sheared and the highest to a laminar flamelet close to extinction due to strain. The plots of the CO_2 mass fraction and the temperature show large deviations between the two limiting cases, while the density is relatively insensitive to the increase of the strain rate. Continuously raised strain rate affects the carbon dioxide mass fraction and the temperature to decrease in the stoichiometric point, whereas the density is slightly increased.

A more common and practical approach to obtain the steady flamelet solution is the calculation of a non-premixed, laminar counterflow configuration by a one-dimensional chemistry solver. In the context of this work, the flamelet solutions are generated using the solver CHEM1D [99], [67], which is based on the GRI 3.0 mechanism exploiting the assumption of equal diffusivities and unity Lewis number Le=1. This burner is characterized by two oppositely arranged nozzles for fuel and oxidizer. In between these two inlets a planar, laminar non-premixed flame is formed, which is assumed to be one-dimensional. The strain rate can be adjusted by the distance of the nozzles and the inlet velocities of both streams. By varying the shear of the flame, the entire chemistry space is generated over the strain rate and the mixture fraction.

As described in section 2.2.1.3, Large Eddy Simulation is based on spatial filtering of the governing equations and hence also the scalar dissipation rate must be available in its

filtered state $\tilde{\chi}$. Therefore, the definition in eq. (2.68) can be transferred into the filtered form

$$\tilde{\chi} = -2(\tilde{D} + D_t)\frac{\partial\tilde{\xi}}{\partial x_i}\frac{\partial\tilde{\xi}}{\partial x_i}. \tag{2.69}$$

In general, even though the flamelet approach creates an opportunity to deviate from the equilibrium state and gives promising results for stable burning flame configurations [68], no kinetics are added to the presentation of the chemistry. That means, the computation of highly transient phenomena like lift off, extinction or re-ignition can only be addressed in a restricted way. For example, if extinction occurs, which is related to a high scalar dissipation rate, the thermo-kinetic state would be determined by this extinct flamelet. Unfortunately, the abrupt drop of the temperature and the correlated density is not physical and would additionally lead to numerical instabilities.

2.3.4.4. Flamelet-Generated Manifolds

The Flamelet-Generated Manifolds (FGM) approach [66] adopts the same basic idea as the flamelet method but extends it by kinetic effects, which are included by adding the chemical manifold approach. Manifolds theoretically represent the collapsed trajectories of slow chemical reactions, including the state of equilibrium. All trajectories leading to this manifold and allegorizing the fast reactions are neglected by assuming the chemical time scale of these reactions to be small compared to the turbulent time scales. Therefore, each calculated flamelet is additionally parameterized by a set of control variables, which define the manifold itself and the determination of the reaction progress on the manifold. Therefore these variables are often referred to as progress variables $\mathcal{Y}_i$ that can be described by i linear combinations of product mass fractions Y_α as

$$\mathcal{Y}_i = \left(\sum_\alpha w_\alpha Y_\alpha\right)_i. \tag{2.70}$$

In this context, w_α represents the weighting factors for the linear combination of the mass fractions. For an explicit indication of the progress of the combustion process, the choice of $\mathcal{Y}_i$ must provide a monotonic behavior over the flame front. In order to avoid excessive computational costs, the number of progress variables i should not exceed 2, but is most commonly limited to one additional progress variable beside the mixture fraction. Therefore, with the application of the FGM approach the thermo-chemical state is determined by $\phi_{FGM} = f(\xi, \mathcal{Y}_i)$. In contrast to the steady flamelet approach, where the scalar dissipation rate is indirectly defined by the calculated mixture fraction field in eq. (2.68), the distributions of the progress variables are obtained by solving transport equations equivalent to eq. (2.4).

The first mixture fraction/progress variable approach was published by Pierce and Moin [73] and was based on non-premixed flamelets, where the scalar dissipation rate of the classical flamelet approach was replaced by the transported progress variable. However, the mixture fraction/progress variable approach can also be used with premixed flamelets in marked contrast to the original mixture fraction/scalar dissipation rate approach since premixed flamelets have a scalar dissipation rate of zero. In this work, the FGM tables

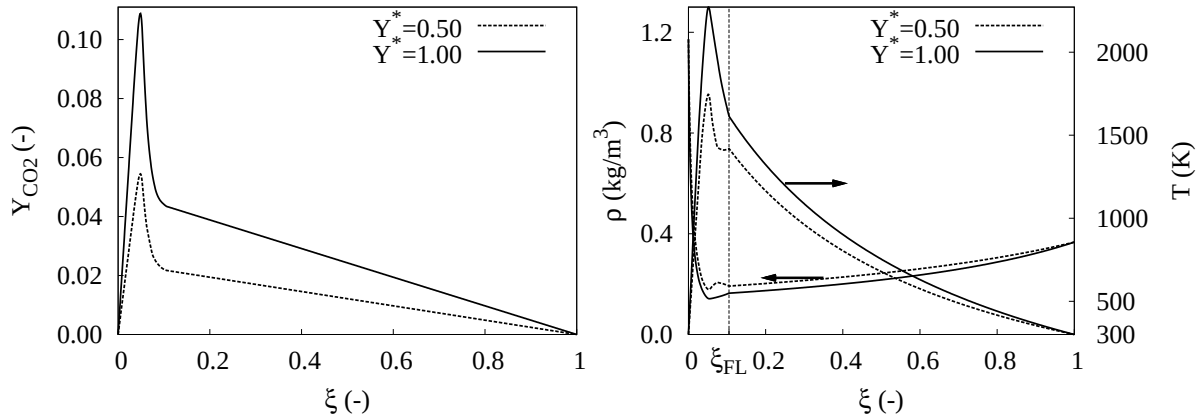

Figure 2.6.: FGM solutions for the CO_2 mass fraction, the density ρ and the temperature T for different values of the normalized progress variable $\mathcal{Y}^* = 0.5, 1.0$. The fuel consists of methane and hydrogen with a mixing ratio of 1:1.

are exclusively based on premixed flamelets, even though the focus lies solely on non-premixed configurations. The reasons are based on the long experience with premixed FGM in the context of LES in non-premixed and partially-premixed burner configurations [30], [68], [104] and furthermore on the work of Vreman et al. [102]. The paper of Vreman et al. describes the differences between premixed and non-premixed flamelets and the impact on LES of non-premixed piloted jet flames. A conclusive argument for the usage of premixed flamelets even in the context of non-premixed flamelets is given in [102]. Both approaches cannot represent the entire ξ-$\mathcal{Y}$-space by solving the underlying one-dimensional equations, but have to use interpolation schemes for the undefined regions [50]. In the case of premixed flamelets, the region is located beyond the flammability limits with very low or very high values of the mixture fraction, where mixing is the prevalent physical phenomenon. Since no chemical reactions occur in these regions, the interpolation of the thermo-kinetic state is comparatively easy to realize. In the context of non-premixed flamelets, the undefined regions are limited by the last burning flamelet with the highest scalar dissipation rate, which is followed by the non-burning solution of the flamelet equations. The area between these two flamelets, ranges over the entire mixture fraction space, even in the region of stoichiometry, where chemical reactions are present. Therefore, even the chemical source term $\omega_{\mathcal{Y},i}$ has to be modeled and interpolated, respectively. Since the transport of the progress variable is very sensitive with respect to $\omega_{\mathcal{Y},i}$, a high level of accuracy cannot be expected.

Figure 2.6 shows profiles of CO_2 mass fractions (left), the density and the temperature (right) parameterized by the normalized progress variable $\mathcal{Y}^*$, which is defined by the mass fraction of CO_2 weighted by its molar mass and normalized by the corresponding equilibrium value. Here, profiles for $\mathcal{Y}^* = 0.5, 1.0$ are depicted. It can be seen, how the CO_2 mass fraction and the temperature are increased by raising the progress variable from 0.5 to unity and how the density decreases. Furthermore, the temperature profiles obviously illustrate the extrapolation from the rich flammability limit ξ_{FL} and the related discontinuity in this location.

The normalization of the progress variable has two main reasons: firstly, the transformation of the progress variable to a region from zero to unity and secondly, to provide statistical independence from the mixture fraction ξ. The latter reason is related to turbulence-chemistry interaction and thus will be described in detail in section 2.3.5. For the normalization procedure, the equilibrium values (cf. figure 2.4) of the mass fractions included within $\mathcal{Y}_i$ are used and one obtains

$$\mathcal{Y}_i^* = \frac{\mathcal{Y}_i}{\mathcal{Y}_{i,eq}(\xi)} \qquad \text{with} \qquad \mathcal{Y}_{i,eq} = \left(\sum_\alpha w_\alpha Y_{\alpha,eq}(\xi) \right)_i . \tag{2.71}$$

For the application of the FGM approach, the filtered progress variables need to be transported. The transport equation looks analogous to the filtered mixture fraction transport equation (2.67) and reads as

$$\frac{\partial}{\partial t}(\bar{\rho}\tilde{\mathcal{Y}}_k) + \frac{\partial}{\partial x_i}(\bar{\rho}\tilde{\mathcal{Y}}_k\tilde{u}_i) = \frac{\partial}{\partial x_i}\left(\bar{\rho}D_{\text{eff}}\frac{\partial\tilde{\mathcal{Y}}_k}{\partial x_i}\right) + \tilde{\omega}_{\tilde{\mathcal{Y}},k}. \tag{2.72}$$

2.3.5. Turbulence-Chemistry Interaction

During the preceding sections, the simulation techniques and modeling approaches of turbulence and chemistry have been individually introduced and described in detail. The following sections will give insights into the interaction between these two phenomena in the context of numerical simulations of turbulent flows. Therefore, the models that have been applied in this work are shown and explained for the flamelet and the FGM approach. The focus here lies on the approach of the transported filtered density function (FDF), which will be extensively characterized below.

Principally, the turbulence-chemistry interaction deals with the sub-filter distributions of the transported scalars that define the thermo-chemical state. The key point is that the mesh size in RANS and the filter width in LES are too large in order to consider the smallest occurring scales of turbulence. This was already particularized in previous sections. Similar to the Kolmogorov length scale η_k, there is a length scale for the smallest scalar structures, the Batchelor length scale λ_B [3]. The Batchelor scale is directly related to the Kolmogorov scale by $\lambda_B = \eta_k/\text{Sc}^{1/2}$. For typical Schmidt numbers of gases in the order of unity, the Batchelor scale has approximately the same dimension as the Kolmogorov length.

Unfortunately, by the discretization of a simulation domain with a numerical grid and in LES context, the subsequent calculation of the filtered transport equations, only spatial mean values for the transported scalars are obtained. However, the chemistry is strongly connected to the mixing on the molecular level. The issue behind that is depicted in figure 2.7

which illustrates the spatial filtering operation in a one-dimensional problem. The actual distribution of the scalar ψ is given with the dashed line, while the solid lines represent the spatially filtered values $\tilde{\psi}$. As one can easily see in the plot, the sub-filter information are entirely neglected and information about the variance around the spatial mean value are also not considered anywhere. Unfortunately, because of its highly non-linear relation, the thermo-chemical state cannot be determined by the knowledge of

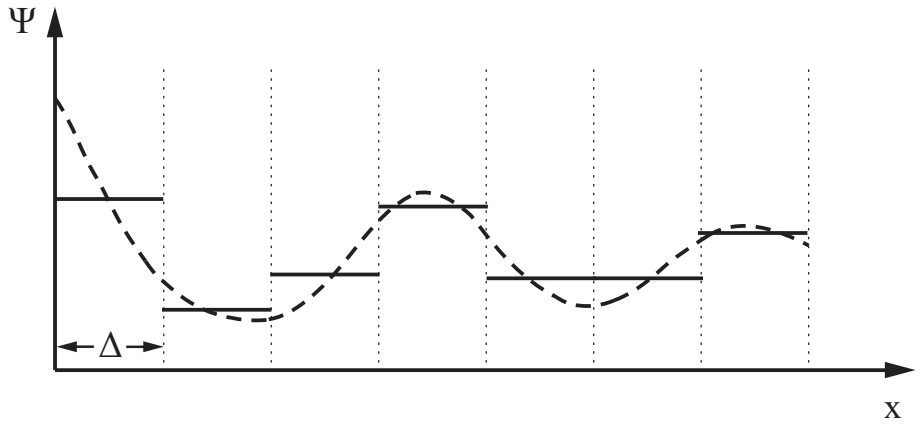

Figure 2.7.: Schematic of a one-dimensional quantity distribution. Actual profile of ψ (dashed) and the corresponding spatial mean (dashed). The vertical dotted lines represent the filter width Δ.

the filtered value of the defining scalar alone, but with the knowledge of the sub-filter probability density function (PDF), mathematically expressed as

$$\tilde{\phi}(\psi) \neq \phi(\tilde{\psi}) \qquad \text{but} \qquad \tilde{\phi}(\psi) = \int \phi(\psi)\mathcal{P}(\psi)\, d\psi. \tag{2.73}$$

Here, $\phi(\psi)$ stands for the chemical kinetics in this work provided by the one-dimensional chemistry solver CHEM1D and $\mathcal{P}(\psi)$ represents the probability density function (PDF) of the defining scalars ψ. In the LES context, the PDF represents the sub-filter distribution of a quantity within a control volume not spatially, but statistically. For the introduction into the basics of probability density functions the reader is referred to appendix A. The following sections give an overview of the approaches and models applied in this work, firstly for the steady flamelet model and secondly for the FGM approach.

2.3.5.1. PDF-Modeling in Steady Flamelet Context

In section 2.3.4.3, the steady flamelet model has already been introduced and characterized. Following the remarks made previously, the thermo-chemical state in the steady flamelet model is defined by $\phi = f(\xi, \chi)$. Therefore, in simulations of turbulent flows the filtered thermo-chemical state is given as

$$\tilde{\phi}_{SF}(\xi, \chi) = \iint \phi(\xi, \chi)\mathcal{P}(\xi, \chi)\, d\xi\, d\chi. \tag{2.74}$$

Here, $\mathcal{P}(\xi, \chi)$ represents a two-dimensional joint PDF of the mixture fraction and the scalar dissipation rate. With the assumption of statistical independence of these two scalars, the joint PDF can be transformed into the product of two single PDFs, viz

$$\mathcal{P}(\xi, \chi) = \mathcal{P}(\xi)\, \mathcal{P}(\chi). \tag{2.75}$$

Unfortunately, the PDFs of the two properties are not known and models need to be applied. A common modeling approach is the usage of presumed PDF shapes. With

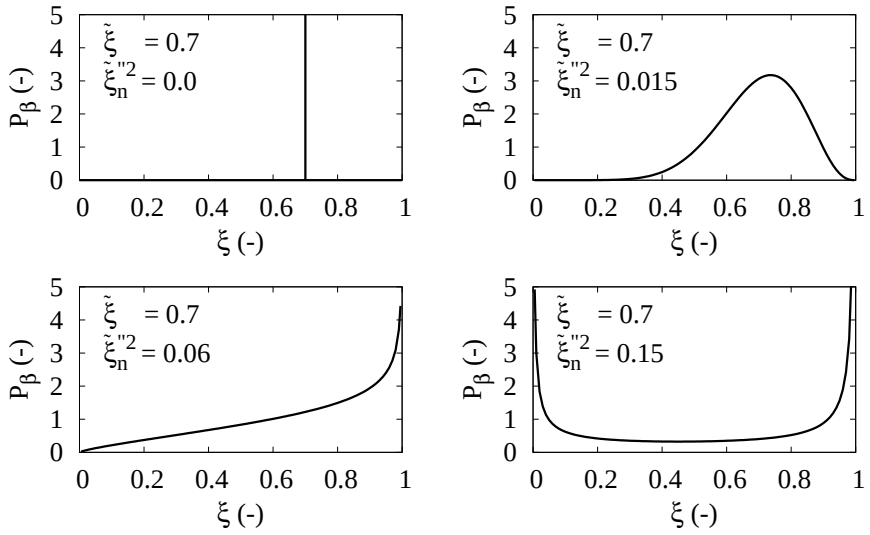

Figure 2.8.: Shapes of the β-function $\mathcal{P}_\beta(\xi;\tilde{\xi},\widetilde{\xi''^2_n})$ for a filtered mixture fraction value of $\tilde{\xi}=0.7$ with varying sub-filter variances.

this ansatz, the shapes of the PDFs are previously assumed by certain parameterizable functions. The most common presumed PDF shape for the mixture fraction ξ is the so called β-function [85], which is defined by equation (2.76).

$$\mathcal{P}_\beta(\xi;\tilde{\xi},\widetilde{\xi''^2}) = \frac{\xi^{(\alpha-1)}(1-\xi)^{(1-\beta)}}{\int_0^1 \xi^{(\alpha-1)}(1-\xi)^{(\beta-1)}\,d\xi} \tag{2.76}$$

Obviously, the β-PDF is parameterized by the filtered mean and the sub-filter variance $\widetilde{\xi''^2}$, that are included in the parameters α and β.

$$\alpha = \tilde{\xi}\left(\frac{\tilde{\xi}(1-\tilde{\xi})}{\widetilde{\xi''^2}} - 1\right) \qquad \text{and} \qquad \beta = (1-\alpha) \tag{2.77}$$

The sub-filter variance is commonly not known, but can be obtained by several approaches. The most accurate and likewise computationally most costly, is to solve an additional transport equation for this quantity. Alternatively, different models are known to compute $\widetilde{\xi''^2}$. The model which is used here is based on a similarity ansatz and deals with a test filter. Details are given below in the numerics chapter. For simplification reasons, the sub-filter variance is normalized by the largest possible variance depending on the filtered mean value and is then called unmixedness $\widetilde{\xi''^2_n}$.

$$\widetilde{\xi''^2_n} = \frac{\widetilde{\xi''^2}}{\tilde{\xi}(1-\tilde{\xi})} \tag{2.78}$$

Figure 2.8 demonstrates the different appearances of the β-function. Therefore, the function is evaluated for a constant filtered mean value of the mixture fraction of $\tilde{\xi}=0.7$

and varying sub-filter variances. The representable shapes range from a Dirac-function for $\widetilde{\xi''^2}_n = 0.0$ via Gaussian-like functions to bimodal shapes for high sub-filter variances. Due to this distinct adaptability the β-function is the most common model for modeling the sub-filter PDF.

The probability density function for the scalar dissipation rate $\mathcal{P}(\chi)$ is here and most commonly modeled by a Dirac-function, which corresponds to a neglect of the sub-filter distribution of χ. It follows

$$\mathcal{P}_\delta(\chi;\tilde{\chi}) = \delta\chi. \tag{2.79}$$

2.3.5.2. PDF-Modeling with Flamelet Generated Manifolds

Within the FGM modeling, the thermo-chemical state is defined by $\phi = f(\xi, \mathcal{Y})$. Actually, the procedure is the same as depicted in the previous section. The filtered thermo-chemical state is obtained analog to eq. (2.74) and leads to

$$\tilde{\phi}_{FGM}(\xi, \mathcal{Y}_i) = \iint \phi(\xi, \mathcal{Y}_i)\mathcal{P}(\xi, \mathcal{Y}_i)\, d\xi\, d\mathcal{Y}_i. \tag{2.80}$$

In this case, the separation of the joint PDF of the mixture fraction and the progress variables is not trivial. This is due to the fact that the progress of the reaction indicated by $\mathcal{Y}_i$ depends strongly on the mixture fraction and hence the assumption of statistical independence cannot be justified. Therefore, the progress variables need to be uncoupled from the mixture fraction. This is achieved by the normalization of $\mathcal{Y}_i$ with their corresponding equilibrium values, as shown in equation (2.71). Now, the separation of the joint PDF can be accomplished, which leads to

$$\mathcal{P}(\xi, \mathcal{Y}_i^*) = \mathcal{P}(\xi)\, \mathcal{P}(\mathcal{Y}_i^*). \tag{2.81}$$

The PDF of the mixture fraction is again estimated by a presumed β-function, whereas the modeling of the progress variables' PDF is still an object of research. There are several approaches for the representation of the PDF of $\mathcal{Y}^*$, ranging from Dirac-functions via β-functions [69] to clipped Gaussian distributions and a so called 'statistically most likely distribution' (SMLD) [33]. The analysis of suitable sub-filter PDFs for the progress variable is part of this thesis and is discussed further below.

2.3.5.3. Transported PDF Approach

Instead of modeling the joint PDF appearing in eq. (2.74) and (2.80) it is also possible to derive a transport equation for $\mathcal{P}$. The introduced models are admittedly promising but limited to the shapes of the chosen presumed function. It is known for instance that there are multimodal statistical distributions of the determining scalars in real flame configurations that cannot be represented by the previously described comparatively simple models.

Based on the species transport equation (2.4) the joint PDF transport equation can be derived [77]. In the following, the derivation of the transport equation for the sub-filter PDF $\mathcal{P}(\psi)$ in LES context is described. According to Gao et al. [26],

$$\mathcal{F}(\psi; x_j, t) = \delta[\psi - \phi(x_j, t)] = \prod_{\alpha=1}^{N_\alpha} \delta[\psi_\alpha - \phi_\alpha(x_j, t)] \tag{2.82}$$

is the fine-grained density function related to the sub-filter PDF by

$$\mathcal{P}(\psi; x_j, t) = \frac{1}{\bar{\rho}} \int_{-\infty}^{\infty} \rho(x_j - x'_j, t)\, \mathcal{F}(\psi; x_j - x'_j, t)\, h(x'_j)\, dx'_j. \tag{2.83}$$

Therefore the sub-filter PDF in LES context is often referred to as the filtered density function (FDF). In this work, both notations are synonymously used.

By multiplying equation (2.83) with the density $\bar{\rho}$ and taking the time derivative, the following equation is obtained.

$$\frac{\partial \bar{\rho}\,\mathcal{P}}{\partial t} = -\frac{\partial}{\partial \psi_\alpha}\left[\bar{\rho}\left(\overline{\frac{\partial \phi_\alpha}{\partial t}|\psi}\right)\mathcal{P}\right] + \bar{\rho}\left(\overline{\frac{1}{\rho}\frac{\partial \rho}{\partial t}|\psi}\right)\mathcal{P} \tag{2.84}$$

The necessary mathematical rules for the derivation of this equation, which are related to the δ-function and the fine-grained density function, are found in the appendix. Furthermore, a conditional spatially filtered value is introduced, defined as

$$(\overline{Q|\psi})(x_j, t) = \frac{1}{\mathcal{P}(\psi; x_j, t)}\left(\frac{1}{\bar{\rho}} \int_{-\infty}^{\infty} \rho(x_j - x'_j, t)\, Q(x_j - x'_j, t)\, \mathcal{F}(\psi; x_j - x'_j, t)\, h(x'_j)\, dx'_j\right). \tag{2.85}$$

Properties for the conditional spatially filtered values are also found in the appendix.

The inclusion of a general scalar transport equation in the form of eq. (2.4) into eq. (2.84) leads eventually to the following FDF transport equation,

$$\frac{\partial \bar{\rho}\mathcal{P}}{\partial t} + \frac{\partial}{\partial x_i}(\bar{\rho}(\overline{u_i|\psi})\mathcal{P}) = -\frac{\partial}{\partial \psi_\alpha}\left[\bar{\rho}\left(\overline{\frac{1}{\rho}\frac{\partial}{\partial x_i}\left(\rho D \frac{\partial \phi_\alpha}{\partial x_i}\right)\middle|\psi}\right)\mathcal{P}\right] - \frac{\partial}{\partial \psi_\alpha}\left[\bar{\rho}\hat{\omega}_\alpha(\psi)\mathcal{P}\right]. \tag{2.86}$$

Here, only the first term on the LHS, the accumulation and the last term on the RHS, the chemical source term appear in closed form. The remaining two terms, convective flux and the molecular diffusion term need modeling.

The convective term can be modeled according to the sub-grid scalar flux definition in eq. (2.65) with an eddy diffusivity approach, which yields

$$\overline{u_i|\psi}\mathcal{P} = \tilde{u}_i\mathcal{P} - D_t\frac{\partial \mathcal{P}}{\partial x_i}. \tag{2.87}$$

For the modeling of the molecular diffusion term a splitting into two separate terms is necessary, where the first one appears in closed and the second one in unclosed form.

$$\frac{\partial}{\partial \psi_\alpha}\left[\bar{\rho}\left(\overline{\frac{1}{\rho}\frac{\partial}{\partial x_i}\left(\rho D \frac{\partial \phi_\alpha}{\partial x_i}\right)\middle|\psi}\right)\mathcal{P}\right] = \frac{\partial}{\partial x_i}\left(\tilde{D}\frac{\partial \mathcal{P}}{\partial x_i}\right) + \frac{\partial^2}{\partial \psi_\alpha \psi_\beta}\left[\bar{\rho}\left(\overline{D\frac{\partial \phi_\alpha}{\partial x_i}\frac{\partial \phi_\beta}{\partial x_i}\middle|\psi}\right)\mathcal{P}\right] \tag{2.88}$$

The final version of the transport equation reads as

$$\frac{\partial \bar{\rho}\mathcal{P}}{\partial t} + \frac{\partial}{\partial x_i}(\bar{\rho}\tilde{u}_i\mathcal{P}) = \frac{\partial}{\partial x_i}\left[\bar{\rho}(\tilde{D}+D_t)\frac{\partial \mathcal{P}}{\partial x_i}\right] - \frac{\partial^2}{\partial \psi_\alpha \partial \psi_\beta}\left[\bar{\rho}\left(\overline{D\frac{\partial \phi_\alpha}{\partial x_i}\frac{\partial \phi_\beta}{\partial x_i}\middle|\psi}\right)\mathcal{P}\right] - \frac{\partial}{\partial \psi_\alpha}\left[\bar{\rho}\hat{\omega}_\alpha(\psi)\mathcal{P}\right]. \tag{2.89}$$

Equation (2.89) is now completely closed except for the second term on the RHS, which is the so called sub-grid or micro mixing term. This term is the only remaining unclosed part in the FDF transport equation and will be further described in the following chapter. Contrarily to the common way of transporting the filtered species mass fractions, the chemical source term here is presented in its closed form.

Chapter 3.

Numerical Descriptions

The previous chapter introduced the equations for the description of flows in general and turbulent flows in particular. Furthermore, the most important spatially filtered density averaged equations have been derived. The partial differential equations derived in chapter 2 are either not analytically solvable at all or not efficiently manageable using analytical solving procedures. Therefore, efficient numerical methods are applied to the equations, which are in the case of computational fluid dynamics based on the Finite Volume (FV) method. The following chapter gives an overview of the applied numerical tools and methods for the efficient computation of the derived equations in the context of turbulent reactive flows. The chapter is separated in the description of the FV method and all belonging numerical issues, like the discretization in space and time of all fluxes, the proper definition of boundary conditions and the overall numerical procedure for that kind of problems. The subsequent part will introduce the discretization of the FDF transport equation employing a particle-based Eulerian Monte Carlo method.

All computations presented in this work are performed with the Large Eddy Simulation tool FLOWSI. The tool was originally developed for DNS and LES in isothermal flows [90] with further developments towards adequate numerical simulations of turbulent reactive flows by [24] and [45]. The code is based on a low Mach number assumption, which was previously mentioned in section 2.1. The Monte Carlo (MC) solver for the transported FDF method has been included [5] and allows an efficient computation for the sub-filter FDF even for high dimensional joint FDF.

3.1. Discretization in Space

In computational fluid dynamics the Finite Volume method is the preferred approach for the discretization of the governing equations, whereas for numerical simulations of structural problems the Finite Element method is used. In the following, the general procedure for the discretization of the characteristic fluid dynamic equations using a Finite Volume method is shown.

3.1.1. Finite Volume Method

The Finite Volume method is based on a partitioning of the computational domain into finite volumes, so called control volumes (cv). By this separation, a computational mesh is generated which creates the spatial discretization of the problem. For every cv, the integral form of the governing transport equations is solved. This formulation implies the

usage of approximations for interpolations, derivatives as well as integrals and transforms the set of coupled partial differential equations to a system of coupled linearized equations. The derivation of the entire procedure is demonstrated using a non-filtered general scalar transport equation,

$$\frac{\partial \rho\phi}{\partial t} + \frac{\partial}{\partial x_i}(\rho u_i \phi) = \frac{\partial}{\partial x_i}(\rho D \frac{\partial \phi}{\partial x_i}) + \omega_\phi. \tag{3.1}$$

3.1.1.1. Integral Form

Equation (3.1) is now integrated over the finite volume V and leads to

$$\underbrace{\int_V \frac{\partial \rho\phi}{\partial t}\, dV}_{\text{accumulation}} + \underbrace{\int_V \frac{\partial}{\partial x_i}(\rho u_i \phi)\, dV}_{\text{convection}} = \underbrace{\int_V \frac{\partial}{\partial x_i}(\rho D \frac{\partial \phi}{\partial x_i})\, dV}_{\text{diffusion}} + \underbrace{\int_V \omega_\phi\, dV}_{\text{source}}. \tag{3.2}$$

The divergence theorem, also known as the Gauss theorem (eq. (3.3)), now relates the fluxes over the volume's boundaries A to the flow within the volume.

$$\int_V \frac{\partial \phi}{\partial x_i}\, dV = \int_A \phi\, n_i\, dA \tag{3.3}$$

With the application of the divergence theorem, the order of the equation is decreased and the outward directed unit vector n_i is introduced. In the accumulation term, the time derivative can be extracted from the integral and one obtains eq. (3.4).

$$\frac{\partial}{\partial t}\int_V (\rho\phi)\, dV + \int_A (\rho u_i \phi) n_i\, dA = \int_A (\rho D \frac{\partial \phi}{\partial x_i}) n_i\, dA + \int_V \omega_\phi\, dV \tag{3.4}$$

Equation (3.4) is an exact mathematical transformation of the general transport equation. In the simulation practice, only certain values of the integrands can be stored. These are commonly the values at the center of the cv's and the center of the surrounding surfaces instead of continuous distributions within the entire volume and on the surfaces. For the following explanations, figure 3.1 shows the general notations and arrangements of a sample control volume. In this figure, the center control volume is denoted with a C and the neighbors are named for the wind directions, north N, east E, south S and west W. The corresponding surfaces of the cv and the related fluxes over them are labeled analogously with $\mathrm{A}_{n,e,s,w}$ and $\mathrm{F}_{n,e,s,w}$. In a three dimensional domain, the additional upper U and lower L neighbors are present. The distinct stored values in each cell are the mean values over the control volume ΔV, $\phi^{\Delta V}$ and $\omega_\phi^{\Delta V}$. Using these definitions, eq. (3.4) can be approximated for a single control volume by

$$\frac{\partial}{\partial t}(\rho^{\Delta V} \phi^{\Delta V} \partial V) + \sum_{n,e,s,w} F_{f,C} = \sum_{n,e,s,w} F_{f,D} + \omega_\phi^{\Delta V} \partial V. \tag{3.5}$$

Here, the subscripts C and D for the fluxes differentiate the convective and the diffusive fluxes over the face f. For simplification reasons, in the following sections constant density

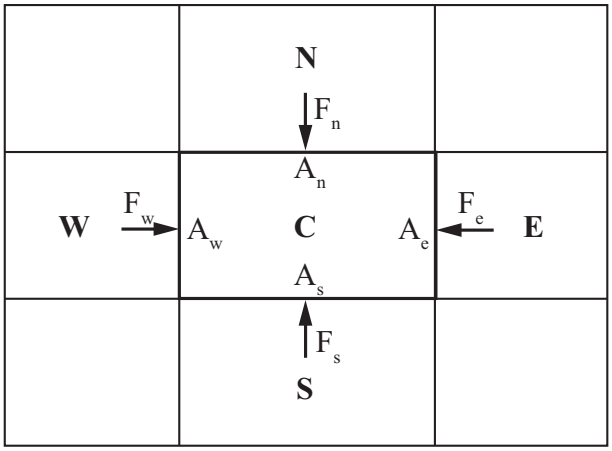

Figure 3.1.: Sketch of a two-dimensional sample control volume arrangement. Center cell C is surrounded by the adjacent cell neighbors, named for the wind directions, N, E, S and W. The surfaces and the fluxes are analogously called $A_{n,e,s,w}$ and $F_{n,e,s,w}$, respectively.

is assumed and hence vanishes in the equation except for the source term. Now, the appearing volume and surface integrals need to be modeled. Therefore, the stored mean value of the transported scalar in the center cell is denoted by ϕ_C and is located in the middle of the control volume. With this assumption, the volume integral is modeled as

$$\int_V \phi \, dV = \phi^{\Delta V} \Delta V \approx \phi_C \Delta V. \tag{3.6}$$

An analogous model is applied for the approximation of the surface integrals. The values of the scalars on the surface A_f are represented by ϕ_f and stored in the center of the face.

$$\int_{A_f} \phi \, dA = \phi^{\Delta A_f} \Delta A_f \approx \phi_f \Delta A_f \tag{3.7}$$

This so called midpoint rule for the numerical integration is one of the simplest models, but is still sufficient for a global scheme accuracy of second order [89].

3.1.1.2. Computational Grid

The previous sections made already use of the control volumes and their surfaces. These control volumes are created by a numerical grid, which is superimposed on the computational domain. Here, the present simulation tool FLOWSI applies cylindric structured grids instead of cartesian ones. This is advantageous for most of the academically investigated burner configurations, since a predominant amount is axisymmetrically arranged. Furthermore, it offers the opportunity to coarsen a mesh in the radially ambient regions or refine close to the centerline in a comparatively easy way by just varying the distance of the grid points in the radial direction. A sketch of the computational grid is shown in figure 3.2 (left). The coordinate system is represented by x in axial, φ or y for the circumferential and r or z for the radial direction. The mesh can be refined in radial

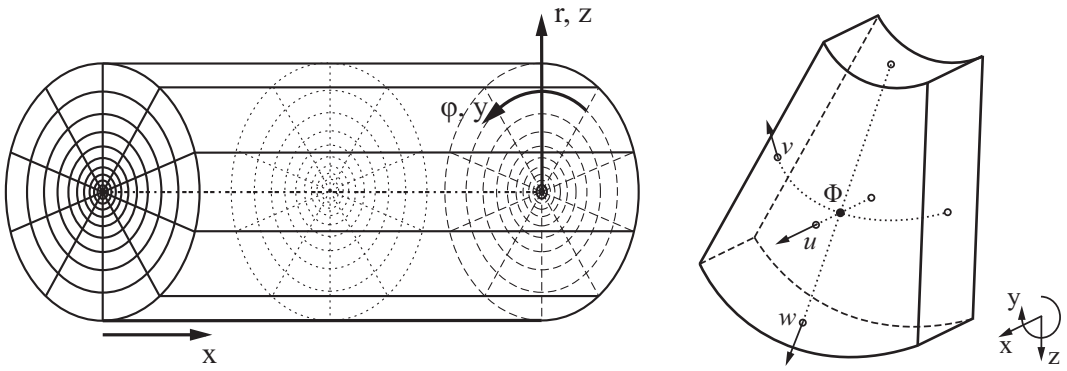

Figure 3.2.: The axisymmetric computational grid and the corresponding coordinate system on the left. On the right the staggered grid arrangement with the storage locations for the velocities u, v, w and the scalars Φ.

direction, whereas in axial and azimuthal direction only uniform grid spacing is available. Another detail about the computational grid is the arrangement of the stored quantities. As previously described, the mean values are stored in the center of the control volume. However, this leads to numerical issues known as odd-even decoupling of the pressure and the velocities and results in a checkerboard pattern of the solution. In order to avoid this problem, the velocity components u, v, and w are stored at the regarding volume surface. This method is called staggered grid and was proposed by [31]. The arrangements of the storing locations are illustrated in figure 3.2 (right).

3.1.1.3. Diffusive Fluxes

The diffusive fluxes $F_{f,D}$ in eq. (3.5) are defined by

$$\sum_{n,e,s,w} F_{f,D} = \int_A \left(D \frac{\partial \phi}{\partial x_i} \right) n_i \, dA. \tag{3.8}$$

With application of the midpoint rule for the integration it reads as

$$F_{f,D} \approx D \left(\frac{\partial \phi}{\partial x_i} n_i \right)_f \Delta A_f. \tag{3.9}$$

Obviously, the diffusive flux includes the spatial gradient of the quantity ϕ, which can be approximated by the values ϕ_1 and ϕ_2 of two adjacent control volumes and their distance from each other Δx_i. Assuming the grid to be rectangular with uniform grid spacing simplifies the expression for the diffusive fluxes to

$$F_{f,D} \approx D \frac{\phi_1 - \phi_2}{\Delta x} \Delta A_f. \tag{3.10}$$

3.1.1.4. Convective Fluxes

Convective fluxes $F_{f,C}$ represent the predominant part of the transport in a turbulent flow. In contrast to the smoothing behavior of diffusion, convection conserves the shape

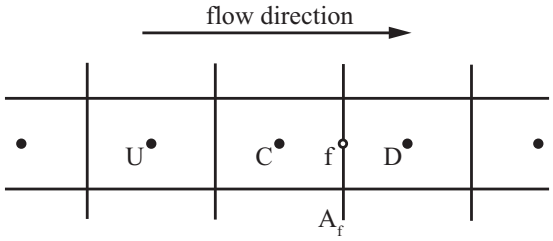

Figure 3.3.: Neighboring relations and notation of a sample control volume for visualization of the interpolation schemes.

of the transported scalar field. In order to avoid any smoothing or steepening effects due to numerical discretization errors, the approximation of the convective fluxes need special treatment. The applied procedure is demonstrated below.

Following the divergence theorem, $F_{f,C}$ is represented by the surface integral

$$\sum_{n,e,s,w} F_{f,C} = \int_A (u_i \phi) n_i \, dA, \tag{3.11}$$

which can be approximated with the rectangle method (eq. (3.7)) to

$$F_{f,C} \approx u_f \, \phi_f \, \Delta A_f. \tag{3.12}$$

With the assumption of orthogonal grids, the product of the velocity and the unit vector $(u_i \, n_i)$ can be replaced by the normal velocity component u_f at the surface A_f. ϕ_f and u_f are the values of the quantity ϕ and the normal velocity component on the surface A_f. As mentioned previously and shown in fig. 3.2 (right), in a staggered grid arrangement the velocities are already stored on the surfaces, whereas ϕ_f needs to be interpolated from the adjacent cell centers. The chosen interpolation scheme has a strong impact on the behavior of the global numerical scheme with respect to accuracy and stability.

In the following, different approaches for the interpolation of a quantity onto the surface center are introduced and discussed. For visualization of the presented schemes, figure 3.3 depicts the structure and notation of a sample control volume and its neighbors.

Upwind Differencing Scheme The simplest approach to obtain the value on the surface A_f is the so called upwind differencing scheme (UDS). This scheme is not an interpolation in the proper meaning of the word. In this case, the value on the surface is just determined by the next known upstream value. In figure 3.3, the upstream point of the unknown surface center f is the point C (center). This leads to

$$(\phi_f)_{\mathrm{UDS}} = \phi_C. \tag{3.13}$$

The UDS is known for its stability, which finds expression in the suppression of oscillations in the solution. These oscillations can cause inadvertent problems and the consequently following divergence of performed simulations. While suppressing occurring oscillations effectively, the upwind discretization is only of first order accuracy [89] and hence shows a high level of numerical diffusion. This is given by artificial smoothing of the scalar

profiles. Unfortunately, turbulent combustion includes high gradients over the flame front (i.e. density), which needs to be conserved rather than being smoothed out by numerical diffusion. Therefore, higher order accurate schemes need to be applied.

Central Differencing Scheme The central differencing scheme (CDS) represents the common interpolation method. The CDS computes the surface value ϕ_f by both adjacent cell center values. For the problem given in fig. 3.3, these are the values at the points C and D (downstream). The interpolation rule reads as

$$(\phi_f)_{\mathrm{CDS}} = \frac{\phi_C + \phi_D}{2} \tag{3.14}$$

for an equidistant computational grid. The CDS has an interpolation error of second order, which can be obtained by a Taylor series expansion [89]. The higher order accuracy is expressed by a very low level of numerical diffusion, but has a tendency to unphysical oscillations in the solution [45].

To overcome both problems, excessive numerical diffusion and unphysical oscillations, an interpolation scheme needs to be found, which combines UDS and CDS. This method is commonly known as total variation diminishing (TVD).

Total Variation Diminishing A TVD scheme ensures the transported scalar field to be bounded within the given limits and therefore preserves monotonicity [32]. That means, a point within a scalar profile located between a local minimum and a local maximum must remain between both extremes during convective transport. For further theoretical information on TVD, the reader is referred to [45] and [68].

The application of a TVD based limiter scheme is introduced below. It actually combines the two previously described schemes UDS and CDS and takes advantage of both interpolation methods. A general definition valid for a variety of limiter functions is given by eq. (3.15). This definition is again shown for equidistant computational grids only.

$$(\phi_f)_{\mathrm{TVD}} = \phi_C + B(r)\frac{\phi_C - \phi_U}{2} \tag{3.15}$$

$B(r)$ represents the flux-limiter function depending on the gradient ratio r,

$$r = \frac{\phi_D - \phi_C}{\phi_C - \phi_U}. \tag{3.16}$$

With varying limiter functions, different interpolation schemes can be obtained, even the already presented ones, UDS and CDS. Setting $B(r) = 0$ results in the upwind discretization, whereas $B(r) = r$ leads to the central differencing scheme. As already mentioned, in this work, a limiter function is used that combines these two schemes. The applied non-linear CHARM flux-limiter function [108], [109], is defined by

$$B(r) = \begin{cases} \frac{r(3r+1)}{(r+1)^2}, & \text{for} \quad r > 0 \\ 0, & \text{for} \quad r \leq 0 \end{cases}. \tag{3.17}$$

Apparently, the CHARM flux-limiter function is valid for gradient ratios greater than zero, otherwise the first order UDS is used.

A considerable list of different flux-limiter function and their characteristics can be found in [45].

3.2. Discretization in Time

Similar to the spatial discretization of the convection and diffusion terms of equation (3.1) the time derivative needs to be modeled numerically. Here, the density is again neglected and the general transport equation can be transformed to

$$\frac{\partial \phi}{\partial t} = -\frac{\partial}{\partial x_i}(u_i \phi) + \frac{\partial}{\partial x_i}(D \frac{\partial \phi}{\partial x_i}) + \frac{1}{\rho}\omega_\phi. \tag{3.18}$$

In the following, the right hand side of eq. (3.18) is referred to as $F(\phi)$, viz

$$\frac{\partial \phi}{\partial t} = F(\phi). \tag{3.19}$$

Analog to the computational grid for the spatial discretization, the time is split into finite intervals Δt. The derivative can now be obtained by

$$\frac{\partial \phi}{\partial t} = \frac{\phi^{n+1} - \phi^n}{\Delta t^n} \tag{3.20}$$

with ϕ^n and ϕ^{n+1} the values at time step n and $n+1$, respectively. Including eq. (3.20) into eq. (3.19) the quantity ϕ at the new time step can be approximated by

$$\phi^{n+1} \approx \phi^n + \Delta t^n F(\phi^n). \tag{3.21}$$

This explicit Euler scheme is of first order accuracy and unfortunately unstable applied onto the Navier-Stokes equations. For a stable scheme an implicit form of eq. (3.21) is derived by using $F(\phi^{n+1})$ instead of the right hand side of time step n. This implicit Euler scheme is stable with the Navier-Stokes equations and allows comparatively large time steps. The solution cannot be obtained directly but a system of equations needs to be solved. Nevertheless, the accuracy of this scheme is of first order, whereas the spatial discretization is second order accurate. In order to match the second order an explicit Runge-Kutta scheme is used. This method uses substeps to be stabilized and hence needs more computational effort. Therefore, in the present work, a storage space efficient implementation of a three stages Runge-Kutta scheme by Williamson [106] is applied. In general, this scheme is known to be of third order but for nonlinear problems like the Navier-Stokes equations, the scheme is only of second order accuracy. ϕ^{n+1} can now be obtained by the use of two substeps ϕ_a^n and ϕ_b^n with the following definition:

$$\begin{aligned}
\phi_a^n &= \phi^n + \Delta t_a^n [\alpha_a F(\phi^n)] \\
\phi_b^n &= \phi_a^n + \Delta t_b^n [\alpha_b F(\phi_a^n) + \beta_b F(\phi^n)] \\
\phi^{n+1} &= \phi_b^n + \Delta t_c^n \left[\alpha_c F(\phi_b^n) + \beta_c \left(F(\phi_a^n) + \frac{\beta_b}{\alpha_b} F(\phi^n) \right) \right].
\end{aligned} \tag{3.22}$$

The corresponding coefficients α and β are determined by

$$\alpha_a = \frac{1}{3} \qquad \alpha_b = \frac{15}{16} \qquad \alpha_c = \frac{8}{15} \qquad \beta_b = -\frac{75}{144} \qquad \beta_c = -\frac{51}{81} \tag{3.23}$$

and the definitions of the substep time widths are

$$\Delta t_a^n = \frac{1}{3}\Delta t^n \qquad \Delta t_b^n = \frac{5}{12}\Delta t^n \qquad \Delta t_c^n = \frac{1}{4}\Delta t^n. \tag{3.24}$$

3.2.1. Time Step Criterion

For the discretization in time the time step size needs to be estimated and also limited. Therefore, the so called CFL-criterion is utilized, which relates the time step size to the occurring velocities and the computational grid. The criterion is named after Courant, Friedrich and Lewy [15] for their time step size condition, eq. (3.25).

$$\mathrm{CFL} = \frac{\Delta t|u|}{\Delta x} \qquad \text{with} \qquad \mathrm{CFL} \leq 1 \qquad \text{to} \qquad \Delta t \leq \frac{\Delta x}{|u|} \tag{3.25}$$

This definition for a one-dimensional case is valid for explicit time advancement schemes and limits the time step size to the duration where a fluid parcel would cross an entire control volume driven by its advection. The limit of CFL = 1 is a theoretical value, which cannot be applied on the simulations performed in this work. Due to stability reasons, the used values for CFL are located within the range of CFL $= 0.1, ..., 0.4$ depending on the simulated configuration and the used models.

3.3. Global Solution Algorithm

The used LES code FLOWSI is based on the conservative transport of the fuel $\overline{\rho\xi}$ and the oxidizer $\overline{\rho(1-\xi)}$. The applied methodology was mainly developed by Kempf [45] and is referred to as EKT-method. It is a fractional step method using a predictor/corrector scheme to fulfil the continuity equation. Further details regarding this global solution algorithm will be given in the following sections.

The single steps of the EKT-procedure are illustrated in figure 3.4.

1. Calculate the turbulent viscosity ν_t^{n+1} for time step $n+1$ with values from time step n
2. **Predictor** Scalar transport with the uncorrected velocities $\widetilde{u^p}_i^n$ to obtain the mixture fraction $\bar{\xi}^{n+1}$, the estimated density $\overline{\rho^p}^{n+1}$ and for FGM, the progress variable $\widetilde{\mathcal{Y}^p}^{n+1}$
3. Compute the specifying quantities for the chemical submodel, e.g. sub-grid variance of the mixture fraction $\widetilde{\xi''^2}_n^{n+1}$ and for FGM the normalized progress variable $\widetilde{\mathcal{Y}^{*p}}^{n+1}$ (see eq. (2.71))
4. Obtain the molecular viscosity $\tilde{\nu}^{n+1}$, the chemical target density $\overline{\rho}_{\mathrm{chem}}^{n+1}$ and the source term for the progress variable $\omega_{\mathcal{Y}}$
5. Compute the pressure and the velocity corrections and adapt the velocity fields $\widetilde{u^p}_i^n$ to get $\widetilde{u}_i^n$
6. **Corrector**. Transport of scalars using the corrected velocities $\widetilde{u}_i^n$ to compute the density field $\overline{\rho}^{n+1}$ and for FGM the progress variable $\widetilde{\mathcal{Y}}^{n+1}$
7. Integration in time of the momentum equation to predict the $\widetilde{u^p}_i^{n+1}$ for the next time step

Figure 3.4.: Sketch of the general procedure for the EKT-method

Step 1 In step 1 of the EKT-method, the turbulent viscosity ν_t^{n+1} for the following time step is computed according to the Smagorinsky model (section 2.2.1.3) and the related dynamic procedure proposed by Germano (section 2.2.1.3). The equations for the turbulent viscosity are solved using the predicted velocities $\tilde{u^p}_i^n$ from the previous time step.

Step 2 The predictor step in this algorithm is characterized by the transport of scalars with the predicted velocities. The important transported scalars depend on the chemical submodel. In this work all applied chemistry models are based on the mixture fraction and for the flamelet generated manifolds model an additional progress variable $\widetilde{\mathcal{Y}}$ is transported.

For the transport of the mixture fraction a special transport scheme is used. Therefore, the transport equation (2.67) is solved for a fuel fraction $\tilde{\xi}^+ = \tilde{\xi}$ and an oxidizer fraction $\tilde{\xi}^- = \widetilde{(1-\xi)}$. From the obtained solutions of $\bar{\rho}\tilde{\xi}^+$ and $\bar{\rho}\tilde{\xi}^-$ the final mixture fraction $\tilde{\xi}^{n+1}$ and the predicted density $\overline{\rho}^{p,n+1}$ are computed with

$$\overline{\rho}^{p,n+1} = (\bar{\rho}\tilde{\xi}^+)^{p,n+1} + (\bar{\rho}\tilde{\xi}^-)^{p,n+1} \qquad \text{and} \qquad \tilde{\xi}^{n+1} = \frac{(\bar{\rho}\tilde{\xi}^+)^{p,n+1}}{\overline{\rho}^{p,n+1}}. \tag{3.26}$$

This scheme is introduced, because a conservative transport of the mixture fraction is only ensured by solving the conservation equations of the product $\bar{\rho}\tilde{\xi}$ instead of $\tilde{\xi}$ alone. However, the correlation between $\bar{\rho}\tilde{\xi}$ and the chemical state is not unique [24] and so the product must be split for the use with the chemical submodel. In this step, the progress variable $\widetilde{\mathcal{Y}}^{p,n+1}$ is also obtained by solving the related transport equation. The necessary source term is taken from the previous time step.

Step 3 Step 3 now provides the missing quantities for the chemistry model. This is for all models applied in this work, the sub-grid variance of the mixture fraction $\widetilde{\xi''^2}^{n+1}$. In equation (2.78) the normalized sub-grid variance of the mixture fraction was introduced in the context of the turbulence-chemistry interaction for the definition of the β-shaped PDF. As mentioned before, the variance is obtained by a similarity ansatz. Therefore, the mixture fraction field is filtered using a larger filter width. The mean value of the center control volume with the new filter width is computed by the use of the adjacent cells.

$$\hat{\tilde{\xi}}_C = \frac{6}{12}\tilde{\xi}_C + \sum_n \frac{1}{12}\tilde{\xi}_n \quad \text{with} \quad n = N, E, S, W, U, L \tag{3.27}$$

This leads to eq. (3.28) for the sub-grid variance.

$$\widetilde{\xi''^2}_C = \frac{6}{12}\left(\tilde{\xi}_C - \hat{\tilde{\xi}}_C\right) + \sum_n \frac{1}{12}(\tilde{\xi}_n - \hat{\tilde{\xi}}_C) \tag{3.28}$$

To obtain the unmixedness, the sub-grid variance is normalized by

$$\widetilde{\xi''^2}_{n,C} = \frac{\widetilde{\xi''^2}_C}{\tilde{\xi}_C(1-\tilde{\xi}_C)}. \tag{3.29}$$

In the FGM case, the progress variable is normalized by its equilibrium value that depends on the mixture fraction (eq. (2.71)).

Step 4 This step includes the chemistry into the simulation. In section 2.3.4 the different chemistry models have been described theoretically as well as the turbulence-chemistry interaction in section 2.3.5. The practical application in numerical simulations is described in the following. Obviously, it is not efficient to compute the entire chemical kinetics in each time step of the simulation. To avoid this unnecessary computational effort, tabulated chemistry is applied in practice. For tabulated chemistry, the chemical kinetics are calculated chronologically before the simulation and all occurring thermo-chemical states are stored within a table. Therefore, the thermo-chemical states are correlated with the determining scalars. In the flamelet model it is the mixture fraction and the scalar dissipation rate, which is kept constant in the present work, and for FGM it is the mixture fraction and the normalized progress variable. The mixture space and the progress variable space are discretized with an adequate number of grid points for which the properties are computed and stored. For the integration of the turbulence-chemistry interaction the presumed probability density functions can be included within the table. Therefore, the unmixedness is added to the chemistry table as another determining quantity. As equations (2.76) and (2.77) show, the β-PDF shape is characterized by the mean and the variance of the considered scalar. This preintegration can also be performed prior to the actual simulation. The final chemistry table with a presumed β-PDF approach for the mixture fraction in the context of flamelet generated manifolds provides the relation

$$\tilde{\phi} = \tilde{\phi}(\tilde{\xi}, \widetilde{\xi''^2}_n, \tilde{\mathcal{Y}}). \tag{3.30}$$

The molecular viscosity $\tilde{\nu}$, the density $\overline{\rho}$ and for the FGM model the source term for the progress variable $\omega_{\mathcal{Y}}$ are included in the thermo-chemical state. These are read out for each cv as a function of the three determining quantities.

Step 5 In order to compute the correct velocity $\widetilde{u}_i^n$, the predicted velocity has to be adapted. Therefore, the correction Ψ of the momentum is introduced and is defined as

$$\Psi_i = (\bar{\rho}\tilde{u}_i)^{p,n} - (\bar{\rho}\tilde{u}_i)^n. \tag{3.31}$$

Ψ represents the momentum correction to satisfy the continuity equation. The difference between the predicted density $\overline{\rho}^p$ computed by transport and the one obtained by the chemical submodel $\overline{\rho}_{\text{chem}}$ is used to formulate a Poisson equation (3.32) for the pressure correction ψ.

$$\frac{\partial}{\partial x_i}\Psi_i = \frac{\partial^2}{\partial x_i^2}\psi = \frac{\overline{\rho}_{\text{chem}}^{n+1} - \overline{\rho}^{p,n+1}}{\Delta t} \tag{3.32}$$

For the Poisson equation an explicit direct solver proposed by Schumann and Sweet [93] is applied.

Step 6 In this corrector step the corrections for the momentum Ψ and the pressure ψ define the real velocities and all scalars are transported again using this corrected velocities. This results in the new density (eq. (3.26)) and progress variable for the FGM model.

Table 3.1.: General boundary condition description

Scalar	Inflow	Annular Surface	Outflow
axial velocity $\tilde{u}$	$\tilde{u} = \tilde{u}(x_i, t)$	$\partial\tilde{u}/\partial n_z = 0$	$\partial\tilde{u}/\partial n_x = 0$
radial velocity $\tilde{v}$	$\tilde{v} = \tilde{v}(x_i, t)$	$\partial\tilde{v}/\partial n_z = 0$	$\partial\tilde{v}/\partial n_x = 0$
azimuthal velocity $\tilde{w}$	$\tilde{w} = \tilde{w}(x_i, t)$	$\partial\tilde{w}/\partial n_z = 0$	$\partial\tilde{w}/\partial n_x = 0$
turbulent viscosity ν_t	$\partial\nu_t/\partial n_x = 0$	$\partial\nu_t/\partial n_z = 0$	$\partial\nu_t/\partial n_x = 0$
pressure parameter $\tilde{P}$	$\partial\tilde{P}/\partial n_x = 0$	$\tilde{P} = 1\text{bar}$	$\partial\tilde{\tilde{P}}/\partial n_x = 0$
mixture fraction $\tilde{\xi}$	$\tilde{\xi} = \tilde{\xi}(z)$	$\tilde{\xi} = 0$	$\partial\tilde{\xi}/\partial n_x = 0$
sub-grid variance $\widetilde{\xi''^2}$	$\partial\widetilde{\xi''^2}/\partial n_x = 0$	$\widetilde{\xi''^2} = 0$	$\partial\widetilde{\xi''^2}/\partial n_x = 0$

Step 7 In the final step, the time integration of the momentum equation is accomplished in order to estimate the velocities for the following time step.

For stabilization reasons, an underrelaxation of the density correction is included within the solution algorithm. Therefore, the relaxation factor is set to be 0.5 to smoothen the momentum and pressure corrections Ψ and ψ in time. For smoother density distribution in space, the fields are additionally filtered in every time step. Both arrangements ensure the stability of the simulations for reactive flows.

3.4. Boundary Conditions

Besides the governing equations as introduced above, boundary conditions are essential to describe flow problems properly. These conditions define properties at the outer surfaces or interfaces of the computational domain. In this work, Dirichlet as well as Neumann conditions are used. Dirichlet conditions define a quantity directly by setting discrete values, whereas the Neumann conditions determine a quantity via its gradient normal to the boundary. Both alternatives are given below:

- Dirichlet condition: $\phi = \phi_b$
- Neumann condition: $a(\partial\phi/\partial x_i)n_i = b_b$

The subscript b stands for the values or functions defined at the boundaries, while a denotes a proportionality factor.

For the presented configurations, a variety of boundary conditions are identical and can be defined in general. The settings for these conditions are shown in table 3.1. The velocity boundaries at the inflow plane depend on the location and on time. Especially, the dependency on time is very important for time-resolved simulation techniques like LES. The issue appearing here is the proper representation of turbulence at the inflow plane without performing very costly simulations of the inflow pipes. Therefore, experimentally obtained mean value and fluctuation fields of the velocity components are used to generate artificial turbulent inflow conditions.

The method of artificially generated turbulence applied in this work is based on the work of Klein et al. [52] and was modified by Kempf et al. [48]. The idea behind this

approach is the adaptation of a randomly generated noise to a field with a turbulence-like spectrum and length-scale. In Klein's work, this is done by the application of an appropriate filter that ensures the fluctuations to show these turbulent characteristics, whereas Kempf applies diffusive transport on the random noise to compute the proper length-scales. By superposing these fluctuations on the mean velocity fields, a three-dimensional time-dependent velocity inlet condition can be provided. The drawback of the artificially generated turbulence is, that the velocity components and at least the turbulence intensity at this location must be known previously. This is indeed possible for academic configurations as investigated in the present work, but for real applications the turbulence level at the inlet needs to be estimated.

Another interesting treatment of boundaries, is the application of immersed boundaries [51]. For certain configurations it is helpful to model walls inside the computational domain. Therefore, the technique of immersed boundaries enforces the no-slip condition at walls and sets the fluxes over the walls to zero. This approach is mainly applied for the modeling of nozzles at the inlet regions of the configurations in order to avoid the spatial coincidence of the inflow plane and parts of the nozzle or the bluff body.

3.5. Discretization of the PDF Transport Equation

The PDF transport equation has been introduced and derived in section 2.3.5.3. Analog to the discretization of the governing equations above, the transport equation of the FDF cannot be solved directly. Therefore, methods from the numerical analysis are applied for an adequate approximation of the equation. A finite difference scheme, similar to the finite volume method can be used for the discretization, but due to a high dimensionality of the solution vector $\phi(x_i, t)$, the application of such a method is not efficient and hence not feasible. In a finite difference scheme, the computational effort rises exponentially with the number of dimensions. Thus the PDF transport equation is commonly discretized using a so called Monte Carlo method, which is described in detail in the following.

3.5.1. Monte Carlo Methods

Monte Carlo methods are statistical approaches for solving differential equations, such as applied for the PDF transport. MC methods have a higher efficiency than the ordinary approaches finite volume or finite difference. Here, the computational effort rises only linearly with the dimensionality of the solution vector. This is especially noticeable for a large number of dimensions greater than three [77]. The methods mainly used for the solution of turbulent reactive flows can be differentiated into two major classes, the Lagrangian and the Eulerian approach. The difference between these two can be explained with the position of the observer. In the Lagrangian method, the observer is located on a fluid particle and hence moves with the flow, whereas in the Eulerian approach, the observer's location is fixed and the flow passes by. Even though the Lagrangian Monte Carlo methods are more popular in combustion sciences, this work is about an Eulerian Monte Carlo method as described by Pope [77].

The basic idea behind Monte Carlo methods in the PDF context is the representation of a probability density function by an ensemble of N values as in figure 3.5.

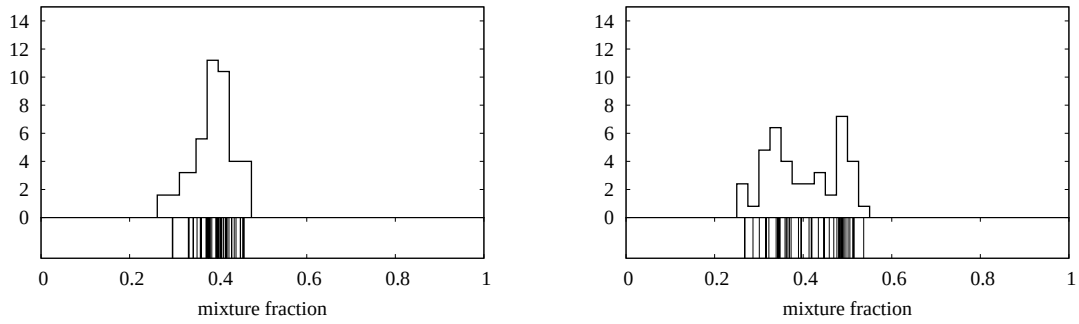

Figure 3.5.: Reconstructed PDF of the mixture fraction with $N = 50$. The Dirac functions are depicted at the lower part of the plot. The bin width in mixture fraction space is set to $\Delta\xi = 0.025$

Therefore, the values are binned in finite intervals of the represented space and then the attained surface needs to be normalized in order to get an integral value of unity (eq. A.3). These values can be interpreted as δ Dirac functions and so the PDF is discretely reproduced by the obtained distribution. Thereby, the statistical error ε depends on the magnitude of the ensemble and follows the relation

$$\varepsilon \sim \frac{\phi''^2}{\sqrt{N}}. \tag{3.33}$$

Consequently, assuming a fixed variance of the considered scalar, the statistical error of a discrete PDF representation can be halved by a quadruplication of the number of values N.

The differences in the variety of Monte Carlo methods now arise by the appearance, the behavior and the properties of the statistic values.

In Lagrangian methods the values are represented by stochastic particles without mass that move with the fluid flow. Hence, additional to the composition information, the particle movement is described with

$$x_i^k(t + \Delta t) = x_i^k(t) + \tilde{u}_i^k \Delta t + \Gamma\, dW. \tag{3.34}$$

The change in the position of the kth particle at a time $t + \Delta t$ is defined by the convective part including the particle's velocity $\tilde{u}_i^k$ and a diffusive term $\Gamma\, dW$ that includes a random term, the so called Wiener process [87]. The movement of the particle constitutes both an advantage and a major practical disadvantage of the Lagrangian Monte Carlo method. Due to the prevalent velocity field the finite amount of particles is distributed within the computational domain, which causes high regional distinctions of the particle density $N/\Delta V$. On the one hand, this makes the statistical error more uniform, since N is implicitly correlated to the variance of ϕ by the velocities. On the other hand, the distinctions of the particle density cause issues in the averaging of the ensemble in regions with a low amount of particles and can lead to poor representations of the PDF. For a more detailed description of Lagrangian PDF methods the interested reader is referred to Pope [78].

Eulerian Monte Carlo methods can again be differentiated into particle based and field based methods. The stochastic fields method for PDF transport was initially proposed by

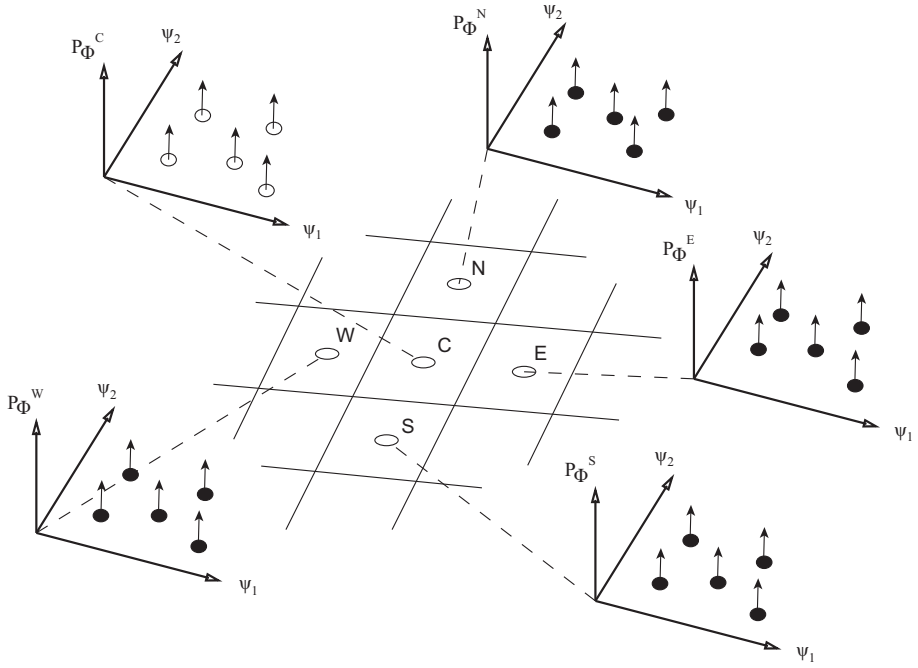

Figure 3.6.: Sketch of a sample two-dimensional computational grid with the corresponding Eulerian particle distribution $P_\phi(\psi_1, \psi_2)$.

Valino [101] and further developed by Sabel'nikov [88]. It is based on a set of stochastic partial differential equations, which represents an equivalent to the closed form of the PDF transport equation [42], [43]. The statistical ensemble in this case is represented by an ensemble of statistical fields, that differ due to a superposed Wiener process. Further information about the stochastic fields method can be obtained in Olbricht [68] and the works of Navarro-Martinez [44], [41].

In the present work, a particle based Eulerian Monte Carlo approach is applied. In this case, the particles are fixed in the control volumes and ensure a uniform and constant particle density in the entire computational domain. Figure 3.6 depicts a two-dimensional computational domain with the corresponding particle distributions. The PDF in the sample case is two-dimensional and is represented by an ensemble of $N = 5$ particles or δ-functions. The two properties generating the composition space are ψ_1 and ψ_2. The discretization of the PDF transport equation is now performed by interactions between the center cell's particle ensemble and the adjacent cell ensembles and interactions of particles within the center cell. Contrary to the Lagrangian method, the particles in the Eulerian context are stored in the nodes of the computational mesh and hence do not provide any information of their locations inside the control volume.

A disadvantage of the Eulerian Monte Carlo method is the non-uniformly distributed statistical error in the domain. Based on eq. (3.33), it is obvious that with a constant ensemble magnitude N, the statistical error ε is now directly proportional to the spatially varying sub-grid variance ϕ''^2. That means that in regions with a low sub-grid variance, ε is low, too, but in regions of interest, where ϕ''^2 is high, the statistical error is comparatively large. Therefore, an adaptive Eulerian Monte Carlo scheme was proposed [56], which

redistributes the particles within the computation domain depending on the cell-based Reynolds number and the unmixedness (eq. (2.78)). Using this procedure, the statistical error can be kept more uniform in the computational domain. The adaptive Eulerian Monte Carlo method is unfortunately not available for parallel computations, because of the resulting unbalanced work load of the processors. This is why the particle densities in the presented test cases are constant as well as uniform and hence, the distribution of the statistical error is not constant over the numerical mesh.

3.5.1.1. Eulerian Monte Carlo Discretization for the PDF Transport Equation

In this section, the discretization of the FDF transport equation using an Eulerian particle based Monte Carlo method is described. Therefore, each term of equation (2.89) is considered separately and the chosen modeling is introduced. The discretization of the transport equation is based on a fractional step method [78]. This approach splits the FDF transport equation (2.89) into single steps, which are executed in rotation. After discretization in time and application of the fractional step method, the change of the PDF in the center cell $\mathcal{P}^C$ within one time step Δt can be described with

$$\begin{aligned}\mathcal{P}_\phi^{(C)}(\psi, t+\Delta t) &= (I + \Delta t\mathcal{C} + \Delta t\mathcal{M} + \Delta t\mathcal{R})\mathcal{P}_\phi^{(C)}(t) \\ &= (I + \Delta t\mathcal{C})(I + \Delta t\mathcal{M})(I + \Delta t\mathcal{R})\mathcal{P}_\phi^{(C)}(t).\end{aligned} \tag{3.35}$$

In this equation $\mathcal{C}$, $\mathcal{M}$ and $\mathcal{R}$ represent the processes convection together with diffusion, mixing and reaction, whereas I is the current state. The processes are executed one after another and every step has the same time step Δt. The total solution of one time step is reached as soon as the last fractional process is completed.

Below, each fractional step is discussed and the applied models are described.

Convection and Diffusion $\mathcal{C}$ The first step of the applied Monte Carlo method is the convection and diffusion part. The computation of this step is accomplished by an exchange of particle values between the center cell and the adjacent neighbors as depicted in figure 3.6 and is based on a finite differencing scheme. For the transport itself, a specific number of particles $n_\mathcal{C}$ is calculated, which has to be exchanged between control volumes. This amount of particles is calculated using the quantities on the cell surfaces f for convection and diffusion. The exchange of the particles happens randomly, which means that particles are randomly chosen out of the supplying ensemble and substitute particle values of the considered control volume also selected at random. In the following, the models are presented and discussed for a two-dimensional problem with an equidistant cartesian mesh. The rate of diffusion is calculated using the effective diffusion coefficients (eq. (2.66)) interpolated on the surfaces

$$D_{\text{eff}}^f = \frac{1}{2\bar{\rho}^C \Delta x}((\bar{\rho}D_{\text{eff}})^n + (\bar{\rho}D_{\text{eff}})^C) \quad \text{with} \quad f = n, e, s, w \quad \text{and} \quad n = N, E, S, W. \tag{3.36}$$

The number of particles n_{diff}^n representing the diffusive transport from cv C to the neighbor n is computed by

$$n_{\text{diff}}^n = D_{\text{eff}}^f \frac{\Delta t}{\Delta x} N^C. \tag{3.37}$$

N^C denotes the size of the particle ensemble in the central cell, while f stands for the surface separating the C cell from the $n = N, E, S, W$ cell.

The convective part is also modeled using the finite differencing scheme. Here, a first and a second order accurate scheme is introduced. For the first order accurate scheme, an upwind discretization is chosen, which determines the percentage of particles due to convection. Applying the first order UDS, the mass flux on the surface f is computed by

$$\dot{m}^f_{\text{UDS}} = \begin{cases} |(\bar{\rho}\tilde{u})^f|, & \text{for} \quad (\overrightarrow{\tilde{u}}\,\overrightarrow{n})^f < 0 \\ 0, & \text{for} \quad (\overrightarrow{\tilde{u}}\,\overrightarrow{n})^f \geq 0 \end{cases}. \tag{3.38}$$

Analog to equation (3.37) a number of particles representing the convective transport can be defined.

$$n^n_{\text{conv}} = \dot{m}^f_{UDS} \frac{\Delta t}{\Delta x \bar{\rho}^C} N^C \tag{3.39}$$

The complete fractional step of convection and diffusion is then determined by the addition of both equations (3.37) and (3.39), viz

$$n^n_{\mathcal{C}} = n^n_{\text{conv}} + n^n_{\text{diff}} = \left(\frac{\dot{m}_{\text{UDS}}}{\bar{\rho}^C} + D_{\text{eff}} \right) \frac{\Delta t}{\Delta x} N^C. \tag{3.40}$$

Obviously, the number of particles to be exchanged must be integer and therefore the residual fractions are added over consecutive time steps until a full particle can be exchanged. Hence, the transport scheme is not conservative for every instance, but averaged over a couple of time steps this procedure ensures the conservativity of the transported scalar PDF.

In the following section, the quasi second order accurate scheme for the discretization of the convective transport for the conserved mixture fraction is introduced. This scheme has been proposed by Chen [13] and was applied to a piloted jet flame configuration with a steady flamelet chemistry representation. In order to describe the method, a one-dimensional flow problem without diffusion is assumed. Generally, the Eulerian transport approach can be expressed by the explicit formulation

$$\mathcal{P}_i(t + \Delta t) = \sum_{j=1}^{L} \omega_j \mathcal{P}_j(t) \tag{3.41}$$

where ω_j represents the weighting factor for the control volume j and L is the total number of adjacent neighbor cells of the considered control volume. Equation (3.41) shows the calculation of the new probability density function due to a weighted addition of the PDF of the neighbor's particle ensembles. In the Eulerian approach with a fixed ensemble magnitude in each control volume, it is essential to provide a transport scheme that does not compute negative weight factors, since a negative number of particles cannot be selected from ensembles. Algorithms providing positive weight factors are called positive weighting schemes (PWS). The already presented first order accurate upwind transport scheme (UDS) in eq. (3.39) is such a PWS. For higher orders of accuracy in the transport of scalars, Total Variation Diminishing (TVD) schemes have been developed and have

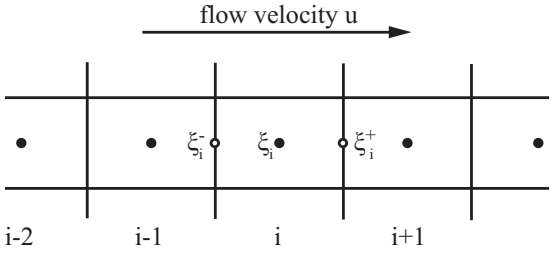

Figure 3.7.: Locations and definitions of the one-dimensional arrangement for the description of the second order accurate Monte Carlo transport scheme.

been introduced in section 3.1.1.4 for the finite volume transport of the mixture fraction. Unfortunately, the TVD schemes are not generally PWS and hence cannot be directly applied for a higher order accurate transport in the context of Monte Carlo simulations. In order to formulate a PWS based on the described TVD scheme, the weighting factors need to be modified. The defined goal is a second order accurate formulation for the mass flux $\dot{m}^f_{\mathrm{TVD}}$ that can be included into eq. (3.39) to reach higher accuracy within the Monte Carlo transport discretization.

The derivation of the second order transport scheme follows the description presented by Chen [13]. Starting from the model equation for the mixture fraction ξ without diffusion

$$\frac{\partial \xi}{\partial t} + u\frac{\partial \xi}{\partial x} = 0 \tag{3.42}$$

the discretized form using a finite differencing scheme and an explicit time integration scheme can be written as

$$\xi_i(t+\Delta t) = \xi_i(t) - \frac{\Delta t}{\Delta x}(u\xi_i^+ - u\xi_i^-). \tag{3.43}$$

In this equation a constant velocity u is assumed and the quantities ξ_i^+ and ξ_i^- denote the mixture fraction values at the boundary of the control volume i as shown in figure 3.7. As already mentioned, a TVD scheme is used in order to interpolate the mixture fraction values on the boundaries of the control volumes. As in the finite volume context, the CHARM limiter function is used and it follows for the downwind boundary value

$$\xi_i^+ = \xi_i(t) + \frac{B_i^+}{2}(\xi_i(t) - \xi_{i-1}(t)) \quad \text{with} \quad B_i^+ = \frac{r^+(3r^+ + 1)}{(r^+ + 1)^2}, \tag{3.44}$$

with the gradient ratio r^+ defined as

$$r^+ = \begin{cases} \frac{\xi_{i+1}(t)-\xi_i(t)}{\xi_i(t)-\xi_{i-1}(t)}, & \text{for} \quad u \geq 0 \\ \frac{\xi_{i-1}(t)-\xi_i(t)}{\xi_i(t)-\xi_{i+1}(t)}, & \text{for} \quad u < 0 \end{cases}. \tag{3.45}$$

For the upwind boundary, the mixture fraction value ξ_i^- is interpolated following

$$\xi_i^- = \xi_i - 1(t) + \frac{B_i^-}{2}(\xi_{i-1}(t) - \xi_{i-2}(t)) \quad \text{with} \quad B_i^- = \frac{r^-(3r^- + 1)}{(r^- + 1)^2}, \tag{3.46}$$

using the definition of the gradient ratio r^-

$$r^- = \begin{cases} \frac{\xi_i(t)-\xi_{i-1}(t)}{\xi_{i-1}(t)-\xi_{i-2}(t)}, & \text{for} \quad u \geq 0 \\ \frac{\xi_{i-2}(t)-\xi_{i-1}(t)}{\xi_{i-1}(t)-\xi_i(t)}, & \text{for} \quad u < 0 \end{cases}. \tag{3.47}$$

In all cases, the limiter functions B_i are limited to values of $0 \leq B_i \leq 3$.

The substitution of equations (3.44) and (3.46) into the discretized form of the model equation (3.43) leads to the following expression for the mixture fraction value of the new time step $t + \Delta t$.

$$\begin{aligned} \xi_i(t+\Delta t) = &\left[1 - \left(1 + \frac{B_i^+}{2}\right)\frac{u\Delta t}{\Delta x}\right]\xi_i(t) + \left[\left(1 + \frac{B_i^-}{2} + \frac{B_i^+}{2}\right)\frac{u\Delta t}{\Delta x}\right]\xi_{i-1}(t) \\ &+ \left[\left(-\frac{B_i^-}{2}\right)\frac{u\Delta t}{\Delta x}\right]\xi_{i-2}(t) = \omega_i\xi_i(t) + \omega_{i-1}\xi_{i-1}(t) + \omega_{i-2}\xi_{i-2}(t). \end{aligned} \tag{3.48}$$

Equation (3.48) now shows a second order accurate discretization using a TVD scheme, which decreases the numerical diffusion. Since B_i^+ and B_i^- are non-negative by definition, the weight factors ω_i and ω_{i-1} are positive. However, the weighting factor of the $(i-2)^{th}$ cell is lower or equal to zero, which invalidates this approach to be a positive weighting scheme. Nevertheless, eq. (3.48) can be transformed in a way that a PWS is achieved. Therefore, the weighted portion $\omega_{i-2}\xi_{i-2}$ should not be interpreted as a negative amount of particles to be exchanged with the i^{th} control volume, but rather as a modulation of the mass flux from the $(i-1)^{th}$ control volume. With that knowledge, the discretized form of the model equation can be rewritten as

$$\xi_i(t+\Delta t) = \left[1 - \left(1 + \frac{B_i^+}{2} + X\right)\frac{u\Delta t}{\Delta x}\right]\xi_i(t) + \left[\left(1 + \frac{B_i^-}{2} + \frac{B_i^+}{2} + Y\right)\frac{u\Delta t}{\Delta x}\right]\xi_{i-1}(t). \tag{3.49}$$

The two variables X and Y now represent unknowns that need to be determined. Performing a factor comparison between (3.49) and the original discretization (3.48) leads to the determination of X and Y, viz

$$X = (1 + C^-)\frac{B_i^-}{2} \quad \text{and} \quad Y = \frac{C^- B_i^-}{2} \tag{3.50}$$

with the definition

$$C^- = \begin{cases} \frac{\xi_i(t)-\xi_{i-2}(t)}{\xi_{i-1}(t)-\xi_i(t)}, & \text{for} \quad \xi_{i-1}(t) - \xi_i(t) \neq 0 \\ 0, & \text{otherwise} \end{cases}. \tag{3.51}$$

By substitution of eq. (3.50) into eq. (3.49) the eventual form of the second order accurate PWS for the mixture fraction transport is obtained and reads as

$$\begin{aligned} \xi_i(t+\Delta t) = &\left[1 - \left(1 + \frac{B_i^+}{2} + (1 + C^-)\frac{B_i^-}{2}\right)\frac{u\Delta t}{\Delta x}\right]\xi_i(t) \\ &+ \left[1 + \frac{B_i^+}{2} + (1 + C^-)\frac{B_i^-}{2}\right]\frac{u\Delta t}{\Delta x}\xi_{i-1}(t) = \omega_i^*\xi_i(t) + \omega_{i-1}^*\xi_{i-1}(t). \end{aligned} \tag{3.52}$$

Here, ω^* represent the modified weighting factors for the direct neighbor of the considered control volume. The monotonicity preservation of equation (3.48) ensures both modified weight factors to be non-negative and hence, qualifies the derived method (3.52) to be a positive weighting scheme with second order accuracy.

At this place it shall be stated expressively, that this second order transport scheme is only valid for the mixture fraction scalar. For a high-dimensional PDF, the accuracy of the transport is as best increased from first order to an order in between first and second. A detailed analysis of this behavior is given below in section 4.2.

Molecular Mixing $\mathcal{M}$ Contrarily to the convection and diffusion processes, which happen in physical space, the molecular mixing takes place in the so called composition space. That means, instead of an interaction between particle ensembles of neighboring control volumes, the mixing process is modeled by an interaction within a cell's particle ensemble.

In this contribution two different mixing models are applied, which differ in terms of its basics. The two models are the IEM (Interaction by Exchange with the Mean) model [7], also referred to as the LSME (Linear Mean Square Estimation) [21], [65] and the modified Curl's model [39]. To complete the list of commonly used micro mixing models, the EMST (Euclidean Minimum Spanning Tree) model [100] needs to be mentioned, which is not used in this work. The main difference of the applied models is the procedure to represent the mixing. The IEM model involves the entire particle ensemble in order to perform the mixing process, whereas the modified Curl's model includes only parts of the control volume's particle ensemble.

Following Subramanian and Pope [100], micro mixing models need to fulfil certain criteria in order to adequately represent the physical phenomena. These desirable and partially necessary features are listed and described in the following:

- *Conservation of means* The mean values of the transported scalar must not be changed due to the mixing process, but need to be conserved. This is related to the conservation equation for the mean scalar quantity within the high Reynolds number limits. Therefore mixing models are not allowed to affect the mean values of the considered scalars.

- *Decay of variances* Unlike the conservation of means, the variances of transported scalars need to be decreased by the mixing process. This feature can be derived from a covariance transport equation and is commonly guaranteed by the applied mixing models.

- *Boundedness of the scalars* Based on the conservation of mass, the considered scalars need to be bounded within their physical limits. This must also be ensured by the used mixing models, in order to avoid unphysical compositions.

- *Linearity and independence* Mixing models need to follow linear transformations of the scalars and hence should not change their behavior. This is due to the linearity of the scalar transport equations with the considered fields themselves. The independence feature states that each scalar field should be unaffected by any other transported field in terms of the mixing.

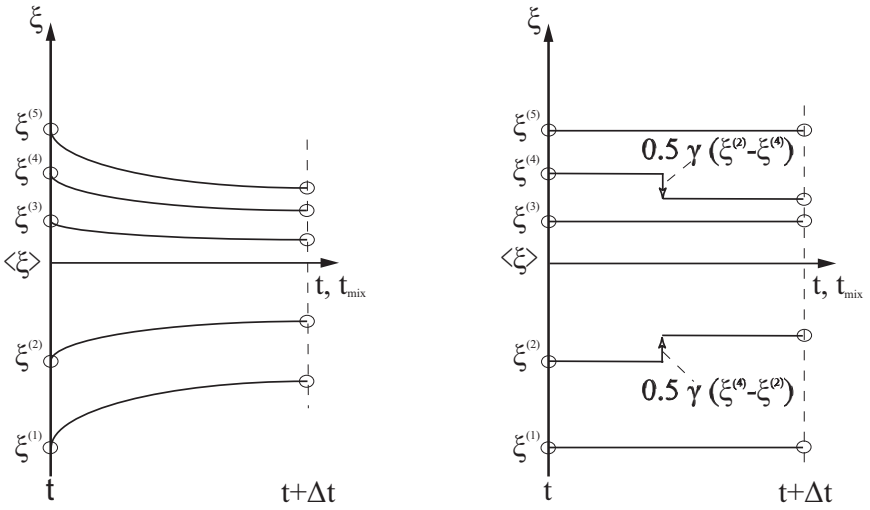

Figure 3.8.: Schematic of the procedures of the two applied micro mixing models; IEM (left) and modified Curl's (right).

- *Relaxation to Gaussian shapes* PDF shapes have to be independent of the initial condition after a sufficient time has elapsed and will end up in a Gaussian shape. Jayesh and Warhaft [40] verified this behavior by experimental data as well as direct numerical simulations. The mixing models applied in the present contribution do not ensure the formation of a Gaussian shape. However, for inhomogeneous turbulent flows reasonable results can be obtained anyway.

- *Localness* The mixing models should ensure that particles only interact with other particles that are close in composition space. That means, e.g. particles representing a thermo-kinetic state near the equilibrium state should not interact with particles totally off this region. This characteristic is referred to as localness, because the stochastic particles should only be mixed with particles which are in the local neighborhood of the composition space.

The applied micro-mixing models, IEM and modified Curl's, do not fulfil each and every of the presented features, but however give reasonable results. The models are described below and the characterization using the six mentioned features is performed as well.

Figure 3.8 schematically shows the procedures of the IEM (left) and the modified Curl's (right) model using a particle magnitude of $N = 5$. As mentioned above, the IEM model affects the entire considered particle ensemble within a control volume, which means, the values of each of the five particles are changed due to an equation described below. In contrast, the pairwise acting modified Curl's model selects a number of particle pairs, that interact with each other.

Both models make use of a frequency of mixing within the sub-grid [38] ω_{mix}, which is not known a priori and hence needs to be modeled. This mixing frequency can be linked to the diffusion coefficients and the filter width Δx [14]. The mathematical formulation of Ω_{mix} is given by

$$\Omega_{\text{mix}} = C_{\Omega} \frac{D_{\text{eff}}}{\Delta x^2} \tag{3.53}$$

where the constant C_Ω is assumed to be 8 [94].

With the definition of the mixing frequency, the IEM model in the context of particle based Monte Carlo methods can be formulated as

$$\phi^{(i)}(t+\Delta t) = \phi^{(i)}(t) + (\phi^{(i)} - \bar{\phi})\exp(-\Delta t \Omega_{mix}). \tag{3.54}$$

Equation (3.54) exemplifies the principle of operation of the IEM model, which lets every particle of the ensemble with the quantity value $\phi^{(i)}$ interact with the ensemble averaged mean value $\bar{\phi}$. The influence of time is added by a exponential factor including the actual computational time step Δt and the mixing frequency Ω_{mix}. The time dependency of the IEM/LMSE model is also illustrated on the left hand side of fig. 3.8. The here presented IEM micro mixing model satisfies the first four characteristics for mixing models but does not fulfil the feature of relaxation to a Gaussian and the localness. Nevertheless, results obtained using this model are satisfying, especially in the context of Large Eddy Simulations, where smaller time steps occur and hence the influence of sub-grid mixing is reduced compared to RANS simulations.

The alternative modified Curl's mixing model has the same restrictions as the IEM model in terms of the listed desirable features. As already mentioned above, the modified Curl's model is not affecting each particle of the considered ensemble but a pairwise chosen amount of particles. As figure 3.8 (right) shows the values of a particle pair $\phi^{(a)}$ and $\phi^{(b)}$ are changed according to

$$\begin{aligned} \phi^{(a)}(t+\Delta t) =& \phi^{(a)} + \frac{1}{2}\gamma(\phi^{(b)} - \phi^{(a)}) \\ \phi^{(b)}(t+\Delta t) =& \phi^{(b)} + \frac{1}{2}\gamma(\phi^{(a)} - \phi^{(b)}) \end{aligned} \tag{3.55}$$

with γ denoting a randomly distributed number within $[0, 1]$.

The number of particle pairs n_p that are interacting with each other is computed using eq. (3.56).

$$n_p = \text{int}\left[\frac{\frac{1}{2}\Delta t C_f \Omega_{\text{mix}}}{\text{int}(\frac{1}{2}\frac{1}{0.3}\Delta t C_f \Omega_{\text{mix}} + 1)}\right] N^C \tag{3.56}$$

Here, int denotes the integer part of the obtained values in order to ensure a definite number of particle pairs. The calculated number of particle pairs are then chosen randomly out of the considered ensemble.

Chemical Reaction $\mathcal{R}$ In case of reactive scalars within the PDF dimensions chemical reaction needs to be considered and modeled. For the present work, this is only valid in the context of flamelet generated manifolds and the therefore transported progress variable. Contrarily, the steady flamelet approach does only include the non-reactive mixture fraction for the determination of the thermo-kinetic state and thus needs no consideration within the PDF transport procedure.

The transport equation for the reactive progress variable, defined by eq. (2.70), now includes a chemical source term. The source term itself, i.e. the change of the variable in time due to reaction, is taken from the tabulated FGM chemistry, as it is presented in

section 2.3.4.4. In the Monte Carlo formulation each particle receives its chemical source term according to its thermo-kinetic state from the chemistry table. This leads to

$$\phi^{(i)}(t + \Delta t) = \phi^{(i)}(t) + \Delta t\, \omega_{\mathrm{FGM}} \tag{3.57}$$

with ω denoting the chemical source term for the considered transported reactive scalar ϕ taken from the FGM chemistry table.

With all described fractional steps, the particle based Eulerian Monte Carlo discretization of the PDF transport equation is completed. For consistency the inclusion of the quasi second order accurate discretization of the convective flux, the accuracy of the time advancement also needs to be increased. Instead of the proposed time integration scheme by Chen [13], the order of accuracy in time for this work is increased by a repeated execution of the fractional steps using an explicit first order time discretization within a time step Δt according to the Runge-Kutta method. That means, the Monte Carlo PDF transport is performed three times within the computed time step using the suggested time step fractions from the described Runge-Kutta scheme (eq. (3.22)) and considering the new properties like velocity, density and viscosity. This does definitely not increase the time advancement to a full second order accuracy, but nevertheless reduces the numerical error in contrast to the uniquely performed time stepping immensely. Furthermore, the increase of accuracy in time makes the time advancement more consistent to the spatial discretization in physical and composition space.

3.6. Parallelization

Large Eddy Simulation is still connected with a high computational effort. Especially, the simulation of large turbulent reactive flow configurations close to real technical applications are time and memory consuming. In cases where LES is part of a hybrid calculation procedure, like the coupled Monte Carlo PDF transport, but also, for example in relation with computational aeroacoustics, the computational costs rise immensely. Therefore, parallelization of the used numerical methods is absolutely necessary in order to obtain results earlier or realize more variations within the same time. Parallelization in the context of numerical simulations describes the partitioning of a given problem into sub-problems that can be run parallel on different CPU with a minimum of communication between those processors. This does definitely not reduce the total computational effort for the simulation of a given problem, it is actually increased due to communication processes, but it ensures more output in the physical timeframe.

The simulation tools presented in this contribution are parallelized by a technique referred to as domain decomposition. This means, the created computational mesh is divided into partitions preferably with the same size and is distributed to a provided cluster of processors. Each of the processors now needs to solve only a subpart of the actual problem defined by either global boundary conditions (see section 3.4) or by boundary conditions defined and communicated by one of the other processors. The communication between the involved processors is performed using the standardized message passing interface (MPI) library [29], which also allows a switching to different computational architectures.

The parallelization of the Large Eddy Simulation code FLOWSI has been implemented and described by Freitag [25]. The implementation allows a partitioning onto 2^n processors which goes up to $n = 4$. This restriction on the number of the used processors is due to the implemented pressure-correction scheme. The parallelization of the introduced Monte Carlo PDF method is based on this technique and handles the particle ensemble fields similar to all other fields.

Chapter 4.

Generic Test Cases

The derived governing equations for the mathematical description of turbulent reactive flows together with the introduced approaches and numerical models represent the basis for sophisticated computations of turbulent combustion configurations. The consideration of generic test cases is essential in order to verify the implementation and the underlaying assumptions and in addition to check out the validity of the mathematical and numerical description. Therefore, simple, preferably one-dimensional test cases are performed that can be adapted for the considered issues. The following chapter illustrates and discusses the results of simple configurations for verification of the quasi second order accurate Eulerian Monte Carlo PDF transport scheme proposed by Chen [13] and modified by Kuehne et al. [55].

4.1. Pure Mixing Case

In section 3.5.1.1 the discretization of the PDF transport equation with a Eulerian Monte Carlo method is described. For the numerical realization of the convective fluxes, a quasi second order accurate transport scheme in space and time is depicted and has been implemented in the existing CFD solver FLOWSI. The verification of the implementation will be performed on a one-dimensional pure mixing test case.

4.1.1. Numerical Setup

The pure mixing test case is not a realizable configuration, that can be experimentally investigated, but rather a thought experiment. The configuration is meant to be a one-dimensional mixing case with forced convection and neglected diffusion. Since the test case is built for verification of the second order accurate transport scheme and the related analysis of the occurring numerical diffusion, the appearance of physical diffusion would obscure the effects of the developed transport scheme.

The basic idea of this thought experiment is the convective transport of a block profile with mixture fraction equal to unity through a region of zero mixture fraction. Both mixtures, $\tilde{\xi} = 0$ and 1, are pure air under ambient conditions of $T_{\mathrm{amb}} = 294\,K$ and $p_{\mathrm{amb}} = 1\,bar$. The density is $\rho = 1.18\,kg/m^3$ and the kinematic viscosity has a value of $\nu = 1.84 \cdot 10^{-5}\,m^2/s$. The initialization of the mixture field within the domain consists of a block profile with a thickness of $0.02\,m$ and a peak value of $\tilde{\xi} = 1.0$ at the inlet.

The configuration consists of a computational domain with a length of $l = 0.216\,m$. It is resolved with a numerical grid using 128 control volumes, which leads to a resolution of

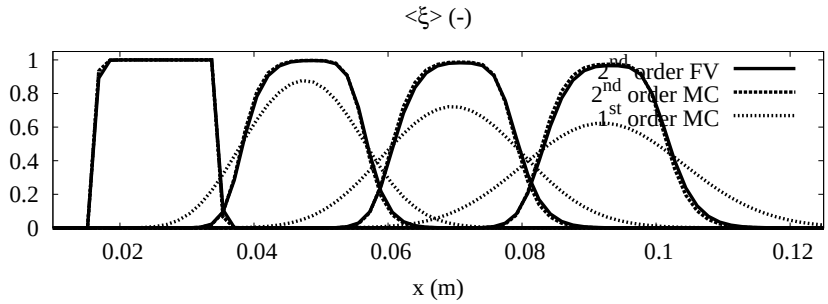

Figure 4.1.: Mixture fraction profiles of the pure mixing case under forced convection for four different time instances. Three different discretizations are shown: 2^{nd} order accurate finite volume (solid), 2^{nd} order accurate Monte Carlo PDF transport (dashed) and 1^{st} order Monte Carlo PDF transport (dotted).

$\Delta x \approx 1.7\,mm$. The velocity is set to $U = 15\,m/s$ in the entire domain and the time step has a constant value of $\Delta t = 10^{-5}\,s$. The PDF of the mixture fraction is represented by an ensemble of 500 particles per cell (ppc) and employing well mixed conditions for the micro mixing. Under these well mixed conditions, each particle ensemble is uniformly set to its average value in every time step and hence, the statistical error is almost negligible in this case.

4.1.2. Results

For verification of the quasi second order accurate discretization of the convective fluxes, the introduced thought experiment is simulated employing both, a first order and the second order accurate scheme. For an additional comparison, the results of a second order accurate finite volume discretized mixture fraction equation are calculated as well. Figure 4.1 shows the transported mixture fraction block profile at four different time instances $t = (10^{-5}, 1.5 \cdot 10^{-3}, 3 \cdot 10^{-3}, 4.5 \cdot 10^{-3})s$. The solid line represents the finite volume discretization with second order accuracy, while the dashed line depicts the new second order and the dotted line the common first order accurate discretization of the convective flux within the PDF transport. The flow velocity is directed from left to right, where the very left profiles represent the time step right after initialization. At this moment all three different discretizations obtain an identical solution and hence only a single profile is visible. When proceeding to the next visualized time steps, the differences in the implementations are becoming clearly visible. Starting with the most obvious one, the discrepancies of the first order accurate scheme are immense compared to both other ones. The included numerical diffusion in this simulation is very strong and affects the profiles to fade out by lowering the existing peak values and broaden the previous block profile. The spatial gradients of the mixture fraction are not conserved as actually expected during the transport but are continuously reduced. This leads to a broadening of the profile thickness from once $0.02\,m$ to more than $0.06\,m$ in the last shown time instance and a loss in the peak value of $\Delta\tilde{\xi} \approx 0.4$ from the initial unity mixture fraction peak. The comparison of the two second order accurate discretizations, finite volume and Monte Carlo PDF transport, also shows a smoothing of the block profile edges between the first

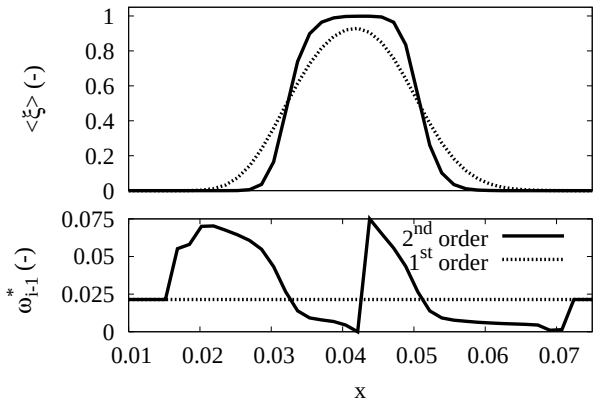

Figure 4.2.: Comparison between the first (dotted) and the second order (solid) accurate Monte Carlo discretization. At the top of this figure profiles are shown for $t = 1.1 \cdot 10^{-3}\, s$. The computed weighting factors ω^*_{i-1} from eq. (3.52) are illustrated at the bottom for both first and second order accuracy.

and the second time instance. This is caused by the facts that the sharp edges cannot be transported accurately by any method and the finite resolution of the computational grid. This changes the initial block profile more into a wave shaped profile but with approximately the same peak value and profile thickness and hence the gradients are also conserved within an adequate range. The differences between both implementations are almost negligible but can nonetheless be observed in the last given time instance. It seems as if the Monte Carlo transport computes the profile to be convected with a slightly lowered velocity than the finite volume method. This may be caused by two different reasons: either due to statistical errors within the Monte Carlo method or more likely due to the more complex finite volume mixture fraction transport scheme described in section 3.3 and the related pressure correction. Compared to the errors calculated by a transport with the commonly used first order accurate Monte Carlo scheme, this discrepancy can be ignored. Further insight into the implemented quasi second order Monte Carlo discretization is given by figure 4.2. At the top of this figure again profiles for both Monte Carlo implementations are shown, the solid line stands for the second and the dotted line for the first order accurate formulation. The solutions are plotted for a time instance of $t = 1.1 \cdot 10^{-3}\, s$. At the bottom, the correlated weighting factors for the directly adjacent neighbor cell ω^*_{i-1} are given. In the distributions of these weighting factors, one can easily see the effect of the new developed method. The first order implementation computes a weighting factor following eq. (3.39), which is constant over the entire domain at a value of around $\omega^{1st}_{i-1} \approx 0.023$. The second order accurate discretization now calculates values of the weighting factors that strongly depend on the existing mixture fraction value and hence on the spatial location in this case. In the regions of zero mixture fraction in front and behind the block profile both implementations obtain the same weight factors. In contrast, the weight factors within the block profile differ between both approaches. There are regions with an increased ω^*_{i-1} and others with reduced values compared to the first order accuracy. For the ranges where the strong numerical diffusion of the first order scheme transforms the shape of the block profile, the second order scheme shows a behavior

that counteracts the numerical diffusion. Furthermore, the gradients are conserved more accurately by this behavior, since the weighting factors are spatially adapted in a way, that the transport is increased upstream and reduced downstream of the gradients.

From these obtained results, the second order accurate positive weighting scheme for the mixture fraction transport can be assumed to be verified and implemented correctly. The solutions for the transported block profile are comparably accurate to the ones computed with a second order accurate finite volume discretization. Based on that fact, some flame configurations can be numerically investigated employing a steady flamelet chemistry model, where the mixture fraction is the only transported and determining quantity. The considered configurations are described and analyzed explicitly in following sections of this work.

4.2. Reactive Case

In the previous section, results of the developed transport scheme with second order accuracy for the application in a Eulerian Monte Carlo PDF method have been compared with first order implementations and finite volume ones. As mentioned before, the scheme proposed by Chen [13] is valid for the mixture fraction transport only. There arises the question, whether this approach can also be applied with more sophisticated chemistry models like the flamelet generated manifolds, which includes another transported scalar, the progress variable. In order to prove the impact and effects of the second order accurate PWS onto the additional reactive scalar an analog test case to the previous one is investigated.

4.2.1. Numerical Setup

This test case is again an one-dimensional configuration considering a convectively transported mixture fraction profile. In addition to the previous configuration, the reactive progress variable $\mathcal{Y}$ is transported as well and the occurring effects are analyzed. In this case, the progress variable is defined by $\mathcal{Y} = Y_{CO_2}/M_{CO_2}$, with Y_{CO_2} denoting the mass fraction of carbon dioxide and M_{CO_2} the related molecular weight. As before, the physical diffusion is neglected in order to study the impact of the numerical diffusion.

The chemistry of this test configuration corresponds to the later considered Sydney bluff body burner HM1e [16] representing the combustion of a fuel mixture of $50\,\mathrm{vol}-\%$ hydrogen and $50\,\mathrm{vol}-\%$ methane with air and a stoichiometric mixture fraction at $\xi_{\mathrm{st}} = 0.05$. This chemistry is pretabulated and β-integrated with 901 nodes for the mixture fraction space, 101 nodes for the mixture fraction variance and 201 for the progress variable space in the context of the finite volume approach. For the Monte Carlo PDF method the chemistry is tabulated using 901 nodes for mixture fraction and 301 for progress variable space representation. The normalization is performed using the equilibrium values of the carbon dioxide mass fraction $Y_{CO_2,\,eq}/M_{CO_2}$.

The initialized mixture fraction profile is no longer a block profile, but rather a wave shaped profile. The peak value of the wave is $\tilde{\xi} = 0.1$ and has an extent of 42 control volumes, which corresponds to a range of $\Delta x_{\mathrm{wave}} \approx 0.0175\,m$. The gradients of the shape are defined by an increase or decrease of $\Delta\tilde{\xi} = 0.01$ every two control volumes. The

initialization of the progress variable follows the initialized mixture fraction field according to the normalization table, including the equilibrium values in dependence of the mixture. The start field of the progress variable then corresponds to a double peaked shape due to the relation between the stoichiometric mixture of the applied fuel and the peak value of the given wave shape.

The numerical domain covers $l = 0.432\,m$ and consists of 1024 equidistantly arranged control volumes. This leads to a resolution of $\Delta x \approx 0.42\,mm$. As in the pure mixing case, the velocity is set constant to $U = 15\,m/s$ while the time step is again $\Delta t = 10^{-5}\,s$. This corresponds to a Courant number of CFL ≈ 0.356, which has a similar magnitude to the following calculations performed in the context of this work.

In order to ensure better comparison between the finite volume approach and the Monte Carlo PDF method, the sub-filter variance in the FV context is set to zero, whereas the well-mixed micromixing model is applied within the MC context. The PDF is represented by a particle density of 50 particles per cell, which is sufficient for an adequate accuracy under the well-mixed circumstances.

4.2.2. Results

For analyzing the effects of the quasi second order accurate scheme on the transport of the reactive progress variable, again a finite volume as well as a first order Monte Carlo implementation is taken into account. Thus it is possible to draw conclusions on the impact of the new developed scheme. For comparison, three different quantities are considered, the mixture fraction, the progress variable and the normalized progress variable. Through the normalization a combination of the transported mixture fraction and the progress variable is given and the differences in the combustion process can be seen more obvious, due to the restrictions of this quantity from zero (unburnt) to unity (completely burnt).

The profiles are compared in two time instances at $t = 10^{-5}\,s$ and $8 \cdot 10^{-4}\,s$, where the first one is directly related to the initialization. Figure 4.3 shows the three quantities mixture fraction (top), transported progress variable $\tilde{\mathcal{Y}}$ (middle) and normalized progress variable $\tilde{\mathcal{Y}}^*$ (bottom) for the three different implementations. The finite volume solutions are illustrated with the solid line, while the second order MC scheme uses the dashed and the first order MC approach the dotted lines.

Looking at the mixture fraction profiles, one can see the step like gradients in the first instance on the left side caused by the discrete initialization. Here, all implementations obtain the same solution and no differences can be observed. At the later time instance, the first order accurate MC scheme shows a relatively large discrepancy to both of the other approaches in terms of the peak value as well as the broadening of the profile due to numerical diffusion which represents the same behavior as in the pure mixing case. The two other methods show almost the same solutions except for the bulge at around $x = 0.03\,m$ in the second order Monte Carlo scheme, which might be an enhanced left over of the initialization. However, the impact on the mixture fraction has already been investigated above in section 4.1, whereas the progress variable transport is within the focus of this test case.

The initialized shape of the transported non-normalized progress variable $\tilde{\mathcal{Y}}$ consists of two peaks with $\tilde{\mathcal{Y}} \approx 2.5 \cdot 10^{-2}$ at the locations of stoichiometric mixture fraction and a

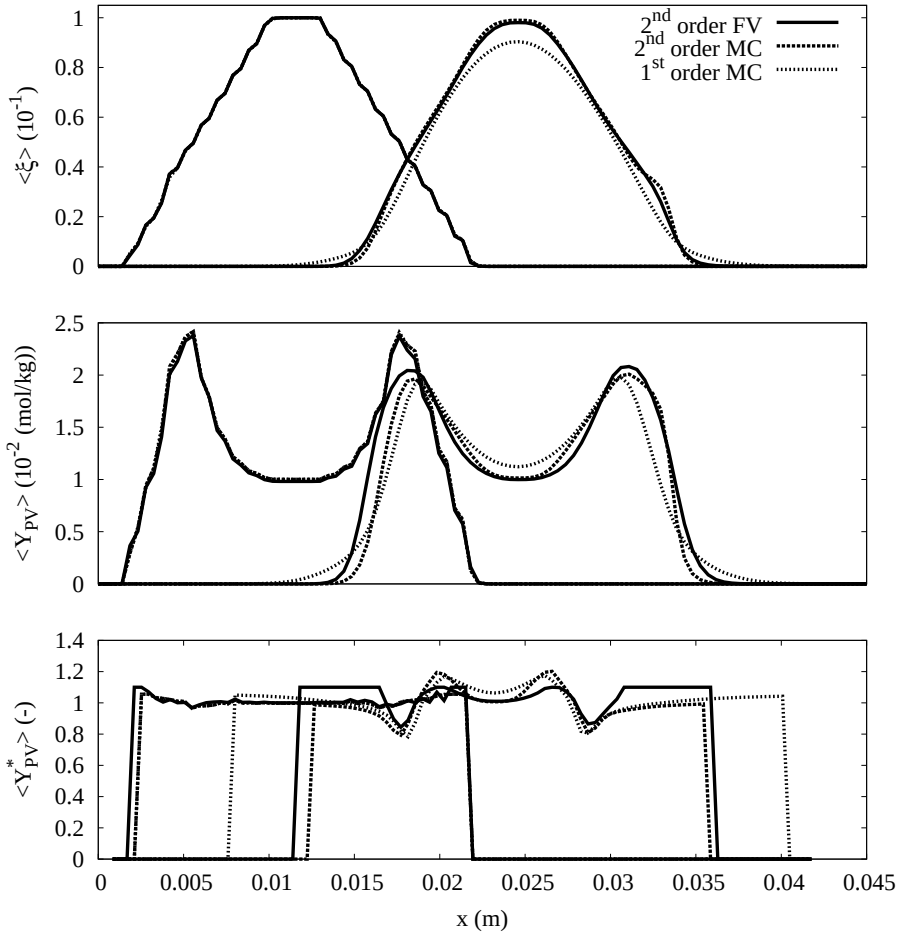

Figure 4.3.: Profiles of the reactive case under forced convection for two different time instances. Mixture fraction (top), progress variable $\tilde{\mathcal{Y}}$ (middle) and the normalized progress variable $\tilde{\mathcal{Y}}^*$ (bottom) are depicted employing three different discretizations: 2^{nd} order accurate finite volume (solid), 2^{nd} order accurate Monte Carlo PDF transport (dashed) and 1^{st} order Monte Carlo PDF transport (dotted).

region of $\tilde{\mathcal{Y}} \approx 10^{-2}$, where the mixture fraction exceeds the stoichiometry and reaches the value $\tilde{\xi} = 0.1$. All three implementations obtain the same initialization solution with a slight discrepancy at the tops of the peaks, which is caused by transport effects during the first time step. At the second time instance of $t = 8 \cdot 10^{-4}\, s$, the differences between the transport schemes are more obvious. By assuming the second order accurate finite volume scheme as the reference for the MC discretization, the quasi second order MCPDF solution agrees nicely while the first order scheme again shows the characteristically increased numerical diffusion. This leads to an enlarged decrease of the peaks and a broadening of the profiles, due to the flattening of the gradients. However, some discrepancies between both second order accurate schemes can be seen and have to be discussed. The transport scheme in the context of the Monte Carlo discretization shows surprisingly a lower broadening of the profile as the finite volume solution. Even though it looks like the gradient at the right branch of the double peak shape is steepened compared to the FV transport.

This effect appears at the same x-location where the bulge in the mixture fraction solution has been observed. Neglecting this behavior, the MC transport obtains even better results for the progress variable in terms of conservation of the initialized thickness l of the profile. Nevertheless, the peak values of the FV transport cannot be reached but range in the magnitude of the first order transport scheme. In the center section the results of both second order accurate schemes fit nicely corresponding to the value of $\tilde{\mathcal{Y}} \approx 10^{-2}$ but show differences in the gradient conservation. It can be concluded that, even though the quasi second order accurate MCPDF scheme is mathematically only valid for the mixture fraction, it gives reasonable solutions for the transported progress variable, which are in addition yet more accurate than the first order calculation.

The last subplot of figure 4.3 at the bottom depicts the solutions of the normalized progress variable $\tilde{\mathcal{Y}}^*$. It gives further insights to the actual combustion progress by directly illustrating it on a scale from zero to unity. The first time instance for comparison already shows differences in the profiles although it is just shortly after the initialization. A reason for that is the strong sensitivity on the mixture fraction field especially in the region around $\tilde{\xi} = 0$, where the equilibrium values for the normalization show a very steep gradient. This leads to the different starting points of the profile, even though the mixture fraction field and the transported progress variable do not show any visible discrepancies. Despite that, the profiles of the first time instance show acceptable matching with some slight differences at the transition areas between the gradients and the level of fully burnt state of $\tilde{\mathcal{Y}}^* = 1$. It is very interesting to see conditions of values greater than unity, which should not appear and upon first sight do not have any physical validity. However, further investigation gives a persuasive explanation, which will be presented later in this work.

By taking a closer look at the transported profiles later in time at $t = 8 \cdot 10^{-4}\,s$ one gets similar conclusions as at the comparison of the non-normalized progress variable depicted in the middle of figure 4.3. The first order scheme gives a huge distortion of the initial profile thickness l justified by the increased numerical diffusion seen before in both $\tilde{\xi}$ and $\tilde{\mathcal{Y}}$, whereas the higher order MCPDF scheme computes even lower broadening than the finite volume method. The mid region of the shapes again fits quite well for both non-unity accurate transport schemes, while the first order scheme obtains to large values exceeding unity in this region. Issues can be seen in the transition between this center section and the descent to zero. Here, the differences are clearly visible and need some discussion. The distribution of this symmetric profile to the outer regions differ starting from the indentations till the steep gradient to zero. The FV scheme computes a relatively fast rise to values greater than unity where the MCPDF schemes slowly converge to unity and the subsequent descent to zero. Within this range, the MC schemes compute a different reaction progress as the FV implementation eventually leading to discrepancies in temperature or other thermo-chemical property distributions.

Conclusively, the reactive test case in the given framework consolidates the findings of the pure mixing case in terms of the mixture fraction transport and furthermore shows an increase of accuracy in the transport of the reactive progress variable compared to the first order implementation. However, this is surprising due to the fact, that the introduced quasi second order accurate MC transport scheme should present this accuracy only for the mixture fraction transport. Based on the performed calculations, the exact order of accuracy belonging to this scheme cannot be determined, but estimations lead to an order

between one and two. That means, the accuracy is not reduced below first order and hence legitimates the application of this quasi second order accurate positive weighting scheme in the context of flamelet generated manifolds and the additional transported progress variable $\tilde{\mathcal{Y}}$.

Chapter 5.

Sydney Bluff Body Configurations

The Sydney bluff body configurations are a series of non-reacting and reacting flow problems, developed and investigated by the research group around Masri at the University of Sydney, Australia. The first contribution considering these flow configurations has been presented at the TNF workshop 1996 [18]. Since then, they are part of the so called TNF target flames, representing experimentally well investigated configurations for the validation of numerical methods.

The series consists of non-reacting and reacting cases with variations in the Reynolds number, the used fuel and even swirl inlet conditions with an unchanged burner geometry. The variations of the conditions allow a vast variety of different flow and combustion problems in terms of effects like partial premixing of fuel and oxidizer or local extinction phenomena. Furthermore, it is possible to simulate a set of different configurations, starting from simple non-reacting cases to reacting ones with locally occurring extinction following the continuously rising complexity for model validation.

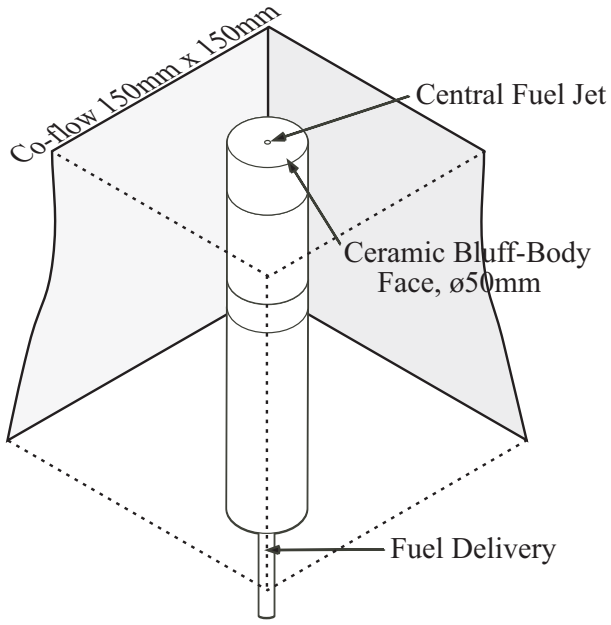

Figure 5.1.: Sketch of the geometry of the Sydney Bluff Body configuration consisting of a ceramic bluff body with a diameter of $d_{\mathrm{bb}} = 50\,mm$ and a central fuel jet with $d_{\mathrm{jet}} = 3.6\,mm$ coaxially arranged. The entire geometry is located within a quadratic wind tunnel with an edge length of $l_t = 150\,mm$. (Source: [63])

Table 5.1.: Parameters of the isothermal and reacting bluff body configurations

	$U_{\text{jet}}\,(m/s)$	$U_{\text{co}}\,(m/s)$	Re_{jet} (-)	Fuel	ξ_{st} (-)
B4C2	50	20	15900	CNG (CH_4)	-
HM1e	108	35	15800	CNG (CH_4)/H_2 (1:1)	0.05
HM3e	195	35	28500	CNG (CH_4)/H_2 (1:1)	0.05

The geometry for all Sydney bluff body configurations is illustrated in figure 5.1. As it is depicted, it consists of a ceramic bluff body with an outer diameter of $d_{\text{bb}} = 50\,mm$ and a central coaxially arranged fuel jet with a diameter of $d_{\text{jet}} = 3.6\,mm$. This configuration is installed inside a quadratic wind tunnel with an edge length of $l_t = 150\,mm$. For the cases with additional swirl inlet conditions, an annulus ($d_{\text{ann}} = 60\,mm$) around the bluff body is complemented where inlet velocities with a tangential component can be added. The additional swirl component is a very interesting flow characteristic commonly applied in today's gas turbine combustion chambers. Nevertheless, the non-swirled cases of the bluff body configuration embody flow features important for practical applications in combustion devices. Especially the stabilization effect of the bluff body flames is of particular importance, which is mainly characterized by recirculation of hot burnt gas back to the inlet region. This heats up the inflow streams of air and fuel and hence leads to a stabilization of the flame just at the outer edge of the bluff body.

The following sections discuss only selected cases of the Sydney bluff body series, the non-reacting B4C2 case and two reacting cases HM1e and HM3e without swirling conditions. Both latter ones differ in terms of the global Reynolds number and hence differences in the flow field as well as in the chemistry can be observed. For the chemistry these are especially impacts of local extinction that changes the thermo-chemical properties and additionally the flow field. Analyses of the different cases are performed in respect of the application of the artificially generated turbulent inflow boundary conditions, the particle density within the Monte Carlo PDF transport method, the model for the sub-filter variance and the differences between calculations using steady flamelet chemistry and flamelet generated manifolds. The latter one is particularly very interesting regarding the representation of local extinction phenomena for the high Reynolds number case HM3e. Furthermore, the work focusses on analyzing the sub-filter PDF shapes of both, the mixture fraction and the reactive progress variable and a related comparison with the most commonly employed modeling strategies. The inflow boundary conditions and chemical properties of all three investigated cases are depicted in table 5.1. The given quantities are the jet velocity U_{jet}, the coflow velocity of the wind tunnel U_{co}, the Reynolds number based on the jet velocity and the jet diameter Re_{jet}. In addition, the used fuel composition and the corresponding stoichiometric mixture fraction ξ_{st} are given. The most important fact from this table is the similar Reynolds number of the non-reacting B4C2 and the reacting HM1e case, which makes it possible to assume B4C2 to be the isothermal counterpart of the HM1e configuration. This way, conclusions drawn from B4C2 can somehow be transferred to the reacting cases. A special attribute of the non-reacting case is the usage of pure CNG (compressed natural gas) instead of a mixture of CNG and hydrogen as in the flame cases.

5.1. Experiments

The experimental investigation of the Sydney bluff body series was initially published by Dally and Masri [18] in 1996 and was followed by further publications of flow and scalar field measurements of several non-reacting and reacting cases ([16] and [17]).

As table 5.1 shows, the fuel compositions of all considered cases include CNG. Since CNG is just a general description for locally provided natural gas, the compositions are not definitely known. Therefore, only the flow field measurements have been performed using the CNG, which in this case consists of approximately 90% methane and additional 10% butane and other hydrocarbons. The differences between the thermo-chemical properties of CNG and methane regarding the velocities are negligible and for cost reasons the CNG option has been employed. However, the experiments for the compositional measurements have been conducted using pure methane rather than the natural gas composition. This allows for accurate experimental investigations of the scalar field distributions and precisely defined boundary conditions.

All experimental investigations, velocity and scalar measurements, have been performed using advanced laser diagnostics. A special feature of the experiments is the fact, that the velocity measurements were accomplished at the Thermofluids Research Group by the University of Sydney, Australia, while the compositions were measured at the Combustion Research Facility of the Sandia National Laboratories, Livermore, USA. This is justified with the unique equipment available at the Sandia National Laboratories for scalar field experiments.

The velocity distributions have been investigated using Laser-Doppler-Anemometry (LDA) and the method of Particle-Image-Velocimetry (PIV) achieving simultaneous axial and radial velocity components for different axial and radial locations within the region of interest. For the measurements of temperature and species concentrations the single-point Raman/Rayleigh/LIF (Laser-Induced-Fluorescence) technique was used, where the Rayleigh signal provides the temperature data and the Raman signal determines the concentrations.

5.2. Non-Reacting Mixing Configuration B4C2

This section is about the non-reacting mixing configuration B4C2 from the described Sydney bluff body series. The numerical investigation mainly serves as a basis for the simulations of the reacting combustion cases. This way it is possible to validate isolated mixing and flow field simulations with experimental data without the influence of chemical reactions and the related impact on mixing and flow patterns. Furthermore, isothermal configurations with similar Reynolds numbers as corresponding reacting cases feature smaller flow and turbulence structures than the burning cases due to missing thermal expansion of the hot gases. Due to this, accurate isothermal simulations are an adequate tool for the validation of a numerical grid resolution for application to the burning cases.

As illustrated in table 5.1 the B4C2 case has a jet velocity of $U_{\text{jet}} = 50\,m/s$ and the surrounding air stream of the wind tunnel has a speed of $U_{\text{co}} = 20\,m/s$. The jet velocity and the jet diameter lead to a global Reynolds number of 15900, which is in a moderate turbulence regime and is chosen by analogy to the reacting case HM1e. As

already mentioned above, the velocity field measurements were performed using CNG as fuel mixture, whereas the compositions were experimentally obtained by using pure methane in order to ensure an adequate accuracy of the measurements.

5.2.1. Sensitivity on Inflow Boundary Conditions

5.2.1.1. Numerical Setup

The simulations of the B4C2 configuration are performed on a numerical domain with the dimensions $0.25\,m$ in axial, $0.22\,m$ in radial and 2π in azimuthal direction. The computational grid consists of approximately $1.2 \cdot 10^6$ control volume, which are given by 400 nodes for the axial resolution, 94 for radial and 32 for the tangential direction. The radial distribution of the nodes is equidistant for the region from the centerline to the outer edge of the bluff body and non-equidistant beyond the bluff body. Application of this refinement allows for a finer resolution in the area of interest around the inner jet and the mixing layer at the bluff body edges, but also decreases the computational costs by minimizing the number of grid points in the coflow stream. The domain size and the grid resolution have been adapted from earlier publications by Kempf [49], who showed promising results for similar configurations.

For the simulations of the non-reacting configuration only the finite volume solutions are computed, since the mixing results should be congruent by definition no matter if a finite volume method or a Monte Carlo PDF method is used.

In order not to start the computational domain directly at the upper edge of the bluff body, which can cause instabilities of the simulations, parts of the bluff body are modeled using the immersed boundary technique (see section 3.4). The modeled bluff body penetrates the domain by $8.75\,mm$, which is sufficient to observe the characteristic flow patterns around the bluff body and additionally increases the stability of the simulation. Calculations with varying penetration depth of the immersed boundaries did not show any impact on the results and hence for all simulations of the bluff body configurations the modeling of the geometry is kept the same.

In numerical simulations the mathematical definition of boundary conditions is of significant importance for the accuracy and quality of the obtained results. Therefore, the analysis of the B4C2 configuration focusses on the adequate choice of the inlet boundary condition. This analysis should also be seen in relation to the investigations regarding the inflow boundary conditions of the reacting flow HM1e in section 5.3.1.

As described above, for the inflow boundary condition, the LES solver FLOWSI provides two kinds of Dirichlet boundary conditions. The first one describes the conditions at the boundary as time independent, whereas the second one calculates time dependent definitions for the simulation of turbulent flow structures at the inflow plane. The method used for the latter one has been described earlier in section 3.4. The simulations here obtain results showing the effects of constant and time dependent velocity boundary conditions at the inflow plane. Both approaches are based on the same experimental data for the determination of the boundary velocities. Therefore, experimentally obtained radial velocity profiles in immediate vicinity of the bluff body are taken to represent the mass flow into the computational domain. Instead of keeping them constant like in the time independent RANS-like definition, the velocity inflow conditions are transformed on the

basis of the also measured velocity fluctuations. This way, not only the mean values are defined but also the fluctuations in time.

5.2.1.2. Results

Results of the B4C2 case are compared qualitatively in terms of streamlines and time averaged mixing field plots as well as quantitatively by comparison of selected radial profiles with experimental data.

An idea of the general appearance of the B4C2 case is given by figure 5.2. Each plot, the streamlines and the mixing field distribution, is divided into the variant without on the left and the one with artificial inflow turbulence on the right. Streamlines based on the time averaged velocity fields for both different inflow methods are shown on the left. Both approaches show the same general flow patterns except for some differences in the locations of the recirculation zones that will be discussed below. The flow structure consists of two toroidal recirculation zones, creating three mixing layers. Both recirculating regions are situated just above the bluff body and reach to about $x = 0.05\,m$ axially downstream. The outer recirculation is radially located from about $r = 0.01\,m$ to the outer edge of the bluff body at $r = 0.025\,m$, while the inner one ranges from the central jet to $r = 0.01\,m$ where it meets the outer one. The three mixing layers are created by the velocity gradients between the coflow and the outer recirculation, between both recirculation zones and between the inner recirculation and the central CNG or methane jet. The flow is characterized by a strong necking close behind the recirculation zones, where all streamlines tend to the centerline till the flow is oriented almost parallel. The varieties between both inflow approaches can obviously be seen. The missing turbulence in the simulation without the usage of time-dependent inflow data causes the jet to penetrate deeper into the domain than in the case with artificial turbulence in the inflow stream. This is apparent, because the additional superposed turbulence structures increase the momentum transport to all directions and hence increase the jet's opening angle and shorten the jet penetration depth. Thus, the centers of rotation and the sizes of both recirculation zones are affected and show differences between the two calculations. Through the additional inflow turbulence and the corresponding increased momentum transfer, the centers of rotation are shifted further upstream closer to the bluff body. Since the recirculation zone is limited by the bluff body, the sizes of the zones are decreased which again causes the flow necking to happen further upstream compared to the non turbulent inflow. Another very interesting feature that distinguishes the two computations from each other is the interaction of the inner recirculation zone with its outer counterpart close to the nozzle. In the left case, the inner recirculation occupies more space and distracts streamlines from regions above $r = 0.01\,m$ radially back to the centerline, while the outer rotation loses impact on the flow close to the upper edge of the bluff body. In contrast, the turbulent inflow case shows a behavior the other way around. Here, the inner recirculation is shifted towards the centerline and thus does not affect the flow as much as the outer rotation by the radial deviation of the flow to the outer mixing layer created by the coflow.

The mixing field distributions, illustrated on the right side of figure 5.2, are strongly affected by the recirculating flow structure with a jet like penetration close to the centerline. Starting with the jet flow, the observations made at the streamline distribution plot are all transferable to the mixing field. On the left side of the mixture fraction plot,

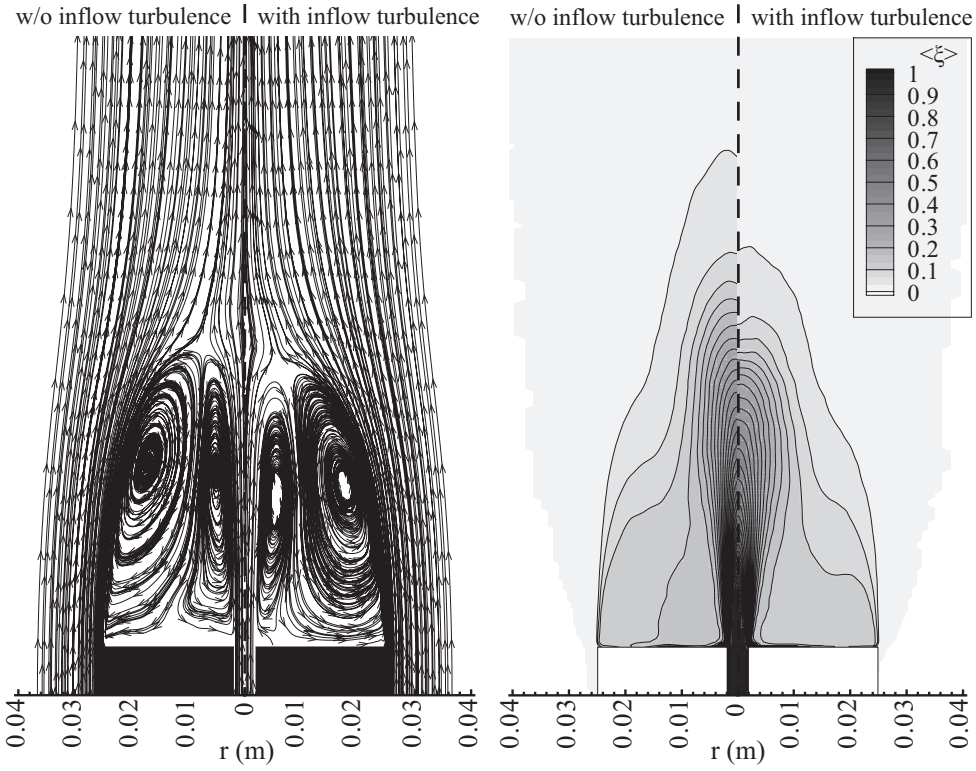

Figure 5.2.: Comparison of streamline distributions and mixing fields between time independent inflow boundary conditions (left) and artificially generated inflow turbulence (right) for the non-reacting Sydney bluff body configuration B4C2.

the resulting field without application of the inflow turbulence generator is depicted and show a deep fuel jet penetration, while the result with artificial inflow turbulence has a shorter jet penetration. Therefore, the jet opening angle is larger, which is caused by the increased turbulent mixing rate. The other apparent observation is directly correlated to the interaction of the occurring recirculation zones as described above. The change of the flow structure due to the superposed inlet turbulence has tremendous impact on the composition, depending on the radial transport of the rather rich mixture at $r = 0.01\,m$ to either the centerline (without inflow turbulence) or to the outer regions (with inflow turbulence). This is visible through the enhanced mixture transport to the outer edge of the bluff body in the case with inflow turbulence, which is not existent in the case without turbulent inflow boundary conditions. Conclusively, it can be stated that the entire mixture distribution is situated more compact around the bluff body with the superposed turbulent structures than it is the case without it.

After comparing and interpreting the qualitative results, quantitative statements need to be done and validations employing experimental data are necessary. This allows for a final conclusion, which approach is more suitable for this case and what reasons are responsible for that. At this point it should be stated, that this work is not focussed on the matching of simulated results with the experimental data, but rather on the analysis of sensitivities regarding different modeling approaches. A profound argument is the fact, that computed results can always be tuned to fit measured results, but the gain

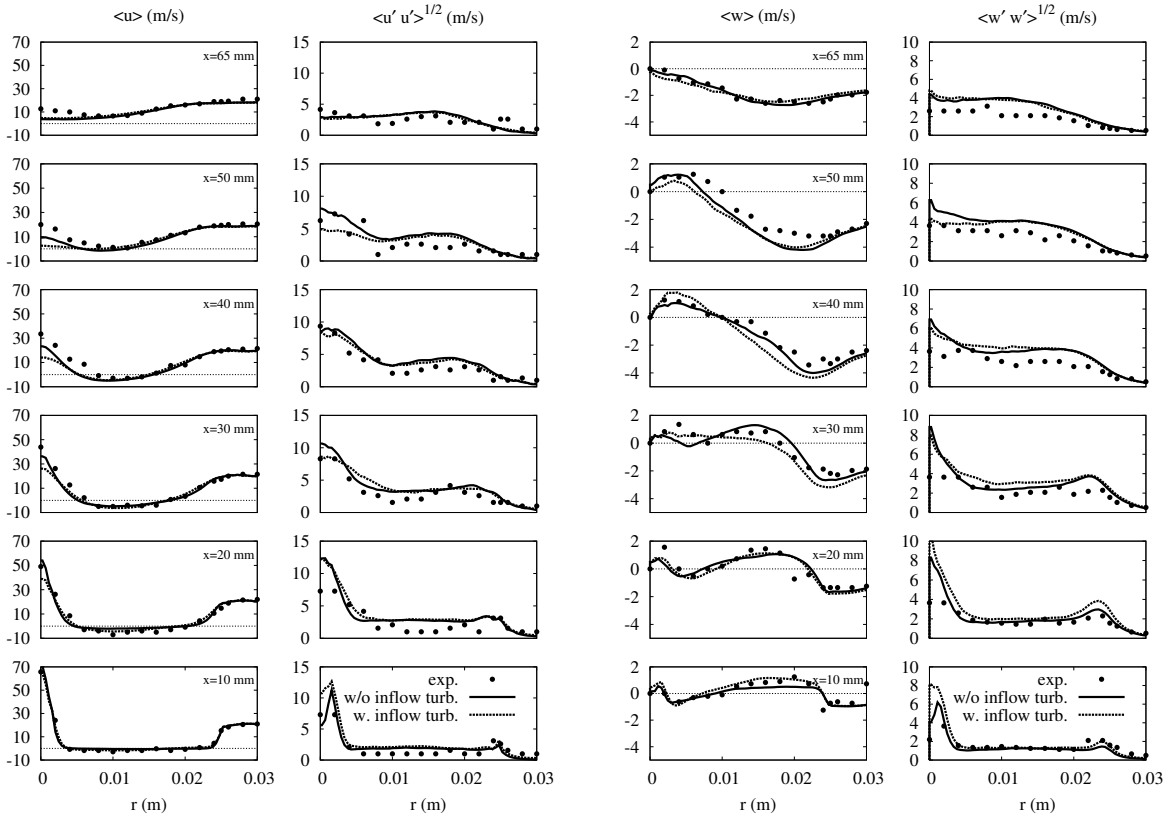

Figure 5.3.: Time averaged radial profiles of the axial (left) and the radial (right) velocity components and their corresponding fluctuations of the non-reacting Sydney bluff body configuration B4C2 for distinct axial locations. Comparison of experimental data (symbols), a simulation without (solid) and with (dotted) artificial inflow turbulence. The horizontal lines in the mean value plots represent zero velocity for a more apparent separation of the recirculation zones.

in experience and knowledge concerning Large Eddy Simulations is negligible. However, it makes more sense to characterize the change in behavior due to a model replacement than to adjust simulations to experiments. Furthermore, in practical applications one does not know the profiles prior to the simulation and hence it is not possible to adapt parameters or boundary conditions to fit measured profiles. Nevertheless, the experiments act as an adequate reference for the assessment and evaluation of model behavior and as a validation basis for checking feasibility and validity of employed models.

Figure 5.3 shows time averaged radial profiles of the axial (left) as well as the radial (right) velocity components together with their corresponding fluctuations for different axial locations at $x = 10,\ 20,\ 30,\ 40,\ 50,\ 65\,mm$. Illustrated are experimentally obtained results given by the symbols, the calculated results without inflow turbulence represented by the solid line, while the dotted lines stand for the simulation with additional turbulence at the inflow boundary condition. Additionally, the zero velocity axis is highlighted in order to separate the recirculations from the rest of the flow. Within the plots of the mean axial velocity profiles only the behavior of the inner fuel jet differs regarding the varied models in terms of the penetration depth. This has already been observed

in the qualitative results in figure 5.2, where the superposed artificial inflow turbulence decreased the jet length due to the raised turbulent momentum transfer. Even though, the velocity plots close to the nozzle at $x = 10\,mm$ and at the most downstream location at $x = 65\,mm$ show no differences between the two calculations, whereas in between those positions the mismatch is not negligible. This is, where both interacting and counter-rotating recirculation zones are situated. Compared to the experimental data, the solid line shows good agreement for the flow relatively close to the bluff body, while the axial velocity is underestimated further downstream at $x = 40\,mm$ and $x = 50\,mm$. However, the simulation employing the inflow generator obtains an even larger decrease of the axial centerline velocity in almost the entire domain. Interpretable differences of the axial velocity plots between the two simulations for regions beyond the inner fuel jet cannot be observed. Here, both computations either with or without inflow turbulence are in very good agreement with the experimental measurements.

The fluctuations of the axial velocity component show some discrepancies between both, the simulations with each other and with the experiments. Already at the most downstream position at $x = 10\,mm$ both calculations obtain overpredicted fluctuations at the outer limit of the jet flow, while the turbulence generator also increases the level of fluctuations at the centerline. This can be explained by the additional turbulence-like structures superposed on the time-independent velocity boundary condition. Further downstream, this raised level of turbulence near the center axis leads to a broadened shear layer between the jet flow and the inner recirculation zone, indicated by the flat gradient of the fluctuation at $x = 20\,mm$ and $x = 30\,mm$. The elevated fluctuation level of the simulation with additional inflow turbulence leads also to a high dissipation rate and hence the shortening of the inner jet as already described above. However, even the simulation without turbulence in the inflow stream overpredicts the fluctuations at the centerline in the first three measured locations, which also yields to the underestimated jet penetration depth observed in the mean axial velocity plots. As in the axial mean value plot, except for the inner jet flow region, the fluctuations show a promising and comparably good agreement with the experiments and with each other.

The phenomenon of the increased fluctuation level near the centerline has already been observed in earlier publications using the Large Eddy Simulation code FLOWSI [45], [23]. Reasons for that have neither been documented nor have there been any efforts and investigations about that issue. Nevertheless, the solutions for the axial velocity are very promising and give reasonable predictions of the flow.

Taking a closer look at the radial velocity component on the right side of figure 5.3 reveals the actual effects of the inflow turbulence more apparently. The mean value profiles confirm the observations and conclusions drawn from the axial velocity component, especially the better agreement of the simulation without inflow turbulence in comparison to the measurements. The plots show the radial velocity component of the B4C2 configuration, where positive values indicate a flow to larger radii and negative ones represent flow to the centerline.

Generally, both computations reproduce the trends of the flow structure in a sufficient way, but the differences appear in terms of the calculated radial gradients. Close to the bluff body, both approaches provide similar results, but in positions further downstream mismatches are more obvious. At $x = 30$ and $40\,mm$ the widening of the fuel jet due to the

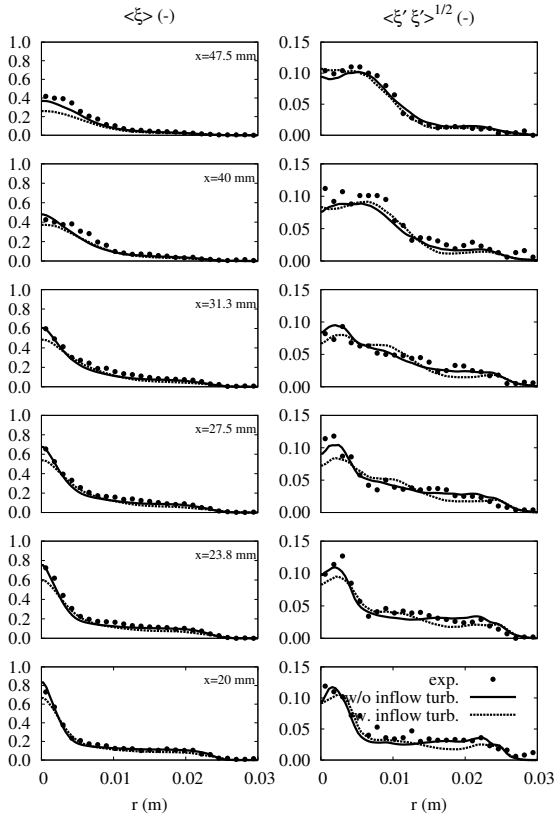

Figure 5.4.: Time averaged radial mixture fraction profiles (left) and its corresponding fluctuations (right) for selected axial locations of the non-reacting B4C2 configuration. Symbols depict the experiments, the solid line represents the simulation without inflow turbulence and the dotted line shows the computation with inflow turbulence.

superposed inlet turbulence is visible in terms of the increased values near the centerline, which leads to the overestimation of the radial gradient. That again is another argument for the incorrectly represented interaction between the two existent recirculation zones. Unfortunately, the region close to the nozzle, where the inner recirculation is changed in terms of its extent, as described in figure 5.2 (left), is not measured and hence an evaluation and interpretation using experimental data is not possible. However, employing and evaluating the rest of the radial flow field, yields to the conclusion, that the broadened inner rotation is closer to reality than the narrowed one as obtained by the usage of the turbulence generator. The fluctuations in radial direction show good agreement with the experiments except for the regions near the centerline. The fluctuations are overestimated by more than 100 %, which fortunately does not have a large impact on the flow simulations. In conclusion, the radial velocity distributions shown are very good especially for the computation without inflow turbulence, but the turbulence level represented by the velocity fluctuations near the centerline shows large deviations from the experimental data. The reasons are unknown and have not been investigated in detail.

Figure 5.4 illustrates time averaged radial mixture fraction profiles (left) and the related fluctuations (right) of the B4C2 bluff body configuration for selected axial locations. The

mean values show a distinct preference for the simulation without inflow turbulence. The jet penetration depth in terms of mixture fraction matches with the experiments almost perfectly, whereas the alternative computation shows too low mixture fraction values at the centerline. This is definitely caused by the increased transport of rich mixture to larger radii by the changed interaction of the two recirculation zones as shown in figure 5.2. Thus, more fuel is shifted to the outer edge of the bluff body, which unfortunately cannot be seen in the radial profiles, and hence is no longer available for the axial transport into the domain. Also the fluctuations of the mixture fraction on the right side of figure 5.4 show almost a perfect matching with the experiments and the non-turbulent inflow case. Even though the velocity fluctuations close to the centerline have been increased tremendously, the numerically obtained mixture fraction fluctuations fit very well. Interestingly, even though additional velocity fluctuations have been superposed in the simulations with inflow turbulence, the mixture fraction field of this computation yields even lower mixture fraction fluctuations close to the centerline than the simulation without inflow turbulence. This behavior is most probably caused by the correlation between the viscosity and the diffusion coefficient in the momentum and the mixture fraction transport equation, respectively. The relation between the two properties is determined by the already described Schmidt number (see section 2.3.3) and the impact can obviously be seen in the time-averaged mixture fraction fluctuations. The trend is as follows: viscosity and diffusion affect the transport of either momentum or diffusion in a damping way, which means, that small flow structures are dissipated. In the case of the velocity and the mixture fraction fluctuations of the non-reacting B4C2 configuration, the chosen Schmidt numbers are $\mathrm{Sc} = 0.7$ for the laminar and $\mathrm{Sc}_t = 0.45$ for the turbulent one. That means in the mixture fraction transport, the diffusion term is approximately doubled compared to the viscous flux within the momentum transport equation. This behavior might be the reason for the almost perfectly matching mixture fraction fluctuations, while the velocity fluctuations show an increased level of turbulence in the same positions.

5.2.1.3. Conclusions

Two simulations of the non-reacting case B4C2 of the Sydney bluff body configuration series have been performed in order to analyze the effect of artificially generated inflow turbulence. No grid variations in terms of resolution are made, since the chosen grid point distribution is based on a grid sensitivity analysis published by Kempf [49]. Computations of isothermal configurations in general serve as a basis for reacting cases, because of missing additional complex chemistry effects.

Qualitative and quantitative results of time-averaged velocity fields, their related fluctuations, the mixture fraction and the corresponding root-mean-square values have been presented and interpreted regarding the sensitivity in terms of inflow turbulence application. Furthermore, experimental measurements have been used as a reference to validate the simulations. By analyzing all solutions, a distinct trend towards the simulation without the superposed inflow turbulence is obvious. Especially the mean values of the velocities as well as the mixture fraction show explicit differences in terms of the penetration depth of the inner fuel jet. However, the fluctuation levels of both calculations do not feature characteristic behaviors that would lead to a preferability of one of the applied approaches. Nevertheless, the results of the obtained mixture field give the crucial

reason for the preferred choice, since the calculation without additional inflow turbulence represents the measurements almost perfectly. With regard to the following reacting configurations, where the mixture fraction is the defining quantity for the applied flamelet chemistry, the accuracy of the composition is decisive and hence defines the quality of the flame simulation.

5.3. Reacting Configuration HM1e

The reacting flow configuration HM1e is considered in the following section. This turbulent combustion system has the identical geometrical framework as the already described non-reacting B4C2 case. Even though the Reynolds numbers based on the jet velocity are almost the same in both cases, there are some differences in terms of the inflow velocities as well as the used fuel composition, as depicted in table 5.1. The fuel jet velocity is $U_{\text{jet}} = 108\,m/s$, while the surrounding coflow velocity is set to $U_{\text{co}} = 35\,m/s$. Dally et al. [17] specify the jet velocity as 50 % of the fuel composition's blow off speed. The fuel consists of 50 vol-% CNG (CH_4) and 50 vol-% hydrogen, where CNG is used for the velocity and methane for the composition measurements. Due to its moderate turbulence level, the HM1e configuration does not show any severe local extinction phenomena and hence is a good case for the application of steady flamelet chemistry.

In the context of the HM1e configuration various simulations are presented in this work, investigating a multitude of sensitivities and analyzing sub models employing the Eulerian Monte Carlo PDF transport method. At first, an analog comparison in terms of inflow boundary conditions is performed as it has been presented for the non-reacting case B4C2 above. Based on results of that section, an error analysis regarding the particle density in the Eulerian Monte Carlo solver is accomplished. Furthermore, the sub-model for the sub-filter variance of the mixture fraction is investigated explicitly before varying the chemistry model from steady flamelet to the flamelet generated manifolds formulation. In this context, the differences obtained by the differing velocity fields and the more complex chemistry representation are analyzed as well as an investigation of the sub-filter PDF shapes is performed. In addition, the validity of assumed statistical independence between mixture fraction and the progress variable (see section 2.3.5) is proved using joint PDF of both scalars obtained from the PDF transport.

5.3.1. Sensitivity on Inflow Boundary Conditions

5.3.1.1. Numerical Setup

The numerical framework of this sensitivity analysis is similar to the non-reacting configuration in terms of the used numerical grid. The domain size and the control volume distribution as well as the usage of the immersed boundaries are kept the same. The major differences between both cases are represented by the reactive circumstances and the related change in the thermo-chemical properties like density and viscosity. Furthermore, as mentioned before, the magnitudes of the inflow velocities are increased as well. For all numerical simulations, the fuel composition consists of pure methane and hydrogen which differs from the experiments, where CNG is used for the velocity and only

for the species measurements pure methane has been used. The discrepancies within the properties should be negligible, however it should be kept in mind while analyzing the results.

The chemistry is represented employing a steady flamelet approach with a constant strain rate of $a = 10\,s^{-1}$. The chemistry table is precalculated using the one-dimensional flamelet code CHEM1D [99] and additionally preintegrated applying a presumed β-shaped PDF approach. The filtered mixture fraction space $\tilde{\xi}$ is resolved with 200 and the normalized sub-grid variance $\widetilde{\xi_n''^2}$ with 100 equally distributed sampling points.

This section considers the sensitivity on the inflow boundary conditions as it is done in the previous section of the non-reacting B4C2 case. Therefore, two simulations in the finite volume context are performed, one is using the time constant Dirichlet boundary condition, while the alternative one employs the inflow turbulence generator. This allows for time-dependent velocity boundary conditions at the inflow plane, providing additional artificial turbulent structures onto the commonly used constant Dirichlet condition.

5.3.1.2. Results

In the following, qualitative results in terms of time averaged streamline and mixture fraction contour plots will be shown and discussed in detail with the focus on the impact of the superposed inflow turbulence. Furthermore, quantitative plots of the velocity components, the mixture fraction and the dependent scalar temperature are depicted. Dependent quantities are very important for the evaluation of the turbulence-chemistry interaction since these scalars are not transported but read from the precalculated chemistry table. At this point, the turbulence-chemistry interaction is not yet analyzed, however it is interesting to see the effect of the inflow boundary conditions on the temperature field. The simulated quantitative radial profiles are also compared to experimental measurements, giving a reference for evaluation of the simulations.

Figure 5.5 (left) shows the streamline distributions of the time averaged velocity field for the reacting methane hydrogen case HM1e. The figure is separated into the two alternatives of the inflow boundary condition formulation without (left) and with (right) artificial turbulence. Apparently, the characteristic formation of the two recirculation zones in this reactive case is not as definite as it is in the non-reactive case. The flow structure does not show the formation of both counterrotating zones between the jet and the coflow but rather an immense interaction between the two rotation systems. This leads to a complex velocity field, which differs tremendously depending on the usage of the alternative inflow boundary condition formulation. On the left, without the additional turbulent structures in the fuel jet, the inner circulation zone is established, while the outer one is degenerated. However, the separation of the recirculating gas flow towards or away from the centerline is still existent and the plane of splitting proceeds diagonally from about half of the bluff body radius to the edge of the fuel jet. The comparison with the simulation using artificial inflow turbulence shows a shift of the inner recirculation center further upstream and a more visible but still degenerated outer recirculation zone. Again, the splitting plane is not vertical as in the non-reacting case but rather diagonal with an angle of about 60 degrees to the bluff body surface. Another obvious characteristic in comparison with the B4C2 case is the nearly nonexistent necking of the flow behind the recirculation. This is also caused by the modified outer recirculation, which affects the non-reacting case to

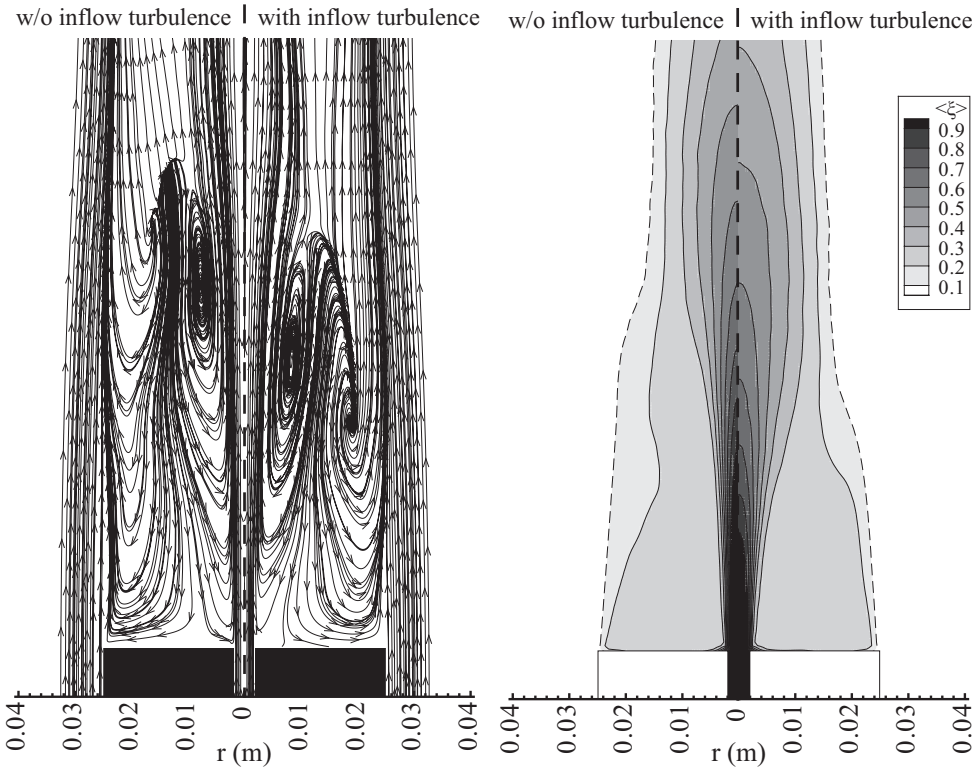

Figure 5.5.: Comparison of streamline distributions and mixing fields between time independent inflow boundary conditions (left) and artificially generated inflow turbulence (right) for the reacting Sydney bluff body configuration HM1e. Within the mixture field comparison, the dashed line depicts the stoichiometric mixture fraction of the methane hydrogen fuel mixture of $\tilde{\xi} = 0.05$.

build up this strong neck zone. Furthermore, due to the higher velocities of the fuel jet and the coflow, but also because of the density gradients and heat release the area of recirculating flow is larger and ranges further downstream as in the isothermal configuration. The plot on the right hand side of figure 5.5 illustrates the characteristic time averaged mixture fraction distribution of the HM1e case again consisting of both computations with the modified inflow boundary condition formulations. The contours depict the different values of the mixture fraction, where the outermost dashed line represents the stoichiometry of $\xi_{\mathrm{st}} = 0.05$ of the methane hydrogen fuel. The line of stoichiometry in nonpremixed combustion approximately depicts the location of the flame front. In this case, the flame stabilizes on the outer edge of the bluff body and follows a slight necking further downstream. The location and the shape of the neck zone depend strongly on the chosen inflow condition. Further downstream behind the neck zone the flame front is again positioned parallel to the centerline. The mixture contour close to the axis shows a similar behavior as obtained in the non-reacting flow case, where the simulation without turbulent fluctuations at the inflow leads to a narrow and long jet-like penetration of the fuel stream. The superposed turbulent structures in the alternative calculation widen the jet in radial direction due to its increased turbulent momentum transport and hence decrease the momentum at the centerline and shorten the penetration depth. The general

appearance of the mixture distribution is also similar to the non-reacting case, where in this case hot gas and comparably rich mixture is transported to the outer edge of the bluff body by the existent circulating flow patterns. This transport provides high temperatures and reactive mixture close to the bluff body and hence stabilizes the attached flame front at the surface of the ceramic body.

The validation of the flow and mixture field can only be performed employing experimental data. Therefore, radial profiles of the axial and radial velocity components as well as the corresponding fluctuations of both simulations are compared with measurements at distinct axial positions. The profiles are shown in figure 5.6, where the left hand side depicts the axial velocity component and its fluctuations and the right side the radial ones. The six positions of the performed measurements are $x = 3$, 10, 30, 50, 70, $90\,mm$ starting from the upper surface of the bluff body. In contrast to the non-reacting configuration B4C2 the first measurement location is very close to the bluff body surface with a distance of $x = 3\,mm$, which provides interesting profiles for the validation of the radial flow separation of the recirculation. The experimentally obtained data profiles at $x = 90\,mm$ are just above the end of the recirculation zones and hence represent an almost uniform axial velocity profile. In addition to the experiments, both simulation results are shown, without inflow turbulence depicted by the solid and with superposed inflow turbulence illustrated by the dotted line. In general, the measurements of the axial velocity component unveil a double peak shaped radial profile with a high velocity magnitude of the fuel jet at the centerline and the increased velocity at the coflow close to the nozzle. While proceeding further downstream starting from the surface of the bluff body, the peaks lose their intensity and broaden while decreasing their spatial radial gradients. Additionally, within the mid section between $r \approx 8\,mm$ and $r \approx 18\,mm$ the axial velocity becomes negative due to the existent recirculation zones and thus transfers hot burnt gases back to the nozzle region.

The comparison of both calculations with the experiments leads to interesting observations. Apparently, the turbulent inflow case shows a very good agreement with the measurements for the axial locations from the bluff body until $x = 50\,mm$. Within this upstream region the non-turbulent inflow boundary condition formulation yields too little radial momentum transport and hence too high velocities at the centerline. However, in marked contrast the profiles further downstream at $x = 70\,mm$ and $90\,mm$ depict a different behavior of the calculated results. Here, the turbulent inflow case underestimates the jet velocity, while the non-turbulent one leads to a perfect matching with the experimental data. It also seems, as if within the turbulent inflow simulation the calculated recirculation zone is too short, whereas the non-turbulent inflow condition still results in negative axial velocities for $x = 70\,mm$ like the measurements. A similar behavior of the simulations can be observed in the depicted axial velocity fluctuation profiles. Except for an overestimation at $x = 30\,mm$ the simulation with turbulent inflow yields very good agreement with the experiments until $x = 50\,mm$ while further downstream the fluctuations are underestimated close to the centerline. Again in this region the computation without artificial inflow turbulence shows consistency with the measurements, while that simulation showed neither the correct magnitude nor the right location for the occurring peaks and gradients in the range from the bluff body to $x = 70\,mm$. Furthermore, the fluctuations in the coflow stream are overestimated by both simulations for the locations

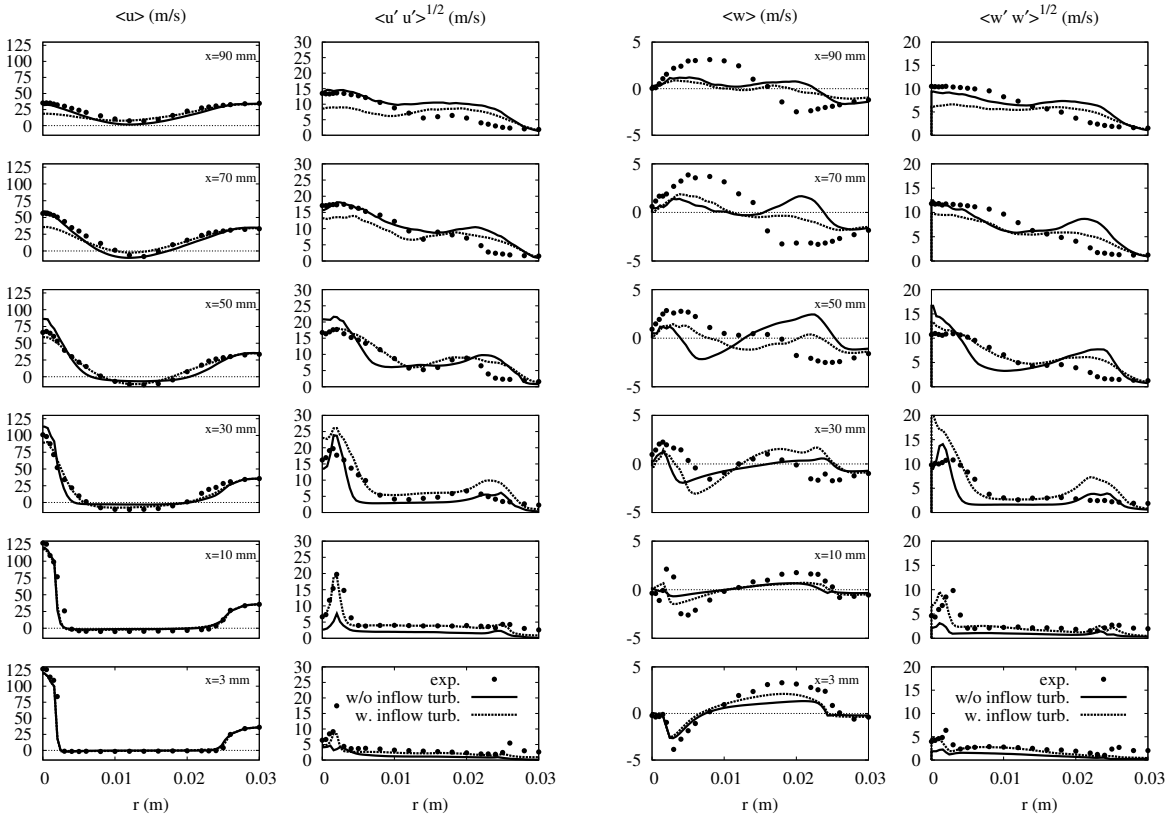

Figure 5.6.: Time averaged radial profiles of the axial (left) and the radial (right) velocity components and their corresponding fluctuations of the reacting Sydney bluff body configuration HM1e for distinct axial locations. Comparison of experimental data (symbols), a simulation without (solid) and with (dotted) artificial inflow turbulence. The horizontal lines in the mean value plots represent zero velocity for a more apparent separation of the recirculation zones.

further afar from the nozzle. The reason for that might be the generation of coherent structures at the edge of the bluff body leading to larger structures instead of small turbulent structures. In order to prevent this phenomenon, artificial turbulent structures could also be superposed on the coflow stream, which was not realized in this work. The impact of the increased fluctuation level in this region of the flow is not severe, which can be seen later in the mixture fraction and temperature profiles.

The right side of figure 5.6 illustrates profiles of the radial velocity component and the fluctuations. This will give insight to the radial motion of the flow and the correlated fuel distribution to the flame front at the outer edge of the bluff body. First of all, a general consideration and interpretation of the radial velocity measurements is performed. At the first axial location the radial separation of the recirculating flow is clearly visible. Starting at the outer radius of the fuel jet, there is a flow towards the centerline, which is part of the inner recirculation zone. Further outwards the radial velocity turns into the positive range, which means the flow is directed to larger radii. This flow provides the comparably rich and hot gases for the stabilization of the flame front. Proceeding to the following axial locations, the widening of the fuel jet represented by the outwards directed velocity and

a continuously decreasing flow towards the centerline is visible. At larger radii starting at $r \approx 15\,mm$, the influence of the outer recirculation zone can be observed. While in the first two axial positions the flow is directed outwards, the orientation turns at $x = 30\,mm$ to a flow directed towards the centerline, which means that the center of rotation of the outer recirculation zone is situated in between $x = 10\,mm$ and $x = 30\,mm$. At the downstream locations also a necking of the flow is given, which is represented by the inwards directed flow.

The analysis of the simulations employing the measurements shows issues of both calculations concerning an adequate prediction of the radial velocity component. Starting from the first location the peak values are underestimated even though the trends are generally captured well. The computation with applied inflow turbulence shows better matching with the reference measurements for the remaining profile locations, while the calculation with time-independent boundary conditions even leads to wrong trends with peaks on the opposite range of values. The fluctuations of the radial velocity obtained by the simulation with inflow turbulence again agree nicely with the experiments for the first four levels, although the centerline value at $x = 30\,mm$ is massively overpredicted, which has also been observed in the isothermal case. In contrast, the alternative calculation with constant velocity boundary conditions in time does not match nor follow the given trends of the measurements but rather calculates the shear layer at a wrong radial position. This is again caused by the prediction of the narrow and deep jet penetration instead of the widening of the jet due to turbulent momentum transport.

The consequences of the velocity field predictions are now evaluated and analyzed based on time averaged radial profiles of the mixture fraction, the dependent scalar temperature and their related fluctuations. Those profiles for different selected axial positions are illustrated in figure 5.7. The radial mean value profiles of the mixture fraction are basically characterized by the penetrating fuel jet, which widens in radial direction while proceeding further downstream. The widening is expressed by a decrease of both, the peak value at the centerline and the radial gradient. Another detail is the slightly increased mixture fraction just above the bluff body surface, which is caused by the recirculating structures and the correlated mixture transport back to the nozzle region. The first axial position at $x = 13\,mm$ depicts very good agreement of both computations with the experiments showing just small deviations, which stands in marked contrast to the remaining axial measured positions. Already the second location at $x = 30\,mm$ unveils the shortcomings of the time independent inflow boundary condition formulation for this case. Due to the lack of additional turbulent fluctuations, the jet penetration depth is overestimated and hence, related through the continuity, the radial widening of the fuel jet is underestimated. A similar behavior has already been observed in the axial velocity profile in figure 5.6. This characteristic is existent for all depicted axial positions except for the last one at $x = 90\,mm$, where the centerline value is eventually matching the experimental data. Nevertheless, the simulation with superposed artificial turbulence on the inflow stream obtains nearly perfect agreement with the measured profiles in terms of the fuel jet penetration depth as well as the widening determined by the magnitudes and the locations of the occurring radial gradients. The only misfit can be seen at the very downstream location, where the position of the gradient is not represented accurately. It is again very interesting to observe this perfect matching of the mixture fraction profiles

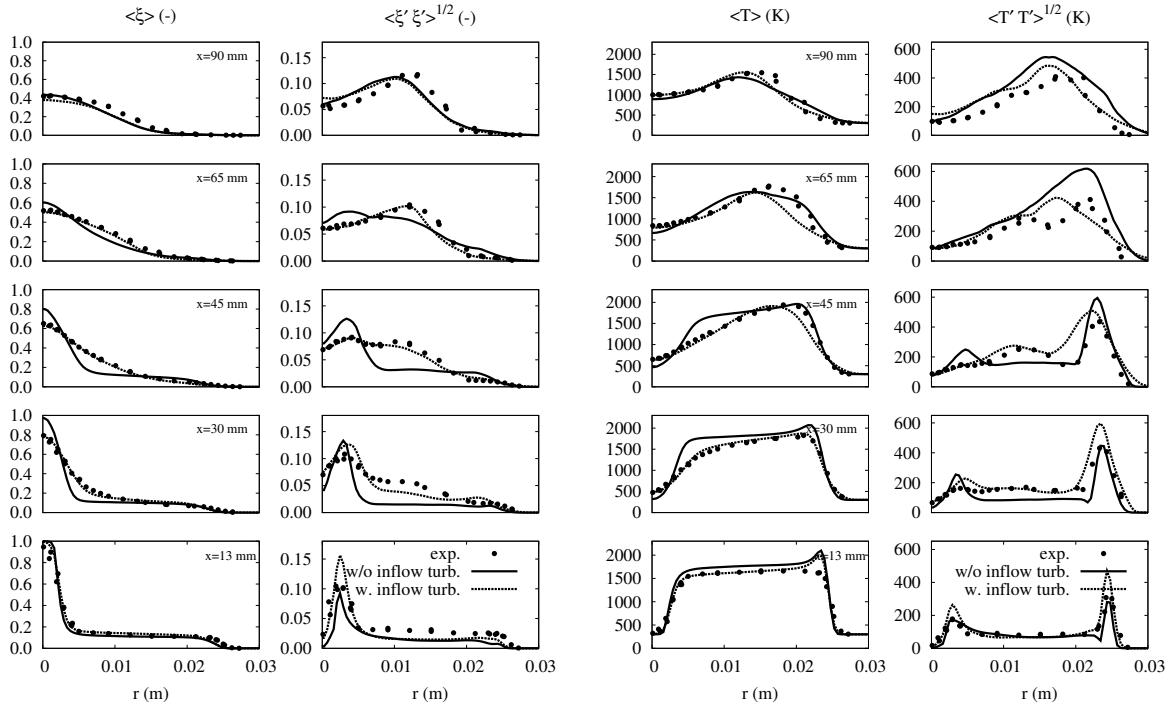

Figure 5.7.: Time averaged radial mixture fraction (left) and temperature (right) profiles and their corresponding fluctuations for selected axial locations of the reacting HM1e configuration. Symbols depict the experiments, the solid line represents the simulation without inflow turbulence and the dotted line shows the computation with an time dependent turbulent inflow boundary condition formulation.

with the experimental data, even though the velocity profiles do not show this accurate predictions especially in the measurement planes further downstream.

Taking a closer look at the mixture fraction fluctuations $\widetilde{\xi'\xi'}^{1/2}$ gives related results to the mean values. The non-turbulent inflow case leads to inadequate predictions of the mixing layers between the jet and the inner recirculation zone, where the fluctuation levels are overpredicted and located at the wrong radial locations. Except for an overestimation of the fluctuations of the inner mixing layer in the first two axial measured positions, the simulation with inflow turbulence yields also promising results not only for the mean mixture fraction values but also for the fluctuations. The interaction of the degenerated outer recirculation zone with the coflow and a related mixing layer creation is almost not visible in the mixture fraction fluctuations, which can be explained by the lack of fuel at this radius range and thus small mixture fraction differences of the two mixing substreams.

A very interesting plot is depicted in figure 5.7, where time averaged radial temperature profiles for selected axial locations are shown. In this performed steady flamelet simulation the temperature represents a scalar depending on the mixture fraction, its sub-filter variance as well as the presumed β-shaped PDF approach. That means, the determination of the temperature distribution includes not only the influence of the transport scheme, but also of the chosen sub-filter variance model and the validity of the assumed β-PDF approach for the representation of the turbulence-chemistry interaction. For this

sensitivity analysis, the impact of the two latter ones is not of current interest, because both of the performed simulations employ the same models for the sub-filter variance and the PDF representation. Analysis concerning these two sub-models are given below in section 5.3.3 and 5.3.4, respectively. At this moment, the focus lies on the occurring differences between the simulated profiles related to the change of the boundary condition formulation. Nevertheless, shortcomings of the used numerical setup compared to the reference measurements can be observed and need to be related to possible infeasibilities of the sub-models.

The measured profiles of the time-averaged temperature mean values show an interesting behavior, which is different from common diffusion jet flames. The recirculation of the hot burnt gas from downstream locations increases the temperature not only at the location of the flame front, but rather in the entire domain. Close to the bluff body surface an uniform temperature profile of $\widetilde{T} \approx 1600\,K$ exists starting from the outer radius of the fuel jet to the outer bluff body edge. This shape changes while proceeding to axial positions further downstream, where the location of the flame front at the bluff body's outer radius increases the temperature and hence builds out a continuously increasing temperature profile from the centerline to the flame front and a sudden drop to the coflow's ambient temperature.

At $x = 13\,mm$ both simulations show an adequate matching with the experiments where the non-turbulent inflow case leads to slightly increased estimations of the high temperature level. An interesting point within this measured plane is the temperature peak at $r \approx 25\,mm$ where the flame front is numerically predicted. The experimental data does not indicate any temperature rise in this region, which can be a sign for a flame lift off from the bluff body's edge. This behavior of the temperature peak in simulations has been observed in many other publications, as in Olbricht [68] and Ihme et al. [34]. Ihme et al. describe a similar phenomenon in the swirling Sydney bluff body configuration and show a decrease of this peak by the inclusion of wall heat losses causing the lift off of the flame. The position at $x = 30\,mm$ depicts immense discrepancies between both variations of the inflow boundary condition. The turbulent inflow case is in perfect agreement with the experiments, while the non-turbulent one overestimates the temperature level over the entire radius. The reason is based on the mixture fraction distribution as illustrated in figure 5.7 (left), where the lack of turbulent motion and hence mixing keeps the mixture fraction almost constant at the stoichiometric value of $\xi_{\mathrm{st}} = 0.05$. At the same time, the mixture fraction has increased in the turbulent inflow case due to the fuel jet widening and decreases the temperature in that region. Interestingly, within the same axial location, the non-turbulent inflow case still shows the temperature peak at the supposed flame front position, while it disappears in the turbulent inflow case. However, a comparison of the mixture fraction profiles does not show any differences at this point. One reasonable explanation for that phenomenon might be the slightly increased mixture fraction fluctuations in this region of the turbulent inflow case, that can have such a decreasing influence on the mean temperature distribution. The next two axial locations at $x = 45\,mm$ and $65\,mm$ provide interesting features of the temperature profiles, showing good matching for the turbulent inflow case within a radius of $r \approx 17\,mm$ from the center axis, while for larger radii the non-turbulent solution yields nice agreement with the measurements. Reasons for that behavior are not obvious, even though at the radial positions

at question in the $x = 45\,mm$ plane small differences in the prediction of the mixture fraction are visible, but would affect the temperature change in the opposite direction. The mixture fraction profile between $18\,mm \leq r \leq 22\,mm$ shows a slight overestimation of the non-turbulent inflow case, which again leads to a larger difference to the stoichiometric mixture fraction. However, in this region, the non-turbulent inflow case obtains higher temperature values as the turbulent inflow case, which is closer to stoichiometry in terms of the existent mixture fraction. For the plane at $x = 65\,mm$, there is no difference in the mean mixture fraction profile apparent, nevertheless the temperature profile for the non-turbulent inflow calculation yields nice matching with the experiments. Interestingly, at the considered location, the temperature fluctuations of the non-turbulent inflow case show a large overestimation, which indicates enhanced differences of the temperature in time and hence are a reason for this pretended temperature profile matching. However, the reason for that seems more like an accumulation of errors and does not indicate a sudden increase of accuracy by the otherwise poorly performing non-turbulent inflow computation.

The general trends of the temperature fluctuations profiles are basically represented by the turbulent inflow case with some overestimation and inaccurate predictions especially at the supposed locations of the flame front. The simulation with non-turbulent inflow conditions indeed obtains some nice agreement with the experiments, but conclusively neglects some features of the profiles and as already mentioned above yields this overprediction of the fluctuations at $x = 45\,mm$ and $x = 65\,mm$.

5.3.1.3. Conclusions

An analysis of the impact of artificial turbulent inflow boundary conditions in the reacting Sydney bluff body configuration HM1e has been performed. Therefore, two variants of the inflow boundary condition formulation have been compared, a simulation with non-turbulent conditions at the inflow boundary and one with superposed artificially generated turbulent structures. The comparison has been made employing qualitative results in terms of time averaged streamline and mixture fraction field plots as well as quantitative results including time averaged radial profiles of the axial and radial velocity components, mixture fraction, temperature and their corresponding fluctuations. The analysis of the radial profiles has been accomplished at selected axial locations throughout the computational domain. A reference for the validation is represented by experimentally obtained profiles of the considered quantities, which are used to evaluate the quality and accuracy of the performed simulations.

Already the qualitative streamline and mixture fraction field plots unveiled major differences between both simulations in terms of the positions and interaction of both existing recirculation zones and hence the distribution of fuel mixture in the computational domain. Thereby, general differences to the non-reacting case B4C2 analyzed in section 5.2 have also been found, which are especially caused by the higher inflow velocities but also by the combustion immanent phenomena like density gradients and heat release of the reacting case HM1e. The distinctions between both variations in the inflow boundary condition formulation have as well been reflected in the quantitative comparison of the radial profiles. Here, the turbulent inflow case has virtually obtained perfect agreement in all quantities with the measured reference profiles, while the non-turbulent inflow case has

shown too few turbulent transport of momentum and mixture fraction, which has in turn led to a too deep penetration and a too small widening of the central fuel jet. Additionally, radial profiles of the dependent scalar temperature have been compared with each other and the measured equivalent. Even this comparison has indicated promising results of the turbulent inflow case, while the results of the simulation employing the non-turbulent inflow boundary condition have not convinced in terms of accurate predictions. However, some differences in the simulation results prompt questions that cannot be answered by the performed analysis, but need further investigations concerning sub-models like the sub-filter variance model or the turbulence-chemistry interaction in general.

A very interesting fact of the analysis performed so far in terms of the application of the artificial inflow turbulence generator is the different behavior between the non-reacting case B4C2 and the reacting configuration HM1e, even though a similar jet Reynolds number of $\mathrm{Re}_{\mathrm{jet}} \approx 16000$ is existent. The conclusion of the non-reacting case clearly tend to prefer the non-turbulent inflow formulation, while the reacting case shows almost perfect matching with the experiments employing the turbulent inflow formulation. This might be reasoned by the increased inflow velocities in fuel jet and coflow in the reacting case as well as the influence of reaction like density gradients and heat release. Nevertheless, for the following investigations concerning the reacting configuration HM1e the turbulent inflow boundary condition formulation is chosen and will be kept unchanged in order to have adequate comparability between the presented simulations.

5.3.2. Sensitivity of the Particle Density on the Transported Monte Carlo PDF Method

In the following section, a sensitivity analysis in terms of the particle density in the context of the Eulerian Monte Carlo PDF transport is performed. Therefore, the HM1e configuration is simulated with a hybrid approach, calculating the velocity field as in the investigation before using a steady flamelet chemistry representation. Additionally, an Eulerian Monte Carlo PDF transport of the filtered mixture fraction is made as depicted in figure 5.8. The figure shows a flowchart of the applied numerical procedure, where all illustrated quantities are assumed to be filtered values. The center of the chart is represented by the LES flow solver, while the left branch stands for the steady flamelet chemistry LES as already applied for the simulation investigation above. The right branch of this flowchart embodies the Eulerian Monte Carlo PDF procedure using a steady flamelet chemistry representation.

Starting from the LES flow solver the three velocities $\tilde{u}$, $\tilde{v}$, $\tilde{w}$, the density $\bar{\rho}$ and the viscosity $\tilde{\nu}$ are passed to the scalar transport schemes. Here, the transport equation for the mixture fraction $\tilde{\xi}$ is solved with the different approaches, finite volume on the left and Monte Carlo PDF on the right. While in the finite volume context the filtered value of the mixture fraction and the modeled sub-filter mixture fraction variance enter the β-integrated flamelet table, in the MCPDF context the non-preintegrated flamelet table is entered with every particle value. From the chemistry tables, the thermo-chemical state is read out and is available for the LES calculation of the following time step. It is clearly pointed out, that in the following section, there is no feedback of the density and viscosity from the MCPDF method to the LES flow solver. That means, the velocity

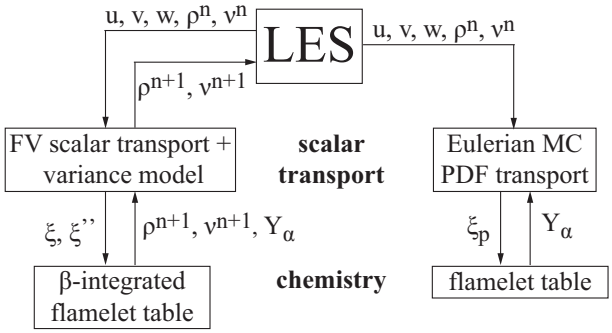

Figure 5.8.: Procedure of the hybrid LES/transported PDF scheme. All variables and quantities depicted are assumed to be filtered values.

fields are still computed based on the finite volume context and the Monte Carlo mixture fraction transport is only performed in a postprocessing step without any impact on the velocities. In this framework, the sensitivity of the Monte Carlo PDF transport of the mixture fraction is investigated in terms of the used particle density (Eulerian stochastic particles per control volume). As given in equation (3.33) the statistical error is inversely proportional to the square root of the particle density N in every control volume. This dependency has already been investigated and published several times, e.g. [13], but in the present work, the sensitivity analysis is performed in order to estimate a sufficient number of particles to reach satisfying results.

5.3.2.1. Numerical Setup

The numerical setup of the finite volume procedure is kept unchanged compared to the analysis in terms of the sensitivity on the inflow boundary condition. The computational grid has again $1.2 \cdot 10^6$ control volumes in total and as mentioned above, the inflow turbulence generator is applied, providing turbulent inflow boundary conditions. In the context of the Eulerian Monte Carlo PDF transport the quasi second order accurate transport scheme is used and the IEM micromixing model is employed. The used flamelet chemistry table is resolved by 282 equidistantly distributed sampling points in the mixture fraction space. For the sensitivity on the number of particles, simulations with three different particle densities are performed: $N = 20, 50, 100$ ppc, leading to a total number of particles in the domain of $24 \cdot 10^6$, $60 \cdot 10^6$ and $120 \cdot 10^6$, respectively.

5.3.2.2. Results

The presented results investigating the statistical error of the Monte Carlo approach are showing radial profiles of mixture fraction, temperature, the OH mass fraction and their corresponding fluctuations in time. The OH mass fraction is like the temperature a scalar directly dependent on the mixture fraction and the sub-filter PDF and is additionally an indicator for the flame front due to its character of being an intermediate species. As shown in the general description of non-premixed flames (see figure 2.3), intermediate species show a peak within the flame front and hence can be used as a flame front marker.

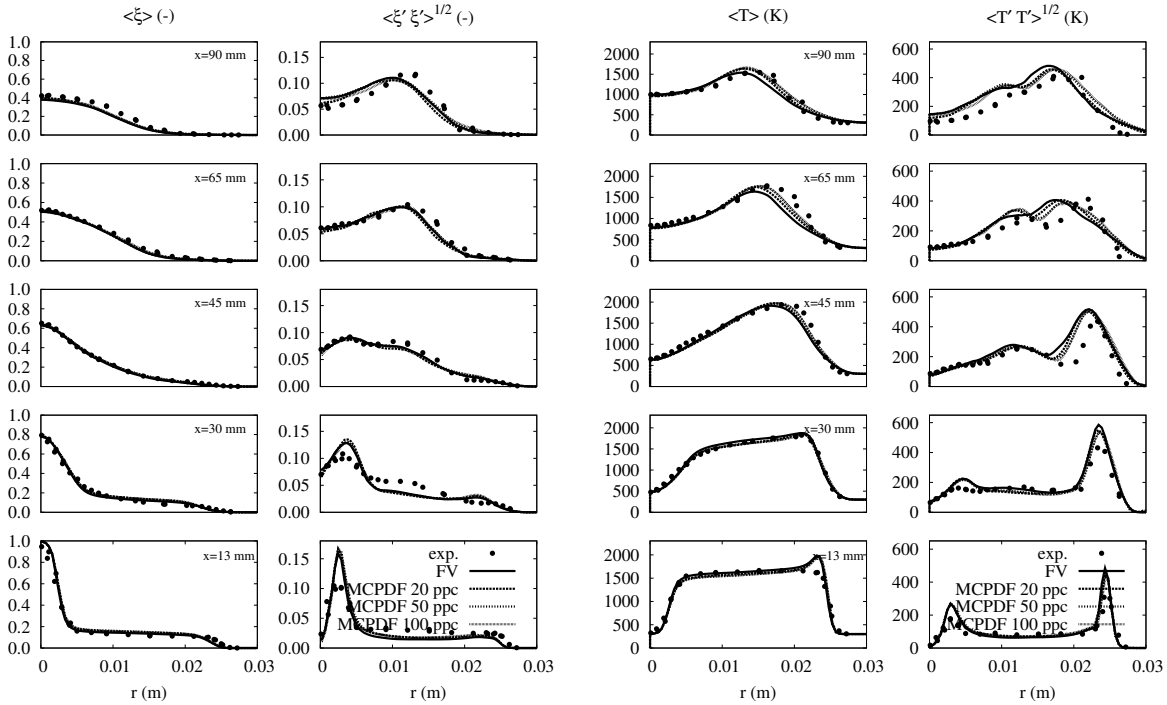

Figure 5.9.: Radial profiles of the time averaged mixture fraction (left), the temperature (right) and their corresponding fluctuations for selected axial locations of the reacting HM1e configuration. Symbols depict the experiments, the solid line represents the finite volume simulation, while all other lines show Monte Carlo PDF solutions for the different particle densities $N = 20$ (dashed), 50 (dotted) and 100 ppc (fine dotted).

Figure 5.9 depicts the mixture fraction (left) and the temperature profiles (right) for five axial locations of the non-premixed turbulent flame configuration HM1e. In addition, the fluctuations in time for the three quantities are illustrated just beside the corresponding mean values. Besides the experimental data (symbols) and the already interpreted finite volume (solid) profiles, the results for the three continuously increased particle densities $N = 20$ (dashed), 50 (dotted) and 100 ppc (fine dotted) are given in the plots. The mean mixture fraction profiles and its fluctuation do not show any differences in between the performed simulations at all. The general accuracy referenced on the measured data points is as high as it is described in the previous section. One can see, that the statistical error has no influence on the transported mixture fraction profiles as it is expected after evaluating the generic test case in section 4.1. In the test case the mixture fraction profiles have been transported consistently without any major differences, which is again validated with the shown time averaged profiles of the mixture fraction. More interesting is the analysis of the dependent scalar profiles temperature $\widetilde{T}$ (see figure 5.9 (right)) and OH mass fraction $\widetilde{Y}_{OH}$ (figure 5.10). The major differences between the calculations in the mean temperature profiles are mainly concentrated on the three axial positions $x = 45$, 65 and $90\,mm$, where large discrepancies to the experiments have been observed in the previous section. An interesting aspect in these three radial planes is the fact that all Monte Carlo PDF simulations obtain better results compared with the experiments than

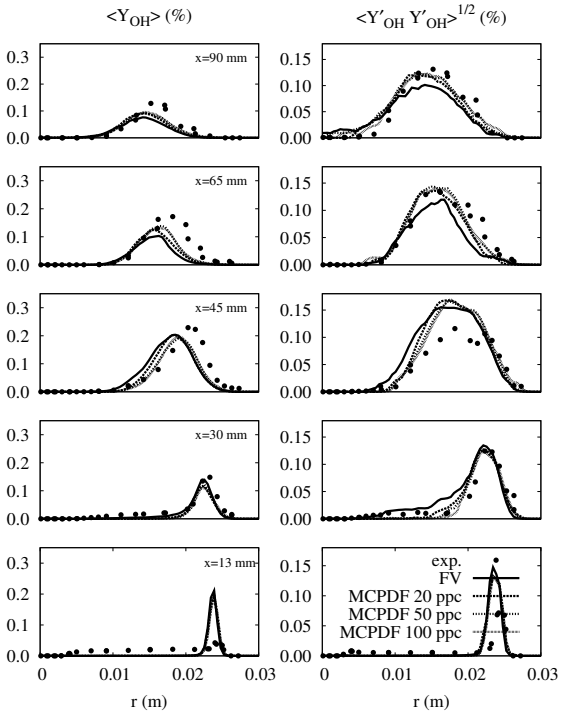

Figure 5.10.: Radial hydroxyl profiles (left) and its corresponding fluctuations (right) for selected axial locations of the reacting HM1e configuration. Symbols depict the experiments, the solid line represents the simulation without inflow turbulence and the dotted line shows the computation with inflow turbulence.

the finite volume computation. It is especially surprising even though the mixture fraction profiles are all congruent and hence have no effect on the temperature profiles. Apparently, the increase of accuracy must be reasoned with an effect of the sub-filter PDF modeling approaches. That means, the combination of the applied sub-filter variance model with the presumed β-PDF approach used in the finite volume context has shortcomings in at least one or both sub-models. However, this question needs to be considered later, since the focus of this section is laid on the statistical error of the Monte Carlo method. In order to evaluate this feature, the differences between the three MCPDF simulations have to be analyzed. In each of the profiles showing differences in the temperatures, the impact of the particle density is clearly visible. The simulation with the lowest particle density of $N = 20$ ppc always shows a trend, which is slightly better than the finite volume calculation and hence closer to the reference measurements. Nevertheless, there is still an expected difference to the computations with $N = 50$ and 100 ppc, where the lines coincide and additionally show even better agreement with the experiments. These results confirm the theory described by equation (3.33) and also show that the increase of accuracy between 50 and 100 particles per control volume is negligible in this case. The same trend can be observed in the profiles of the temperature fluctuations, where the MCPDF simulations obtain results closer to the measured profiles than the finite volume computations. Furthermore, the dependency on the particle density can also be seen by the differences between the three MCPDF simulations.

These observations are even more apparent in the radial profiles of the OH mass fractions $\widetilde{Y}_{OH}$ in figure 5.10. The general appearance of the OH mass fraction distribution is characterized by a single peak at the supposed flame front in every axial location, which is shifted to the centerline while proceeding further downstream. The position at $x = 13\,mm$ confirms the suspicion of a lifted flame in the experiment, since the peak value is negligibly small, which indicates the absence of the flame front in this plane. In contrast, all simulations predict a peak at the radial position of the outer bluff body edge, which is directly correlated to a flame front at this point. At the last three axial measurement planes at $x = 45$, 65 and $90\,mm$, the differences between the simulations are clearly visible. Even though the peak values of all simulations are underestimated compared to the experiments, the location of the flame front and the gradients are captured comparably well. Especially, the MCPDF calculations with 50 and 100 ppc show nice results regarding the positions of the radial gradients, where the computation with only 20 ppc does not obtain comparable solutions. A similar characteristic is existent in the radial profiles of the Y_{OH} fluctuations, where the MCPDF simulations in general reach better agreement with the experiments and additionally show the known dependency on the particle density.

In order to quantify the sensitivity on the particle density N, a detailed analysis of the simulation is performed. Therefore, the relative error ε at four different points in the domain is calculated for the three particle densities. The relative error is calculated as

$$\varepsilon = \frac{|\phi_{\text{sim}} - \phi_{\text{exp}}|}{\phi_{\text{exp}}} \tag{5.1}$$

where ϕ stands for an arbitrary scalar from either the simulation or the experiments. For the investigation, two data points are evaluated for the temperature $\widetilde{T}$ and two for the hydroxyl-radical's mass fraction $\widetilde{Y}_{OH}$. The results are depicted in figure 5.11, where the relative error is plotted against the particle density of $N = 20$, 50, 100 ppc. The four lines represent the four monitoring points for the error analysis, which are chosen depending on their appearance in the radial profiles. The positions are taken from the planes of $x = 45$ and $65\,mm$, where the differences of the profiles are clearly visible. These are for the temperature $x = 45\,mm$, $r = 20.3\,mm$ and $x = 65\,mm$, $r = 18.2\,mm$ and for the mass fraction of the OH radical $x = 45\,mm$, $r = 16.2\,mm$ and $x = 65\,mm$, $r = 18.2\,mm$. Additionally to these data point evaluations, $1/\sqrt{N}$ is plotted in the diagram, which indicates the behavior of the statistical error depending on the particle density. It should be mentioned that the calculated relative errors do not represent the pure statistical error, but rather depict a sum of all occurring errors of the simulations as well as the experiments. That means, the theoretical behavior of $\varepsilon \sim 1/\sqrt{N}$ will neither be expected nor be reached with this analysis. However, figure 5.11 depicts the trend of the relative error correlated to the particle density, which somehow shows a dependency on the number of particles per cell. Even though, the theoretical characteristic is not reached because of the mentioned reasons, the investigation yields a decrease of the relative error, that in parts consists of the statistical error. Starting from the simulation with $N = 20$ ppc, the error is approximately reduced according to $\sim 1/\sqrt{N}$, while increasing the particle ensemble to 50 ppc. Nevertheless, by another duplication of the amount of particles, the error is not decreased to an eighth as expected, but a value larger than that. This means, the additional computational effort for duplicating the number of particles from 50 to 100 is not comparable to the benefit which is obtained in the increased accuracy. Because of

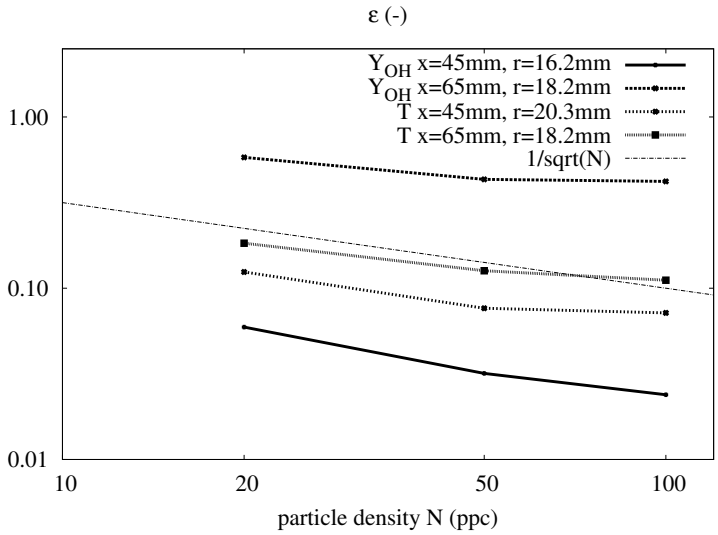

Figure 5.11.: Dependency of the relative error ε on the particle density N. The relative error is assessed at four different positions in the flow domain, two by considering the temperature and two by the OH mass fraction. The lines depict the characteristic of the error evaluated by three simulations with $N = 20$, 50 and 100 ppc. Additionally, the theoretical dependency is represented by the graph representing the relation $\varepsilon \sim 1/\sqrt{N}$.

that, the following investigations are performed with a particle density of $N = 50$ ppc in order to provide an adequate accuracy of the simulations with acceptable numerical costs.

5.3.2.3. Conclusions

The sensitivity of the implemented Eulerian MCPDF method is analyzed by simulations of the reactive Sydney bluff body configuration with varying particle densities of $N = 20$, 50 and 100 ppc. Therefore, the Monte Carlo solver for the PDF transport is used in postprocessing mode, which means that there is no feedback in terms of density or viscosity values to the LES flow solver. Based on this, the velocity field is not changed in comparison with the finite volume results obtained in the previous section. The interesting quantities are hence reduced to the transported mixture fraction and the dependent thermo-chemical scalars, like temperature and OH mass fraction. On the basis of time averaged radial profiles of the mentioned scalars and the corresponding measurements, the influence of the ensemble magnitude on the method's accuracy is investigated. Even though, the mixture fraction profiles of all simulations are consistent with each other the obtained results of the temperature and the OH mass fraction show in parts more accurate estimations than the related finite volume simulations. In addition, a dependency on the particle density can be observed as expected, but cannot be quantified. Hence, a comparison of the relative error between the MCPDF simulations and the experiments is performed in four different positions of the configuration. The discrepancies with the theoretical characteristic behavior of the statistical error lead to the conclusion, that a particle ensemble of 50 ppc is a reasonable compromise between the computational costs and the provided accuracy. For all following simulations and analyses this ensemble magnitude is used,

with the knowledge of an adequately performed assessment of the statistical error.

5.3.3. Investigation of the applied Sub-filter Variance Model for the Mixture Fraction employing the Eulerian Monte Carlo PDF Method

The idea behind the following investigation is based on the findings made in the previous sections. Especially the analysis on the particle density sensitivity in the context of the Eulerian Monte Carlo PDF method showed some advantages of this statistical approach compared to the finite volume discretization scheme. The comparison of the radial profiles of the time averaged temperature $\widetilde{T}$ and the OH mass fraction $\widetilde{Y}_{OH}$ unveiled certain positions in the considered flame configuration, where the MCPDF method obviously obtained better agreement with the measurements and hence most probably more accurate estimations of the real physical and chemical phenomena. The reasons for these differences between the discretization method now have to be analyzed in detail. As depicted in figure 5.9 the time averaged mixture fraction profiles do not illustrate any discrepancies between the MCPDF simulations among themselves nor with the obtained finite volume solution. In addition, the one-dimensional pure mixing test case showed a nearly perfect consistency of the transported mixture fraction profile for each time step. The reasons for the increased accuracy of the MCPDF calculations need to be found elsewhere. Figure 5.8 gives information about the subsequent steps behind the mixture fraction transport until the thermo-chemical state is known. In the case of the finite volume discretization, this is the sub-filter variance model, as introduced in section 3.3 and the implicitly performed calculation of the presumed β-shaped PDF. In this section, the influence of the implemented sub-filter variance model for the mixture fraction is analyzed by using the MCPDF method for reference.

5.3.3.1. Results

The influence of the used scale-similarity mixture fraction sub-filter variance respectively the unmixedness model is analyzed employing time averaged data profiles. Therefore, the already shown mean values of the time averaged temperature and the hydroxyl radical profiles of the finite volume simulation (solid line) and the MCPDF (dashed line) with $N = 50$ ppc are depicted in figure 5.12, showing the temperature on the left and the OH mass fraction on the right. The figure also includes the measurements for reference and gives additional information about the sub-filter variance of the mixture fraction. The idea is to illustrate supposed correlations between the discrepancies in the temperature and the $\widetilde{Y}_{OH}$ results and the time averaged unmixedness profiles. In case of shortcomings of the scale-similarity sub-filter variance model being responsible for the described inaccuracies of the finite volume computations, a distinct correlation between the evaluated quantities must be visible. The sub-filter variance of the mixture fraction indicates the variations from the spatial mean mixture fraction within a control volume and hence influences the chemistry strongly. Generally it can be said, the higher the value of the unmixedness, the larger the decrease of the dependent scalar value compared to the solution obtained with the identical mean value but without sub-filter variance is. The application of the Monte-

Carlo PDF method now allows an analysis of the sub-filter variance, due to the fact that the unmixedness is a quantity which is implicitly obtained by the MCPDF procedure and is mainly affected by the choice of the used micro-mixing model. However, since previous works [6], [5] showed a weak effect of the micro-mixing model on the results in the context of Large Eddy Simulations, the MCPDF solutions for unmixedness can be used for reference purposes.

Taking a closer look at the time averaged sub-filter variance profiles of the mixture fraction at the temperature plot on the left gives interesting information about the correlation. Close to the bluff body surface, at $x = 13$ and $30\,mm$ the profiles of unmixedness depict the two created mixing layers, at the outer radius of the fuel jet and at the outer edge of the bluff body. At the inner mixing layer, the fuel jet with a mixture fraction of unity interacts with the recirculated lean mixture and hence produces the large values of the unmixedness. In contrast, it is apparent, that the outer mixing layer does not show such high variance values, because this mixing layer is generated by the interaction between the very lean recirculated mixture with the coflow of a mixture fraction value zero. Both sub-filter variance profiles indicate the two mixing layers, but with different magnitudes of the peaks. In the inner mixing layer, the Monte Carlo PDF method leads to four times higher values than the scale similarity model employed in the finite volume simulation. At the outer mixing layer both solutions describe the unmixedness similarly, without larger discrepancies. Even though large unmixedness differences in the rich region in terms of the mixture fraction are obvious, the non-existence of major differences in the temperature profiles shows the lack of influence of the sub-filter variance in these regions. The positions further downstream depict an interesting feature: within the inner mixing layer, the scale-similarity model always underestimates the unmixedness, while in the outer one, it is overpredicted compared to the MCPDF profiles. This is in fact very interesting because the outer mixing layer includes the location of the flame front and additionally shows the considered positions of differences between the results obtained by the finite volume and MCPDF method. The behavior of the sub-filter variance profiles corresponds to the temperature discrepancies in the measured planes $x = 45$, 65 and $90\,mm$, because as mentioned before, an increased unmixedness leads to a lower temperature by keeping the mean mixture fraction constant. However, it seems as if the locations of the temperature differences are not perfectly matched with the unmixedness discrepancies, which is very obvious at the axial location of $x = 65\,mm$. The peak of the sub-filter variance has its maximum value at approximately $r \approx 12.5\,mm$ and ranges from $7.5\,mm \leq r \leq 17.5\,mm$, while the difference of the temperature profiles starts at $r \approx 12.5$ and lasts till $r \approx 25\,mm$. An analog characteristic can also be observed at the subsequent downstream position, which means, the unmixedness model cannot be the only reason for the distinctions of the finite volume approach and the Monte Carlo PDF simulation. The same analysis is made with the OH mass fraction profiles instead of the temperature profiles. In these profiles differences between both simulation approaches are rather located on the rich side of the flame front than on the lean as occurring in the temperature results. The correlation of the variations in the OH mass fraction profiles with the unmixedness discrepancies are obvious for the axial planes at $x = 65$ and $90\,mm$. The better agreement of the discrepancy positions can be explained as mentioned before, that the differences in the OH radical predictions are shifted to the rich rather than the lean side of the flame,

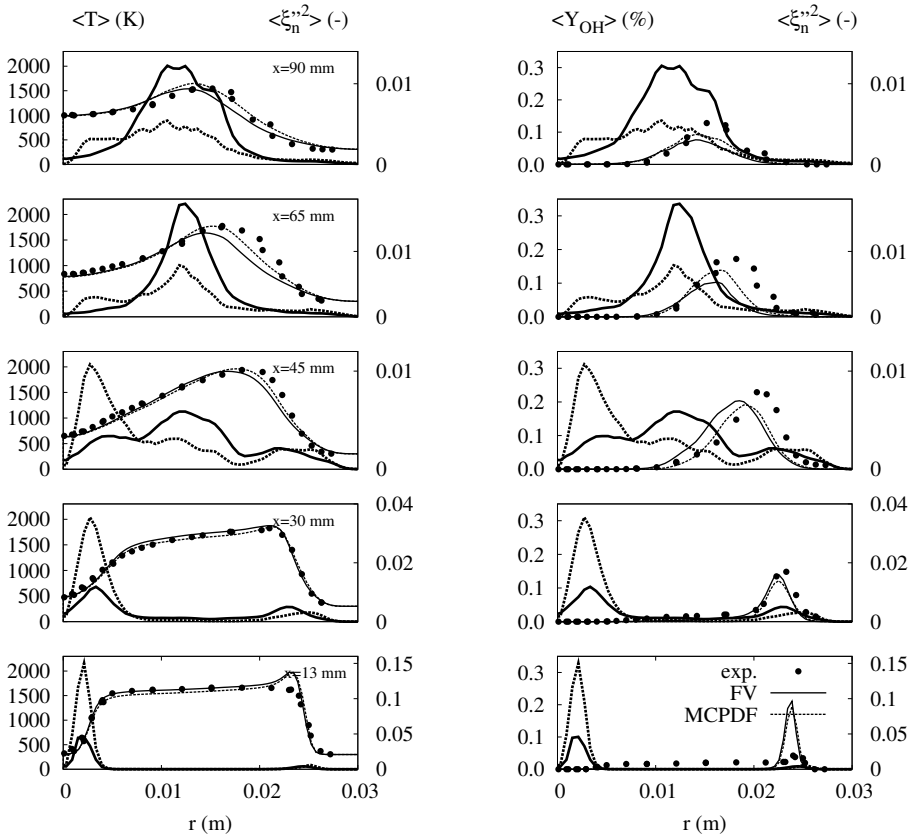

Figure 5.12.: Radial profiles of the time averaged sub-filter variance of the mixture fraction correlated with the temperature (left) and the OH mass fraction (right) profiles. The solid lines depict the finite volume results, while the dashed line stands for the Monte Carlo PDF solutions.

which corresponds nicely to the unmixedness profiles. However, at $x = 45\,mm$ an opposite behavior can be observed. Here, the finite volume simulation overestimates the OH mass fractions on the rich side of the flame, while the MCPDF computation fits the gradient of the experiments nicely. Surprisingly, the mixture fraction sub-filter variance within the FV context is larger than the MCPDF obtained value in this region. From the theoretical point of view it does not make sense that the unmixedness value is exceeded and in addition the hydroxyl radical mass fraction in this area, too. Hence this must be reasoned in another way, like frictions in the averaging process or maybe very small deviations in the mixture fraction mean value, which superposes the impact of the sub-filter variance.

A different approach to investigate the impact of the unmixedness in the given context is the evaluation of so called scatter plots. In contrast to the time averaged profile plots, this kind of diagram depicts a multitude of specific events in a conditional framework. Therefore, results of different axial planes are plotted pairwise in dependency to each other, which leads to a point cloud illustrating the probability of the single events qualitatively. In the present work, scatter plots are shown for the correlations of the mixture fraction with the two dependent scalars temperature and OH mass fraction. Figure 5.13 represents the temperature distribution over the mixture fraction for the five already known axial

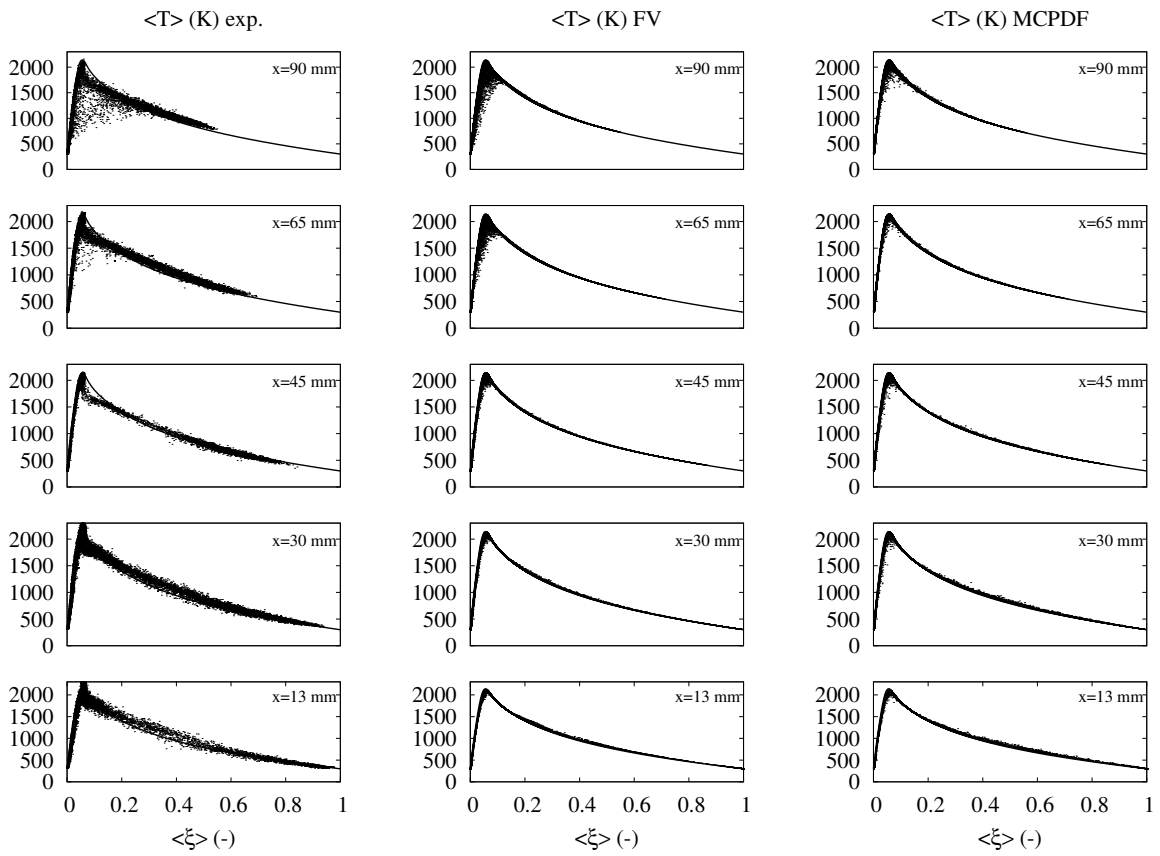

Figure 5.13.: Scatter plots of the filtered temperature versus the filtered mixture fraction for the measured axial positions $x = 13$, 30, 45, 65, 90 mm. The columns depict the experiments on the left, the finite volume simulation results in the center and the Monte Carlo PDF solutions on the right. In addition, the flamelet solution for a strain rate of $a = 10s^{-1}$ is shown as a reference in each plot. The shown variations are solely caused by the influence of the mixture fraction sub-filter variance.

positions $x = 13$, 30, 45, 65 and 90 mm for the experiments (left), the finite volume simulation (center) and the Monte Carlo PDF method (right). For reasons of clarity, the solution of the applied flamelet chemistry with the strain rate of $a = 10\,s^{-1}$ is given additionally. In the context of these scatter plots, it is essential to keep in mind that the flamelet tables used for the chemistry representation are composed from only a single strain rate. That means, all occurring deviations from the flamelet curve in the simulations are solely caused by the influence of the mixture fraction sub-filter variance, whereas the experiments show all possible effects, from strain rate and unmixedness influences right up to local extinction phenomena. An interesting aspect of the given scatter plots is the already observed dependency of the temperature at the lean and the OH mass fraction profiles at the rich side of the flame front, which can be easily analyzed employing these kind of diagrams.

For the investigation, the plots are subsequently analyzed starting with the first axial position at $x = 13\,mm$ and proceeding further downstream. It is apparent that the experiments on the left show more scatter around the flamelet solution than both of the

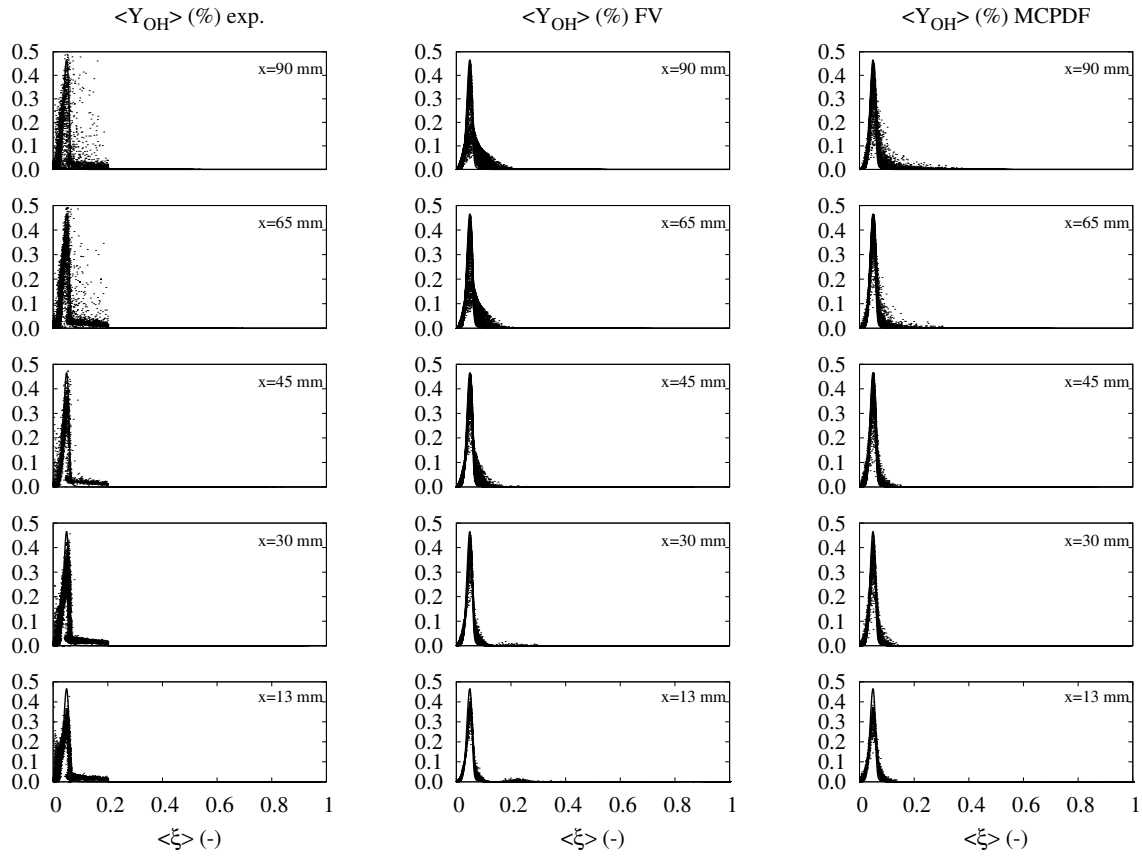

Figure 5.14.: Scatter plots of the filtered OH mass fractions versus the filtered mixture fraction for the measured axial positions $x = 13$, 30, 45, 65, 90 mm. The columns depict the experiments on the left, the finite volume simulation results in the center and the Monte Carlo PDF solutions on the right. In addition, the flamelet solution for a strain rate of $a = 10s^{-1}$ is shown as a reference in each plot. The shown variations are solely caused by sub-filter variance influence of the mixture fraction.

simulations due to the described reasons like strain rate effects. The scatter is mainly concentrated on the region around the stoichiometric mixture fraction and shows increased temperature values for the rich branch of the flame. In contrast, the simulations do almost not give any scattering in the entire mixture fraction space except for slight variations at the stoichiometric point. However, even though only very low scattering of the temperature is visible in the simulations between $0.3 \leq \tilde{\xi} \leq 0.5$, it is very interesting to observe temperatures exceeding the flamelet solution, which is actually the upper limit of the simulations. The appearance of the slightly increased values in this region cannot be based on pure sub-filter variance effects, but on mixing processes. For example, the mixing of a point next to stoichiometry with a point in the rich branch leads to a mixing hyperbola, which lies above the flamelet solution. For the following axial planes, the influence of the unmixedness in the computations is negligible till the position of $x = 45\,mm$. The measurements at $x = 30$ and $45\,mm$ are primarily governed by high variations at stoichiometry and the adjacent rich branch, leading to lowered temperature values in this range. This effect is most probably related to high scalar dissipation and hence high

strain rates in the highly turbulent shear layer of the fuel jet and the recirculating hot gas. The scatter plots at $x = 65$ and $90\,mm$ now reflect the observations made in the comparison between the radial temperature and the unmixedness profiles. The increased mixture fraction sub-filter variance in the FV simulation around stoichiometry decreases the temperature and leads to the differences between both numerical methods. However, qualitatively it looks as if the scattering of the finite volume simulation matches the experiments better than the MCPDF approach, even though the time averaged radial plots show a definitely better agreement of the statistical method with the measurements.

The scatter plots of the OH mass fraction, as depicted in figure 5.14 also confirm the observed characteristics of the radial mean profiles from figure 5.12. In general, the behavior of the hydroxyl radical conditioned on the mixture fraction shows only a small band of created OH in the $\widetilde{\xi}$-space. This narrow peak represents the flame front of the applied fuel composition, which is situated around the stoichiometric mixture fraction value. The most obvious features of this OH scatter plot analysis are the differences in the rich branch of the peak at $0.75 \leq \widetilde{\xi} \leq 0.2$. It is apparent that the finite volume simulation significantly overestimates the scatter at this position and shows the same mixture phenomenon as seen in the temperature scatter plots. This characteristic behavior again affects the simulated OH mass fraction results to exceed the actual upper limit of the flamelet solution clearly and the effect is even larger than in the temperature scatters, related to the larger gradient $|\partial\widetilde{Y}_{OH}/\partial\widetilde{\xi}|$. This overshoot beyond the flamelet solution in turn causes the overestimation of $\widetilde{Y}_{OH}$ in the fuel rich part of the flame front, as depicted in figure 5.12 (right). However, the results obtained by the Monte Carlo simulation depict a nicer agreement with the experiments, where no distinct concentration of the point cloud is visible.

5.3.3.2. Conclusions

An analysis regarding the influence of the mixture fraction sub-filter variance in the context of the reacting Sydney bluff body configuration HM1e is performed. Therefore, both flamelet chemistry based finite volume and Eulerian Monte Carlo PDF approach are compared in terms of the applied mixture fraction sub-filter model. In the FV context the unmixedness is modeled employing a scale-similarity approach, while in the Monte Carlo PDF context this quantity is implicitly included within the particle ensemble information. The investigation is firstly based on time averaged radial profiles of the unmixedness which are correlated to the calculated differences in the radial profiles of the temperature as well as of the OH mass fraction as presented in the previous section. In the temperature profiles, the differences in the temperature are not completely correlated based on the radial position, but the variations of the temperature are rather shifted to the lean side of the flame front. In contrast, the OH mass fraction profiles show a nice spatial correlation between the discrepancies of the modeled variances and the differences within the OH profiles. Secondly, additional to the time averaged results, scatter plots of $\widetilde{T}$ and $\widetilde{Y}_{OH}$ conditioned on the mixture fraction are given and analyzed. In this representation of the data, the same observations are made: the temperature differences between both simulation types are shifted to the lean branch of the flame and hence are not strongly correlated to the unmixedness. On the other side, the OH distributions lead to opposite results, showing the scatter concentrated at the rich branch of the flame front, which

is definitely correlated to the discrepancies in the models of the mixture fraction sub-filter variance. This investigation gives at least an explanation of the differences and the behavior of the OH mass fraction profiles, while the temperature differences in the time averaged results cannot be described by the unmixedness modeling. Nevertheless, it would be interesting to see the performance of alternative unmixedness models in this context.

5.3.4. Capability of the Presumed β-shaped PDF Approach for the Mixture Fraction

The investigation of the sub-filter variance influence on the results of the reacting Sydney bluff body configuration HM1e already documented revealing information about the differences between the finite volume simulation and the Monte Carlo PDF approach. For the radial OH mass fraction profiles the impact of the applied scale-similarity model for the unmixedness modeling in the finite volume context has been proved and additionally showed the shortcomings of this model in reference to the implicit MCPDF unmixedness modeling. Even so, the temperature variations between both simulation approaches has not yet been completely explained by the sub-filter modeling, which brings up the question for other reasons. As mentioned previously, one possible explanation could be an inappropriate presumption of the sub-grid PDF shape. In the used LES code FLOWSI the most common model of a presumed β-shaped PDF for the mixture fraction is applied and will be analyzed in the following section. Therefore, the Monte Carlo PDF approach is employed in order to generate reference data for the actual shape of instantaneous mixture fraction PDF.

5.3.4.1. Results

The following analysis is based on instantaneous data obtained by the implemented MCPDF transport scheme. The focus of this section is to prove the capability of the used presumed β-shaped PDF for the sub-grid mixture fraction PDF. Therefore, real instantaneous sub-grid PDF data from the MCPDF simulation of the HM1e configuration are compared to the corresponding presumed β-shape PDF data, which are based on the identical filtered mean and sub-grid variance values of the mixture fraction provided by the MCPDF transport scheme. This analysis allows for a qualitative comparison of the obtained mixture fraction sub-filter PDF.

Figure 5.15 depicts sub-filter PDF of the mixture fraction for selected monitoring points out of the computational domain of the HM1e configuration. The plot is structured into three columns, representing the axial positions $x = 45$ (left), 65 (center) and $90\,mm$ (right), with five radial position in each case, which are located around the stoichiometric mixture fraction and hence the flame front. The radial positions are arranged with increasing radii from the bottom to the top. Each plot consists of two subplots: the lower one depicting the mixture fraction values of the ensemble with a particle density of $N = 50$, where each line represents a single particle and the upper one showing reconstructed sub-filter PDF for the given particle ensemble. The step function represented by the solid line is the reconstructed Monte Carlo PDF shape, while the dashed line depicts the corresponding β-function (see equation (2.76)). While analyzing this plot, one should keep in mind the goal of this section, which is to identify shortcomings of the presumed

β-PDF approach. Therefore, comparisons are made at selected points, where differences between the finite volume approach and the Monte Carlo PDF method in terms of the temperature were observed before. For the left column, at $x = 45\,mm$, the radial positions are at $r = 22.1$, 22.5, 23.0, 23.4 and $23.9\,mm$, which are situated relatively close to the outer bluff body edge. The ensembles show very low variances around the average value leading to very narrow peaks in the reconstructed PDF shapes. The variance increases for larger radii related to the existing shear and mixing layer close to the outer radius of the bluff body. Obvious differences can be seen in the peak values of the MCPDF reconstructions, which correspond to the discrete representation and the chosen bin width in mixture fraction space. This is directly related to the peak values by the necessity of

$$\int_{\xi=0}^{1} \mathcal{P}(\xi')\, d\xi' = 1, \tag{5.2}$$

which needs to be fulfilled. Besides this negligible phenomenon resulting from the reconstruction procedure, further differences in the PDF shapes can be observed. Especially with increasing radii, the representation of the β-PDF diverges from the Monte Carlo PDF, even though the same mean values and variances are provided. The most significant variations between the two PDF representations are given at the largest radius in this axial position at $r = 23.9\,mm$. In this point, the β-function predicts a large probability density at pure air of $\xi = 0$, although the particle ensemble and consequently the MCPDF does not show any pure air amount. These differences can tremendously affect the dependent scalars like the temperature towards lower mean values in this position, which has in fact happened as observed in figure 5.9. For the center column at $x = 65\,mm$ the sub-filter PDF's are computed for the following radii, $r = 18.5$, 19.0, 19.4, 19.9, $20.3\,mm$. The sub-filter variances in the considered positions are also comparably small and hence PDF shapes close to Dirac δ-peaks are apparent. As in the upstream position depicted in the left column, the presumed PDF shape shifts the PDF to the air side ($\xi = 0$) and thus adds a too large amount of pure air to the filtered dependent scalars, which define the thermo-chemical state. The largest impact in this axial plane can be seen at $r = 19.0\,mm$, where the shapes of the Monte Carlo PDF and the β-function do not fit together at all. At $x = 90\,mm$, the variances in mixture fraction space are larger than in the previous axial positions due to increased turbulent mixing and the broadening of the shear and mixing layers towards further downstream positions. The plots for smaller radii show an adequate matching of both PDF reconstructions, but while increasing the distance to the centerline, the variances are getting smaller and the already described shift towards the pure air side is becoming more obvious and significant.

5.3.4.2. Conclusions

The capability of the β-function as a model for the sub-filter PDF of the mixture fraction is analyzed by a qualitative comparison of reconstructed PDF shapes. Therefore, particle ensembles obtained by the Eulerian Monte Carlo PDF transport scheme serve as a basis for the reconstruction of the discrete PDF and the continuous β-function. In the selected monitoring points some shortcomings of the β-function have been observed and described. These are the overestimated amount of pure air in the control volume even though no air

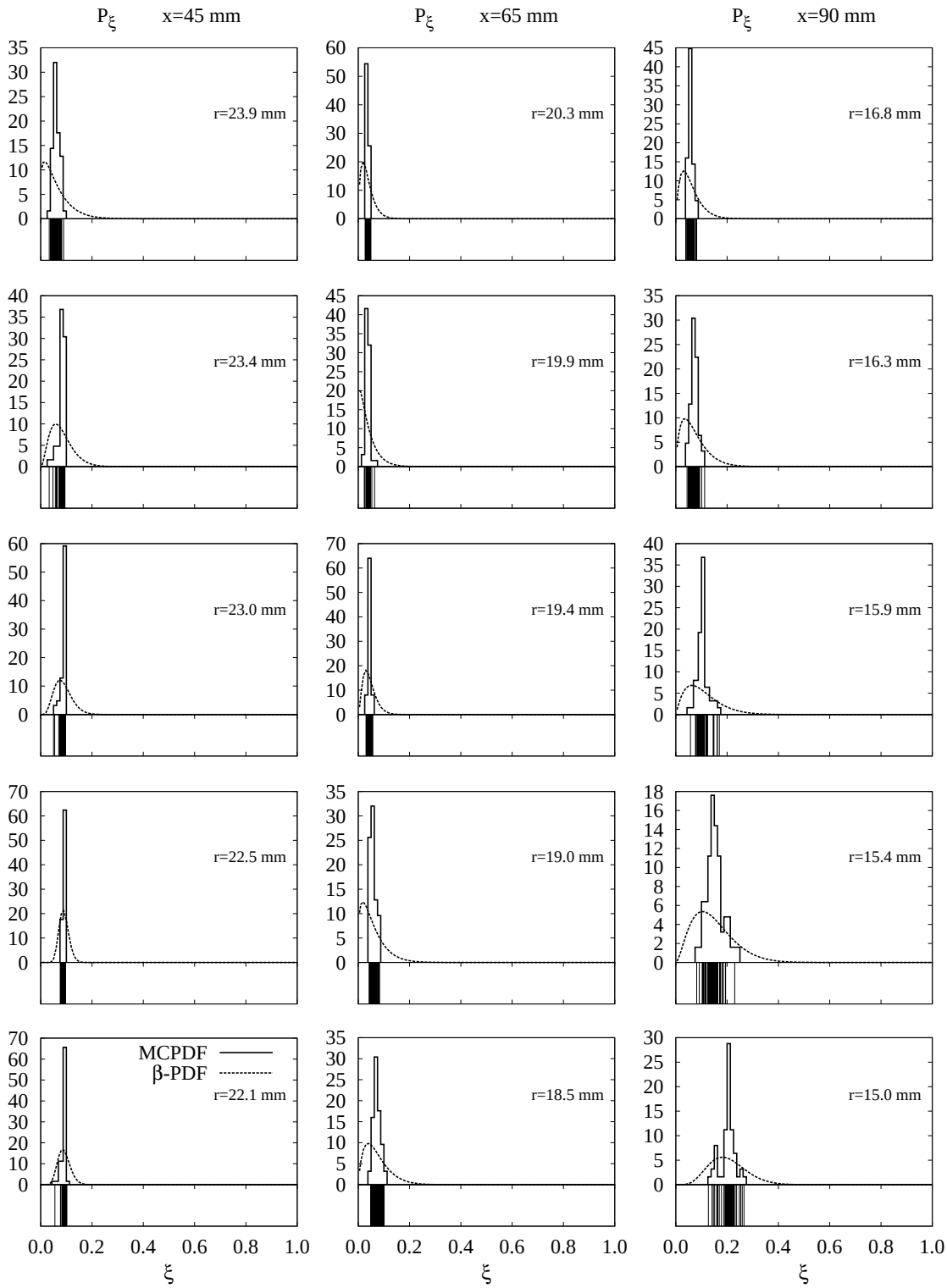

Figure 5.15.: Comparison of reconstructed Monte Carlo PDF shapes (solid lines) with corresponding β-functions (dashed lines) for different axial and radial positions, which are located in the supposed flame front around the stoichiometric mixture fraction of $\xi_{\mathrm{st}} = 0.05$. Both obtained PDF shapes are based on the properties of the additionally illustrated particle ensemble in the related subplots at the bottom of each diagram. There, every line represents one of the 50 stochastic particles in each control volume.

has been represented by the particle ensemble. It can be assumed that this behavior corresponds to the very low stoichiometric mixture fraction of the fuel composition in the presented burner configuration and the correlated small distance between pure air and stoichiometry in ξ-space. It would be interesting to see an analysis of this kind in a flame providing a higher stoichiometric mixture value, which is presented in section 6 on a methane/air flame with $\xi_{\mathrm{st}} = 0.351$. The observed differences can definitely be a reason for the variations between the applied finite volume and the Eulerian Monte Carlo methods, which have been shown in the time averaged radial temperature plot in figure 5.9 (right), but also in the OH mass fraction profiles in figure 5.10. By the tendency of the β-function to assume larger air amount as actually existent, the filtered temperatures and the mass fractions of OH are decreased in these regions.

5.3.5. Application of Flamelet Generated Manifolds in the Context of the Eulerian Monte Carlo Method

All previously performed investigations and analyses of the reacting Sydney bluff body configuration HM1e included the comparably simple steady flamelet chemistry representation considering only a single strain rate. However, the demonstration of the obtained simulation results of selected thermo-chemical quantities shows nice agreement with the corresponding experimental data and thus confirms the implemented LES solver FLOWSI to be a promising tool for adequate estimations of combustion processes. This is also based on the fact that the considered HM1e configuration is a relatively simple test case in terms of unsteady chemistry effects as local extinction phenomena, which cannot be captured with the currently employed steady flamelet chemistry. Therefore, the integration of a more complex chemistry model is reasonable, which led to the implementation of the flamelet generated manifolds (FGM) chemistry representation including the capability to describe unsteady effects like local extinction. General basics of the FGM model have already been introduced in section 2.3.4.4.

As in the preceding simulations, the Monte Carlo transport scheme is only applied in a postprocessing mode, where no feedback or coupling of obtained thermo-chemical quantities is made. This is due to stability problems of the LES solver related to density field fluctuations evoked by the stochastic nature of the Monte Carlo PDF method. The corresponding flowchart to the employed simulation tool is depicted in figure 5.16. The flow simulation is still performed with the thermo-chemical quantities obtained from the flamelet based finite volume branch on the left side. However, the right side, describing the Monte Carlo PDF transport scheme has now been changed. Instead of a flamelet chemistry table, the thermo-chemical quantities are now provided by the FGM chemistry representation. Therefore, additional to the mixture fraction, the progress variable $\widetilde{\mathcal{Y}}$ is transported to define the actual thermo-chemical state and properties. As described in section 2.3.4.4, the transport equation for the progress variable includes a chemical source term, which is also given in the FGM table and tabulated in dependency on the mixture fraction and the progress variable.

The purpose of the following section is the investigation of the FGM chemistry influence on the dependent scalars. Furthermore, the Monte Carlo PDF method is again used for analyzing the impact of presumed probability density functions on the computationally

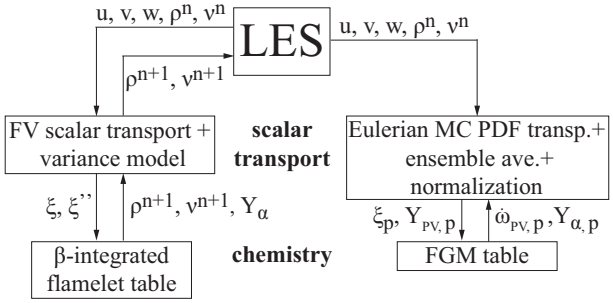

Figure 5.16.: Procedure of the hybrid LES/transported PDF scheme. The chemistry in the MCPDF branch is represented by an FGM formulation. For this chemistry model the additional progress variable Y_{PV} has to be transported and the corresponding source term ω_{PV} is provided by the FGM table. All variables and quantities depicted are assumed to be filtered values, except for the properties subscripted with an p for particle.

obtained results.

5.3.5.1. Numerical Setup

The computational domain and the belonging numerical grid in this investigation are still the same as in the cases before. Also, the flamelet table for the velocity field calculation is kept constant with a single strain rate of $a = 10\,s^{-1}$ and the resolution of 200 sampling points in mixture fraction and 100 points in unmixedness space. The performed changes are all related to the Monte Carlo PDF transport scheme. The table is generated by the one-dimensional solver CHEM1D [99], [67], and is based on premixed flamelets, even though a non-premixed flame configuration is simulated. The main difference in the performed calculation compared to the common flamelet approach is the addition of the reactive scalar $\mathcal{Y}$ representing the progress of the combustion process. That means, the MCPDF method is now transporting a joint probability function of the mixture fraction and the progress variable. Details about the method and the influence of the quasi second order accurate MCPDF transport scheme on the progress variable are already discussed in section 4.2. For the current simulation, the FGM chemistry is represented by a resolution of 901 samples for the mixture fraction and 301 for the normalized progress variable.

5.3.5.2. Results

The investigations within this section are limited to the results of the dependent scalars like the temperature or the hydroxyl mass fraction, since the velocity fields are still obtained by the flamelet chemistry based finite volume approach. Furthermore, the obtained mixture fraction distribution is also not affected by the changed chemistry model. Figure 5.17 depicts the radial profiles of the temperature on the left, the OH mass fraction on the right and their corresponding fluctuations for the axial measurement planes. For reference reasons, experimental data (symbols), the finite volume results (solid lines) and the Monte Carlo PDF method with a flamelet chemistry representation (dashed lines) are shown, while the actual new results of the Monte Carlo PDF in the FGM context are illustrated by the dotted lines. The filtered mean values of the temperature obtained by the MCPDF

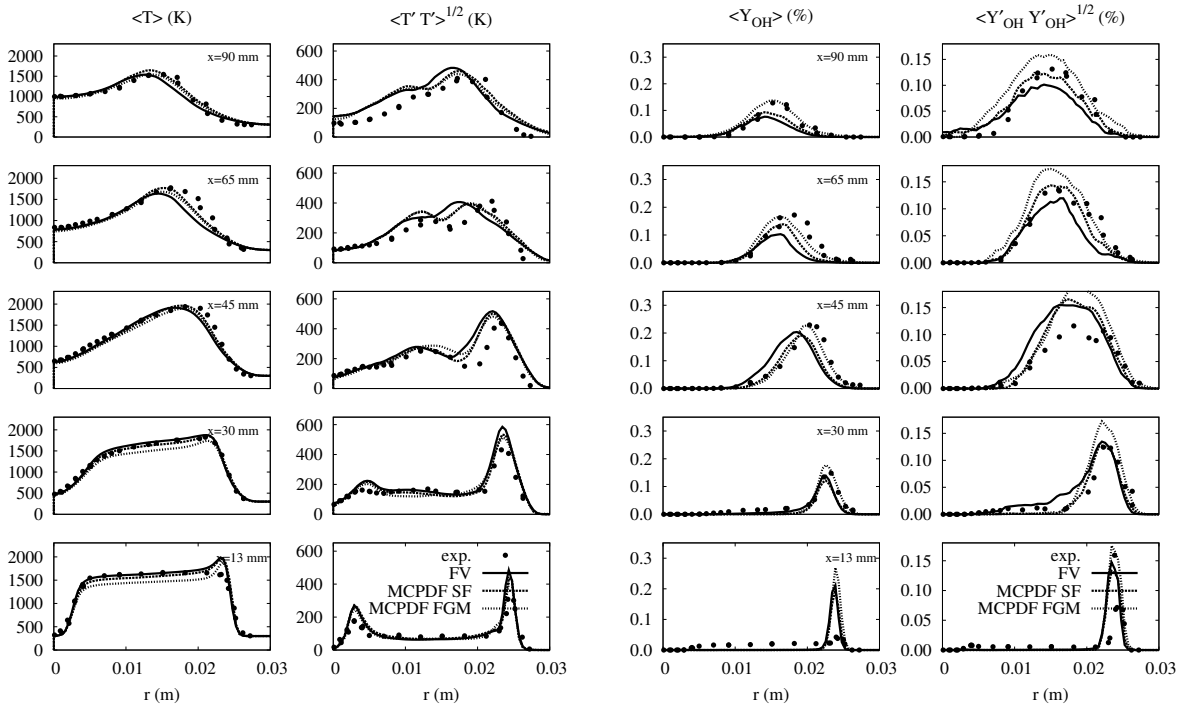

Figure 5.17.: Radial profiles of the time averaged temperature (left), the hydroxyl mass fraction (right) and their corresponding fluctuations for selected axial locations of the reacting HM1e configuration. Symbols depict the experiments, the solid line represents the finite volume simulation, while the two other lines show Monte Carlo PDF solutions for the different chemistry representations steady flamelet (SF) (dashed) and flamelet generated manifolds (FGM) (dotted).

FGM method show an underestimation of approximately $100\,K$ above the upper bluff body surface compared to the experiments and the reference simulations for the first two upstream positions at $x = 13$ and $30\,mm$. This discrepancy must be caused by a too low value of the progress variable leading to lower temperatures in this area. Interestingly, even though the chemistry model is now able to predict local extinction phenomena, the results still yield a temperature peak at the outer bluff body edge like in the previous calculations. This leads to the assumption, that the temperature peak is either related to heat losses at the wall of the bluff body as suggested by Ihme et al. [34] or is related to errors within the experimental data. The FGM results definitely eliminate theories of chemistry related local extinction, which would have been captured by this simulation. The plots at the remaining axial positions further downstream at $x = 45$, 65 and $90\,mm$ do not show major differences between both illustrated MCPDF solutions except for slight underestimations of the peak temperatures in the last two positions. A similar behavior can also be observed in the temperature fluctuations, where no discrepancies are visible except for minor differences at $x = 45\,mm$ showing negligibly increased fluctuations between both mixing layers.

While the temperature profiles of the FGM simulation depicted an almost similar solution compared to the steady flamelet MCPDF computation, the OH mass fraction profiles are very promising. As already described previously, the simulation shows again an at-

tached flame front at the outer edge of the bluff body, leading to the peak at $x = 13\,mm$, which is not present in the measurements. For the next following axial measurement planes, the FGM MCPDF gives nearly perfect agreement with the experiments in terms of the position as well as in the peak magnitude, while all alternative reference calculations underestimate the OH mass fraction values or do not match the positions. This is a very good characteristic, since the hydroxyl radical is an indicator for the flame front and hence hugely important for adequate predictions of combustion systems. However, it needs to be mentioned that the fluctuation level of the OH mass fraction is increased in every measured axial position. A reason for this cannot be given based on the shown time averaged results, but rather needs to be discussed on the basis of scatter data of the hydroxyl radical mass fraction.

OH scatter plots are provided by figure 5.18 showing experiments (left) and the Monte Carlo PDF method with steady flamelet chemistry (center) as well as with FGM chemistry (right) for the axial measurement locations. Before analyzing the represented diagrams it should be mentioned that the scatter obtained by the MCPDF FGM method is now not solely caused by sub-filter variance effects but combined with the additional effect of varying reaction progress. This additional degree of freedom explains larger deviations from the depicted flamelet solution with a strain rate of $a = 10\,s^{-1}$ since the entire solution space is accessible. However, in contrast to the advantages in the representation of finite rate chemistry effects, it is more difficult to make definite interpretations and draw explicit conclusions from the illustrated results. The scatter plots unveil some interesting facts about the implemented Monte Carlo PDF method with FGM chemistry representation. Starting with the plane at $x = 13\,mm$, it is clearly visible that the currently analyzed method shows peak values exceeding the flamelet solution as well as the experimental data in the point of stoichiometric mixture fraction and on the lean side of the flame. The theoretical reason for that is a progress variable of $\mathcal{Y}^* = 1$, which means the reaction is completely executed and only burnt gas is existent at this point. This condition corresponds to a steady flamelet solution with a strain rate of zero, which describes a flame front without shear. The lean branch of the FGM chemistry reproduces the scatter in the experiments comparably well, where the isolated effect of unmixedness in the steady flamelet cannot represent such deviations from the predefined flamelet solution. However, the peak value at ξ_{st} is overestimated by the FGM, which is obvious by comparison with the experiments. Nevertheless, in this axial position, the measured radial profile in figure 5.17 showed almost no flame front due to the mentioned reasons, which makes further interpretations useless. The remaining validation planes leave more space for interpretations since the time averaged profiles show at least the same trends. On the rich side of the flame front almost no differences between both chemistry models are apparent. In these regions of the flame front mixing is the predominant effect of the occurring scatter, which is the same for both steady flamelet and FGM chemistry. In contrast, within the stoichiometric points and in the lean branches of the scatter plots, differing characteristics of the chemistry representations can be observed. It is very interesting to see the increased peak values in the stoichiometry while applying the FGM chemistry, even though the radial profiles show very good agreement with the experiments. The steady flamelet simulation shows promising scatter data for the stoichiometry in comparison with the measurements, but yet underestimated the time averaged OH profiles. A distinct ex-

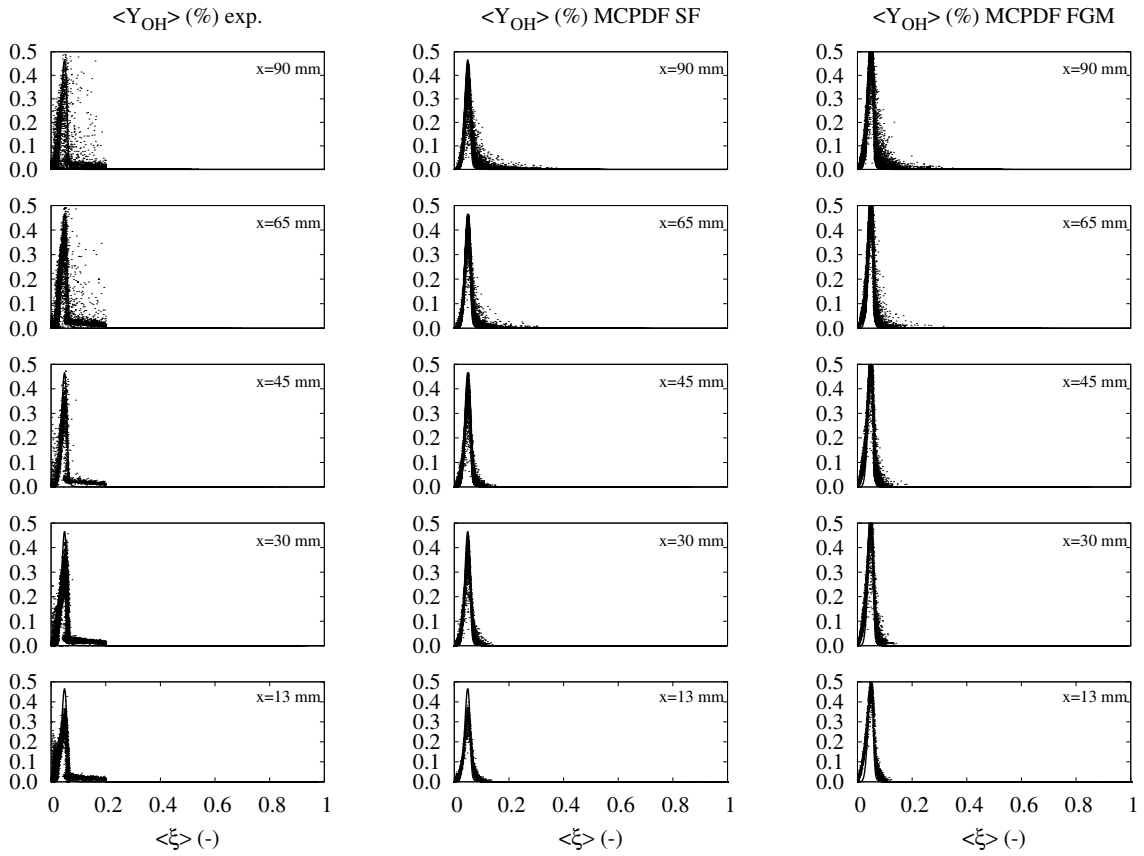

Figure 5.18.: Scatter plots of the filtered OH mass fractions versus the filtered mixture fraction for the measured axial positions $x = 13$, 30, 45, 65, 90 mm. The columns depict the experiments on the left, the MCPDF steady flamelet (SF) simulation results in the center and the Monte Carlo PDF FGM solutions on the right. In addition, the flamelet solution for a strain rate of $a = 10s^{-1}$ is shown as a reference in each plot.

planation for that phenomenon cannot be provided based on the given results. However, the measured scattering at the lean branch of the flame front is matched comparably well with FGM, especially in the last axial position at $x = 90\,mm$, where the SF model has no visible scattering. The reasons for that are the additional degree of freedom provided by the progress variable, which allows the chemistry to enter that region in the ξ-Y_{OH}-space. In the context of FGM chemistry representation, it is interesting to see the behavior of the additional progress variable and the impact on the thermo-chemical quantities. The progress of the combustion processes is indicated by this additional scalar, which is very interesting for the analysis of the given flame configuration. Normalized progress variables with values below unity ,$\widetilde{\mathcal{Y}}^* < 1$, stand for not entirely completed reactions and hence represent a different chemistry than a fully burnt state with $\widetilde{\mathcal{Y}}^* = 1$. Figure 5.19 shows a comparison of scatter plots between experiments (left column) and the transported non-normalized progress variable (right column). The data representing the experiments are

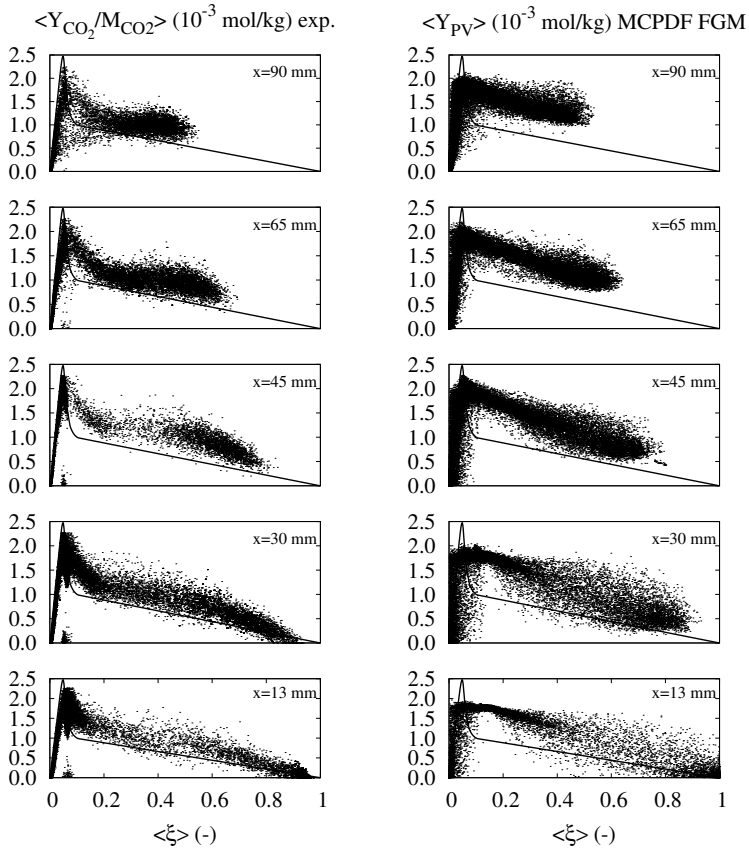

Figure 5.19.: Scatter plots of the filtered progress variable versus the filtered mixture fraction for the measured axial positions $x = 13,\ 30,\ 45,\ 65,\ 90\,mm$. The columns depict the experiments on the left and the Monte Carlo PDF FGM solutions on the right. In addition, the equilibrium solution is shown as a reference in each plot. Data points above or on that line represent completely burnt states, while points under that line stand for an incomplete reaction progress.

given via the definition of the progress variable for this simulation

$$\widetilde{\mathcal{Y}} = \frac{\widetilde{Y}_{CO_2}}{M_{CO_2}}, \tag{5.3}$$

since the progress variable cannot be measured directly. Furthermore, the equilibrium state is depicted by the solid line in each plot, which is used for normalization of the progress variable. This means, all scatters under this line represent incomplete reaction progress, whereas points above and on the line stand for fully burnt chemistry solutions. The region above the line can only be entered by mixing of a burnt with an unburnt fuel rich solution and must be situated inside the range limited by a linear interpolation between a fully burnt solution at stoichiometry and mixture fraction equals unity. This limit actually defines the most extreme mixing case.

The most obvious feature in figure 5.19 is the physically incorrect appearance of scatters beyond the actual limits for both experiments and especially in the simulation. Reasons for that must be errors in the measurements and within the simulation. Nevertheless,

it is very interesting to analyze the differences and characteristics of the scatters. At $x = 13\,mm$ in close vicinity to stoichiometry, the behavior of the simulation differs completely from the experiments. The measurements show large variations from completely burnt states through to extinction phenomena, whereas the calculated solution yields a relatively homogeneous behavior. This again mirrors the missing flame front in the experiments at this axial position due to wall heat losses and hence cannot be used for further analysis. However, experiments in the following downstream position at $x = 30\,mm$ depict again some local extinction effects in the rich branch close to stoichiometry, where the simulation does as well obtain some incomplete reaction progress but not comparably distinct as in the measured data. Another special feature of the simulation is represented by the large variation of the progress variable in the lean branch of the equilibrium line, where the points above the line are again caused by numerical issues. However, even the large variations leading to incomplete reaction states cannot be observed within the experimental data. Another shortcoming of the simulation is the overestimation of the reaction progress in the region at $\widetilde{\xi} \approx 0.2$. For the remaining measuring planes the results of the simulation are relatively promising and show nice agreement except for the increased scattering around the lean region and the mentioned local overestimation.

5.3.5.3. Conclusions

The influence of a more complex chemistry model, the flamelet generated manifolds, in the context of a Monte Carlo PDF method has been investigated using time averaged radial profiles of the temperature and the OH mass fraction. Furthermore, scatter plots of the hydroxyl radical distribution have been analyzed and qualitatively compared with measurements and a MCPDF steady flamelet formulation. In order to analyze the performance of the progress variable transport, scatter plots of the reaction progress have been illustrated and studied employing indirectly obtained experimental data. Velocity fields have not been compared in this section, since the Monte Carlo PDF solver has been operated in a postprocessing mode, where no coupling between the MCPDF method and the LES flow solver is realized. Thus, the velocities are still calculated with thermo-chemical quantities provided by the finite volume steady flamelet approach, which showed good agreement with experimental data in previous chapters and have not changed within the presented simulation.

The time averaged temperature profiles have not shown any major differences to the steady flamelet MCPDF formulation except for an underestimation close to the bluff body. A larger influence has been observed in the $\widetilde{Y}_{OH}$ profiles, where the FGM simulation obtained nearly perfect agreement with the experiments and hence performs better than the previously discussed steady flamelet MCPDF simulation. The OH scatter plots illustrated the additional degree of freedom of the FGM chemistry model in comparison to the applied steady flamelet model by showing larger variations of $\widetilde{Y}_{OH}$ as generally possible for the SF model. The scatter plot comparison of the progress variable distribution unveiled some numerical issues in the variable transport, since physically incorrect thermo-chemical states have appeared, which do not have any negative impact on the simulations at all. Conclusively, it is very interesting to see nearly perfect agreement between the simulation results and measured data in time averaged profiles, while the analysis of unsteady results shows non-neglectable discrepancies with the measurements.

Nevertheless, the applied FGM chemistry representation in the framework of an Eulerian Monte Carlo PDF method has obtained very promising results, even though some details are still unknown and remain inexplicable.

5.3.6. Analysis of the Sub-filter PDF in the FGM Context

The sub-filter PDF modeling in the framework of flamelet generated manifold chemistry representation is still an object of current research activities. The most common method for analysis of the PDF shapes is the utilization of DNS data and performing a priori tests to gain insight of sub-filter properties. That means, DNS data is filtered and so distributions of quantities in the sub-filter scale range can be analyzed in order to develop related models. Such a priori tests are problematic in several aspects: (i) it is very difficult to find sophisticated DNS data which fit the given problem, (ii) it is questionable, whether the provided information is universally valid, (iii) it is difficult to manage the incredible magnitude and multitude of DNS data. Therefore, Monte Carlo PDF methods are a good alternative to analyze sub-filter properties and utilize them as a basis for corresponding model development.

In order to analyze the sub-grid PDF modeling aspect, the following evaluation is made. Instantaneous particle information is taken to rebuilt the sub-grid PDF of the mixture fraction and the progress variable. On the basis of the ensemble average and the variance a β-shaped PDF is calculated. By definition, the mean and variance values in variable space are exactly the same, whereas higher moments differ between the MCPDF and the presumed PDF. First of all it must be said, that the following results are based on instantaneous information of a single time step, but a similar behavior is observed by analyzing further time steps.

5.3.6.1. Results

Figure 5.20 shows sub-filter PDF distributions of the mixture fraction (left) and the progress variable (right) for selected axial and radial positions. The solid line step functions represent the instantaneous discrete MCPDF, whereas the dashed lines depict the modeled continuous β-PDF with the same mean and variance values. Additionally, at the bottom of each plot, the given particle ensemble distribution is shown, where each particle is represented by a single vertical line.

It should be mentioned that the mixture fraction PDF plots are generally the same as for the MCPDF calculation shown previously in the flamelet context. Nevertheless, it is interesting to see and analyze the illustrated shapes for selected positions in the computational domain. The mixture fraction PDF plot at $x = 13\,mm$ unveils a general drawback of the β-PDF in the framework of sub-filter mixture fraction modeling. In this plot, the particle distribution at the radius of $r = 2\,mm$ is shown, which is situated within the inner shear and mixing layer and hence represents a large sub-filter variance. The immanent disadvantage of the β-function as a sub-filter model is the inability to adequately describe sub-filter distributions with a large range of values as seen in this subplot. The function rather represents a double peak distribution, with peaks at the mixture fraction limits of zero and unity and a neglected center section, than the actual uniformly distributed particle ensemble. However, for all other depicted locations the mixture fraction

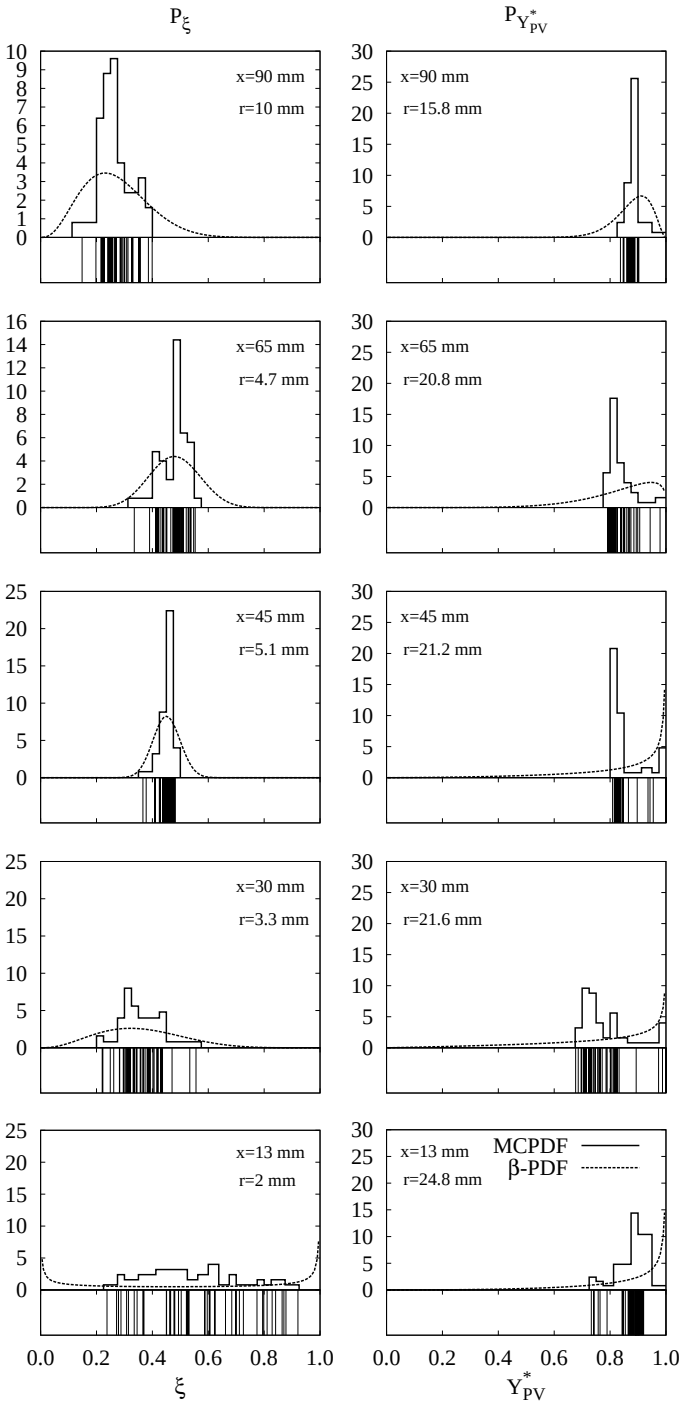

Figure 5.20.: Comparison of reconstructed Monte Carlo PDF shapes (solid lines) with corresponding β-functions (dashed lines) for selected axial and radial positions. Both obtained PDF shapes are based on the properties of the additionally illustrated particle ensemble in the related subplots at the bottom of each diagram, where every line represents one of the 50 stochastic particles of the considered control volume.

particle ensembles show relatively small variances and hence the β-function works well in representing the sub-filter distributions. The region around the stoichiometric mixture is intentionally omitted in this case in order to show the performance of the model for the rest of the ξ-space.

The right column of plots in figure 5.20 now shows sub-grid PDF of the normalized progress variable $\mathcal{P}(\mathcal{Y}^*)$. A special feature of the progress variable behavior in this bluff body flame HM1e is the small influence of finite rate chemistry, which has been depicted by the scatter plots of $\widetilde{\mathcal{Y}}$ in figure 5.19. This means, only very few thermo-chemical states with a small normalized progress variable appear. In turn, this stands for an accumulation of $\mathcal{Y}^*$ around unity and hence the already discussed behavior of the β-function in vicinity of the limits can be expected. In fact, the plots of the reconstructed sub-filter PDF of the progress variable show the very same characteristic. All illustrated positions have been chosen due to their difference of $\widetilde{\mathcal{Y}^*}$ from unity. However, the mean values are still very close to one. As in the mixture fraction PDF reconstructions in section 5.3.4, the β-function shows poor agreement with the actual particle distributions because of the characteristic behavior at the limits. This can be seen in all subplots in this column, where the β-PDF shows either a shift of the peak towards unity as at $x = 65$ and $90\,mm$ or it actually obtains a single peak at unity for all other positions.

5.3.6.2. Conclusions

The interpretations of the reconstructed sub-filter PDF for the mixture fraction lead to the following observation: the β-function as a sub-filter model for the mixture fraction yields good performance, (i) in regions away from the limits at $\xi = 0$ and 1 and (ii) in regions with relatively small sub-filter variances. The first observation and its impact is of particular importance for flame configurations using fuel compositions with the stoichiometry very close to $\xi = 0$. The second fact plays a major role within mixing layers of two streams with large deviations in mixture fraction space, where large variances in the sub-filter composition can occur. The results of the sub-filter PDF shapes for the normalized progress variable show an identical characteristic as observed in the mixture fraction distributions. Due to the low finite-rate chemistry effects included in this configuration, the normalized progress variable ranges around unity, where the quality in terms of a good representation with the β-function is very poor. A recommendation for the sub-filter model choice in the context of progress variables is the application of Dirac δ-peaks and the negligence of sub-filter variance.

5.3.7. Evaluation of Statistical Independence

The usage of the Eulerian Monte Carlo PDF method for the computation of a joint PDF of the mixture fraction ξ and the progress variable $\mathcal{Y}$ allows for a detailed analysis of the correlation between those two properties. As described in section 2.3.5, for the separation of the joint PDF of the two quantities into a product of both single PDF it is assumed that ξ and $\mathcal{Y}$ are not statistical correlated. The procedure of the joint PDF splitting with assumed statistical independence is given by

$$\mathcal{P}(\xi, \mathcal{Y}) = \mathcal{P}(\xi)\,\mathcal{P}(\mathcal{Y}). \tag{5.4}$$

Landenfeld [57] and Landenfeld et al. [47] propose a normalization of the progress variable with its equilibrium value to decrease the correlation between the mixture fraction and the progress variable. With the transformation of the progress variable, equation 5.4 can be rewritten as

$$\mathcal{P}(\xi, \mathcal{Y}^*) = \mathcal{P}(\xi)\,\mathcal{P}(\mathcal{Y}^*), \tag{5.5}$$

where $\mathcal{Y}^*$ stands for the normalized progress variable. This approach has been introduced previously and has additionally been used for all performed FGM calculations in this work so far. The knowledge of particle information from the Eulerian Monte Carlo PDF method now serves as a basis for an investigation of the proposed assumption. Therefore, particle ensembles from a single time step have been used to compare the influence of the normalization by calculating both empiric correlation coefficient $r(\xi, \mathcal{Y})$ and $r(\xi, \mathcal{Y}^*)$. The empiric correlation coefficient $r(x, y)$ [9] is defined by

$$r(x,y) = \frac{\sum_{i=1}^{n}(x_i - \bar{x})(y - \bar{y})}{\sqrt{\sum_{i=1}^{n}(x_i - \bar{x})^2 \sum_{i=1}^{n}(y_i - \bar{y})^2}}, \tag{5.6}$$

with x and y as the two stochastic properties, while x_i and y_i are the related ensemble entries and $\bar{x}$ and $\bar{y}$ stand for the two ensemble averages. The values of $r(x, y)$ are an indicator for the empiric correlation of x and y, where $r = 1$ denotes perfect positive linear , $r = -1$ perfect negative linear and $r = 0$ no linear correlation. In order to proof the assumption of Landenfeld, the absolute values of r need to decrease while changing from $r(\xi, \mathcal{Y})$ to $r(\xi, \mathcal{Y}^*)$.

5.3.7.1. Results

Figure 5.21 illustrates radial profiles of the evaluated empiric correlation coefficients $r(\xi, \mathcal{Y})$ (filled symbols) and $-r(\xi, \mathcal{Y}^*)$ (hollow symbols) for the axial locations $x =$ 13, 30, 45, 65 and 90 mm. The evaluation is performed using particle ensembles of a single time step before and after normalization of the progress variable with the equilibrium values of $\widetilde{Y}_{CO_2,eq}/M_{CO_2}$. For a better understanding, the negative correlation coefficient $r(\xi, \mathcal{Y}^*)$ is plotted, which has no direct impact on the drawn conclusions, but rather elucidates the findings.

The behavior of the empiric correlation coefficients in the range between the centerline at $r = 0\,m$ and the supposed flame front at $0.015\,m \leq r \leq 0.0275\,m$ depending on the axial position, is identical in all planes. The coefficient of ξ and the transported non-normalized progress variable $\mathcal{Y}$ shows a perfect negative linear relation, while the alternative formulation depicts no correlation at all in this range. Except for some freak values, the results confirm the assumption that has been made by Landenfeld. Inside the flame front, the deviations between the two formulations act as expected: by the normalization procedure, statistical independency is not entirely ensured in all positions, but nonetheless the correlation has been decreased. However, since no perfect statistical independency is achieved through the normalization of the progress variable, the splitting procedure of the joint PDF implies a systematical error, which is decreased but not obliterated within the range of the flame front. Besides this promising characteristic behavior, some regions in the

plots show variations from the desired solutions. This is the case on the lean side of the flame front, where the coefficient of ξ and $\mathcal{Y}^*$ depicts a strong correlation while $r(\xi, \mathcal{Y})$ gives no dependency at all between the considered quantities. The reasons for that might be problems with the normalization procedure or other errors somehow related to it.

5.3.7.2. Conclusions

An evaluation of instantaneous particle information with the implied discrete joint PDF $\mathcal{P}(\xi, \mathcal{Y})$ and $\mathcal{P}(\xi, \mathcal{Y}^*)$, respectively, have been used to analyze the impact of the normal-

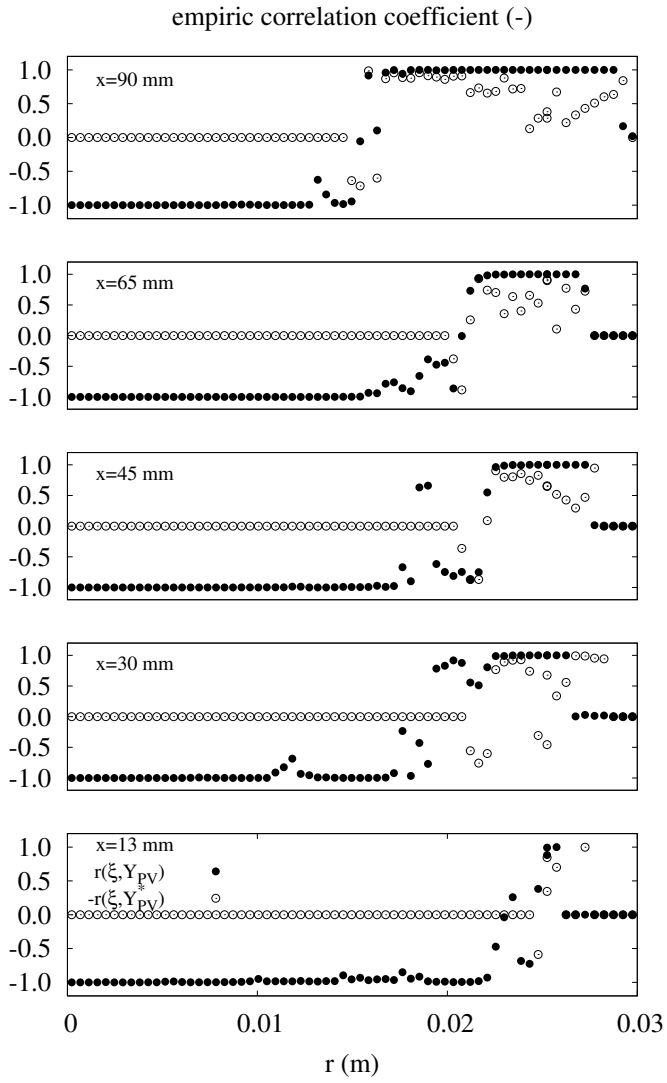

Figure 5.21.: Evaluation of the empiric correlation coefficients using the discrete representation of the joint PDF $\mathcal{P}(\xi, \mathcal{Y})$ shown as radial profiles at different axial locations. The comparison includes the coefficients between the mixture fraction and the transported progress variable $r(\xi, \mathcal{Y})$ (filled symbols) as well as between the mixture fraction and the normalized progress variable $-r(\xi, \mathcal{Y}^*)$ (hollow symbols). The coefficient of ξ and $\mathcal{Y}^*$ is multiplied by -1 in order to yield more clearness in the plot.

ization procedure in terms of the statistical independency of ξ, $\mathcal{Y}$ and $\mathcal{Y}^*$. The assumption of statistical independency is a requirement of the commonly applied joint PDF splitting in the context of turbulence-chemistry interaction using a FGM model. For the investigation, empiric correlation coefficients have been calculated in order to show the change in the statistical dependency due to the described normalization procedure.

Away from the flame front, statistical independency has been achieved by the normalization, whereas within the flame front the correlation has only been decreased but not entirely obliterated. The obtained results confirm the assumptions and evaluations, that had been proposed and performed by Landenfeld [57]. On the basis of this evaluation, the separation of the joint PDF into a product of single PDF will generally lead to smaller errors if the progress variable is normalized by its equilibrium value than without normalization. Furthermore, the error away from the flame front is tending to zero, while in vicinity or within the flame front, the error due to the PDF splitting will be unequal to zero. Unfortunately, by reference to the performed investigation no general statement concerning the magnitude of the occurring error can be made.

5.3.8. Influence of the Progress Variable Definition

The already described FGM Monte Carlo PDF simulation has been performed with the progress variable definition $\widetilde{\mathcal{Y}} = \widetilde{Y}_{CO_2}/M_{CO_2}$. The influence of a different definition is analyzed in the following section. The background for this investigation is depicted in figure 5.19, which shows the scatter plot of the progress variable. As explained, with the given definition, thermo-chemical states beyond the equilibrium solution are possible and appear due to mixing processes. Using an alternative progress variable definition, these chemically undefined states are no longer achievable based on the changed characteristics of the equilibrium solution. For the present investigation, the reaction progress is determined by a linear combination of the CO_2 and the CO mass fraction as given by eq. (5.7)

$$\widetilde{\mathcal{Y}} = \widetilde{Y}_{CO_2}/M_{CO_2} + \widetilde{Y}_{CO}/M_{CO}. \tag{5.7}$$

5.3.8.1. Results

In order to analyze the influence of the alternative definition of the progress variable, a first investigation is based on time averaged radial profiles of temperature and hydroxyl mass fraction. The comparison between both FGM simulations under the same conditions but with a different definition of the progress variable is illustrated in figure 5.22. Figure 5.22 (left) shows the time averaged profiles of the filtered temperature and its fluctuations for five selected axial positions. The solid lines stand for the calculation where the reaction progress is solely described by the CO_2 mass fraction and is labeled as 'MCPDF FGM I'. 'MCPDF FGM II' depicts results obtained by the alternative definition of the progress variable as a linear combination of the CO_2 and CO mass fractions and is illustrated by the dashed lines. The comparison of the mean filtered temperature and the fluctuation profiles do not reveal major deviations in the simulation results obtained by the differently defined progress variables. Both calculations achieve very good agreement with the measurements in all depicted planes. A minor variation can be observed at $x = 65\,mm$, where the FGM II simulation shows a slightly decreased temperature level in the flame

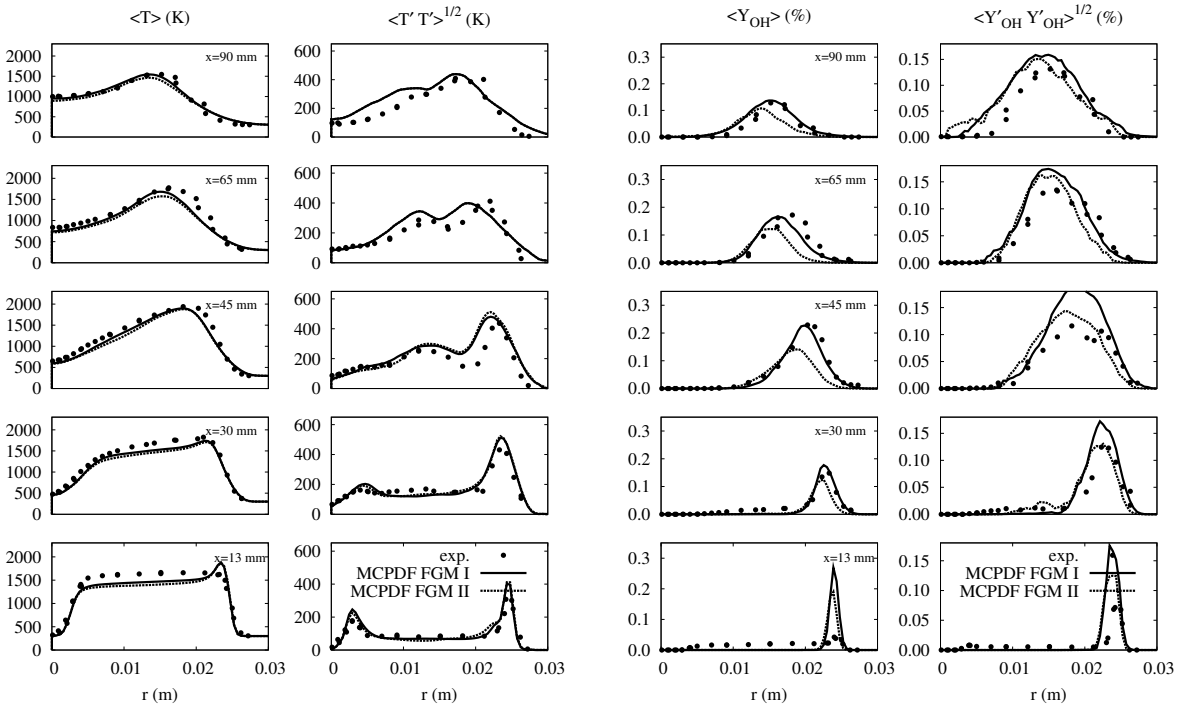

Figure 5.22.: Influence of the progress variable definition on the radial profiles of the time averaged temperature (left), the hydroxyl mass fraction (right) and their corresponding fluctuations for selected axial locations of the reacting HM1e configuration. Symbols depict the experiments, the solid line represents the results obtained with $\widetilde{\mathcal{Y}} = \widetilde{Y}_{CO_2}/M_{CO_2}$, while the dashed lines show solutions for the definition $\widetilde{\mathcal{Y}} = \widetilde{Y}_{CO_2}/M_{CO_2} + \widetilde{Y}_{CO}/M_{CO}$.

front, which is rather a numerical error, than an interpretable systematic shortcoming of this progress variable definition. Contrarily, a different behavior is apparent within the time averaged radial profiles of the hydroxyl radical mass fraction given in figure 5.22 (right). In all measurement planes, the MCPDF FGM II simulation achieves decreased $\widetilde{Y}_{OH}$ peaks, while the FGM I simulation obtains nearly perfect agreement with the experiments. Especially the inaccurate predictions on the lean side of the flame front and at stoichiometry are obvious, while the results on the fuel rich side are comparable to the alternative simulation. In the fluctuations of this quantity it can be seen that the FGM I simulation overestimates the fluctuations in some axial planes, where the FGM II calculation achieves a nice matching with the experiments. In order to analyze the differences in the OH mass fraction profiles, a scatter plot of $\widetilde{Y}_{OH}$ conditioned on the mixture fraction is given in figure 5.23. The plots show the experiments on the left, the MCPDF FGM I scheme in the center column and the MCPDF FGM II on the right. Each column presents results for five different axial measuring planes and for reference the steady flamelet solution for $a = 10\,s^{-1}$. As mentioned before, the interesting regions are situated in the stoichiometric point and the lean fuel range with $\widetilde{\xi} \leq 0.05$. Starting with the evaluation at stoichiometry both numerical schemes differ in terms of the scatter intensity. Actually, both simulations overestimate the peak values at the stoichiometric mixture fraction compared to the experiments, whereas the FGM I scheme shows an in-

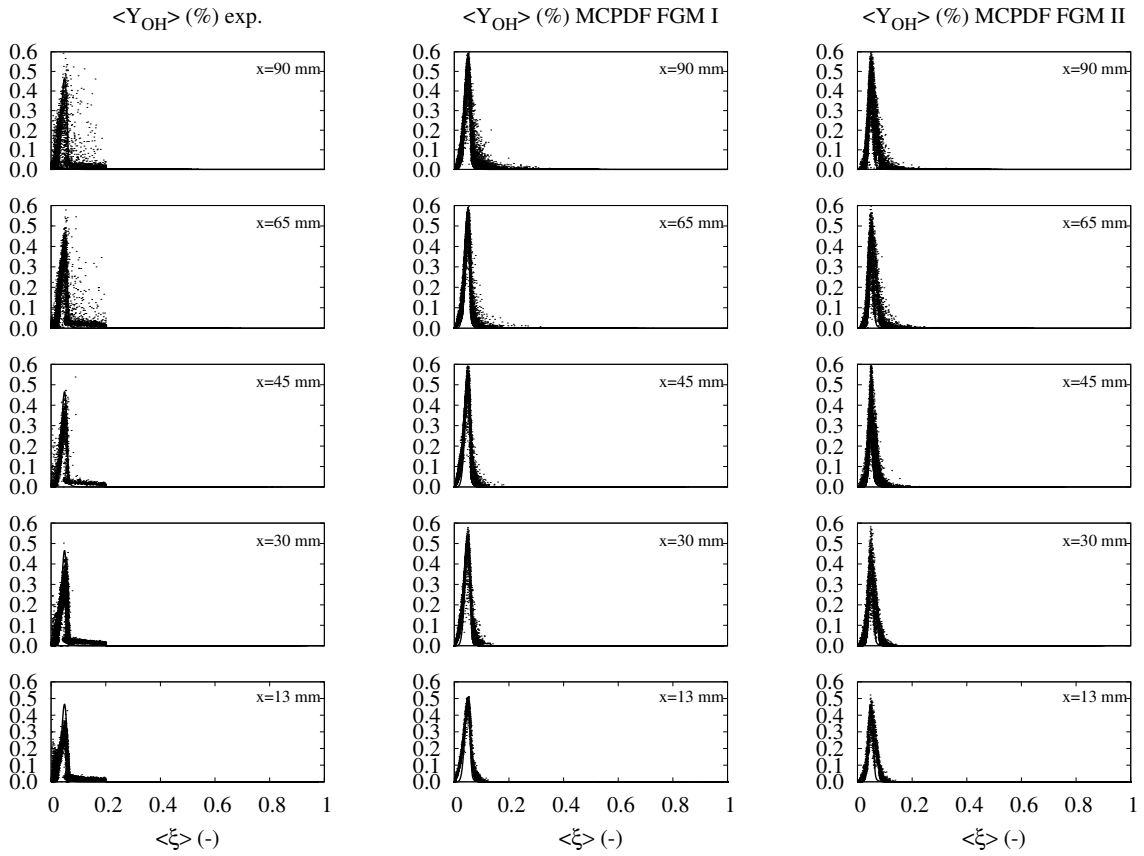

Figure 5.23.: Scatter plots of the filtered OH mass fraction versus the filtered mixture fraction for the different axial positions. The columns depict the experiments on the left, the MCPDF FGM I results in the second and the MCPDF FGM II results in the third column. In addition the steady flamelet solution for a strain rate of $a = 10s^{-1}$ is shown as a reference in each plot, illustrated by the solid line.

creased appearance of these states, while in the FGM II scheme these states are only occasionally achieved. For the particular region of lean fuel mixture, some interesting features are visible. The experiments show an increased scatter in this region around the flamelet solution with a slight tendency to larger $\widetilde{Y}_{OH}$, which corresponds to lower scalar dissipation. This behavior can also be observed in the FGM I scheme, where a distinct trend to larger OH mass fractions relative to the flamelet solution is present. However, the FGM II version does not show this characteristic, but rather reproduces the depicted flamelet solution in this range with some additional scatter. This difference between the two schemes explains the occurring systematic underestimation of the radial profiles of the time averaged OH mass fractions as achieved by the FGM II method.

Another worthwhile analysis in respect of the progress variable definition is the consideration of the computed reaction progress itself. Therefore, a scatter plot of the transported progress variable with the new definition (see eq. (5.7)) is depicted in figure 5.24. For comparison, the corresponding distribution provided by the experiments is illustrated. Additionally, the equilibrium solution is depicted in each subplot, which serves as a refer-

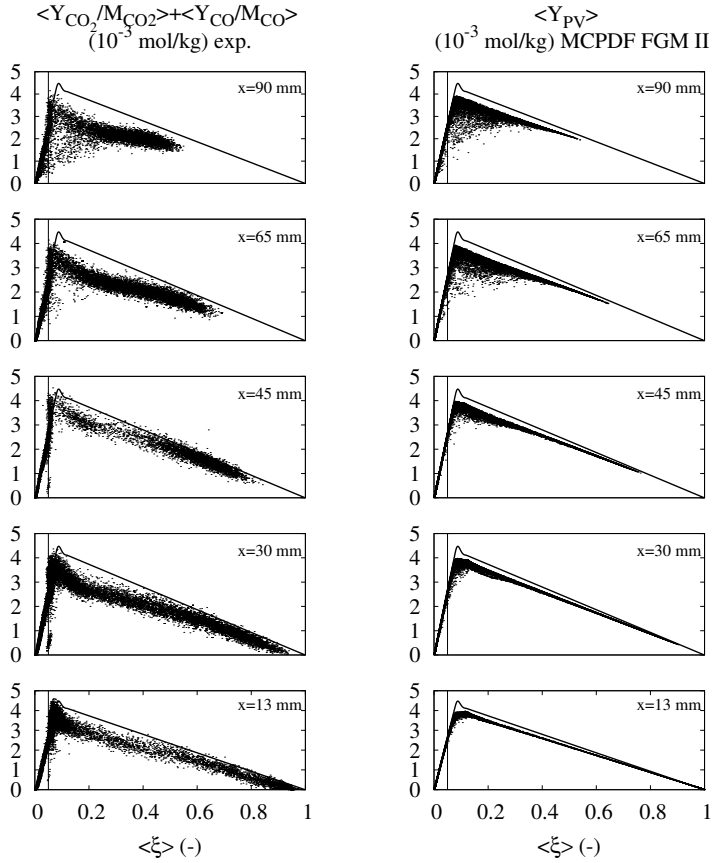

Figure 5.24.: Scatter plots of the filtered progress variable versus the filtered mixture fraction for the measured axial positions $x = 13,\ 30,\ 45,\ 65,\ 90\,mm$. The columns depict the experiments on the left and the Monte Carlo PDF FGM solutions on the right. In addition the equilibrium solution is shown as a reference in each plot. Data points above or on that line represent completely burnt states, while points under that line stand for an incomplete reaction progress. The vertical line depicts the stoichiometric mixture fraction.

ence and represents the upper limit of the progress variable, corresponding to $\widetilde{\mathcal{Y}^*} = 1$. In contrast to the FGM I method, the equilibrium solution of the FGM II is characterized by a nearly linear behavior in the region beyond $\widetilde{\xi} \geq 0.1$, which inhibits the normalized progress variable to exceed unity due to mixing effects. It has to be mentioned that the equilibrium solution for the current progress variable definition does not have its peak value at stoichiometry but shifted into the fuel rich range. At first sight it is surprising that both measurements and simulation do not reach the chemical equilibrium solution starting from a certain mixture fraction value. The reason for that is based on the CO creating reactions that range in relatively large chemical time scales, which theoretically implies a long residence time to reach the equilibrium state. This means for application, that due to increased turbulent mixing the CO reactions do not reach the equilibrium state. From this certain mixture fraction value the assumption of mixed is burnt is not justified, but rather is the combustion in this case predominated by the mixing effects. In terms of the scatter itself, the simulation achieves accurate predictions in quality and quantity of the sample point clouds. A hypothesis for the poor computation of the OH

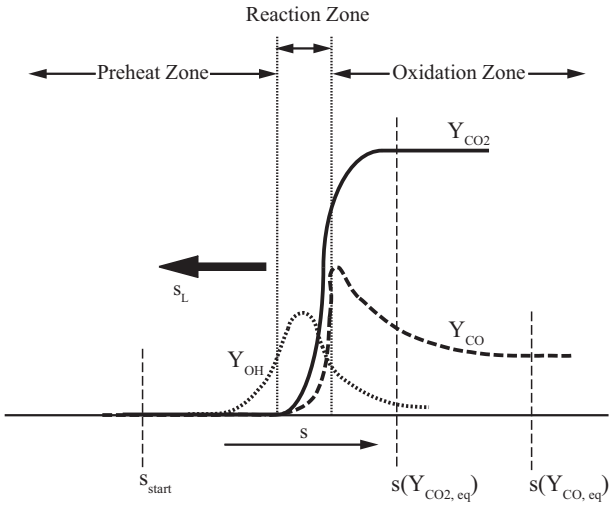

Figure 5.25.: Description of premixed laminar flame front with schematic profiles of the mass fractions of OH, CO and CO_2 across the flame front. The coordinate s determines the spatial dimension of the flame. s_{start} defines the starting point for chemistry tabulation, while $s(Y_{CO_2,eq})$ and $s(Y_{CO,eq})$ define locations in which the considered mass fraction can be assumed to be in its equilibrium solution.

mass fraction is explained in the following: For the generation of the FGM chemistry table, one-dimensional premixed flames are calculated with the chemistry solver CHEM1D, as described in section 2.3.4.4. Figure 5.25 shows a sketch of such a flame with the idealized mass fractions of the two combustion products CO_2 and CO which are employed for the definition of the progress variable. Additionally, the mass fraction distribution of the intermediate species OH is depicted, which has been analyzed previously. Within the FGM table generation, the one-dimensional flame front is now spatially resolved using a finite number of sampling points. The coordinate s is then transformed into the progress variable coordinate. The number of sampling points and the dimension of the coordinate s determine the resolution of the flame. For the FGM I definition of the progress variable, where $\widetilde{\mathcal{Y}}$ is defined by the CO_2 mass fraction, the extend of the flame that has to be resolved ranges from s_{start} to $s(Y_{CO_2,eq})$. This end point corresponds to a position at which the CO_2 mass fraction has reached its asymptotic behavior. For the FGM II definition, the significant range to resolve is larger due to a shifted asymptotic behavior of the CO mass fraction to $s(Y_{CO,eq})$. With a constant number of sampling points in s direction, the resolution in progress variable space is coarser than in the FGM I definition. The problem is now caused by the narrow profile of the Y_{OH} in s direction, which cannot be reproduced as accurate as in the FGM I definition corresponding to the lower spatial and hence progress variable resolution. This problem can be solved, by just increasing the number of sampling points for the resolution of the progress variable. An additional confirmation for this hypothesis is the adequate computation of the temperature profiles in the same simulation. This is due to the fact that the temperature profile is not represented by a narrow peak, but with an asymptotic behavior in s direction.

5.3.8.2. Conclusions

The influence of an alternative progress variable definition, including CO in addition to the CO_2 mass fraction, has been analyzed by comparing time averaged radial profiles of the temperature and the OH mass fractions. With the exception of some minor differences, the obtained temperature profiles matched the ones achieved with the original definition based solely on the CO_2 mass fraction. Contrarily, a considerable underestimation of the hydroxyl mass fraction profiles has been observed, which can be traced to an inadequate resolution of the employed FGM chemistry table, caused by the modified chemistry framework. Another very interesting behavior could be unveiled, which concerns the distribution and implicitly the normalization of the new defined progress variable. It has been seen that the reaction progress does not reach the corresponding equilibrium solution for mixture fraction values starting from a certain point in the fuel rich side to unity. This might be caused by the slow CO chemistry, which leads to regions in the flame, particularly in the fuel rich side, where mixing effects are predominant in contrast to reaction processes. Simulations using this alternative definition of the progress variable generally achieve promising results by avoiding non-physical normalized reaction progress values beyond unity. However, when adding CO mass fractions to the progress variable, attention must be paid to the resolution of the chemistry table in terms of the reaction progress.

5.3.9. FGM Chemistry Formulation in the Finite Volume Context

The following section will give insight into the application of FGM in the context of the finite volume discretization and will provide results of different thermo-chemical quantities that are compared to the previously presented simulations. In contrast to the latest shown analyses, the change of the chemistry model in the finite volume context also modifies the velocity fields.

5.3.9.1. Numerical Setup

The implementation of the FGM chemistry representation in the finite volume discretization is depicted in figure 5.26, which has the same structure as the flowchart in figure 5.16, except for the chemistry model change in the finite volume branch. The application of FGM chemistry in this context involves some additional features in the scalar transport scheme, which are directly related to the additionally transported reactive progress variable $\widetilde{\mathcal{Y}}$. Besides the additional transport equation, the normalization procedure using the equilibrium value $\widetilde{\mathcal{Y}}_{eq}$ is included in order to ensure a decreased statistical dependency of the mixture fraction and the progress variable. Another aspect is the different handling of the chemistry table, which has now three determining quantities for the thermo-chemical state, which are the filtered mixture fraction value $\widetilde{\xi}$, the corresponding sub-filter variance or unmixedness $\widetilde{\xi_n''^2}$ and the normalized filtered progress variable $\widetilde{\mathcal{Y}}^*$. A sub-filter variance of the progress variable is neglected, since a Dirac δ-function is used as the sub-filter PDF approach of this quantity, which is the best choice so far according to the obtained results and conclusions drawn from the MCPDF simulations in section 5.3.6. The progress

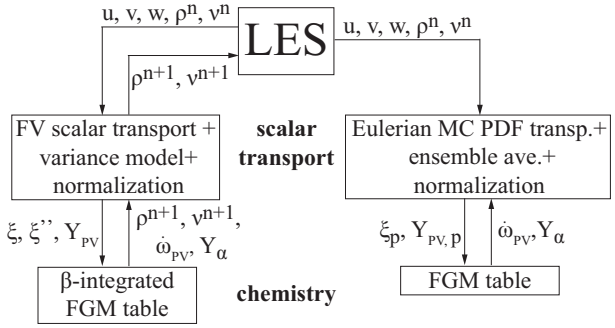

Figure 5.26.: Procedure of the hybrid LES/transported PDF scheme. The chemistry in both branches is represented by the FGM approach. For this chemistry model the additional progress variable Y_{PV} has to be transported and the corresponding source term $\dot{\omega}_{PV}$ is provided by the FGM table. All variables and quantities depicted are assumed to be filtered values, except for the properties subscripted with a p for particle.

variable in this case is again defined by the weighted mass fraction of CO_2 by its molecular weight M_{CO_2}. The implementation of the FGM chemistry into the existent finite volume discretization generated instabilities in the flow calculation, which emanate from the pressure correction scheme and the formulation of the derivative of the density in time. The pressure correction is based on a Poisson equation as described in eq. (3.32), where the time derivative of the density acts as a source term. Actually, the source term is initialized by the divergence of the velocity field and is then substituted by the density derivative in regions, where it exceeds the divergence values. In order to ensure stability of the solver, minor variations in these formulations have been made which decreases the influence of the density derivative in certain regions. A validation of this transformation is performed by a comparison of the velocities obtained with the flamelet model with the newly computed velocity fields employing the FGM chemistry.

Related to these major changes in the general procedure some minor details are also important within the numerical setup. The FGM table is resolved with 901 sampling points in mixture fraction, 201 sampling points in sub-filter variance and 101 points in progress variable space. The equilibrium values for the normalization procedure are taken from a table with 901 points in mixture fraction and 201 points in sub-filter variance space, too. All remaining parts of the simulation are retained unchanged compared to the prior simulation setups.

5.3.9.2. Results

The validation and analysis of the applied changes in the pressure correction are performed by comparing radial profiles of the time averaged velocity profiles and the mixture field with the previously obtained and used distributions which are computed with the flamelet chemistry table. Figure 5.27 shows the axial and the radial velocities and their fluctuations for the measuring planes of configuration HM1e, where the solid lines depict the flamelet results and the dashed lines stand for the solution with FGM chemistry in the finite volume context. The axial velocity profiles do not show any discrepancies between the two variants of simulations. Both depict a very good agreement with the experiments

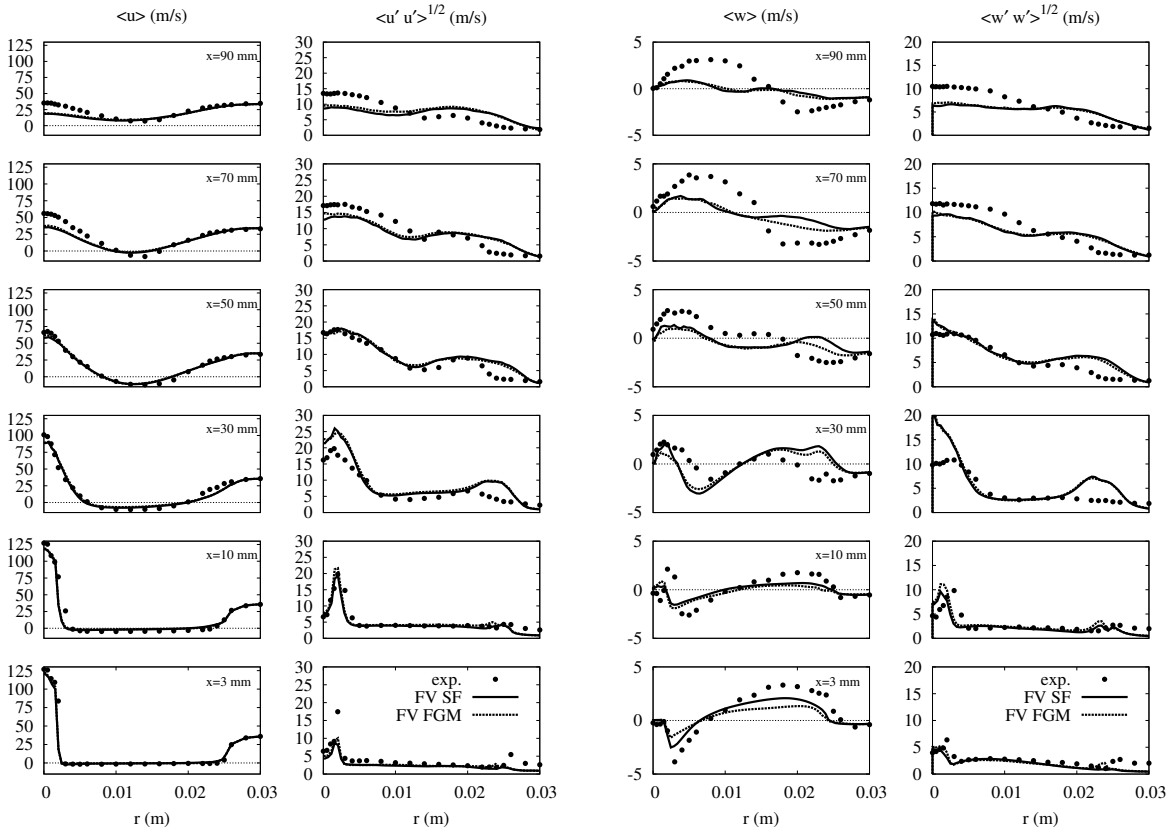

Figure 5.27.: Time averaged radial profiles of the axial (left) and the radial (right) velocity components and their corresponding fluctuations of the reacting Sydney bluff body configuration HM1e for distinct axial locations. Comparison of experimental data (symbols), the simulation employing a flamelet chemistry (solid) and with FGM chemistry representation (dashed). The horizontal lines in the mean value plots represent zero velocity for a more apparent separation of the recirculation zones.

except for some underestimation of the jet penetration depth in the planes $x = 70$ and $90\,mm$. The same behavior is observed for the fluctuations of the axial velocity, where minor differences are visible but negligible. In contrast to the main flow direction, the radial velocity plots illustrate deviations between both chemistry models. Except for the most downstream position at $x = 90\,mm$ all given measuring planes present a more or less large discrepancy between the flamelet and the FGM solution, while the more complex FGM model underestimates the magnitude of the radial velocities. In reference to the experiments and the flamelet chemistry based results, the FGM simulation with the included changes in the pressure correction scheme does not obtain as good results as the flamelet based computation but nonetheless captures the main flow patterns. The fluctuations of the radial velocity give again no visible differences compared to the reference simulation. Unfortunately, it is not possible to unveil, whether the deviations in the radial flow field are due to the change in the chemistry model or if they are caused by the transformation in the pressure correction scheme. However, on the basis of the time averaged velocity profiles, the simulation using FGM chemistry in the finite volume discretization yield promising results, even though the quality is not as good as the flamelet

based solutions.

As figure 5.26 shows, the Eulerian Monte Carlo PDF method using an FGM chemistry approach is again coupled one-way to the LES solver. Due to this, it is possible to obtain the transported and the dependent scalars from the MCPDF method simultaneously to the finite volume FGM (FV FGM) simulation. In this present case, the MCPDF calculation makes use of the provided velocity fields, which are calculated using the FGM chemistry instead of the flamelet chemistry tabulation. This means, the presented FGM simulation provides new results for the transported and the dependent scalar obtained by both methods, the finite volume discretization and the Monte Carlo PDF method. The following comparisons will show computed solutions for both discretization types in order to separate effects based on transport issues from influences based on the differing treatment of the turbulence-chemistry interaction. The ongoing validation is performed by comparing the transported scalar field, mixture fraction, and the dependent quantity, temperature, and their fluctuations in time. Figure 5.28 shows the time averaged mixture fraction (left) and the temperature (right) profiles for the established five axial positions complemented by their corresponding fluctuations. In this case, the mixture fraction field is mainly used in order to estimate possible effects of the radial velocity deviations on the flow simulation. However, even though differences in the radial velocity component are visible, the influence on the mixture distribution seems to be negligible at first sight. The illustration in the left column of figure 5.28 shows only minor deviations at $x = 45$ and $65\,mm$ between both FGM based results and the flamelet based profiles. A critical aspect on these minor discrepancies is the location of appearance, which lies in the range of the stoichiometric mixture fraction and is hence directly connected to changes in the thermo-chemical quantities. Since both FGM based profiles exhibit the variation to the flamelet calculation, it must be caused by the slightly differing radial velocity component. In contrast to the filtered mean values, the fluctuations do not show large deviations, except for the same location where the differences in the filtered mean mixture fraction field are observed. Based on these results, it is very interesting to see the influence on the dependent scalars like the temperature. Therefore, the right side of figure 5.28 depicts the radial temperature profiles plotted over the radius in comparison with the flamelet reference calculation (solid), the MCPDF FGM simulation (dotted) and the measurements (symbols). In the first two measuring planes, the FGM simulations lead to a decreased temperature distribution as already observed in the previous MCPDF FGM simulation based on the flamelet velocity field. However, while proceeding further downstream, the influence of the underestimated mixture fraction profiles is apparent, which finds expression in a distinct decreased temperature prediction and a related shift of the peak temperature to the centerline of the finite volume FGM results. Surprisingly, the MCPDF profile is matching the flamelet results even though the same mixture fraction profiles have been yielded. This means that in addition to the transport effects also further turbulence-chemistry phenomena are responsible for the differences in the dependent temperature scalar. Besides the averaged filtered temperature profiles, the fluctuation profiles do not mirror any revealing or interpretable characteristics. Nevertheless, the analysis of the proposed turbulence-chemistry effect, responsible for the differences in both FGM temperature predictions, is based on scatter plots of the temperature. Figure 5.29 illustrates experimental (left), FV FGM (center) and MCPDF FGM (right) results

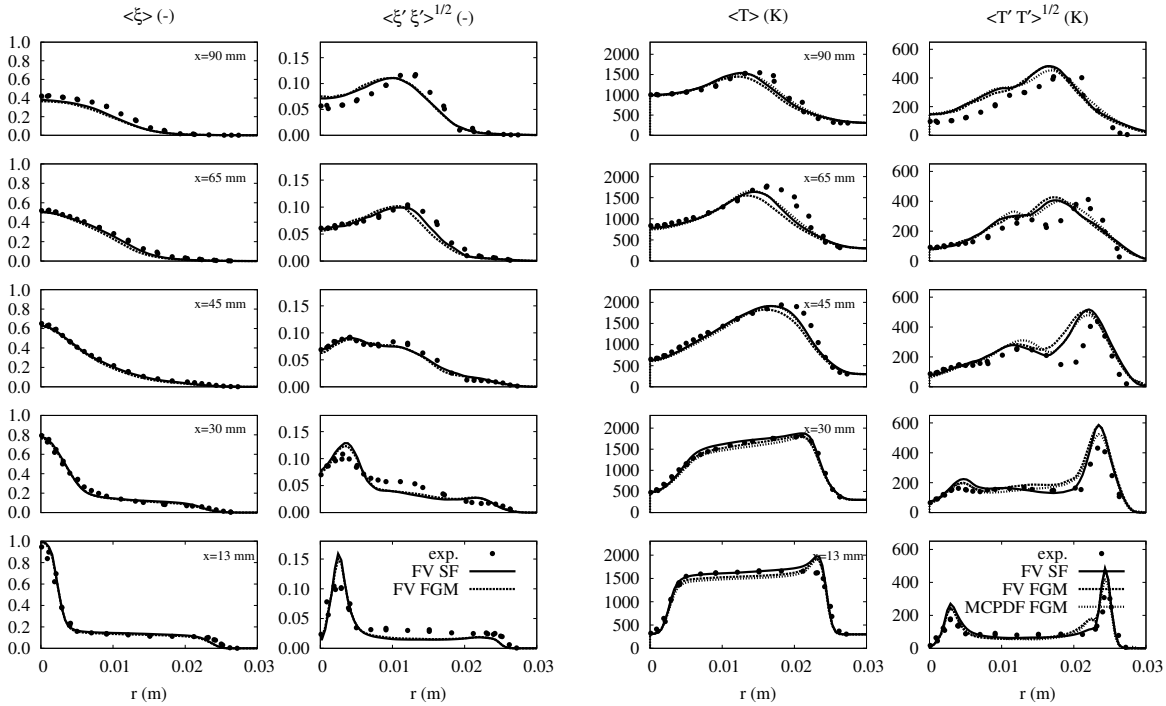

Figure 5.28.: Time averaged radial mixture fraction (left) and temperature (right) profiles and their corresponding fluctuations for selected axial locations of the reacting HM1e configuration. Symbols depict the experiments, the solid line represents the simulation based on the flamelet chemistry and the dashed line shows the computation with an employed FGM chemistry formulation in the finite volume framework. In the temperature plot on the right, the profiles for the MCPDF FGM simulation are additionally depicted by the dotted line.

for the temperature scatter conditioned on the filtered mixture fraction. In each column the scatters for the five axial positions $x = 13$, 30, 45, 65 and $90\,mm$ are depicted and the flamelet solution for a strain rate of $a = 10\,s^{-1}$ serves as a reference. As seen in the temperature profiles, the first major differences in the predictions appear in the plane at $x = 13\,mm$, where the temperature above the upper bluff body surface is underestimated by the FGM simulations. This behavior can also be observed in the present plot, where the scatter of the simulations is very small compared to the one appearing in the experiment. This behavior is obvious for the first two axial locations, while further downstream the amount of scattering especially on the lean side is comparable between the simulations and the experiments. The most interesting position based on the radial temperature profiles is the position at $x = 65\,mm$, where differences in the simulated profiles are existent even though the mixture fraction fields show the same behavior. In the scatter plot, the crucial phenomenon is visible, which is the increased scatter on the lean branch in the FV FGM simulation, while the measurements and the MCPDF FGM calculation show a very low amount of scattering. This characteristic is the reason for the deviations in the temperature profiles, which in turn is provoked by either too high sub-filter variance or more likely due to an increased variation of the progress variable in the lean region. In order to determine the reasons for the distinctions, time averaged

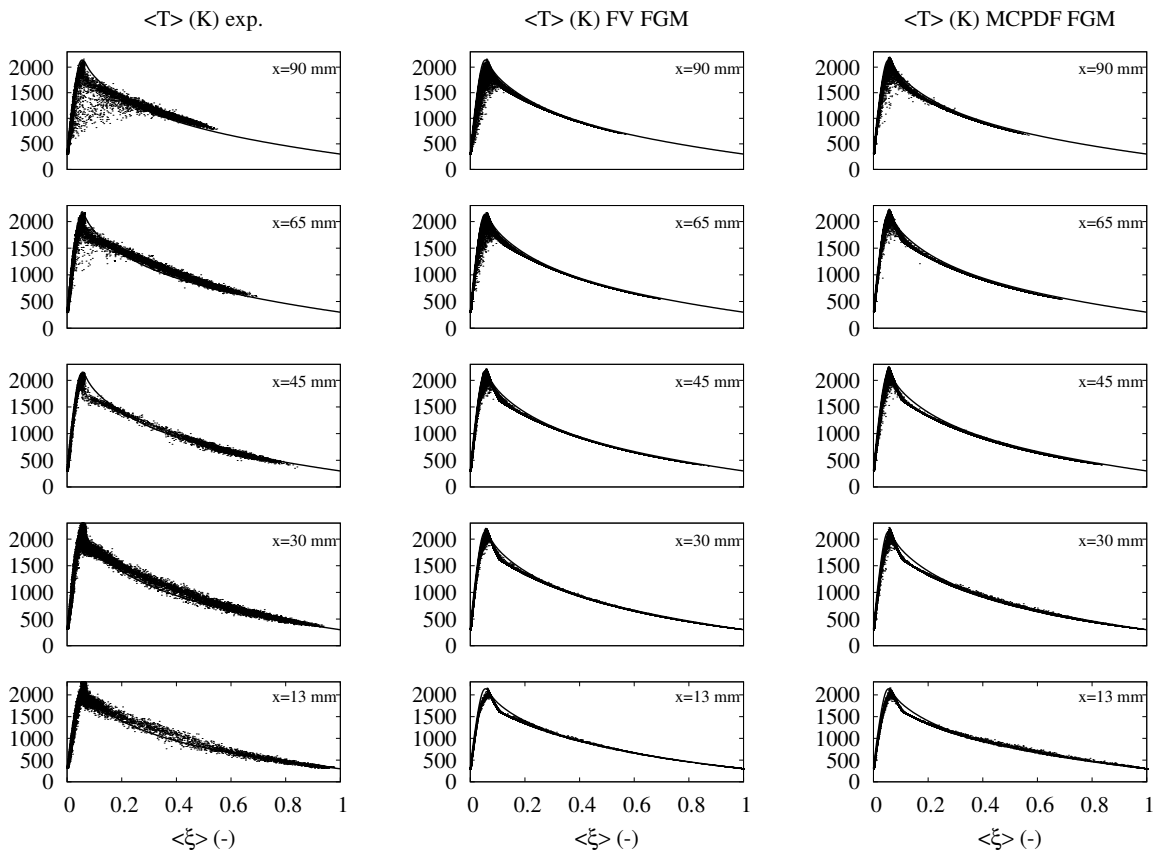

Figure 5.29.: Scatter plots of the filtered temperature versus the filtered mixture fraction for the measured axial positions $x = 13$, 30, 45, 65, 90 mm. The columns depict the experiments on the left, the finite volume FGM simulation results in the center and the Monte Carlo PDF FGM solutions on the right. In addition the flamelet solution for a strain rate of $a = 10s^{-1}$ is shown as a reference in each plot, illustrated by the solid line.

progress variable plots for the different axial positions are illustrated in figure 5.30. The diagrams show the FV FGM solutions depicted by the solid line and the MCPDF FGM results represented by the dashed line. For reference purpose, experimental CO_2 mass fraction data are also shown, which have been transformed to fit the definition of the progress variable $\widetilde{\mathcal{Y}} = \widetilde{Y}_{CO_2}/M_{CO_2}$. The filtered mean values are given on the left and the corresponding fluctuations on the right. Considering the mean progress variable profiles, the FV FGM solution shows a nice agreement with the measurements at $x = 13\,mm$, where the MCPDF FGM presents a distinct overestimation. This characteristic changes in the following downstream positions, where the profile of the finite volume discretization continuously decreases and hence does not reach the experimental peak values. It seems as if this behavior is caused by increased diffusion within the finite volume approach, which cannot be observed in the profiles obtained by the MCPDF method. The statistic transport scheme is overestimating $\widetilde{\mathcal{Y}}$ in all locations, but nonetheless catches the trends of the experiments better than the finite volume discretization. Especially, in the interesting axial location of $x = 65\,mm$ the differences between the two approaches are clearly

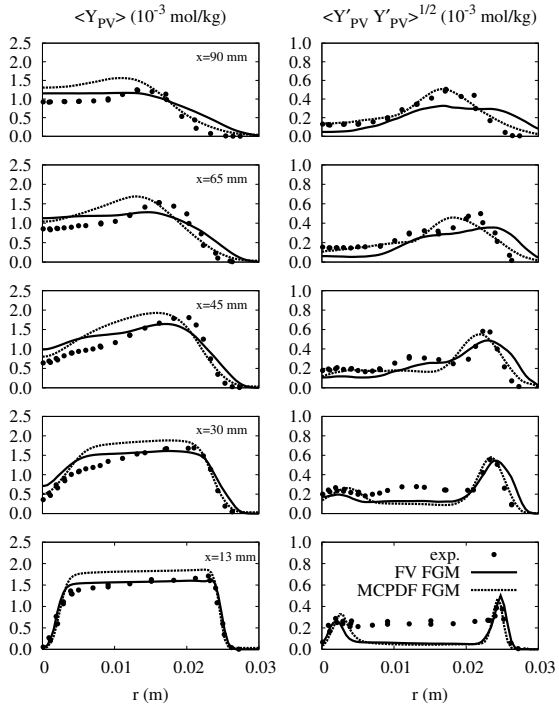

Figure 5.30.: Time averaged radial progress variable profiles (left) and its fluctuations (right) for selected axial locations of the reacting HM1e configuration. Symbols depict the experiments, the solid line represents the finite volume FGM simulation, while the dashed line shows the Monte Carlo PDF FGM results.

visible and explain the temperature deviations in this plane. The MCPDF FGM shows approximately similar magnitudes of the reaction progress compared to the experiments, but shifts the supposed flame front to the centerline. The FV method underestimates the progress, which in turn leads to the observed temperature decrease. The consideration of the fluctuation profiles also confirms the observations made for the mean values. The finite volume method shows increased diffusive transport effects and hence does not fit the reference shape given by the experiments. In contrast, the MCPDF FGM method shows an adequate agreement with the measurement in terms of the matching shape and peak magnitudes.

5.3.9.3. Conclusions

A FGM chemistry formulation has been implemented within a finite volume based transport scheme, where slight changes in the pressure correction were necessary in order to ensure stability of the simulation. For the validation of this approach and the evaluation of the changes in the numerical procedure, profiles of the time averaged axial and radial velocity components have been compared to the previously obtained flamelet based simulation results. Differences have only been observed in the radial velocity component, which in turn affects the mixture fraction distribution. For the analysis of the mixture and the temperature fields, results of a simultaneously performed MCPDF FGM scalar transport scheme have also been used for reference purpose. Even though both scalar

transport formulations achieve similar mixture distributions, the FV FGM temperature field does not show as good agreement with the experiments as the MCPDF results. The reason for this is a shortcoming in the prediction of the reaction progress in the finite volume approach, which exhibits increased diffusion effects within the profiles of $\widetilde{\mathcal{Y}}$. In contrast, the MCPDF FGM method achieved comparably good results, which were only affected by the poor radial velocity computation.

In general, it must be stated that the FGM chemistry model in the finite volume context does not obtain as good results as the flamelet based FV simulation. Furthermore, in this particular case, where no finite-rate chemistry effects like extinction occur, the velocities are predicted more accurately within the flamelet chemistry framework, which is definitely due to the necessary modifications in the pressure correction scheme. This also explains, why the MCPDF FGM method based on the flamelet velocities has achieved the most accurate prediction of the transported as well as the dependent scalars so far. Nevertheless, for configurations with increased Reynolds numbers and hence an increased possibility of extinction phenomena, the introduced FV FGM formulation is reasonable in order to represent changes in the velocity fields, which are related to the occurring density variations.

5.4. Reacting Configuration HM3e

The following numerically investigated HM3e flame is also included in the Sydney bluff body series and features the same geometrical framework as the previously analyzed configurations B4C2 and HM1e. The HM3e flame uses the same methane-hydrogen fuel composition as the HM1e case, but is characterized by an approximately doubled Reynolds number of $\mathrm{Re}_{\mathrm{jet}} = 28500$ as illustrated in table 5.1. The increased jet velocity of $U_{\mathrm{jet}} = 195\,m/s$ corresponds to 90 % of the blow off velocity of the used fuel mixture, while in the former HM1e case the inflow speed of the jet is related to approximately 50 % of the blow off velocity. This means, the probability of local extinction occurring in this case is high, which affects the velocities and the thermo-chemical quantities.

On the knowledge base, provided by the investigations previously performed no analyses in terms of the inflow boundary conditions are made for this configuration. In general, the following section will not provide as much comparisons as for the prior validation case HM1e, but will rather act as an evaluation of the conclusions made previously. However, interesting comparisons of various numerical simulation techniques will be presented, interpreted and discussed in detail.

Since the HM1e and the HM3e configurations differ only in terms of the jet velocity, the numerical setup will be kept unchanged concerning the computational grid and the employed chemistry tables. Additionally, for the investigation of the HM3e configuration no other numerical model than the previously introduced ones will be applied.

5.4.1. Analysis on Finite-rate Chemistry Effects on the Velocity Fields

In numerical simulation of turbulent combustion problems, the velocity field is a major factor for accurate predictions of thermo-chemical quantities or pollutant emissions. For

the present configuration, an adequate computation of the velocity distribution is of high importance because of the high jet inflow velocity and the related probability of local extinction that can lead to massive effects in the velocity fields. In order to investigate the influence of possible finite-rate chemistry effects, both introduced chemistry formulations are applied and compared, the steady flamelet and the flamelet generated manifolds approach. In the framework of the steady flamelet model, again only a single strain rate of $a = 10\,s^{-1}$ is considered for the generation of the look-up table. It needs to be mentioned that the steady flamelet method is not able to represent extinction and hence is not suitable for simulations of configurations with a large amount of occurring extinction phenomena. Even though the HM3e case is described as a validation case for finite-rate chemistry effects, the steady flamelet approach is applied and compared to the FGM chemistry formulation. This more complex approach is theoretically suitable for adequate computations due to the additional transported reactive scalar indicating the progress of the reaction. However, numerical simulations of local extinction phenomena and their related variations in the density field represent challenging demands for the flow solver in terms of stability. For the following investigation, the steady flamelet and the FGM chemistry formulation in the finite volume context are compared in terms of the velocity prediction. For the FGM based simulation, the previously described modifications in the pressure correction scheme have been applied again in order to provide stability of the numerical procedure.

5.4.1.1. Results

The analysis of the velocity fields is based on time averaged radial profiles of the axial as well as the radial velocity components in different measuring planes at $x =$ 4, 10, 30, 50, 70, 90 mm. Experimentally obtained data serve as a reference for the evaluation of the two simulation techniques. Figure 5.31 shows the axial velocity on the left and the radial on the right with their corresponding fluctuations. The steady flamelet results are depicted by the solid lines, the dashed lines stand for the FGM solution and the measured data is represented by the symbols. The general appearance of the axial velocity profiles of this configuration is similar to the one observed in the HM1e case, except for the higher jet inflow velocity and the related radial gradients. The comparison of the axial velocity profiles between both simulation techniques does not indicate any differences, nor do the fluctuations. This is analog to the findings, made in section 5.3.9, where the influence of the two approaches has been compared within the low Reynolds number case HM1e. The variations between both chemistry formulations are observed in the radial velocity component, where the steady flamelet chemistry case shows better agreement with the experiments for the first three upstream locations, while further downstream no distinct deviations between the profiles are visible and hence no statement about the quality can be made. The radial profiles of the fluctuations show very high fluctuation levels in vicinity of the centerline except for the last two downstream planes for both simulations, which has already been observed in the radial velocity fluctuation profiles of the HM1e case in figure 5.6.

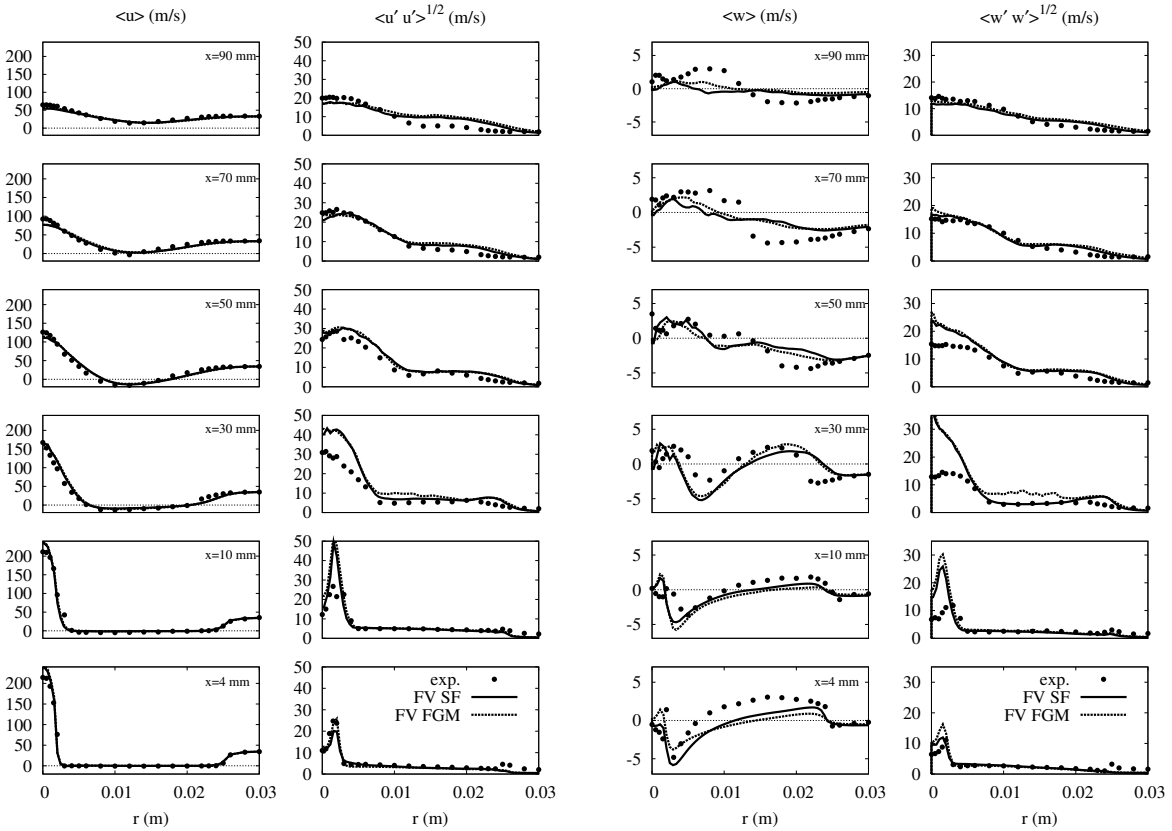

Figure 5.31.: Time averaged radial profiles of the axial (left) and the radial (right) velocity components and their corresponding fluctuations of the reacting Sydney bluff body configuration HM3e for distinct axial locations. Comparison of experimental data (symbols), the simulation employing a flamelet chemistry (solid) and with FGM chemistry representation (dashed) in the finite volume framework. The horizontal lines in the mean value plots represent zero velocity for a more apparent separation of the recirculation zones.

5.4.1.2. Conclusions

The illustrated time averaged radial velocity profiles have not shown major differences in the computation of the axial, but in the radial component, where the steady flamelet based simulation obtained more accurate predictions in reference to the experiments. However, on the basis of the given profiles and the adequate agreement with the measurements, the influence of local extinction on the velocity field is not apparent and hence can be neglected. In accordance to this, a preference for the steady flamelet based velocity field is given due to the unmodified pressure correction scheme and the related numerical consistency.

5.4.2. Evaluation of the Scalar Distributions

In the following part of this work, the scalar distributions of the transported scalar mixture fraction and the dependent scalars as temperature and OH mass fraction are evaluated. Therefore, the time averaged radial profiles of the considered quantity are discussed which

are obtained on the velocity basis of the simulation employing the steady flamelet chemistry formulation as it has been suggested and discussed in the previous investigation. The alternative schemes, which are analyzed in this section, include the steady flamelet chemistry formulation in the finite volume as well as in the Monte Carlo PDF context and the flamelet generated manifold chemistry in connection with the MCPDF approach. Those three schemes are all based on the same velocity field and hence can be directly evaluated in terms of the scalar transport itself and the turbulence-chemistry interaction with all related sub-models. For the Monte Carlo PDF transport schemes, a particle density of 50 ppc is utilized, which showed an adequate compromise between the computational effort and the achieved accuracy of the result in the simulations of the HM1e configuration (see section 5.3.2).

5.4.2.1. Results

The influence of the applied transport scheme and the employed chemistry model on the mixture fraction as well as on the dependent scalars temperature and OH mass fraction is evaluated on the basis of time averaged radial profiles. The comparisons are performed on the well established measuring planes at $x = 13$, 30, 45, 65 and $90\,mm$, where experimental data is existent. As mentioned above, three alternatives are investigated, which differ in terms of the applied transport scheme, finite volume (FV SF) and Monte Carlo PDF (MCPDF SF) transport with a steady flamelet chemistry formulation or in terms of the chemistry model, Monte Carlo PDF transport employing a FGM chemistry (MCPDF FGM). However, all three models are based on an identical velocity field, which is calculated by using the density and viscosity feedback from the FV SF scheme. Figure 5.32 (left) illustrates the transported mixture fraction results for the three different simulation techniques as well as the reference data obtained by the experiments. The simulations provide very good predictions of the mixture fraction field in all illustrated planes, while no major deviations are apparent between the different discretization types. However, some minor variations can be seen close to the upper bluff body surface, where the MCPDF calculations overestimate the amount of fuel, while the profiles of the finite volume transport scheme perfectly match the measured data. For the remaining axial positions, the mean mixture fraction profiles are almost identical and agree very well with the experiments. An analog behavior is given by the fluctuation profiles of the mixture fraction, which also show consistent results for all three simulations. A minor shortcoming in this comparison can be found at $x = 13\,mm$, where the fluctuations of the mixture fraction are overestimated by every calculation. Nevertheless, the mixing field depicts promising and as expected consistent results for both discretization techniques, which provides an adequate basis for the investigation and analysis of the dependent properties as the temperature and the OH mass fraction.

On the right side of figure 5.32 the temperature profiles with the related fluctuations are depicted. In contrast to the mixing field, the influence of the applied numerical schemes on the temperature distribution is not negligible. A special feature in the very upstream plane at $x = 13\,mm$ is the large variation in the measured data, which results from two different experimental campaigns. From the numerical point of view, the steady flamelet finite volume discretization achieves the best agreement with the measurements in terms of the absolute values and the shape of the profile, while both Monte Carlo PDF schemes

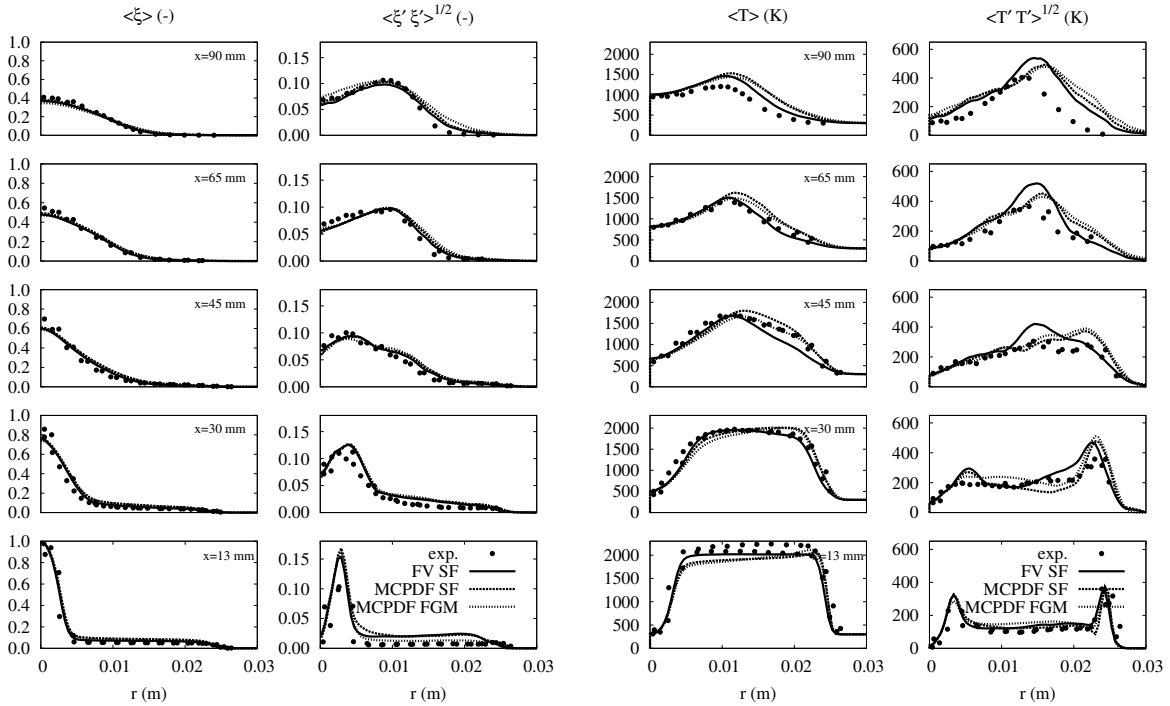

Figure 5.32.: Time averaged radial mixture fraction (left) and temperature (right) profiles and their corresponding fluctuations for selected axial locations of the reacting HM3e configuration. Symbols depict the experiments, the solid lines represent the simulation based on the steady flamelet chemistry, the dashed lines show the Monte Carlo PDF method also using a steady flamelet chemistry while dotted lines depict the Monte Carlo PDF transport employing a FGM chemistry formulation.

underestimate the temperature level and additionally predict a radial increase of the temperature above the bluff body. Interestingly, the peak at the outer edge of the bluff body that has been observed in the simulations of the HM1e configuration is not predicted by both steady flamelet calculations, but by the MCPDF FGM simulation to some extent. The underestimation of the temperature level by the statistical methods reflects the slightly increased mixture fraction in the MCPDF simulations in this region. Due to the proximity to the stoichiometric mixture fraction in this area, the very small variations in the mixture fraction cause relatively large deviations in the temperature profiles. For the following measuring plane at $x = 30\,mm$ the steady flamelet model in the finite volume framework still achieves almost perfect matching with the experiments, while the Monte Carlo methods obtain too low values for lower but increased values for larger radii. This is related to the temperature gradient mentioned previously in radial direction, which has been observed in the first axial position. In the HM1e configuration, the experimentally analyzed planes at $x = 45$ and $65\,mm$ showed a strong dependency on the turbulence-chemistry interaction in terms of the sub-filter PDF modeling that has been described in detail in section 5.3.4. The same behavior seems to be present in the HM3e case, which is apparent at $x = 45\,mm$. Each depicted temperature profile in this plane shows a behavior, which is consistent to the findings in the previous validation configuration HM1e. The radial temperature gradient in the rich mixture starting from the centerline

is captured nicely by all simulations, but large differences can be seen in the temperature profile within the lean side of the flame. The FV SF model presents a large difference to the measured profile, which is related to the presumed β-PDF approach for modeling the sub-filter mixture distribution. As described earlier, the β-function is not suitable for an adequate representation of the sub-filter PDF close to the mixture fraction limits zero or unity. In this particular case, the mixture fraction is very close to zero and a large sub-filter variance due to the mixing layer is present in this region. Related to the inadequate reproduction of the actual PDF shape, an overestimated amount of cold air is assumed to be present in the considered control volumes, which in turn leads to a decreased temperature prediction. In contrast, the profile obtained by the Monte Carlo PDF steady flamelet method shows an increased temperature distribution, while the MCPDF FGM simulation agrees perfectly with the experiments. This difference between the two statistical numerical methods can be explained by finite-rate chemistry or scalar dissipation effects which cannot be captured with the steady flamelet formulation. The profiles at $x = 65\,mm$ depict an unexpected change in the behavior of the results. The FV SF method achieves the best agreement with the measurements whereas an overestimation of the temperature is obvious in the Monte Carlo based simulation profiles. The discrepancy between those two lines can again be reasoned by the appearance of finite-chemistry effects, which leads to the visible temperature decrease. A general overestimation of the temperature by all numerical methods is observable in the last measuring plane, where the statistical methods obtain even higher values than the FV based simulation. Further information about the reasons for the given characteristics in the context of the temperature prediction have to be taken from scatter plots, which are given below. The profiles of the temperature fluctuations show similar characteristics as the mean profiles. The first two upstream locations do not present major differences between the simulations themselves and in reference to the experiments, while at the most interesting measuring planes at $x = 45$ and $65\,mm$ the Monte Carlo and the finite volume approaches show variations in the general prediction of the fluctuations. The observed shift of the profile peaks towards the centerline happens further upstream in the FV SF simulation compared to the experiments and the results from the statistic approaches. For additional information, radial time averaged profiles of the filtered OH mass fraction $\widetilde{Y}_{OH}$ and the fluctuations are provided in figure 5.33. In contrast to the time averaged hydroxyl radical profiles in the HM1e configuration, the HM3e flame shows a broad distribution of this property in vicinity of the bluff body. The low Reynolds number case HM1e is characterized by the narrow flame front, which is depicted by the OH radical, while in the HM3e case the mixture in proximity of the bluff body ranges uniformly around stoichiometry. This means, that the flame front occupies the complete radius of the bluff body close to the inflow plane. The simulations predict a different behavior, where the finite volume discretization achieves the closest profiles to the measurements. However, the statistical transport schemes compute the location of the flame front as in the previous case at the outer edge of the bluff body and hence underestimate the amount of OH radical closer to the centerline. A perfect agreement with the experiments is obtained by the FV SF simulation at $x = 30\,mm$, where the characteristics of the simulations are unchanged. In the following profiles for $x = 45$ and $65\,mm$, analog observations to the temperature profile can be made. The finite volume approach now completely underestimates the magnitude level of $\widetilde{Y}_{OH}$, while the Monte Carlo PDF

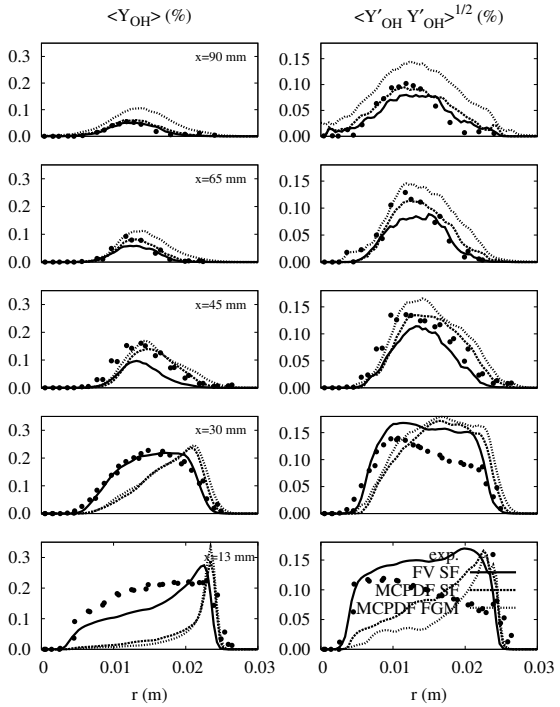

Figure 5.33.: Time averaged radial OH mass fraction (left) profiles and the corresponding fluctuations (right) for selected axial locations of the reacting HM3e configuration. Symbols depict the experiments, the solid lines represent the simulation based on the steady flamelet chemistry, the dashed lines show the Monte Carlo PDF method also using a steady flamelet chemistry, while dotted lines depict the Monte Carlo PDF transport employing a FGM chemistry formulation.

methods show very good predictions in this case. As in the temperature comparison of this particular measuring plane, it seems as if the inclusion of finite-rate chemistry effects through the application of the FGM formulation yields even better results than the steady flamelet model in the MCPDF context. However, the MCPDF FGM approach achieves increased levels of the OH radical for the last two axial locations, while steady flamelet approaches, especially the one employed in the Monte Carlo PDF framework, perform very well in terms of magnitude and general shape of the profile. The fluctuation profiles confirm the findings which have been made in the filtered mean values. Especially the wrong prediction of the flame front at the outer bluff body edge by the MCPDF methods is reflected in the fluctuation profiles close to the inlet. At the remaining axial locations similar behavior as in the mean filtered values can be observed. In order to investigate the differences between the applied transport schemes and chemistry models, respectively, scatter plots of the filtered temperature as well as the OH mass fraction are presented in the figures 5.34 and 5.35. Both figures are limited to the interesting measuring planes of $x = 45$ and $65\,mm$ where finite chemistry effects are expected and deviations in the simulated profiles are apparent, but not obviously explainable. From left to right, the four columns of the figures depict the experiments, the steady flamelet chemistry in the finite volume context, the same chemistry applied in the Monte Carlo PDF framework and the Monte Carlo PDF method combined with the FGM approach. The main feature in

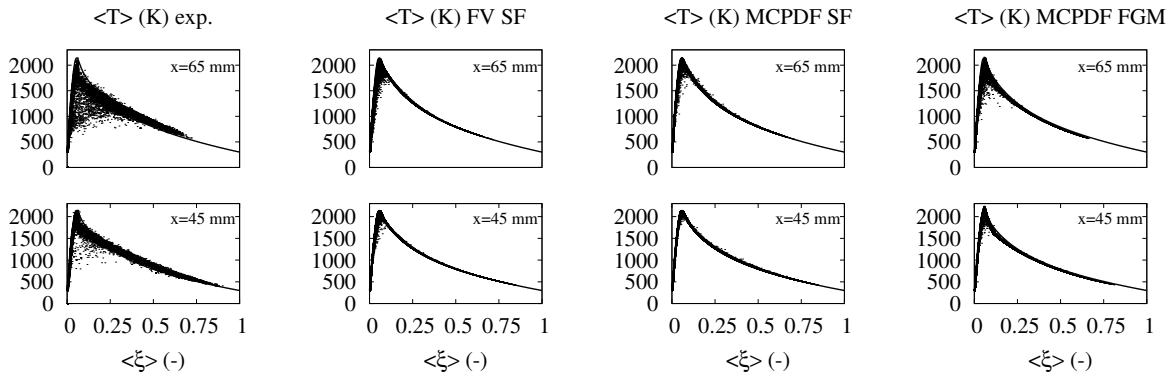

Figure 5.34.: Scatter plots of the filtered temperature versus the filtered mixture fraction for the measured axial positions $x = 45,\ 65\,mm$. The columns depict the experiments on the left, the finite volume steady flamelet simulation results in the second column, the Monte Carlo PDF steady flamelet solutions in the third and MCPDF employing FGM chemistry in the right column. In addition, the steady flamelet solution for a strain rate of $a = 10s^{-1}$ is shown as a reference in each plot, illustrated by the solid line.

the temperature plots is the increased scatter in proximity of the stoichiometric mixture fraction. The experiment illustrates a strong increase of the scatter from $x = 45$ to $65\,mm$ which indicates a raised influence of finite-rate chemistry effects or raised scalar dissipation rate fluctuations in this region. For the axial location at $x = 45\,mm$ it is apparent that both steady flamelet based simulations do not include scalar dissipation rate effects, but rather generate their scatter by sub-filter variance effects only. Since the HM3e case provides a highly turbulent flow field and correspondingly areas of high scalar dissipation and local extinction, the influence of sub-filter variance is not sufficient to reproduce the adequate scatter given by the experiments. Besides that, a very interesting feature in the FV SF simulation is the increased appearance of scatter on the lean branch of the flamelet, which corresponds to the shortcomings in the sub-filter PDF reproduction by the β-function. In comparison with the two alternative simulations as well as with the experiments, this behavior in the lean branch cannot be observed elsewhere. However, the scatter in the rich branch of the depicted flamelet given by the experiment is not captured by any illustrated simulation, but can be observed in the MCPDF FGM computation to some extent. The identical behavior is apparent in the following measuring plane, where the scatter in the MCPDF FGM simulation is increased around the stoichiometry but nevertheless does not reach the dimensions as shown by the experiments. This in turn is the reason for the overestimation of the temperature levels as depicted in the comparison of the radial profiles in figure 5.32. The lack of scatter close to stoichiometry is most likely caused by an inaccurate prediction of the progress variable as it has been observed in the HM1e configuration as well. For a detailed analysis of the OH mass fraction prediction, figure 5.35 illustrates the scatter plots of $\widetilde{Y}_{OH}$ for the two axial locations $x = 45$ and $65\,mm$ because of the supposed influence of increased scalar dissipation and finite-rate chemistry effects. Again, the four columns include, from left to right, the experiments, both steady flamelet formulations, in FV and in MCPDF context and furthermore, the MCPDF with the enhanced FGM chemistry model. It should be kept in mind that the

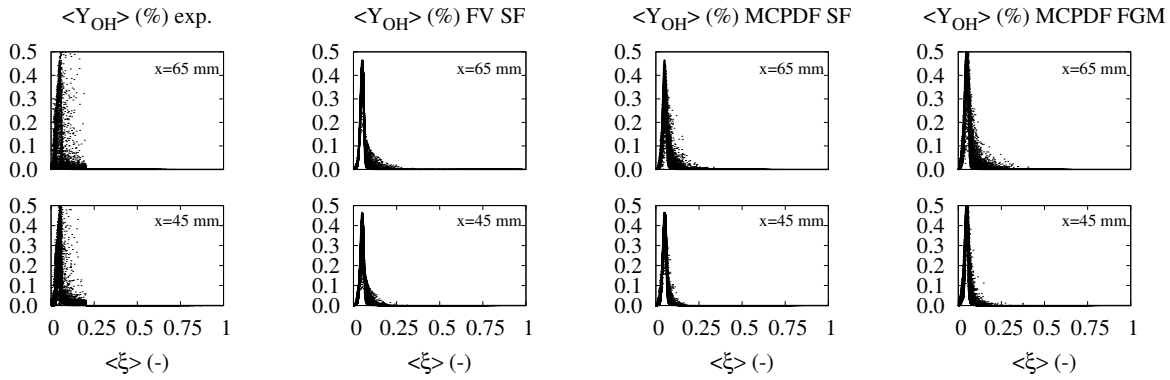

Figure 5.35.: Scatter plots of the filtered OH mass fraction versus the filtered mixture fraction for the measured axial positions $x = 45,\ 65\,mm$. The columns depict the experiments on the left, the finite volume steady flamelet simulation results in the second column, the Monte Carlo PDF steady flamelet solutions in the third and MCPDF employing FGM chemistry in the right column. In addition the steady flamelet solution for a strain rate of $a = 10s^{-1}$ is shown as a reference in each plot, illustrated by the solid line.

SF formulation still includes only a single strain rate and hence is not able to consider scalar dissipation effects, but rather generates scatter around the flamelet by sub-filter variance only. From a theoretical point of view, the MCPDF FGM method is the only model to predict reasonable results for this highly turbulent configuration. Nevertheless, both SF simulations achieve adequate results, which needs to be analyzed as well. The depicted OH mass fraction scatter plots do not show distinct differences between the experiments and the simulations in terms of the scatter intensity. However, the most interesting feature of the given plots is the occurring peak value at stoichiometry for the measurements. This stands for a very low value of scalar dissipation in this point which corresponds to strain rate magnitudes even lower than $a = 10\,s^{-1}$. Unfortunately, only the FGM method can implicitly represent scalar dissipation effects while the single strain rate SF simulations are limited to values which can directly be achieved by the presumed flamelet or by mixing of different parts of it. In the present case, the MCPDF FGM simulation even overestimates this effect of low scalar dissipation and hence achieves to high hydroxyl mass fraction profiles for the two selected planes.

5.4.2.2. Conclusions

The HM3e configuration has been analyzed in terms of the mixing, temperature and OH mass fraction fields. Therefore, three different combinations of numerical transport schemes and chemistry formulations have been used which are all based on the identical velocity field as shown in the previous section. The combinations are a finite volume discretization with a presumed β-PDF steady flamelet scheme, a Eulerian Monte Carlo PDF method coupled with a steady flamelet chemistry formulation and a Eulerian Monte Carlo PDF method providing a joint PDF of the mixture fraction and a progress variable for the enhanced FGM chemistry model. The analysis of the scalar distribution has been performed employing time averaged experimental data as well as scatter information. Based on these investigations, the main findings and hypotheses that had been made

within the detailed analysis of the HM1e case, have also been observed and confirmed. Especially the shortcoming of the presumed β-function in representing the sub-filter PDF at the limits of the mixture fraction space has shown its impact on the temperature and the hydroxyl radical predictions within the flame front region. In addition, the application of the enhanced FGM chemistry formulation achieved adequate results in regions with high scalar dissipation, which could not be reached by the single strain rate chemistry simulations. However, the presented comparison of the implemented models in terms of the scalar distributions has not revealed one unique scheme that reflects all features of the experiments, but rather pointed out the pros and cons of each model.

Chapter 6.

Piloted Methane-Air Jet Flame

The considered turbulent combustion configuration in this section is also part of a target flame series of the TNF workshop [37] as the extensively analyzed Sydney bluff body series. The series includes measurements of different piloted jet flames, which differ in terms of their jet related Reynolds number, ranging from $\mathrm{Re}_{\mathrm{jet}} = 13400$ to 44800. The experimental investigations have been performed at the Livermore Sandia National Laboratories, US, and the Technische Universität Darmstadt and have been published in [1], [2] and [91].

The geometry is based on a burner developed at the University of Sydney, Australia [64] and consists of a central fuel nozzle with a diameter of $D_{\mathrm{jet}} = 7.2\,mm$ and a coaxially arranged pilot burner with $D_{\mathrm{pilot}} = 18.2\,mm$. This configuration is embedded in a wind tunnel providing a uniform low speed air coflow around the nozzle geometry in order to protect the flame from extrinsic interferences. Even though the applied fuel is a premixed composition of three parts air and one part methane CH_4 by volume, the flames show an obvious non-premixed combustion mode which is related to the comparably high mixing rates. The stoichiometric mixture fraction of the used fuel is $\xi_{\mathrm{st}} = 0.351$. The flame stabilizing pilot is operated in lean conditions with a premixed fuel composition of acetylene C_2H_2, hydrogen H_2, air, carbon dioxide CO_2 and nitrogen N_2.

In the present work, simulations of Sandia flame D have been performed, which is defined by the bulk velocities of $U_{\mathrm{jet}} = 49.6\,m/s$ for the fuel jet and $U_{\mathrm{pilot}} = 10.8\,m/s$ for the pilot flow, while the coflow velocity is set to $U_{\mathrm{co}} = 0.9\,m/s$. The Reynolds number based on the fuel jet's properties is $\mathrm{Re}_{\mathrm{jet}} = 22400$. Figure 6.1 shows the inlet boundary conditions for the velocity and the geometry together with a snapshot of the mixing field on the left which is supplemented with the line of stoichiometry and the temperature distribution on the right. It can be seen that the configuration is characterized by a narrow but long flame with a small opening angle. By comparison of the two illustrated property fields, the consistency of the stoichiometry with the position of the flame front, depicted by the high temperatures, is clearly recognizable. It is also observable how the flame front develops from the hot pilot exhaust gases and evolves further downstream in a non-premixed combustion mode with a flame front in the mixing layer rather than in the fuel rich mixtures. Another interesting aspect of the flame is the continuous change of the temperature field which is strongly affected by the flame front in proximity to the nozzle region, but changes further downstream to a more uniform distribution of hot gas, which is directly related to the enhanced mixing in this range.

The following analyses of the Sandia flame D are mainly focused on the influence of the statistical Eulerian Monte Carlo transported PDF approach in comparison with the commonly applied finite volume presumed β-PDF method. This especially includes the

confirmation of the findings and hypotheses that have been made during the intense investigation of the Sydney flame configuration. Therefore, the studies within the framework of this seemingly more simple validation test case are concentrated on the impact of the β-PDF presumption on the prediction of the thermo-chemical properties. Preliminary results of a performed Monte Carlo PDF simulation combined with a FGM chemistry formulation showed inadequate predictions of the flame length and hence are not described in this work.

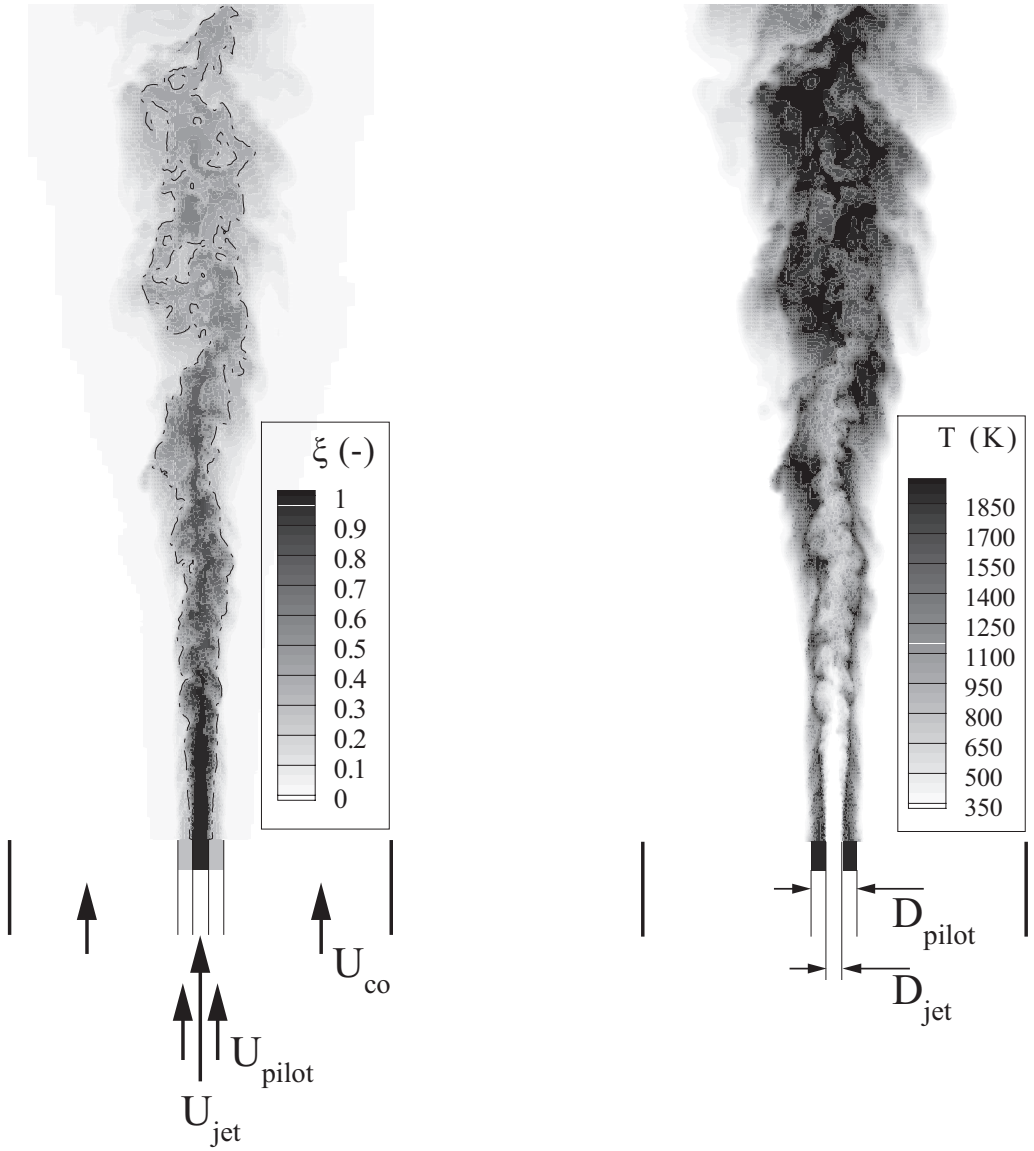

Figure 6.1.: Sketch of the Sandia piloted jet flame geometry with a snapshot of the mixing field (left) and the temperature distribution (right) of the case D. The dashed line in the mixing field plot additionally depicts the stoichiometric value of $\xi_{st} = 0.351$.

6.1. Experiments

As mentioned above, the experiments of the Sandia flame series have been performed at the Sandia Laboratories in Livermore where the scalar data was measured, and at the Technische Universität Darmstadt where the velocity distribution was evaluated.

The experiments in Darmstadt have been performed using two component Laser-Doppler Anemometry (LDA) providing axial and radial velocity data, while the scalar measurements have been obtained by Raman/Rayleigh and CO-LIF techniques. For a detailed description on uncertainties in the measurements, the reader is referred to the publications by Barlow et al. [1], [2] and by Schneider et al. [91]. The experimental data include time averaged axial and radial profiles of the velocities and scalars at selected measuring planes as well as instantaneous scatter data for distinct scalars. The comparisons of the obtained simulation results will hence use most of this provided data to achieve a large variety of interpretable data.

6.2. Sandia Flame D

Unfortunately, the series of the piloted jet flames does not provide an isothermal case, in which a detailed velocity validation could be performed. However, as already mentioned, the investigations in the present work are not mainly focused on achieving accurate results of selected test configurations, but rather to analyze influences and sensitivities of LES sub-models by the additional information available from the implemented Eulerian Monte Carlo PDF method. In this context, the measurements act more as a reference for the evaluation as an ultimate ambition. The Sandia piloted jet flame D is described as a configuration with a small degree of local extinction, but a comparably high Reynolds number at the same time which is desirable for turbulence model validation.

6.2.1. Validation of the Simulated Velocity Fields

The performed analysis for the considered Sandia piloted jet flame D is actually focused on the influence of sub-filter PDF modeling and the correlated sensitivity of the scalar field distributions. However, in turbulent combustion problems the underlying turbulent velocity field plays a major role for the global performance of numerical simulations and hence the quality of the obtained results. Therefore, the velocity field, which is kept unchanged for the investigations on the sub-filter PDF modeling, is analyzed in the following section.

6.2.1.1. Numerical Setup

The computation of the velocity field is performed using a finite volume discretization with a combination of the presumed β-PDF approach for consideration of turbulence-chemistry interaction and a single strain rate ($a = 10\,s^{-1}$) steady flamelet model. The numerical domain has the dimensions of $52\,D_{\text{jet}}$ in axial, $10\,D_{\text{jet}}$ in radial and 2π in azimuthal direction, which is correspondingly resolved by 640, 50 and 32 control volumes. The control volumes are equidistantly distributed in axial and tangential direction, while in

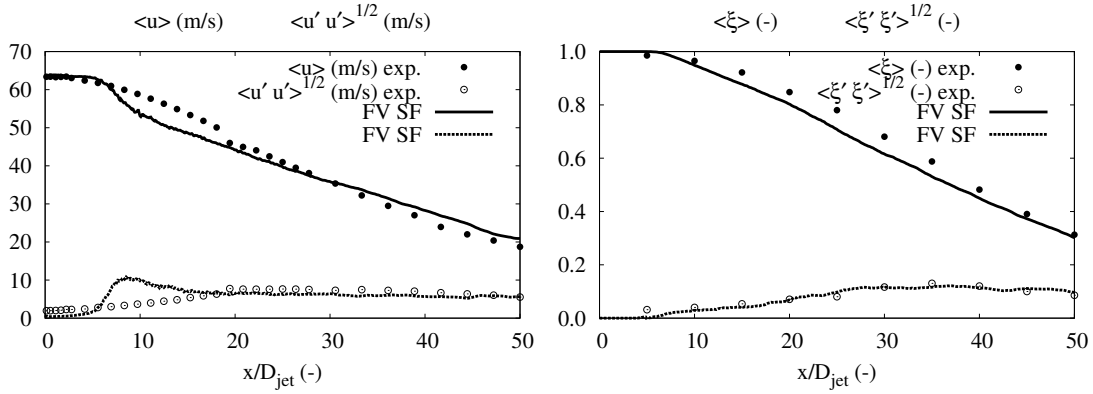

Figure 6.2.: Axial profiles of mean and fluctuation at the centerline of the streamwise velocity (left) and the mixture fraction (right) obtained with the finite volume discretization combined with a steady flamelet chemistry formulation. The experimental data is depicted by the full circles for the mean and the hollow circles for the fluctuation values. The correlated simulation results are given by the solid (mean) and the dashed lines (fluctuation).

radial direction a refinement towards the centerline is realized. The resolution correlates to an approximate cell width of $\Delta x \approx 0.6\,\mathrm{mm}$ in axial and radial direction close to the nozzle. The total number of cv in this case adds up to about one million. The inlet region is modeled using an immersed boundary technique, with a penetration depth of approximately $12\,mm$ into the computational domain. For a reasonable time-dependent description of the velocity boundary conditions, the artificial inflow turbulence generator is used, which superposes turbulence-like structures on the experimentally prescribed velocity profiles. The tabulated and preintegrated steady flamelet chemistry is resolved using 200 sampling points in mixture fraction and 100 in sub-filter variance space. The simulation has been performed parallel on a 16 core machine.

6.2.1.2. Results

The results of the velocity distribution are all calculated using a steady flamelet model, as mentioned before. Since this chemistry formulation depends strongly on the mixture fraction, figure 6.2 depicts the streamwise velocity (left) as well as the mixture fraction (right) distribution on the centerline. This is done in order to give a more detailed insight into the interdependency of the two properties. Additionally, the axial profiles of the corresponding fluctuations are depicted in the same plots. The illustrated profiles for the axial velocity show a clear shortcoming of the simulation which finds expression in a drop of the mean value at $x/D_{\mathrm{jet}} = 10$ of approximately $10\,m/s$ while the fluctuations at this point show a vast increase. This behavior indicates an energy transfer from the large scales to small ones in this region and has been observed in earlier simulations [46], [102]. The reason is assumed to be a hardly resolvable thin mixing and boundary layer at the nozzle, which leads to the differences in here. For $x/D_{\mathrm{jet}} \geq 20$ the deviations are no longer present neither for the mean nor the fluctuations the results show an adequate quality. Nevertheless, the impact of this characteristic velocity behavior is also visible in the mixture fraction profile. Due to the increased turbulent mixing indicated by the high

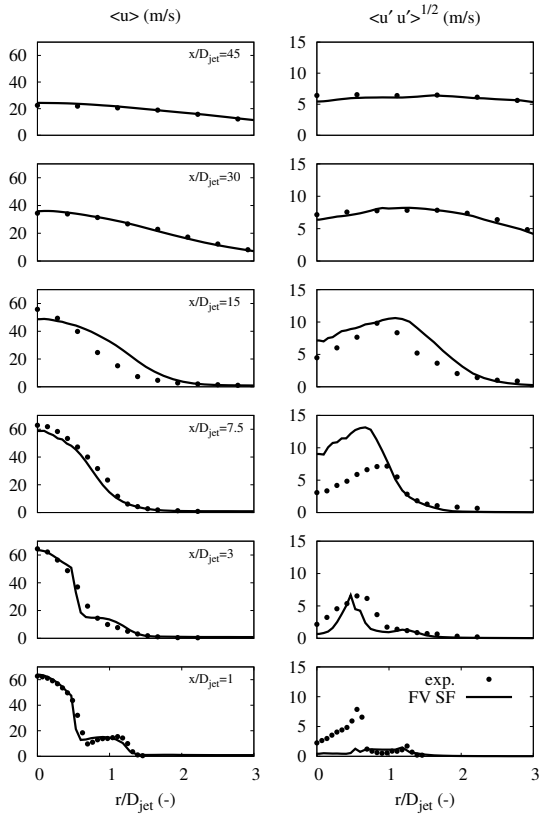

Figure 6.3.: Radial profiles of the axial velocity (left) and the correlated fluctuations (right) for selected measuring planes. Symbols depict the experimental data, while the solid line presents the steady flamelet LES results.

velocity fluctuations, the mean mixture fraction profile at the centerline is underestimated, even so the principal decay is represented reasonable. However, the fluctuation level of $\widetilde{\xi}$ is predicted correctly over the entire range.

In order to see the velocity behavior apart from the centerline, figure 6.3 depicts radial profiles of the mean (left column) and the fluctuations (right column) for the streamwise velocity at the selected measuring planes $x/D_{\text{jet}} = 1$, 3, 7.5, 15, 30 and 45. Considering the mean filtered velocities in the left column, the simulation achieves good matching with the experiments up to the plane at $x/D_{\text{jet}} = 7.5$. However, in the first two upstream locations, the impact of the hardly resolvable thin shear layer can be observed between the main jet and the pilot inlet. The simulation does not capture the early mixing of both streams but predicts a more angular profile especially for $x/D_{\text{jet}} = 3$, where the measurement already shows a smooth behavior in radial direction. At the same time, the fluctuations, depicted in the right column, show a tremendous ascent within the described shear layer which exceeds the experimental data by 100 % in $x/D_{\text{jet}} = 7.5$ in proximity of the centerline. Downstream from this plane, the mean velocity profile is strongly influenced by the increased momentum transport by turbulent motions which leads to an overprediction of the opening angle of the fuel jet, as apparent in $x/D_{\text{jet}} = 15$. At this axial location, the velocity close to the centerline is underestimated, while apart from

there, the flow speed shows an opposite characteristic. Due to dissipation effects further downstream, the turbulent fluctuations are damped and both, mean and root mean square values obtained by the LES are in good agreement with the experiments.

6.2.1.3. Conclusion

Velocity results obtained by a finite volume based LES method coupled with a steady flamelet chemistry formulation have been presented and compared with experimental data. Therefore, both axial and radial profiles of the mean and the fluctuation of the streamwise velocity have been employed. The calculation shows some shortcomings in the prediction of the mean values in the region from $10 \leq x/D_{\text{jet}} \leq 20$, with an underestimation of the mean value within the fuel jet, while the corresponding fluctuation is enormously increased. This behavior might be traced back to an unresolved shear and mixing layer at the nozzle. However, the results are reasonable except for the described issues and therefore represent a good basis for the following sub-filter PDF analysis. In this context, the problems in the velocity prediction can definitely not be neglected, but have to be kept in mind for the interpretation of the scalar fields.

6.2.2. Influence of the Sub-filter PDF Model on the Scalar Distributions

Within the following section, the influence of the applied sub-filter PDF model is analyzed. Therefore, scalar results of the Eulerian Monte Carlo method are compared to the finite volume presumed β-PDF solutions. The scalar results include mixture fraction, temperature and OH mass fraction, where both latter ones are directly affected by the turbulence-chemistry interaction and the employed chemistry model. From the previous investigations of the bluff body flames and the resulting hypotheses, the influence in the scalar prediction for the present jet flame should not be as apparent. This is related to the relatively high stoichiometric mixture fraction value of $\xi_{\text{st}} = 0.351$, which is located far enough from the limits of zero and unity such that the β-function yields high accuracy in reproducing the actual sub-filter PDF within the flame front.

6.2.2.1. Numerical Setup

The numerical setup of the finite volume β-PDF approach has already been described in the previous section about the velocity field calculation. The Monte Carlo PDF method is coupled one-way to the LES solver as depicted in figure 5.8, which means that there is no feedback from the MCPDF method to the flow solver. Hence, the velocity field for both combustion models is identical and is consequently not responsible for any differences within the obtained scalar profiles. The transported sub-filter PDF is discretized by 50 stochastic particles per control volume as in the previous HM1e case, with a comparable spatial resolution of the computational grid. For chemistry representation, also a tabulated single strain rate steady flamelet concept has been employed, which is resolved with 260 sampling points in mixture fraction space. The micromixing term within the PDF transport equation is closed by the modified Curl's model.

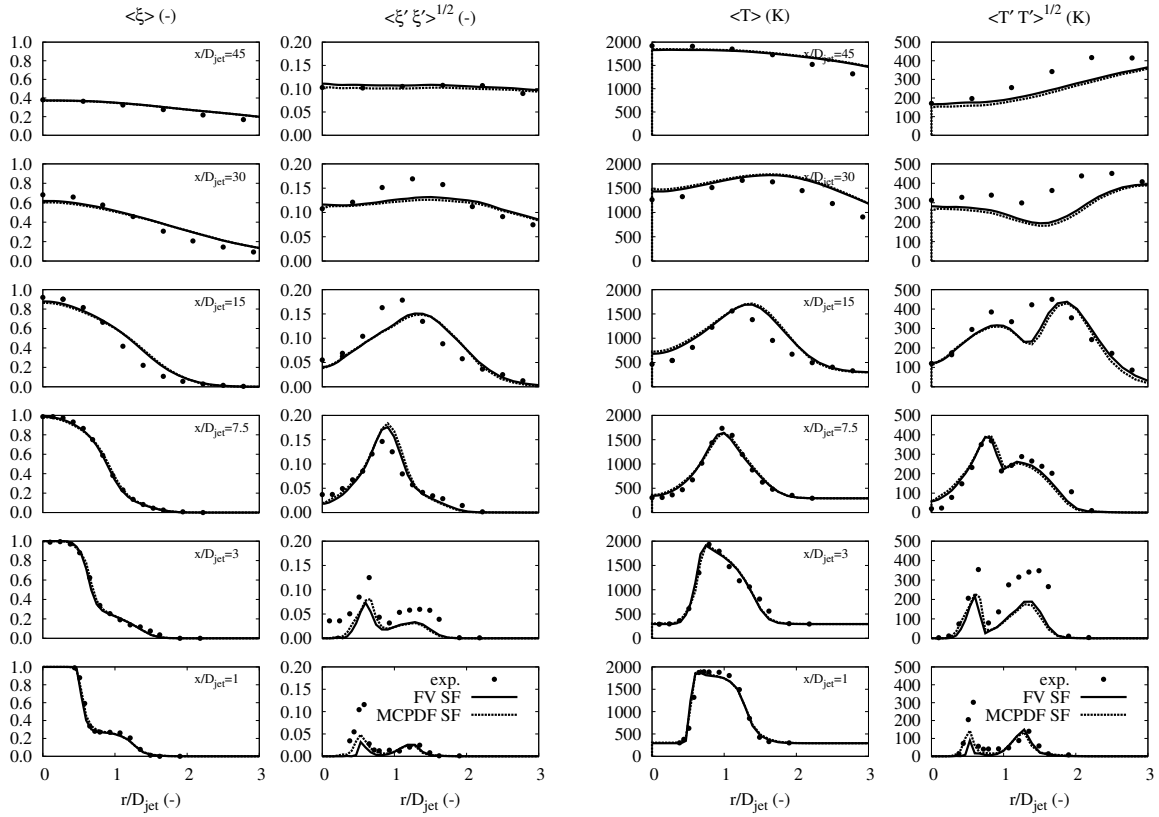

Figure 6.4.: Time averaged radial profiles of the filtered mixture fraction (left) and temperature (right) together with their corresponding fluctuation for selected measuring planes. Symbols depict the experimental data, while the solid line presents the finite volume β-PDF based simulation and the dashed line depicts results obtained by the transported Monte Carlo PDF approach.

6.2.2.2. Results

The following figures 6.4 and 6.5 of time averaged scalar data are structured in the same way and hence will be described once for all. As in the previous sections, each scalar is described by its mean profiles (left column) and the corresponding fluctuations (right column) in time, where symbols depict experimental data, the solid lines stand for the finite volume β-PDF based calculation and the dashed lines represent the Monte Carlo transported PDF approach. Each column includes six different measuring planes at $x/D_{\text{jet}} = 1$, 3, 7.5, 30 and 45 and depicts the radial distribution of the considered quantity from the centerline up to $r/D_{\text{jet}} = 3$. Figure 6.4 illustrates the filtered mixture fraction profiles. As expected, both calculation results achieve almost an identical mixing field, which finds expression in the two lines lying on top of each other in each measuring plane. The corresponding fluctuations show only slight differences in the profiles, which can be traced back to immanent statistical errors of the Monte Carlo PDF transport method. Additionally to the already described centerline profile in figure 6.2, the impact of the velocity field issues can be observed in these radial profiles. Principally, the mean mixture fraction shows an identical behavior as the streamwise velocity, with a very good matching

of the measurement data in the first three upstream planes, followed by an overestimated fuel jet opening angle at $x/D_{\text{jet}} = 15$. This in turn leads to an underestimation of the mixture fraction gradient in radial direction, which is apparent in the subsequent planes $x/D_{\text{jet}} = 30$ and 45. The illustrated results again validate the consistency of the statistical Eulerian Monte Carlo method for the transport of a passive scalar like the mixture fraction in the present case.

The temperature profiles, depicted in figure 6.4 (right) are a more interesting quantity to analyze, based on its direct dependency on the chosen turbulence-chemistry model and chemistry formulation. However, even the temperature profiles do not reveal any major deviations between the two simulation approaches, but rather depict an almost perfect agreement for the mean as well as the fluctuation profiles of both simulations. The comparison with the measurements shows accurate temperature predictions up to the plane of $x/D_{\text{jet}} = 7.5$, but a slight shift of the flame front to larger radii for the last three considered axial locations which is again caused by the inaccurate velocity results. The fluctuation profiles illustrate an underestimation of the turbulence in vicinity of the nozzle, most probably also caused by the issues related to the hardly resolvable thin shear layer. Nevertheless, the profiles of the temperature approve the expected behavior that due to the relatively high stoichiometric mixture fraction, the sub-filter PDF can adequately be reproduced by the presumed β-function approach.

The alternative dependent scalar analyzed in this section is the filtered hydroxyl radical's mass fraction $\widetilde{Y}_{OH}$, of which the time averaged radial profiles are depicted in figure 6.5. In contrast to the other depicted profiles, the OH mass fraction is overestimated in the first measuring plane with a distance of a jet diameter from the inlet. This is definitely related to the restrictions made by the single strain rate flamelet base, which cannot reproduce the high scalar dissipation effects in the region close to the nozzle. While keeping this in mind, the experiments are quite accurately matched in terms of the overall trend, except for the radial shift of the flame front due to the velocity predictions. In contrast to the mean profile in the first measuring plane, the fluctuations show a very good agreement with the experiments, which is an accumulation of errors based on the underestimation of the mixture fluctuation with an overestimation of $\widetilde{Y}_{OH}$. Even for the very sensitive quantity $\widetilde{Y}_{OH}$, deviations between the two different simulation approaches are not apparent, which again confirms the hypothesis made regarding the PDF modeling. In addition, a detailed analysis of instantaneous sub-filter PDF shapes of the mixture fraction is given in figure 6.6. The plot shows the sub-filter PDF for three axial locations $x/D_{\text{jet}} = 3$ (left column), 7.5 (center column) and 15 (right column) of adjacent control volumes over the flame front. The step function depicted by the solid line represents the discrete Monte Carlo PDF reproduced from the stochastic particles, while the dashed line stands for the β-function determined with the same mean and unmixedness values as the MCPDF. On the bottom of each subplot, the considered particle ensemble is illustrated by vertical lines to get an impression of the actual distribution within the distinct control volume. The plots for the $x/D_{\text{jet}} = 3$ plane represent a cross section $r/D_{\text{jet}} = 0.53$ to 0.825 which corresponds to the position of the flame front in this region. The PDF in the first subplot is predominated by a fuel rich mean mixture fraction and a large unmixedness, which is not accurately reproduced with the β-function presuming an attached single peak in the region of pure fuel. Due to the existent mean mixture fraction value far off stoichiometry,

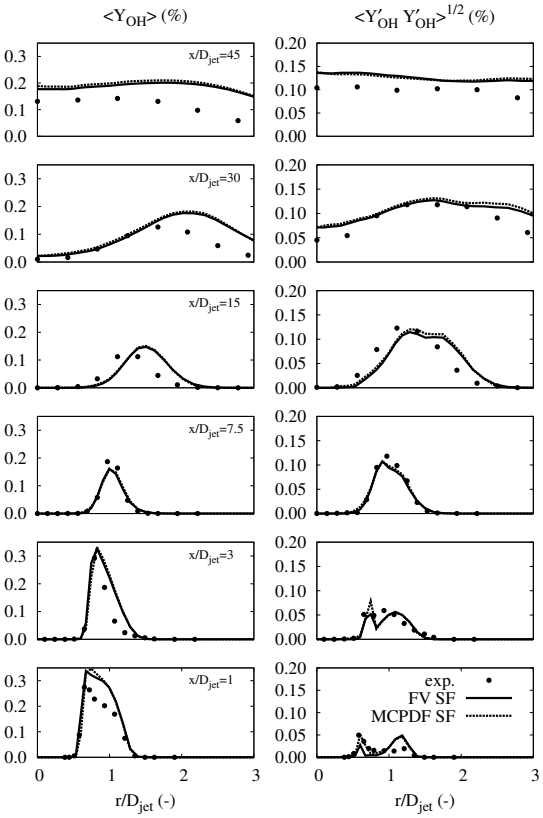

Figure 6.5.: Radial profiles of the time averaged filtered OH mass fraction. The results for the mean values are depicted in the left column and the correlated fluctuations are shown on the right. Measurements are depicted by symbols, FV β-PDF results are given by the solid, while MCPDF profiles are represented by the dashed lines.

the influence of this inaccuracy cannot be observed in the temperature or OH mass fraction profiles. For the next control volume with a larger distance from the centerline, the particle distribution shows a wide range of existent mixture fraction values, which denotes the location to be within the turbulent mixing layer. The PDF in this control volume is reproduced with an adequate accuracy, but overestimates the fuel lean and rich area. As in the previous cv, the mixture composition is not yet situated within the flame front and hence has no direct impact on the dependent quantities. Proceeding to larger radii and as a consequence closer to the flame front, the sub-filter variances decrease and Gaussian-like functions are presumed by the β-function. These shapes show a good agreement with the reconstructed Monte Carlo PDF and hence similar results are expected within the flame front. The center column provides the PDF for the axial measuring plane at $x/D_{\text{jet}} = 7.5$ where large variances are present for all depicted control volumes. This indicates a broad mixing layer around the flame front. In general, the presumed β-PDF agree very nicely with the actual particle distribution for the first three plotted radial positions. In contrast, the last two cv represent a typical case of the β-function's inability to reproduce PDF shapes with a moderate variance close to the outer limits. For these two cases, the amount of pure air in the mixture and hence in the reaction is overestimated. How-

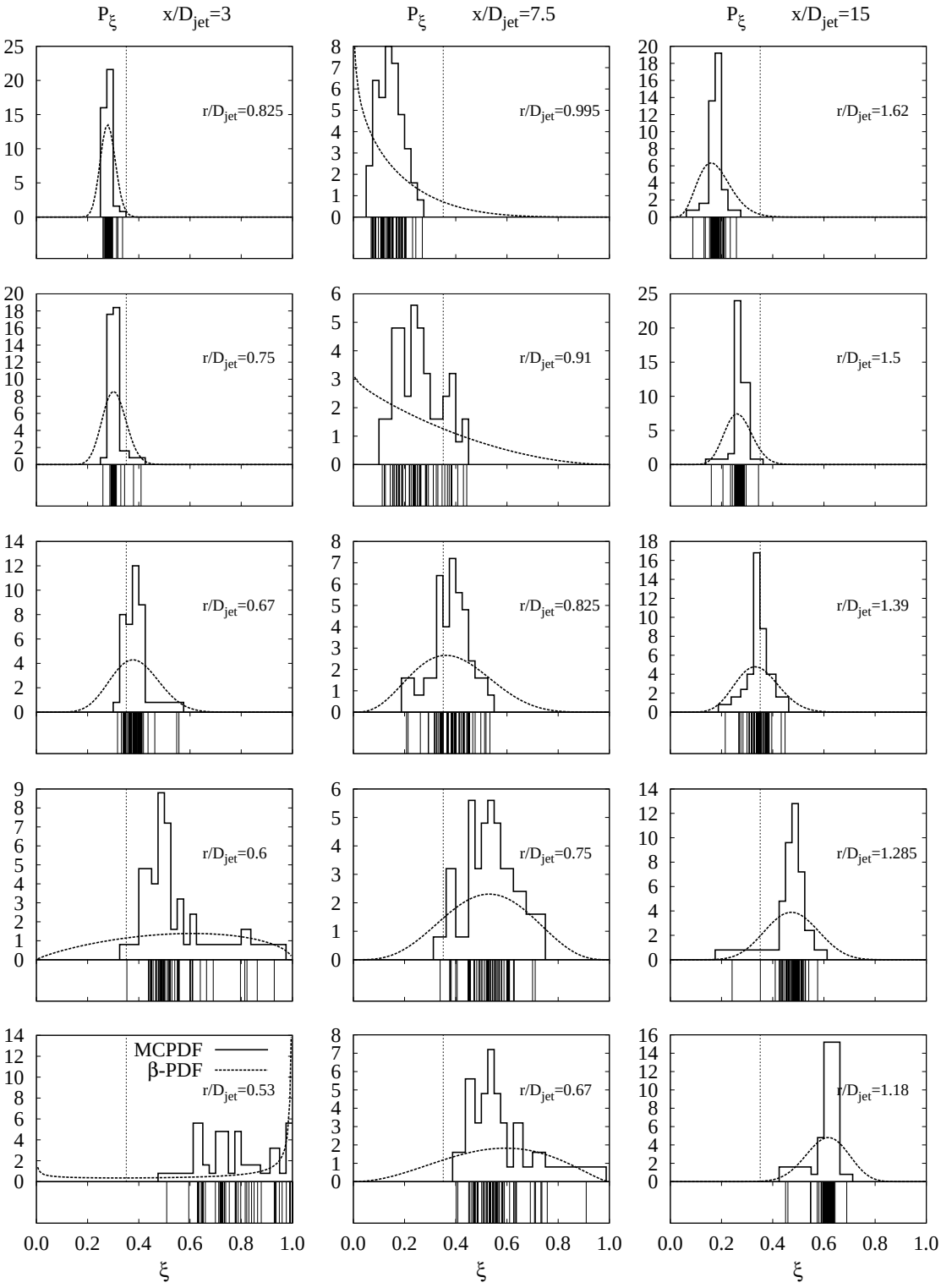

Figure 6.6.: Instantaneous sub-filter PDF obtained from a single time step for three different axial locations $x/D_{\text{jet}} = 3$, 7.5 and 15. For each axial position, the sub-filter PDF are depicted for five radially adjacent control volumes crossing the flame front. The solid line represents the discrete PDF from the Monte Carlo approach, while the dashed line depicts the corresponding β-function obtained by the mean and the unmixedness of the particle ensemble. The vertical lines at the bottom of each subplot illustrate the distribution of the stochastic particles for the considered control volume. For reference, the stoichiometric mixture fraction value is represented by the thin dotted vertical line in each plot.

ever, the distance of the PDF's mean value from stoichiometry and consequently from the actual flame front decreases the influence on the scalar profiles, especially for the OH mass fraction. The right column shows the PDF for $x/D_{\text{jet}} = 15$, where the sub-filter variance is rather small compared to the probability density functions in the previously considered measuring plane. This leads again to an adequate representation of the particle ensemble based PDF shape by the presumed β-function for all depicted control volumes. Conclusively, the β-function shows the same shortcomings in the present case as in the previously investigated HM1e case. However, the presumed PDF shapes are accurate within the range of the flame front around the stoichiometric mixture fraction, which is increased in comparison to the previously investigated bluff-body configurations HM1e and HM3e. That causes the scalar profiles to show no deviations between both simulation approaches.

6.2.2.3. Conclusion

Radial time averaged profiles of the transported mixture fraction, the temperature and the OH mass fraction have been presented. Computed results of a finite volume presumed β-PDF method were compared with transported Monte Carlo PDF profiles. Besides inaccurate predictions in some of the axial cross sections which are caused by the issues in the prediction of the velocity field, both simulations achieved adequate results. Except for minor deviations due to statistical errors in the Monte Carlo method, all scalars show a congruent behavior of the illustrated profiles. As expected, this can be traced back to the good PDF representation with the β-function inside the flame front region. A qualitative comparison of instantaneous sub-filter PDF directly reproduced from the particle information as well as the β-function based on the mean and the variance of the ensemble has been performed. This investigation additionally confirms the hypothesis, that there is a relation between the suitability of the presumed β-PDF and the location of the stoichiometric mixture fraction.

Chapter 7.

Conclusions

The present work focusses on an elaborated analysis of Large Eddy Simulations in the framework of turbulent reacting flows. An Eulerian Monte Carlo PDF transport scheme has been developed and implemented into the existing LES code FLOWSI in order to obtain a sophisticated reference method for detailed investigations of commonly used combustion related LES sub-models. By transporting a statistical representation of sub-filter scalar distributions, additional information for validation of sub-filter PDF models are provided. The obtained results are used as a basis for model assessments in terms of various modeling aspects in general and in the turbulence-chemistry interaction in particular.

The work was initiated with a verification and validation of the introduced quasi second order accurate Monte Carlo transport scheme in a generic pure mixing test configuration. In a similar but reactive framework, the influence of the implemented method on an additional transported reactive scalar has been tested and evaluated, which demonstrated a principal suitability of the new method for additional transported scalars and showed an increase in the order of accuracy to values larger than unity.

The main part of this project is an extensive deliberated analysis of the Sydney bluff body configuration series, including a selected non-reacting and two reactive cases with different Reynolds numbers. For that purpose, the presumed β-PDF steady flamelet based LES code FLOWSI has been used, which was extended by the Monte Carlo scalar transport method. At first, the influence of artificially generated inflow turbulence is evaluated for the non-reacting B4C2 as well as for the reacting low Reynolds number case HM1e in order to find the most adequate boundary condition formulation for the considered cases. Qualitative as well as quantitative comparisons of the velocity and the mixing fields with experiments showed no distinct preference for the usage of the inflow turbulence generator, but rather a strong dependency on the considered case. For the reactive HM1e case, the additionally superposed turbulence structures at the inflow led to a better agreement with the measurements and hence has been used for all further investigations on this burner. Based on these results, the subsequent analysis aimed at the statistical error occurring in the implemented Eulerian Monte Carlo method and showed the characteristic sensitivity on the applied particle density. The obtained results were used to estimate a certain particle density combining a reasonable accuracy with an affordable computational effort.

These general assessments have been used for the investigation on the sub-filter variance model for the mixture fraction, where the implemented scale-similarity based model was evaluated employing corresponding data from the transported PDF approach. The

simulations showed only partial correlation of shortcomings in the considered model and observed disagreements of obtained scalar results with the experiments. This rose the question of the capability of the common presumed β-PDF approach for the representation of the mixture fraction sub-filter PDF. Therefore, a qualitative evaluation of reproduced sub-filter PDF has been performed employing instantaneous particle ensemble information obtained from the Monte Carlo PDF simulation. This analysis led to a very interesting observation, relating the suitability of the presumed β-PDF approach to the existent stoichiometric mixture fraction of the considered configuration. The suitability and hence the accuracy of the predicted results in the flame front decreases for configurations with low stoichiometric mixture fraction values, while for moderate values no large influence is expected.

In addition, the more complex chemistry formulation FGM has been used in combination with the transported PDF method, which provided a joint sub-filter PDF of the mixture fraction and the additionally transported progress variable. Based on this data, the sub-filter PDF shape of the mixture fraction as well as of the progress variable have been analyzed. A comparison of the progress variable's sub-filter PDF shape with presumed β-functions unveiled an inadequate agreement between both and led to the general preference of a δ-PDF presumption as a sub-filter PDF model for this scalar. Furthermore, employing the discrete joint PDF data, the statistical correlation between the mixture fraction and the progress variable has been investigated and the influence of normalizing the reactive scalar has been estimation. The normalization procedure in fact decreases the statistical correlation between the two considered quantities. Therefore it should be applied in common LES for avoiding additional errors caused by an assumed joint PDF splitting.

Another considered aspect in the FGM context was the influence of an alternative definition of the reactive progress variable. This analysis was performed by comparing simulations with two different progress variable definitions: one, based on the CO_2 mass fraction and the other determined by a weighted linear combination of the CO_2 and the CO mass fraction. Both calculations yield comparable results for the thermo-chemical scalars, even though the latter case showed minor shortcomings which could be traced back to the chemistry table generation.

In addition to this detailed and deliberated investigation of the HM1e burner configuration, simulations of the high Reynolds number case HM3e have been made. These analyses were mainly focussed on occurring finite-chemistry effects and the confirmation of the hypotheses made earlier. Some finite-chemistry effects have been observed in this case and have been reasonably predicted by the performed FGM based simulations.

In the end, simulations of a piloted methane air jet flame have been conducted in order to prove the relation between the suitability of the β-PDF assumption and the stoichiometric mixture fraction value. The larger stoichiometry value of the used fuel composition in this configuration represented an adequate counterpart to the Sydney bluff body configurations. The obtained simulation results for this jet flame confirmed the hypothesis by showing comparable accuracy for both, β-PDF and transported PDF.

In general, this work showed a sophisticated approach to make model validation on the basis of a hybrid LES transported PDF method instead of employing DNS data. The findings obtained in this way should show shortcomings in commonly used LES sub-

models and should serve as a basis for future model development in the framework of LES in turbulent combustion.

Appendix A.

Probability Density Function (PDF)

A.1. General Definitions

The usage of stochastic methods allows to exactly describe a given quantity by the entire scope of statistical moments. The other way around, it can be stated, the less statistical moments of a given distribution are known, the less accurate is the statistical description of the quantity. Moments are differentiated by their order, where e.g. the moment of zeroth order represents the mean value and the first order moment characterizes the variance of the given field. A function that includes the entire scope of statistical moments is the so called probability density function (PDF). The definition of the PDF can best be illustrated by figure A.1. In this figure a quantity distribution $\psi(t)$ is shown and an interval $\Delta\psi$ is defined. The sketch on the bottom now demonstrates the intervals Δt where ψ is within the previously defined $\Delta\psi$. On the right, the actual PDF $\mathcal{P}(\psi)$ is given

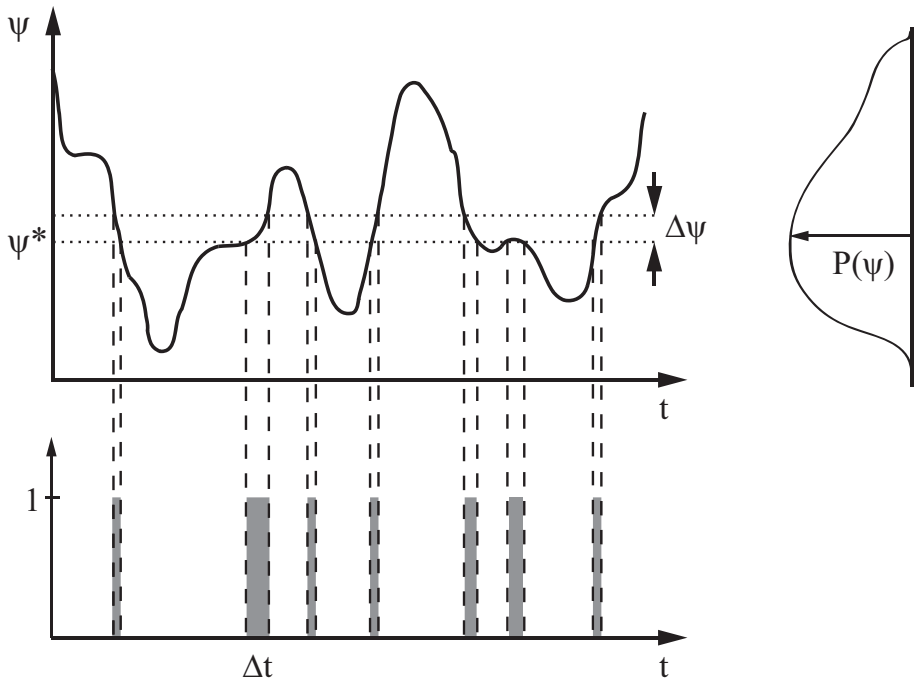

Figure A.1.: Schematic of a one-dimensional quantity distribution ψ over the time t. On the right, the PDF of ψ is depicted, while the plot on the bottom shows the time intervals Δt with $\psi^* \leq \psi \leq \psi^* + \Delta\psi$.

and can be obtained by the following definition. The probability to find $\psi \in [\psi^*, \psi^* + \Delta\psi]$ is determined by $\Delta\psi \cdot P(\Delta\psi)$ using equation A.1.

$$P = \frac{S}{T|\Delta\psi|} \qquad \text{with} \qquad S = \sum \Delta t(\psi^* \leq \psi \leq \psi^* + \Delta\psi) \tag{A.1}$$

Within this equation S defines the sum of all time intervals where ψ is within the defined section $\Delta\psi$ and T stands for the period of observation. The probability density function can be obtained by equation (A.2).

$$\mathcal{P}(\psi) = \lim_{T\to\infty} \lim_{\Delta\psi\to 0} P(\Delta\psi) \tag{A.2}$$

A PDF fulfills by definition the following requirements:

- $\mathcal{P}$ is always positive, since it is a quotient of exclusively positive quantities
- $\mathcal{P}$ asymptotically tends to zero, for $\psi \to -\infty$ and $\psi \to +\infty$
- The probability of $\psi \in [-\infty, \infty]$ is unity,

$$\int_{-\infty}^{\infty} \mathcal{P}(\psi)\, d\psi = 1 \tag{A.3}$$

- $\mathcal{P}$ is differentiable

As said in the beginning, a PDF includes the information of all statistical moments of a distribution. The mean value of ψ can be obtained by

$$\bar{\psi} = \int_{-\infty}^{\infty} \psi\mathcal{P}(\psi)\, d\psi. \tag{A.4}$$

Higher central moments, like the variance with $n = 2$ are calculated using

$$\overline{\psi'^n} = \int_{-\infty}^{\infty} (\psi - \bar{\psi})^n \mathcal{P}(\psi)\, d\psi. \tag{A.5}$$

Vice versa, a PDF can be reconstructed if all statistical moments are available. Two distinct higher central moments must be highlighted in this context. These are in particular the skewness γ_1 and the kurtosis γ_2 which give information about the asymmetry and the peakedness, respectively. The two characteristic values are defined as

$$\gamma_1 = \frac{\overline{\psi'^3}}{\left(\overline{\psi'^2}\right)^{3/2}} \qquad \text{and} \qquad \gamma_2 = \frac{\overline{\psi'^4}}{\left(\overline{\psi'^2}\right)^2}. \tag{A.6}$$

A.2. Derivation of the FDF Transport Equation

A.2.1. Properties of the Dirac δ-function and the Fine-grained Density Function $\mathcal{F}$

For the proper understanding of the derivation of the FDF transport equation, some general mathematical rules for the handling of the δ-function are necessary.

$$\text{(i)} \quad x\delta'(x) = -\delta(x) \tag{A.7}$$

$$\text{(ii)} \quad \frac{d\delta(a-b)}{db} = -\frac{d\delta(a-b)}{da} \tag{A.8}$$

Whereas for the fine-grained density function the following properties apply

$$\text{(iii)} \quad \frac{\partial \mathcal{F}}{\partial t} = \frac{\partial \phi_\alpha}{\partial t}\frac{\partial \mathcal{F}}{\partial \phi_\alpha} = -\frac{\partial \phi_\alpha}{\partial t}\frac{\partial \mathcal{F}}{\partial \psi_\alpha} \tag{A.9}$$

$$\text{(iv)} \quad \frac{\partial \mathcal{F}}{\partial x_i} = \frac{\phi_\alpha}{\partial x_i}\frac{\partial \mathcal{F}}{\partial \phi_\alpha} = -\frac{\partial \phi_\alpha}{\partial x_i}\frac{\partial \mathcal{F}}{\partial \psi_\alpha}. \tag{A.10}$$

With the knowledge of these rules, equation (2.84) can be derived.

A.2.2. Properties of conditional spatially filtered values $\overline{Q|\psi}(x_j, t)$

There are some definitions of the conditional spatially filtered values that are important for the derivation of the FDF transport equation.

$$\text{(i)} \quad Q(x_j, t) = c,\ \overline{Q|\psi}(x_j, t) = c \tag{A.11}$$

$$\text{(ii)} \quad Q(x_j, t) = \hat{Q}(\phi(x_j, t)),\ \overline{Q|\psi}(x_j, t) = \hat{Q}(\psi) \tag{A.12}$$

$$\text{(iii)} \quad \int_{-\infty}^{\infty} \overline{Q|\psi}(x_j, t)\mathcal{P}(\psi; x_j, t)d\psi = \tilde{Q}(x_j, t) \tag{A.13}$$

Bibliography

[1] Barlow, R. S. and J. H. Frank: *Effects of Turbulence on Species Mass Fractions in Methane-Air Jet Flames.* Proc. Combust. Inst., 27:1087–1095, 1998.

[2] Barlow, R. S., J. H. Frank, A. N. Karpetis and J. Y. Chen: *Piloted Methane/Air Jet Flames: Scalar Structure and Transport Effects.* Combust. Flame, 143:433–449, 2005.

[3] Batchelor, G. K.: *Small-scale variation of convected quantities like temperature in turbulent fluid Part 1. General discussion and the case of small conductivity.* J. Fluid Mech., 5(1):113–133, 1959.

[4] Bilger, R. W.: *Turbulent flows with non-premixed reactants.* In Libby, P. A. and F. A. Williams (editors): *Turbulent reactive flows*, pages 65–114. Springer Verlag, 1980.

[5] Bisetti, F.: *Large-eddy simulation and filtered mass density function approach to non-equilibrium turbulent combustion modeling.* PhD thesis, University of California, Berkeley, USA, 2007.

[6] Bisetti, F. and J. Y. Chen: *LES of Sandia Flame D with Eulerian PDF and Finite-Rate Chemistry.* Western States Section/Combustion Institute 2005 Fall Meeting, Stanford University, 2005. Paper number: 05F-33.

[7] Borghi, R.: *Turbulent combustion modeling.* Prog. Energ. Combust., 14:245–292, 1988.

[8] Breuer, M.: *Direkte Numerische Simulation und Large-Eddy Simulation turbulenter Strömungen auf Hochleistungsrechnern.* Shaker Verlag, Aachen, 2002.

[9] Bronstein, I. N. and K. A. Semendjajew: *Taschenbuch der Mathematik.* Teubner Verlagsgesellschaft, Leipzig, 1979.

[10] Buckmaster, J.: *The Mathematics of Combustion.* Society for Industrial and Applied Mathematics, Philadelphia, 1985.

[11] Chen, J. H.: *Direct numerical simulation: Fundamental insights towards predictive models.* Proc. Combust. Inst., 33:99–123, 2011.

[12] Chen, J. Y.: *A General Procedure for Constructing Reduced Reaction Mechanisms with Given Independent Relations.* Combust. Sci. and Tech., 57:89–94, 1988.

[13] Chen, J. Y.: *A Eulerian PDF scheme for LES of nonpremixed turbulent combustion with second-order accurate mixture fraction.* Combust. Theory Modelling, 11:675–695, 2007.

[14] Colucci, P. J., F. A. Jaberi, P. Givi and S. B. Pope: *Filtered density function for large eddy simulation of turbulent reacting flows.* Phys. Fluids, 10(2):499–515, 1998.

[15] Courant, R., K. Friedrichs and H. Lewy: *Über die partiellen Differenzengleichungen der mathematischen Physik.* Mathematische Annalen, 100(1):32–74, 1928.

[16] Dally, B., D. Fletcher and A. Masri: *Modelling of Turbulent Flames Stabilised on a Bluff-Body.* Combust. Theory and Modelling, 2:193–219, 1998.

[17] Dally, B., A. Masri, R. Barlow and G. Fiechtner: *Instantaneous and mean compositional structure of bluff-body stabilized nonpremixed flames.* Combust. Flame, 114:119–148, 1998.

[18] Dally, B. and A. R. Masri: *Turbulent Nonpremixed Flames Stabilised on a Bluff-Body Burner.* International Workshop on Measurement and Computation of Turbulent Nonpremixed Flames, Naples, Italy, 1996.

[19] Deardorff, J. W.: *A numerical study of three-dimensional turbulent channel flow at large Reynolds numbers.* J. Fluid Mech., 41:453–480, 1970.

[20] Deardorff, J. W.: *Three-dimensional numerical study of the height and mean structure of a heated planetary boundary layer.* Bound.-Layer Meteorol., 7:81–106, 1974.

[21] Dopazo, C. and E. E. O'Brien: *Statistical treatment of non-isothermal chemical reactions in turbulence.* Combust. Sci. Technol., 13:99–122, 1976.

[22] Favre, A.: *Equations des gaz turbulents compressibles.* Jour. Mec., 4:391–421, 1965.

[23] Flemming, F.: *On the Simulation of Noise Emissions by Turbulent Non-Premixed Flames.* PhD thesis, Technische Universität, Darmstadt, Germany, 2006.

[24] Forkel, H.: *Über die Grobstruktursimulation turbulenter Wasserstoff-Diffusionsflammen.* PhD thesis, Technische Universität, Darmstadt, Germany, 1999.

[25] Freitag, M.: *On the Simulation of Premixed Combustion Taking Into Account Variable Mixtures.* PhD thesis, Technische Universität Darmstadt, Germany, 2007.

[26] Gao, F. and E. E. O'Brien: *A large-eddy simulation scheme for turbulent reacting flows.* Phys. Fluids A, 5(6):1282–1284, 1993.

[27] Germano, M., U. Piomelli, P. Moin and W. H. Cabot: *A dynamic subgrid-scale eddy viscosity model.* Phys. Fluids A, 3(7):1760–1765, 1991.

[28] Günther, R.: *50 Jahre Wissenschaft und Technik der Verbrennung.* BWK, 39(9), 1987.

[29] Gropp, W., E. Lusk and A. Skjellum: *MPI-Eine Einführung-Portable parallele Programmierung mit dem Message-Passing Interface.* Oldenbourg Wissenschaftsverlag, München, 2007.

[30] Hahn, F.: *Zur Vorhersage technischer Verbrennungssysteme im Hinblick auf flüssige Brennstoffe.* PhD thesis, Technische Universität Darmstadt, Germany, 2009.

[31] Harlow, F. H. and J. E. Welch: *Numerical calculation of time-dependent viscous incompressible flow of fluid with free surface.* Phys. Fluids, 8:2182–89, 1965.

[32] Hirsch, C.: *Numerical computation of internal and external flows.* John Wiley & Sons, 1990.

[33] Ihme, M. and H. Pitsch: *Prediction of extinction and reignition in nonpremixed turbulent flames using a flamelet/progress variable model: 1. A priori study and presumed PDF closure.* Combust. Flame, 155(1-2):70–89, 2008.

[34] Ihme, M., C. Schmitt and H. Pitsch: *Optimal artificial neural networks and tabulation methods for chemistry representation in LES of a bluff-body swirl-stabilized flame.* Proc. Combust. Inst., 32:1527–1535, 2009.

[35] International Energy Agency (IEA): *World energy outlook*, 2007.

[36] International Energy Agency (IEA): *CO_2 Emissions from Fuel Combustion - Highlights*, 2010.

[37] International Workshop on Measurement and Computation of Turbulent Nonpremixed Flames (TNF). `http://public.ca.sandia.gov/TNF/abstract.html`, 2008.

[38] Jaberi, F. A., P. J. Colucci, S. James, P. Givi and S. B. Pope: *Filtered mass density function for large-eddy simulation of turbulent reacting flows.* J. Fluid Mech., 401:85–121, 1999.

[39] Janicka, J., W. Kolbe and W. Kollmann: *Closure of the transported equation for the probability density function of turbulent scalar fields.* J. Non-Equilib. Thermodynamics, 4:47–66, 1979.

[40] Jayesh and Z. Warhaft: *Probability distribution, conditional dissipation, and transport of passive temperature fluctuations in grid-generated turbulence.* Phys. Fluids A, 4(10):2292–2307, 1992.

[41] Jones, W. P., S. Lyra and S. Navarro-Martinez: *Large Eddy Simulation of a swirl stabilized spray flame.* Proc. Combust. Inst., 33, 2011. In Press, Corrected Proof.

[42] Jones, W. P. and S. Navarro-Martinez: *Large eddy simulation of autoignition with a subgrid probability density function method.* Combust. Flame, 150:170–187, 2007.

[43] Jones, W. P., S. Navarro-Martinez and O. Röhl: *Large eddy simulation of hydrogen auto-ignition with probability density function method.* Proc. Combust. Inst., 31:1765–1771, 2007.

[44] Jones, W. P. and Navarro-Martinez S.: *Numerical Study of n-Heptane Auto-ignition Using LES-PDF Methods.* Flow Turb. Combust., 83:407–423, 2009.

[45] Kempf, A.: *Large-Eddy Simulation of Non-Premixed Turbulent Flames.* PhD thesis, Technische Universität, Darmstadt, Germany, 2003.

[46] Kempf, A., F. Flemming and J. Janicka: *Investigation of lengthscales, scalar dissipation, and flame orientation in a piloted diffusion flame by LES.* Proc. Combust. Inst., 30:557–565, 2005.

[47] Kempf, A., M. Klein and J. Janicka: *A turbulence-chemistry interaction model based on a multivariate presumed beta-PDF method for turbulent flames.* Flow Turb. Combust., 68:111–135, 2002.

[48] Kempf, A., M. Klein and J. Janicka: *Efficient Generation of Initial- and Inflow-Conditions for Transient Turbulent Flows in Arbitrary Geometries.* Flow Turb. Combust., 74:67–84, 2003.

[49] Kempf, A., R. P. Lindstedt and J. Janicka: *Large-eddy simulation of a bluff-body stabilized nonpremixed flame.* Combust. Flame, 144:170–189, 2005.

[50] Ketelheun, A., C. Olbricht, F. Hahn and J. Janicka: *Premixed Generated Manifolds for the Computation of Technical Combustion Systems.* ASME Turbo Expo, Orlando, Florida, USA, (GT2009), 2009.

[51] Kim, J., D. Kim and H. Choi: *An Immersed-Boundary Finite-Volume Method for Simulations of Flow in Complex Geometries.* Jour. Comput. Physics, 171:132–150, 2001.

[52] Klein, M., A. Sadiki and J. Janicka: *A digital filter based generation of inflow data for spatially developing direct numerical or large eddy simulations.* Jour. Comput. Physics, 186:652–665, 2003.

[53] Kolmogorov, A. N.: *The local structure of turbulence in incompressible viscous fluid for very large Reynolds-numbers.* Proc. R. Soc. London A, 434:9–13, 1991.

[54] Kraichnan, R. H.: *Eddy viscosity in two and three dimensions.* J. Atmos. Sci., 33:1521–1536, 1976.

[55] Kuehne, J., A. Ketelheun and J. Janicka: *Analysis of sub-grid PDF of a progress variable approach using a hybrid LES/TPDF method.* Proc. Combust. Inst., 33:1411–1418, 2011.

[56] Kuehne, J., C. Olbricht, A. Sadiki, J. Janicka and J. Y. Chen: *Hybrid LES Monte-Carlo PDF Modeling of Turbulent Piloted Jet Flames.* The 5th International Symposium on Turbulence and Shear Flow Phenomena, Munich, Germany, 2007.

[57] Landenfeld, T.: *Numerische Beschreibung turbulenter Methandiffusionsflammen mit Schließungsmodellen zweiter Ordnung und angenommenen Wahrscheinlichkeitsdichtefunktionen.* PhD thesis, Technische Universität, Darmstadt, Germany, 1999.

[58] Libby, P. A.: *Introduction to Turbulence.* Taylor & Francis, New York, 1996.

[59] Lilly, D. K.: *The representation of small-scale turbulence in numerical simulation experiments.* Proceedings of IBM Scientific Computing Symposium on Environmental Sciences, pages 195–210, 1967.

[60] Lilly, D. K.: *A Proposed Modification of the Germano Subgrid Scale Closure Method.* Phys. Fluids A, 4(3):633–635, 1992.

[61] Maas, U. and Pope S. B.: *Simplifying chemical kinetics: Intrinsic Low-Dimensional manifolds in combustion space.* Combust. Flame, 88:239–264, 1992.

[62] Mallampalli, H., T. H. Fletcher and J. Y. Chen: *Evaluation of CH_4/NO_x Reduced Mechanisms Used for Modeling Lean Premixed Turbulent Combustion of Natural Gas.* Journal of Engineering for Gas Turbines and Power, 120:703–712, 1998.

[63] Masri, A. R., R. W. Bilger, R. W. Dibble, R. S. Barlow, B.B. Dally and D. Fletcher: *Sydney Bluff Body Configuration.* `http://sydney.edu.au/engineering/aeromech/thermofluids/bluff.htm`, 2011.

[64] Masri, A. R., R. W. Dibble and R. S. Barlow: *The Structure of Turbulent Nonpremixed Flames Revealed by Raman-Rayleigh-LIF Measurements.* Prog. Energy Combust. Sc., 22:307–362, 1997.

[65] O'Brien, E. E.: *The probability density function (pdf) approach to reacting turbulent flows.* In Libby, P. A. and F. A. Williams (editors): *Turbulent reactive flows*, pages 185–218. Springer Verlag, 1980.

[66] Oijen, J. van and L. P. H. de Goey: *Modelling of Premixed Laminar Flames using Flamelet-Generated Manifolds.* Combust. Sci. Tech., 161:113–137, 2000.

[67] Oijen, J. van and L. P. H. de Goey: *Modelling of premixed counterflow flames using the flamelet-generated manifold method.* Combust. Theory Modelling, 6(3):463–478, 2002.

[68] Olbricht, C.: *Numerische Berechnung technischer Verbrennungssysteme.* PhD thesis, Technische Universität Darmstadt, Germany, 2009.

[69] Olbricht, C., F. Hahn, A. Ketelheun and J. Janicka: *PDF Modeling Strategies for LES of a Bluff-Body Stabilized Swirl Combustor Using Premixed Generated Manifolds.* The 6th International Symposium on Turbulence and Shear Flow Phenomena, Seoul, Republic of Korea, 2009.

[70] Peters, N.: *Local quenching due to flame stretch and non-premixed turbulent combustion.* Combust. Sci. Technol., 31:1–17, 1983.

[71] Peters, N.: *Laminar diffusion flamelet models in non-premixed turbulent combustion.* Prog. Energ. Combust., 10:319–339, 1984.

[72] Peters, N.: *Laminar flamelet concepts in turbulent combustion.* Proc. Combust. Inst., 21:1231–1250, 1986.

[73] Pierce, C. D. and P. Moin: *Progress-variable approach for large-eddy simulation of non-premixed turbulent combustion.* J. Fluid Mech., 504:73–97, 2004.

[74] Pitsch, H.: *Large-eddy simulation of turbulent combustion.* Annu. Rev. Fluid Mech., 38:453–482, 2006.

[75] Pitsch, H., M. Chen and N. Peters: *Unsteady flamelet modeling of turbulent hydrogen-air diffusion flames.* Proc. Combust. Inst., 27:1057–1064, 1998.

[76] Pitsch, H. and H. Steiner: *Large eddy simulation of a turbulent piloted methane/air diffusion flame (Sandia flame D).* Phys. Fluids, 12(10):2541–2554, 2000.

[77] Pope, S. B.: *A Monte-Carlo Method for the PDF Equations of Turbulent Reactive Flow.* Combust. Sci. Tech., 25:159–174, 1981.

[78] Pope, S. B.: *PDF Methods for Turbulent Reactive Flow.* Prog. Energy Combust. Sci., 11:119–192, 1985.

[79] Pope, S. B.: *Turbulent Flows.* Cambridge, UK: Cambridge University Press, 2000.

[80] Prandtl, L.: *Bericht über die Entstehung der Turbulenz.* Zeitschrift für Angewandte Mathematik und Mechanik, 5:136–139, 1925.

[81] Raman, V. and H. Pitsch: *A consistent LES/filtered density function formulation for the simulation of turblent flames with detailed chemistry.* Proc. Combust. Inst., 31:1711–1719, 2007.

[82] Raman, V., H. Pitsch and R. O. Fox: *Hybrid large-eddy simulation/Lagrangian filtered-density-function approach for simulating turbulent combustion.* Combust. Flame, 143(1-2):56–78, 2005.

[83] Reynolds, O.: *III. An experimental investigation of the circumstances which determine wether the motion of water shall be direct or sinuous, and of the law of resistance in parallel channels.* Phil. Trans. R. Soc. London, 174(935), 1883.

[84] Reynolds, O.: *IV. On the dynamical theory of incompressible viscous fluids and the determination of the criterion.* Phil. Trans. R. Soc. London A, 186(123), 1894.

[85] Rhodes, R. P.: *A probability distribution function for turbulent flows.* In Murthy, S. N. B. (editor): *Turbulent mixing in nonreactive and reactive flows*, pages 235–241. Plenum Press, New York, 1975.

[86] Richardson, L. F.: *Weather Prediction by Numerical Process.* Cambridge University Press, Cambridge UK, 1922.

[87] Sabelfeld, K.: *Monte Carlo methods in boundary value problems.* Springer Verlag, Berlin, 1991.

[88] Sabel'nikov, V. and O. Soulard: *Rapidly decorrelating velocity-field model as a tool for solving one-point Fokker-Planck equations for probability density functions of turbulent reactive scalars.* Phys. Rev. E, 72(1), 2005. doi:10.1103/PhysRevE.72.016301.

[89] Schäfer, M.: *Numerik im Maschinenbau.* Springer Verlag, Berlin, 1999.

[90] Schmitt, L.: *Numerische Simulation turbulenter Grenzschichten (Large-Eddy-Simulation) Teil 1.* Bericht 82/2, 1982. Lehrstuhl für Strömungsmechanik, Technische Universität München.

[91] Schneider, C., A. Dreizler and J. Janicka: *Flow Field Measurements of Stable and Locally Extinguishing Hydrocarbon-Fuelled Jet Flames.* Combust. Flame, 135:185–190, 2003.

[92] Schumann, U.: *Subgrid scale model for finite difference simulations of turbulent flows in planar channels and annuli.* Jour. Comput. Physics, 18:376–404, 1975.

[93] Schumann, U. and R. Sweet: *A direct method for the Poisson's equation with Neumann boundary conditions on a staggered grid of arbitrary size.* Jour. Comput. Physics, 20:171–182, 1976.

[94] Sheikhi, M. .R. .H., T. G. Drozda, P. Givi, F. A. Jaberi and S. B. Pope: *Large eddy simulation of a turbulent nonpremixed piloted methane jet flame (Sandia Flame D).* Proc. Combust. Inst., 30:549–556, 2005.

[95] Shvab, V. A.: *Relation between the temperature and velocity fields of the flame of a gas burner.* Gos. Energ. izd. M.-L., 1948. In Russian: Issledovanie protessov gorenia naturalnogo topliva.

[96] Smagorinsky, J.: *General circulation experiments with the primitive equations - I. The basic experiment.* Monthly Weather Rev., 91(3):99–164, 1963.

[97] Smith, G.P., D. M. Golden, M. Frenklach, N. W. Moriarty, B. Eiteneer, M. Goldenberg, C. T. Bowman, R. K. Hanson, S. Song, W. C. Gardiner, Jr., V. V. Lissianski and Z. Qin: *GRI-Mech 3.0.* `http://www.me.berkeley.edu/gri_mech/`, 1999.

[98] Smooke, M. D.: *Reduced kinetic mechanisms and asymptotics approximations for methane-air flames.* Lecture notes in physics, 384, 1991. Springer, New York.

[99] Somers, B.: *The simulation of Flat Flames with detailed and Reduced Chemical Models.* PhD thesis, Technische Universiteit, Eindhoven, The Netherlands, 1994.

[100] Subramanian, S. and S. B. Pope: *A Mixing Model for Turbulent Reactive Flows based on Euclidean Minimum Spanning Trees.* Combust. Flame, 115(4):487–514, 1998.

[101] Valino, L.: *A Field Monte Carlo Formulation for Calculating the Probability Density Function of a Single Scalar in a Turbulent Flow.* Flow Turb. Combust., 60:157–172, 1998.

[102] Vreman, A. W., B. A. Albrecht, J. A. van Oijen, L. P. H. de Goey and R. J. M. Bastiaans: *Premixed and nonpremixed generated manifolds in large-eddy simulation of Sandia flame D and F.* Combust. Flame, 153(3):394–416, 2008.

[103] Warnatz, J., U. Maas and R. W. Dibble: *Verbrennung: physikalisch-chemische Grundlagen, Modellierung und Simulation, Experimente, Schadstoffentstehung.* Springer Verlag, Berlin, third edition, 2001.

[104] Wegner, B.: *A Large-Eddy Simulation Technique for the Prediction of Flow, Mixing and Combustion in Gas Turbine Combustors.* PhD thesis, Technische Universität Darmstadt, Germany, 2006.

[105] Williams, F. A.: *Recent advances in theoretical descriptions of turbulent diffusion flames.* In Murthy, S. N. B. (editor): *Turbulent mixing in nonreactive and reactive flows*, pages 189–208. Plenum Press, New York, 1975.

[106] Williamson, J.: *Low-storage Runge-Kutta Schemes.* Jour. Comput. Physics, 35:48–56, 1980.

[107] Zel'dovich, Y. B.: *On the theory of combustion of initially unmixed gases.* Zhur. Tekh. Fiz., 19(10):1199–1210, 1949. In Russian: K Teorii Gorenia Neperemeshannykh Gazov; Engl. translation: NACA Tech. Memo. No 1296, 1951.

[108] Zhou, G.: *Numerical simulations of physical discontinuities in single and multi-fluid flows for arbitrary mach numbers.* PhD thesis, Chalmers University of Technology, Sweden, 2009.

[109] Zhou, G., L. Davidson and E. Olsson: *Transonic inviscid/turbulent airfoil flow simulations using a pressure based method with high order schemes.* Lecture notes in physics, 453:372–377, 1995. Springer, New York.

Lebenslauf

Name	Jens Kühne	
Geburtsdatum	20. Februar 1980	
Geburtsort	Ehringshausen	
Schulbildung	08/1996 – 07/1999	**Goetheschule Wetzlar** Allgemeine Hochschulreife
Zivildienst	08/1999 – 07/2000	**Königsberger Diakonie, Wetzlar** Alten- und Pflegeheime
Studium	10/2000 – 04/2006	**Technische Universität Darmstadt** Fachrichtung: Allgemeiner Maschinenbau Vertiefungen: Energietechnik, Thermodynamik, Strömungen, Verbrennung, Numerische Simulation
	09/2002	Vordiplom
	04/2006	Abschluss zum Dipl.-Ing.
Wissenschaftlicher Mitarbeiter	seit 05/2006	**Technische Universität Darmstadt** Wissenschaftlicher Mitarbeiter am Fachgebiet Energie- und Kraftwerkstechnik (EKT)